Institut für Erd- und Umweltwissenschaften
Mathematisch-Naturwissenschaftliche Fakultät
Universität Potsdam

# Fault interaction at different time- and length scales: The North Tehran Thrust and Mosha-Fasham Fault (Alborz mountains, Iran)

**Dissertation**
zur Erlangung des akademischen Grades
Doktor der Naturwissenschaften (*Dr. rer. nat.*)
in der Wissenschaftsdisziplin Geologie

eingereicht an der Mathematisch-Naturwissenschaftlichen Fakultät
der Universität Potsdam

Angela Landgraf

Potsdam im Juli 2010

# Acknowledgements

First of all, I would like to thank my supervisor, Manfred Strecker, for continuous support, encouragement, and scientific guidance from the very first research idea towards this final of a PhD thesis. While the German government just started to improve the situation for parents in science, Manfred Strecker has realized this already and I especially appreciate his understanding for these sometimes special circumstances. I would also like to thank Anke Friedrich, who helped developing this project and watched it proceed while she was on her way from Potsdam via Hannover to Munich. Her encouragement and enthusiasm has bridged one or another low during the time of the thesis.

I would like to thank my colleague and friend Paolo Ballato for the great time we had conducting field work, surviving the Tehran traffic (jam), for endless discussions, for the secrets of good coffee, and continuous motivation during the past years.

I thank our Iranian colleagues, friends, and their families, especially Saeid Tabatabaei, Majid Shahpasandzadeh, Mohammad Ghassemi, Mahdi Hekmatnia, Yahya Djamour, H. Mirzaei, and M. Shakeri, as well as Babak and the drivers of the Shakeri-team. I highly appreciate the great opportunity to experience your way of living in Iran and the rich culture, your country inheres. I'm glad to have learned about the generosity and hospitality of the Iranians allowing me a more detailed view on this far and conflicting part of the world.

I thank Ramon Arrowsmith for his support, great discussions, and encouragement. Thank you very much for inviting me to work at ASU, which not only permitted the modeling part of this study, but also gave me the opportunity to being involved in trenching the San Andreas fault at Parkfield. In this regard, I'm especially grateful to Nathan Toké, who shared his knowledge about paleoseismology with me and became a friend during the months in Arizona and the long, but spectacular drive home from San Francisco. I would like to thank Kelin Whipple for sharing his knowledge in advanced geomorphology, and Olaf Zielke for continuous supply on add-on's to FIMoz, whenever it was needed. Thanks for enriching the time in Arizona also to Dave, Erin, Meagan, Melanie and Josh, and the team of the McKemy Middle school.

I've been introduced into the amazing world of neutrons and muons (reminding me that such little things can shape the world) by Lucilla Benedetti, Regis Braucher, Didier Bourlès, Silke Merchel and Irene Schimmelpfennig at CEREGE in Aix en Provence. Moreover, they always provided me a great stay at their institute, their labs or even their homes. Further thanks for discussions go to Bob Finkel and the Chronus EU summerschool in Hungary and for assistance in the lab to Khemrak Pou and Laetitia Lëanni.

At various stages during the PhD-study, partly in the course of the Institutskolloquium, I've had the opportunity to discuss my work with assigned specialists in the fields of earthquake geology and tectonic geomorphology. This work has benefitted from discussions with Jean-Francois Ritz, James Jackson, Alex Densmore, Bodo Bookhagen, George Hilley, and Florian Kober.

I thank Antje Musiol, Christine Fischer, and Christina Günther for various support with chemical analysis and mechanical preparation; Margit Wieprich, Dana Pilz, Sabrina Andrae for help with the mineral separation and lab work; Birgit Fabian for applying magic to some of my figures, and Ines Münch and Rene Muschkorgel for killing viruses, saving hard drives and thus rescuing the thesis from virtual plagues.

In Golm, at the University of Potsdam, so many have contributed to the successful accomplishment of this work and in providing a good time that it is impossible to thank everyone. In particular, I would like to mention Matthias Ohrnberger, Sebastian Hainzl, and Frank Krüger, Martin Trauth, Daniel Vollmer, Rasmus Thiede, and Gerold Zeilinger. Special thanks to my office mates from “Das schöne Büro”, for keeping me awake, making me laugh, and for submitting me Nele's messages whenever she couldn't reach me!

I would like to thank my family for continuous support, never questioning the big step from being a nurse to become a geologist. I'm especially grateful for the logistical support and the caring compensation they offer to look after Nele, when I'm and her dad are coevally abroad. Special thanks also to Joachim, Dana, Manu and Reyko, Esther, and Sabine for being around me.

Financial support was provided by the German Research Foundation (Leibniz Award to M. Strecker and grant STR 373/19-1 to M. Strecker and A. Friedrich), and the German Academic Exchange Service (DAAD-D/07/42739).

Finally, as much as I love to be in the field, to meet different people and their culture and to see new parts of the world, as much I appreciate to come home afterwards. You, Nele, are my best reason for it. I admire and thank you for your flexibility in dealing with my repeated absences during field or lab work. I hope that soon you will also understand my excitement for geology.

# Abstract

The seismically active Alborz mountains of northern Iran are an integral part of the Arabia-Eurasia collision zone and offer an excellent opportunity to study continental faults and their interaction at various time and length scales. Linked strike-slip and thrust/reverse-fault systems in this mountain belt are characterized by slow loading rates, and large earthquakes are highly disparate in space and time. Similar to other intracontinental deformation zones such a pattern of tectonic activity is still insufficiently understood, because recurrence intervals between seismic events may be on the order of thousands of years, and are thus beyond the resolution of short-term measurements based on GPS, InSAR or instrumentally recorded seismicity.

This study bridges the gap of deformation processes on different time scales. In particular, my investigation focuses on deformation on the Quaternary time scale, beyond present-day deformation rates, and it uses present-day and paleotectonic characteristics to model fault behavior. The study includes data based on structural and geomorphic mapping, fault-kinematic analysis, DEM-based morphometry, and numerical fault-interaction modeling. In order to better understand the long- to short term behavior of such complex fault systems, I used geomorphic surfaces as strain markers and dated fluvial and alluvial surfaces using terrestrial cosmogenic nuclides (TCN, $^{10}$Be, $^{26}$Al, $^{36}$Cl) and optically stimulated luminescence (OSL). My investigation focuses on the seismically active Mosha-Fasham fault (MFF) and the seismically virtually inactive North Tehran Thrust (NTT), adjacent to the Tehran metropolitan area.

The results show that the deformation field has changed over time. Fault-kinematic data reveal an early mechanical linkage of the NTT and MFF during an earlier dextral transpressional stage, when the shortening direction was oriented northwest. This regime was superseded by Pliocene to Recent NE-oriented shortening, which caused thrusting and sinistral strike-slip faulting. In the course of this kinematic changeover, the NTT and MFF were reactivated and incorporated into a nascent transpressional duplex, which has significantly affected landscape evolution in this part of the range. Two of three distinctive features which characterize topography and relief in the study area can be directly related to their location inside the duplex array and are thus linked to interaction between eastern MFF and NTT, and between western MFF and Taleghan fault, respectively. The close agreement between vertical displacement calculated from fault-interaction modeling and real topography and relief, calculated from an SRTM based DEM, suggests that such fault interaction results in both, short-term and long-term effects.

To account for inferred inherited topography from the previous dextral-transpression regime, a new concept of tectonic landscape characterization has been used. Accordingly, I define simple landscapes as those environments, which have developed during the influence of a sustained tectonic regime. In contrast, composite landscapes contain topographic elements inherited from previous tectonic conditions that are inconsistent with the regional

present-day stress field and kinematic style. Using numerical fault-interaction modeling with different tectonic boundary conditions, I calculated synoptic snapshots of artificial topography to compare it with the real topographic metrics. However, in the Alborz mountains, E-W faults are favorably oriented to accommodate the entire range of NW- to NE-directed compression. These faults (western MFF and Taleghan Fault) show the highest total displacement, as reflected by basement-involved faulting and exhumation, which might indicate sustained faulting under changing boundary conditions as suggested by the models.

In contrast to the fault system within and at the flanks of the Alborz mountains, Quaternary deformation in the adjacent Tehran plain is characterized by oblique motion and thrust and strike-slip fault systems. In this morphotectonic province fault-propagation folding along major faults, limited strike-slip motion, and en-échelon arrays of second-order upper plate thrusts are typical. While the Tehran plain is characterized by young deformation phenomena, the majority of faulting took place in the early stages of the Quaternary and during late Pliocene time. TCN-dating, which was performed for the first time on geomorphic surfaces in the Tehran plain, revealed that the oldest two phases of alluviation (units A and B) must be older than late Pleistocene. Due to an unexpectedly high terrace denudation rate, steady-state conditions of the nuclide concentrations are reached early. The oldest dated surface at the location Saboo is 195 ka old. From abandonment of late Pleistocene fluvial terraces, I have calculated a mean incision rate of 0.7 mm/a for rivers that drain the east and west of the Tehran plain, respectively.

A deviation from this trend are pulses of increased Holocene incision that might be related to repeated earthquake ruptures. The corresponding vertical offsets creating fluvial knickpoints and straths in longitudinal stream profiles has been calculated to be 0.58 m and 2.10 m. From these relationships, associated moment magnitudes of 6.74 and 7.19, respectively, were calculated. Although rupture can be inferred for areas near the eastern tip of the NTT, the entire length of this fault may have been affected. With regards to fault interaction between NTT and MFF, it is reasonable that slip on the eastern MFF segment has been transferred onto the NTT. This allows higher average and maximum slip at the NTT tip, i.e., the position of the inferred paleo-earthquakes. While urban development in Tehran increasingly covers and obliterates the active fault traces, the present-day kinematic style, the vestiges of formerly undeformed Quaternary landforms, and paleo-earthquake indicators from the last millennia attest to the threat that these faults and their related structures pose for the megacity.

# Zusammenfassung

Das seismisch aktive Elburs Gebirge im Nordiran ist Bestandteil der Arabisch-Eurasischen Kollisionszone und ist für die Untersuchung kontinentaler Schwächezonen und ihrer Interaktion auf verschiedenen zeitlichen und räumlichen Skalen hervorragend geeignet. Gekoppelte Blattverschiebungs- und Überschiebungssysteme dieses Gebirges zeichnen sich durch geringe Spannungsaufbauraten aus. Dementsprechend treten große Erdbeben räumlich und zeitlich weit verteilt voneinander auf. Diese Muster tektonischer Aktivität in Intraplattenbereichen sind nur unzureichend verstanden, da die Wiederkehrperioden solcher Erdbeben tausende von Jahren dauern können und nicht von kurzzeitigen Messmethoden, wie GPS, InSAR oder instrumenteller Seismologie erfasst werden.

Diese Arbeit überbrückt verschiedene Zeitskalen. Meine Untersuchungen konzentrieren sich auf Quartäre Deformation, jenseits heutiger Verformungsraten, aber auch auf heutige und paläotektonische Charakterisierungen der Schwächezonen. Diese Studie beinhaltet insbesondere Auswertungen struktureller und geomorphologischer Kartierungen, störungskinematische Analysen, auf digitalen Höhenmodellen basierende Morphometrie und numerische Modellierung von Störungsinteraktion. Um das lang- und kurzfristige Verhalten solcher komplexen Schwächezonen besser zu verstehen, benutze ich geomorphologische Oberflächen als Deformationsmarker und datiere alluviale und fluviatile Oberflächen mittels kosmogener Nuklide (TCN, $^{10}$Be, $^{26}$Al, $^{36}$Cl) und optisch stimulierter Lumineszenz (OSL). Mein Untersuchungsgebiet umfasst die seismisch aktive Mosha-Fasham Störung (MFF) und die als seismisch quasi inaktiv geltende Nordteheranstörung (NTT), die sich in unmittelbarer Nähe zum Teheraner Ballungsgebiet befinden.

Die Ergebnisse zeigen, dass sich das Deformationfeld mit der Zeit verändert hat. Die störungskinematischen Daten haben ergeben, dass NTT und MFF bereits seit einer früheren dextral-transpressionalen Phase unter NW-gerichteter Einengung mechanisch gekoppelt sind. Dieses System wurde von pliozäner und bis heute andauernder NE-gerichteter Einengung ersetzt, woraufhin sich Überschiebungen und linkslaterale Blattverschiebungen herausbildeten. Während dieses kinematischen Wechsels wurden NTT und MFF reaktiviert und in ein beginnendes transpressionales Duplexsystem eingebunden, welches die Landschaftentwicklung in diesem Teil des Gebirges signifikant beeinflusst hat. Zwei von drei ausgeprägten topographischen Besonderheiten des Untersuchungsgebietes können direkt mit deren Lage in der Duplexanordnung in Verbindung gebracht werden und spiegeln Interaktion zwischen den östlichen Segmenten von NTT und MFF, bzw., zwischen dem westlichen Segment der MFF und der parallelen Taleghan Schwächezone wider. Die hervorragende Übereinstimmung zwischen dem modellierten vertikalen Versatz und der aus den digitalen Höhendaten berechneten Topographie und Relief lassen vermuten, dass es sich bei der Interaktion der Schwächezonen sowohl um ein kurzfristiges, als auch ein langfristiges Phänomen handelt.

Um diejenige Topographie auszuweisen, die möglicherweise aus der vorhergehenden dextraltranspressionalen Phase vererbt wurde, wurde ein neues Konzept tektonischer Landschaftscharakterisierung benutzt. Demnach definiere ich einfache Landschaften als diejenigen Umgebungen, die unter dem Einfluß gleichbleibender tektonischer Randbedingungen entstanden sind. Dagegen enthalten zusammengesetzte Landschaften vererbte Elemente vergangener tektonischer Randbedingungen, die mit dem heutigen Spannungsfeld und kinematischen Stil unvereinbar sind. Mittels numerischer Störungsinteraktionsmodellierungen teste ich verschiedene Randbedingungen und berechne synoptische Momentaufnahmen künstlicher Topographie um sie mit reellen topographischen Maßen zu vergleichen. Im Elburs Gebirge treten allerdings auch E-W streichende Schwächezonen auf, die so günstig orientiert sind, dass sie Verformung unter der gesamten Einengungsspanne von Nordwest nach Nordost zeigen. Diese Störungen (westliche MFF und Taleghan Störung) weisen den höchsten totalen Versatz auf. Hier tritt das Grundgebirge zutage und wird versetzt, was, wie die Modellierunegn vermuten lassen, auf langanhaltende Verformung unter sich ändernden Randbedingungen hinweisen kann.

Quartäre Deformation in der benachbarten Teheran Ebene ist durch Schrägbewegungen, Überschiebungen und Blattverschiebungssyteme gekennzeichnet, die typischerweise in Auffaltungen entlang von Hauptstörungen, vereinzelten Blattverschiebungen und en-échelon Anordnungen untergeordneter oberflächlicher Überschiebungen resultieren. Junge Deformation tritt auf, die Hauptbewegungen fanden allerdings im frühen Quartär und wahrscheinlich späten Pliozän statt. TCN-Datierungen, die erstmalig an geomorphologischen Oberflächen in der Teheran Ebene durchgeführt wurden, ergeben dass die beiden älteren Sedimentationsphasen (Einheiten A und B) älter sind als spätes Pleistozän. Aufgrund unerwartet hoher Terrassenabtragungsraten erreichen die Nuklidkonzentrationen früher das Sättigungsgleichgewicht. Die älteste direkt datierte Terrasse nahe Saboo ist 195.000 Jahre alt. Aus der Einschneidung der Flußterrassen mit spätpleistozänem Alter konnte ich eine Hintergrundeinschneidung von 0,7 mm/a berechnen.

Davon abweichend treten im Holozän Impulse verstärkter Einschneidung auf, die möglicherweise mit wiederholtem Versatz durch Erdbeben zusammenhängen. Der entsprechende vertikale Versatz, wurde mit 0,58 und 2,1 m bestimmt, tritt allerdings nahe des östlichen Endes der NTT auf. Aufgrund der zu erwartenden Störungsinteraktion zwischen NTT und MFF ist es durchaus möglich, dass Versatz von der MFF auf die NTT übertragen wird. Das ermöglicht höhere Versatzbeträge nahe des NTT-Endpunktes. Unter der Annahme einer Oberflächenruptur entlang der gesamten Störungslänge ergibt sich eine Momentenmagnitude von 6,74, bzw., 7,19. Obwohl die urbane Entwicklung im Teheraner Ballungsraum die aktiven Störungslinien zunehmend verdeckt und ausradiert, zeugen der heutige kinematische Stil, die Überreste ehemals unverstellter Quartärer Landschaftsformen und Hinweise auf Paläoerdbeben während der letzten Jahrtausende von der Gefahr, die diese Schwächezonen und deren Strukturen für die Megastadt bedeuten.

# Contents

# List of Figures

# List of Tables

# Chapter 1

# Introduction

Increasing evidence for large earthquakes in continental interiors far away from plate boundaries and regions with low deformation rates demonstrates that such environments are subjected to earthquakes of considerable size, which might cause catastrophic damage (e.g., Tuttle & Schweig, 1995; Johnston, 1996a; Johnston & Schweig, 1996; Crone et al., 1997; Camelbeeck & Meghraoui, 1998; Camelbeeck et al., 2000; Rastogi et al., 2001; Crone et al., 2003; Singh et al., 2004). While the importance of these types of earthquakes is generally recognized now, the recurrence intervals of such events are often poorly known and are typically on the order of thousands to ten thousands of years, thus beyond the time scale covered by instrumental recordings or historic accounts. The level of tectonic activity in these environments is also very difficult to assess, because the location of these earthquakes often involves inherited zones of crustal weakness and is spatially variable. Short-term indicators of tectonic deformation such as space-geodetic techniques (GPS, InSAR) and instrumentally recorded seismicity have not yet measured complete deformation cycles and only provide insufficient datasets to understand the present-day and long-term tectonic characteristics of intraplate or low-strain regions (e.g., Friedrich et al., 2003; Stein & Liu, 2009; Stein et al., 2009). Furthermore, even in densely populated parts of central Europe with a long history of written documents, such as the Lower Rhine Embayment, records of historical seismicity span no more than two thousand years, which is insufficient to constrain the size of the largest possible earthquakes or return period by statistical techniques alone (e.g., Schmedes, et al., 2004; Fäh et al., 2009). The low level of seismic activity and the scarcity of empirical data are thus major obstacles in correctly evaluating and understanding such highly disparate and diachronous tectonic deformation. Furthermore, especially in mid-continent settings, it has been observed that large magnitude events might be clustered along specific faults for a while, and then migrate to others, such that clusters in the past few thousand years do not necessarily reflect the long-term fault behavior (Stein et al., 2009). It is possible that such faults "turn on" and "turn off" on time scales of hundreds to thousands of years, an effect that probably results from transient stress migration and interaction between faults in a region (Stein et al., 2009). Because faults are loaded at very slow rates in continental interiors, such interaction can give rise to earthquakes on other faults after a long period of quiescence and seismicity can migrate from one fault to the other. Slow loading rates also affect the duration of aftershocks, i.e., the reloading does not overwhelm the effects of the main shock and aftershocks can last for several hundreds of years (Stein & Liu, 2009), complicating the seismic characterization of a region. To overcome this dilemma, a rigorous identification and characterization of regions experiencing intraplate earthquakes is required. Observations concerning recent events and timescales of $10^3$ to $10^4$ years need to be integrated with long-term geological processes in order to compare and assess short- and medium-term processes and deformation rates, respectively. This is a major challenge in the geosciences and requires the integration of different datasets covering a variety of time and length scales and involving a broad set of methods spanning structural field observations, landform analysis, assessment of kinematic fault behavior, modeling fault interaction, and geochronology. This thesis addresses most of these aspects.

The key objective of this study is to characterize the spatio-temporal behavior of such faults in the Alborz mountains of seismically active northern Iran. Current crustal deformation is related to the Arabian-Eurasian continental collision, which is part of the Alpine-Himalayan orogeny, where a portion of convergence is absorbed by significant intraplate deformation along major fault systems (e.g., Molnar & Tapponnier, 1975; Jackson & McKenzie, 1984; Hancock & Skinner, 2000). The Alborz range is located several hundreds of kilometers north of the suture between the Arabian and Eurasian plates. The mountain range is part of the Eurasian continental interior, which is an assemblage of multiple terranes that have been attached in repeated phases since more than 200 million years ago (e.g., Stampfli & Borel, 2002; Moix et al., 2007). This assemblage is probably the reason why some areas of the larger convergence zone are actively deforming and other blocks are quasi-stable. Thus, as tectonic setting, the Alborz mountains differ from clear intraplate zones as the New Madrid area, but can be considered as a diffuse plate-boundary zone, comparable to the Basin and Range of the western USA, where loading rates are low and deformation is spatially and temporally distributed (Stein & Liu, 2009).

In Iran, deformation is expressed in spectacular, thrust-fault bounded, high-relief mountain ranges and activity along strike-slip fault systems. There is ample evidence that such fault systems are active now or have been repeatedly active during the recent past. Four out of the forty worst global natural catastrophes in terms of victims between 1970 and 2008 were caused by Iranian earthquakes (Enz et al., 2009). Importantly, these four events were distributed across the whole country and were partly related to hitherto unrecognized faults or occurred in regions known to have been seismically quiescent for centuries (Berberian, 1979; Mohajer-Ashjai & Nowroozi, 1979; Berberian et al., 1992; Gao & Wallace, 1995). This underscores the importance of mid- to long-term geological investigations along faults with known Quaternary activity, but also points at the possibility of limited preservation of earthquake-related landforms in such low-strain environments even in an arid climate.

Geological and geomorphic analysis will thus play a crucial role to constrain the potential for large earthquakes in regions with highly disparate and diachronous tectonic deformation. The increased availability of new dating techniques, including cosmogenic radionuclides, digital topography, and remote sensing data have enriched tectonic and geomorphologic methodology and now enable us to investigate such issues on different spatial and temporal scales with a much higher temporal resolution compared to previous efforts. Accordingly, I have combined extensive fieldwork, structural and geomorphic fault-kinematic analysis, morphometry using digital topography, boundary element modeling, as well as cosmogenic nuclide dating of Pleistocene and Holocene deposits to analyze landscape evolution in response to tectonic deformation on short- to intermediate time scales.

Following the Introduction, I will give a brief overview of the striking range-wide orographic characteristics, which impressively reflect the large-scale tectonic and climatic interplay and which help to illustrate the orogen-wide pattern of tectonic activity. Subsequently, the main study focus on a smaller area along the southern border of the central Alborz mountains, in the greater Tehran area. Two prominent faults with a disputed seismic history there are the North Tehran Thrust (NTT), immediately north of Tehran, and the Mosha-Fasham Fault (MFF) to the east. Destructive historical earthquakes and the vestiges of long-term tectonic deformation contrast virtual instrumental seismic quiescence along most of the faults. Based on these issues I asked the following research questions that formed the framework of this study.

(1) What is the kinematic relationship between the NTT and MFF? How is the deformation distributed along these faults in space and time? (2) Does the long-term deformation pattern help explain the current and short-term tectonic behavior?

This thesis is organized into three main chapters that address the evolution of the North Tehran Fault and its linkage with the Mosha-Fasham Fault or deformation in the Tehran plain foreland, respectively (Chapters 3-6).

Chapter 3 is primarily based on field work and combines fault-kinematic with geomorphic and morphometric analysis in order to reveal the kinematic history of the major faults in the study area. Combined, the newly obtained data suggest an early mechanical linkage of the NTT and MFF fault systems during a former dextral transpressional stage, during regional NW-directed shortening. During subsequent NE-oriented shortening, the NTT and MFF were reactivated and incorporated into a nascent transpressional duplex. The youngest manifestation of motion in this system is ongoing extension in a field of sinistral transtension. However, this deformation must be very young. It is not observed everywhere and has not yet resulted in topographic inversion. This chapter (*''Fault-kinematic and geomorphic observations along the North Tehran Thrust and Mosha Fasham Fault, Alborz mountains Iran: implications for fault-system evolution and interaction in a changing tectonic regime''* by Angela Landgraf, Paolo Ballato, Manfred R. Strecker, Anke M. Friedrich, Saeid H. Tabatabaei, and Majid Shahpasandzadeh) was published in the Geophysical Journal International, 177(2), 676-690.

Chapter 4 (*"Differentiating simple and composite tectonic landscapes using numerical fault-slip modeling. Insights from the south-central Alborz mountains, Iran"* by Angela Landgraf, Olaf Zielke, J. Ramon Arrowsmith, Paolo Ballato, Manfred R. Strecker, Anke M. Friedrich, and Saeid H. Tabatabaei) is in preparation for re-submission to the Journal of Geophysical Research - Earth Surface. In this chapter, I use numerical simulations to determine the vertical displacement field caused by mechanically interacting faults that are subjected to a uniform tectonic stress field. For this study, I have implemented those faults which correspond to the duplex structure described in Chapter 3. Because of the change in the direction of $S_{Hmax}$, this study addresses the question as to what extent the present-day topography still reflects the influence of the old stress field, and which topographic elements are indicative of the recent stress field and thus the presently active tectonism. To address this issue, I have introduced the definitions of simple (tectonic) landscapes (compatible with motion on currently active faults) and composite landscapes. The latter also comprise additional landscape elements that are inherited and unrelated to active deformation. While progressively rotating the axis of maximum horizontal stress ($S_{Hmax}$) in the structural model setup, I produce a synoptic overview of simple landscapes and compare them with topographic features of the real composite landscape in the south-central Alborz mountains. I am able to show that topographic residuals, calculated from Digital Elevation Models (DEMs), reveal distinct zones of inferred high rock-uplift rates in the south-central Alborz. Certain areas of high elevation and rock-uplift rates can only be reproduced under a restricted range of $S_{Hmax}$-directions. The long-lived, steep Mosha Fasham Fault is able to maintain a predominant left-lateral motion under NE-directed $S_{Hmax}$, while in general, the fault array accommodates NNE-oriented shortening. However, the faults bounding the Taleghan range in the orogen interior are less indicative of changes in the $S_{Hmax}$-direction. This area of inferred inherited topography is favorably oriented to undergo reactivation under a wide range of NW- to NE-directed compression.

Chapter 5 (*"Quaternary deformation and landscape evolution in the greater Tehran area"* by Angela Landgraf, Lucilla Benedetti, Regis Braucher, Didier Boules, Irene Schimmelpfennig, Silke Merchel, Paolo Ballato, Manfred R. Strecker, and Anke M. Friedrich) will be submitted to the Geophysical Journal International. Here, I use cosmogenic radionuclide dating (TCN), field work, as well as geomorphic airphoto mapping to reveal a relative chronology of deformation in the Tehran plain. Because the typical target mineral for TCN dating, quartz, is rare and the surfaces are subjected to relatively high denudation rates, I have used a new approach of separating quartz and calcite from the same set of amalgamated depth profile samples and analyzing them separately using $^{10}$Be and $^{36}$Cl, respectively. This approach gives some additional details of differential erosion processes on the abandoned surfaces. Furthermore, the dating clearly shows that because of erosion, surface sampling alone is insufficient to define the age of the associated geomorphic surfaces. The Tehran plain shows evidence for Quaternary left-oblique and pure thrusting, displacing Quaternary fluvial sediments and alluvial fan deposits. The western sector of the plain is deforming by (partly blind) thrusting, as manifested by segmented and internally deformed anticlines and abandoned and diverted channels on both sides of this structure. The recency of faulting at depth and corresponding surface deformation can be inferred from $^{10}$Be-dating of an adjacent river terrace and possibly postdates 25 ka. The central sector of the plain, which forms the substratum of the Tehran megacity, is affected by thrusting and left-lateral strike-slip faulting and contains several sets of uplifted fluvial terraces. These terraces and the associated deformation pattern are reminiscent of a transpressional foreberg structure. Chi-squared-fitting of a TCN depth profile reveals that the second-highest terrace level is in steady-state, yielding an effective age of about 195 ka, hence indicating a Pleistocene or older deformation age. In contrast to these environments, the eastern footwall of the NTT is affected by left-transtension, possibly related to either the left-bending of the NTT or a horsetail-termination of eastern NTT strike-slip faulting. The topography reflects the geometry of a relay ramp with an elevated footwall, which progressively decreases in elevation towards the west, and terraces which become increasingly abandoned westward. The second highest terrace level of this ramp-structure is about 195 ky old, as independently determined by Chi-squared-fitting of $^{10}$Be and $^{36}$Cl-depth-profiles, indicating activity since at least the middle Pleistocene. Where the eastern NTT bounds this structure, a channel is currently incising a dioritic sill, forming a pronounced knickpoint and leaving behind two abandoned narrow bedrock channels at 5 m and 1.70 m above the recent channel. $^{36}$Cl dating of these paleo-channels resulted in ages of 3290±408 and 1591±223 years, respectively. This could indicate pulsed Holocene incision related to dip-slip motion of the NTT. In any case, although the manifestations of ongoing deformation along the NTT are scarce, numerous faults and deformed Quaternary units in its footwall and in the Tehran plain unambiguously demonstrate that this region is tectonically active, although perhaps not on time scales spanning the ultimate millenia.

Finally, Chapter 6 comprises the principle conclusions and an outlook for future work in the region.

# Chapter 2

# Orography, climate, and distribution of rock-uplift in the Central Alborz mountains

The use of high-resolution remote sensing and digital elevation data (DEM) has enriched the tools to analyze surface geomorphology and tectonics and their related physical processes on various spatial scales. Here, we use DEMs derived from the Shuttle Radar Topography Mission (SRTM) in order to visualize the topography and to calculate the channel response to orographic boundary conditions as tectonism and orographic precipitation on the orogen scale. The Alborz mountain chain in northern Iran is an integral part of the wide deformation zone of the Alpine-Himalayan belt, the archetypical collisional orogen, assembled of different fragments of Gondwana which have successively collided with Eurasia (e.g., Horton et al., 2008). In Iran, this deformation is related to the Arabian-Eurasian continental collision, which is accommodated by shortening and strike-slip faulting in the Zagros, the Alborz and Kopeh Dagh mountains, as well as the Aspheron Sill in the Caspian Sea, and is documented by widespread seismicity (e.g., Jackson & McKenzie, 1984). These seismically active regions are separated by relatively rigid, aseismic crustal blocks, such as the South Caspian Basin, Central Iran, and the Lut Block (Fig. 2.1). While the majority of earthquakes is fairly distributed across the entire Zagros range, the Alborz mountains show few and spatially more disparate events, but also higher magnitudes (Fig. 2.1).

The Alborz mountains constitute a doubly verging orogen, which straddles the South Caspian basin in an arcuate shape (Fig. 2.2A). This shape is conditioned by the strike of the main faults: NW-SE in the west and NE-SW to ENE-WSW in the eastern part of the range (Fig. 2.1 and 3.1).

Space geodetic measurements in Iran suggest NNE-directed shortening at a rate of 22±2 mm/a relative to a Eurasian reference frame, of which 6±2 mm/a are apparently accommodated across the Alborz mountains (Vernant et al., 2004a,b; Masson et al., 2007). In addition to the NNE-directed shortening component, range-wide left-lateral shearing at a

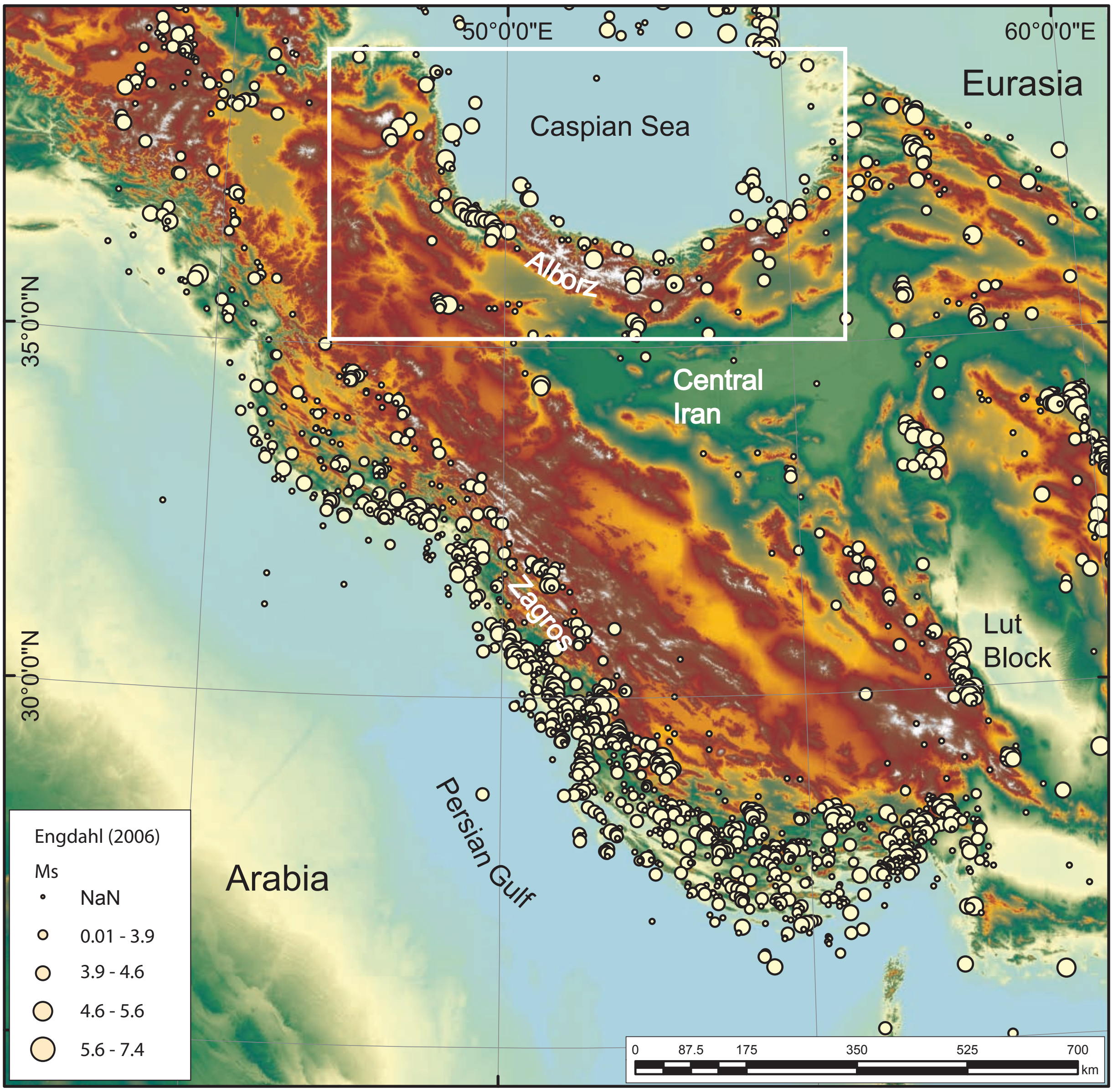

Figure 2.1: Overview of Middle Eastern and Iranian seismicity, and regional geographic setting on a GTOPO30 DEM. Note that seismicity in Iran is focused in the Zagros and Alborz mountains. While the majority of earthquakes are distributed across the entire Zagros, the Alborz mountains show rather disparate events, but also higher magnitudes. Compare Fig. 3.1 for relative motion of the crustal blocks and sense of motion along the major active structures. Box outlines Fig. 2.2

.

rate of 4±2 mm/a is observed in the Alborz, because the adjacent South Caspian basin moves northwestward relative to western Eurasia at a rate of 6±2 mm/a (Vernant et al., 2004b)(Fig. 3.1, 4.1). The oblique shortening with respect to the main strike of the range has led to strain partitioning into thrusting and strike-slip faulting (e.g., Priestley et al., 1994; Jackson et al., 2002b) (Fig. 4.1).

Mountain tops in the Alborz reach up to 4850 m, culminating in the 5590 m high Mt. Damavand, a Quaternary volcano. Despite these high elevations, the Alborz range seems isostatically unsupported due to a relatively low crustal thickness of only about 54 km with a local thickening below Damavand volcano (Sodoudi et al., 2009). However, the high topography might be regionally compensated by the adjacent Iranian Plateau and South Caspian Basin (Radjaee et al., 2010). The high topography makes the Alborz chain an effective orographic barrier to northerly moisture derived from the Caspian Sea (Fig. 2.2B and C). This climatic gradient results in a humid environment with dense vegetation cover on the northern flank and semiarid to arid, sparsely vegetated conditions on the southern flank (e.g., Alijani & Harman, 1985; Alijani, 2002; Alijani et al., 2007). Furthermore, precipitation is focused at the lower two thirds of the northern flank and decreases towards the divide. Interestingly, the sector of the orogen between the exceptionally deep South Caspian Basin and the Central Iranian Plateau is highly asymmetric in cross-section. The northern boundary is below sealevel and the southern boundary is located at elevations between several hundred to more than one thousand meters (Fig. 2.2A and B).

The topographic asymmetry renders the northern flanks steeper than their southern counterparts. An inspection of satellite images suggests that the landscape in this sector is starting to adjust to this topographic imbalance, with headward migration of the northern channels, thus causing a southward migration of the drainage divide (Fig. 2.2B). This process is associated with the capture of large transversal tributaries, as the Haraz, Nur, Sharud, and Alamut rivers, which finally drain northwards (Fig. 2.2B and 2.3B). This in turn means that northern catchments, or their halfwidth, respectively, are for the most part larger than southern catchments. Enhanced by the extreme N-S gradient in precipitation, this results in higher runoff to the Caspian compared to Central Iran (Fig. 2.2C), and thus in a higher potential of fluvial erosion and basin excavation on the windward side. Examples from the Himalayas and numerical modeling studies suggest that such protracted focused erosion may eventually alter rock-deformation patterns and strain rates and thus increase the rock-uplift rate (e.g., Koons, 1994, 1995; Wobus et al., 2003; Hilley et al., 2004; Thiede et al., 2004; Bookhagen et al., 2005; Whipple & Meade, 2006; Roe et al., 2006; Stolar et al., 2006, 2007).

To reveal trends in the gross distribution of rock-uplift in the Central Alborz mountains, I have calculated concavity and normalized steepness indices of the main trunk channels, derived from DEM data of slope and contributing drainage area using the Stream Profiler toolbox (http://www.geomorphtools.org/, Wobus et al. (2006)). This is a powerful tool to assess the influence of tectonic forcing on landscape evolution and may help identify sets of pronounced tectonic activity. Rock-uplift rate is assumed to exert a first-order control on the power-law scaling between channel slope and contributing drainage area (e.g., Whipple & Tucker, 1999; Kirby & Whipple, 2001; Wobus et al., 2006) as expressed by the following equations

$$S = k_s * A^{-\theta} \tag{2.1}$$

or

$$S = (U/K)^{1/n} * A^{m/n} \tag{2.2}$$

where S refers to the local channel slope, A is the upstream drainage area, $k_s$ is the steepness index, $\theta$ the concavity index, U is rock-uplift rate, K is the coefficient of erosion, and m and n are constants describing the basin hydraulic parameters. While equation 2.1 is an observation for many river basins, equation 2.2 is valid under steady-state condition and for fluvial processes, thus drainage areas larger than a critical threshold. A power-law relation and positive correlation exists between $k_s$ and rock-uplift rate (e.g., Whipple & Tucker, 1999), and it varies depending on the geological setting (e.g., Wobus et al., 2006). Steepness indices reveal differences in rock-uplift rate. This concept only works with uniform boundary conditions, such as erosivity (Equation 2.2), because channel steepness reflects the ratio between uplift and the coefficient of erosion. If rock uplift is spatially uniform, the concavity index is independent of rock-uplift rate and erosional process and is found to vary only in a narrow range between 0.35 and 0.6 (e.g., Whipple & Tucker, 1999). Any spatial (downstream) change in erosivity or rock-uplift rate will be manifested by a change in channel concavity (e.g., Kirby & Whipple, 2001; Wobus et al., 2006). Thus, channels have low concavity or convex-up slopes, if the rock-uplift rate increases downstream, and vice versa (Kirby & Whipple, 2001).

The central Alborz mountains reveal spatially distinguishable trends in channel concavity and steepness, indicating spatially non-uniform rock-uplift rates. Many channels or channel reaches do not fit into the expected range of concavity values, and are mainly higher and sometimes lower or even convex-upward (Fig. 2.3A). More striking, however, is the fact that north-draining streams show generally higher normalized steepness indices than transverse or south-draining streams (Fig. 2.3B and 2.4A). Alongside with the generally higher steepness, the northern channels exhibit a pronounced knickpoint or transition zone, separating steep upper reaches from even steeper lower reaches (2.4B, illustrated in Chalus example (Ch)), indicating transient behavior. In light of a typical channel response to tectonic forcing (e.g., Whipple & Tucker, 1999), this would suggest that the northern part of the Central Alborz mountains is currently undergoing higher rates of rock-uplift than the southern part, with an additional gradient from west to east.

However, this tectonic signal needs to be distinguished from possible influences of climate or different erosivity. From the geological map (Fig. 2.3A) it could be argued that the difference in steepness might be related to differences in rock type (low steepness and higher erosivity in Tertiary units vs. high steepness and low erosivity in pre-Tertiary units). In fact, Pre-Cambrian to Paleozoic units exposed in the Alborz have been described as being very resistent to erosion (e.g., Assereto, 1966). However, these units rather occur locally on the southern flanks or in the interior of the range, near the drainage divide (e.g., Fig. 4.2A).

The majority of the northern flanks is characterized by Mesozoic units (mainly limestone, some marl, dolomite, or sandstone). Of these Mesozoic assemblages, some sub-units (e.g., Tiz-Kuh, Lar, or Abnak formations) are considered to be resistent to erosion, but they occur only locally and with limited thickness (e.g., Assereto, 1966). Thus, the striking difference in channel steepness between north and south is not simply owed to variable rock types. In contrast, the observed orographic precipitation, with a maximum at the northern flanks, but decreasing gradient towards the drainage divide, is expected to develop higher relief with steeper channel slopes in the upper reaches and a higher concavity (e.g., Roe et al., 2003; Bookhagen & Burbank, 2006). Moreover, the rain distribution also shows a pronounced west-east gradient, leaving the two less steep north-eastern channels (NN2, NN3) in a low-rain zone (Fig. 2.2C, inner frame). These observations indicate a strong correlation between the observed channel steepness and the pattern of orographic precipitation. However, this does not exclude a further correlation with differences in rock-uplift rate. Accelerated uplift will cause a positive feedback on the precipitation-steepness coupling, as it elevates the profile, and therefore increases the longitudinal precipitation gradient (Roe et al., 2003). Moreover, the knickzones suggest a transient stage with non-equilibrium conditions. Thus, without quantifying the singular effects, it is reasonable to assume that at intermediate to short timescales, the north-central Alborz mountains are undergoing higher rock-uplift rates than the south-central Alborz (or pulses of base-level fall in the South Caspian). This first-order assessment may be supported by the trends in seismicity. Although rare, teleseismically recorded earthquakes also seem to be more frequent on the northern flanks of the Alborz (Fig. 2.1 and 2.3B), supporting the inference of higher tectonic activity in the north. On the southern flank, only the Garmsar fault area (GF in Fig. 2.3A) shows significant earthquake activity. It may be a coincidence, but this area spatially correlates with the steepest southern channel (Fig. 2.3B, channel G). In fact, this area differs from the general characterization of the southern flanks because of Oligocene-Miocene salt deposits, which might focus the deformation (e.g., Jackson et al., 1990; Ashtari et al., 2005).

These inferences concerning the current state of tectonic activity are very intriguing, because they are at odds with the degree of tectonism exhibited by major faults along the northern and southern flanks, respectively. In contrast to the present-day, faults in the southern sector and internal domain reveal an important protracted deformation history and higher total displacements than structures in the northern sector (e.g., Zanchi et al., 2006; Yassaghi & Madanipour, 2008). Furthermore, Eocene sediments, which are widespread on southern flanks and reach in places more than 5 km thickness, have no exposures on the northern flanks, which are instead dominated by Mesozoic rocks. Several apatite fission track samples from northern flanks (Rezaeian, 2008) are only partially reset or even unreset, arguing for less than 4-5 km, in places less than 3 km burial of these sites. This in turn indicates that probably less post-Mesozoic rocks have been deposited there, that instead Mesozoic formations might have already formed a relative topographic high, and that less total exhumation took place in the north since that time. These observations combined indicate a temporal shift in the focus of deformation from southern and internal to northern domains. Ultimately, such a shift could have been associated with the formation of a threshold elevation of the orographic barrier, associated forcing of precipitation, and accompanying focused erosion.

Exhumation rates increased in the inner domain by approximately 20 Ma, probably in response to enhanced crustal shortening and thickening (Rezaeian, 2008). At the same time, foreland basin initiation started in the south (Ballato et al., 2008, 2010a), also indicating significant deformation at this time. Such shortening may have caused progressive increase in surface uplift resulting in an effective barrier to moisture-bearing northerly winds (Ballato et al., 2010b). An increase in southern aridity, as indicated by a positive isotopic shift in $\delta^{18}O$, suggests that such a barrier was effective by at least 17.5 to 17.2 Ma (Ballato et al., 2010b). While the transience in the drainage system infers higher tectonic activity on a time-scale that is probably shorter than few million years, a lower temperature thermochronometer, as the U/Th-He system might be helpful to track the timing of this shift in the focus of deformation.

Nevertheless, deformation is ongoing in the southern range, as strongly deformed Quaternary deposits attest. In addition, the historical record of destructive earthquakes lists numerous events on faults at the southern flank (e.g., Ambraseys & Melville, 1982; Berberian & Yeats, 1999, 2001).

The following chapters will therefore focus on the deformation history in a study area in the south-central Alborz, immediately adjacent to the Iranian capital, Tehran.

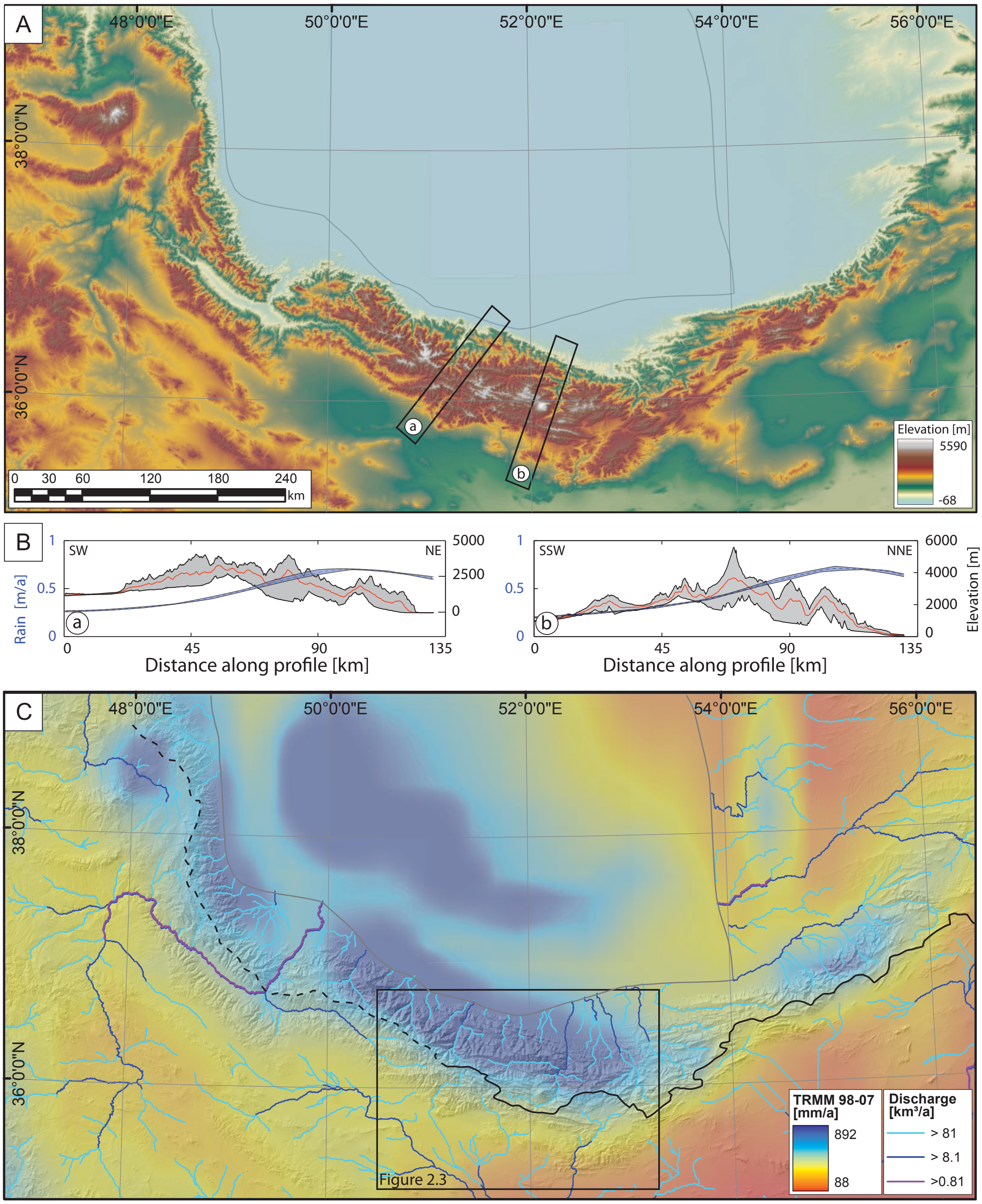

Figure 2.2: Topography and rainfall distribution of the Alborz mountains and surrounding regions. (A) SRTM-DEM and hillshade with locations of swath profiles. (B) Swath profiles, showing asymmetric topography (max, mean, and min) and pronounced gradient of orographically driven rainfall distribution (derived from TRMM data). (C) Annual mean rain fall rate (1998-2007), derived from TRMM data (courtesy of B. Bookhagen) showing strong spatial gradient of rainfall distribution across the Alborz. Water discharge was calculated by multiplying the flow accumulation with the TRMM rain data. As a result, most north-draining streams have higher runoff, and thus may have higher erosional potential than south-draining streams. Black line depicts drainage divide; solid line depicts division between northern and southern channels; dashed line between northern and large transverse channels.

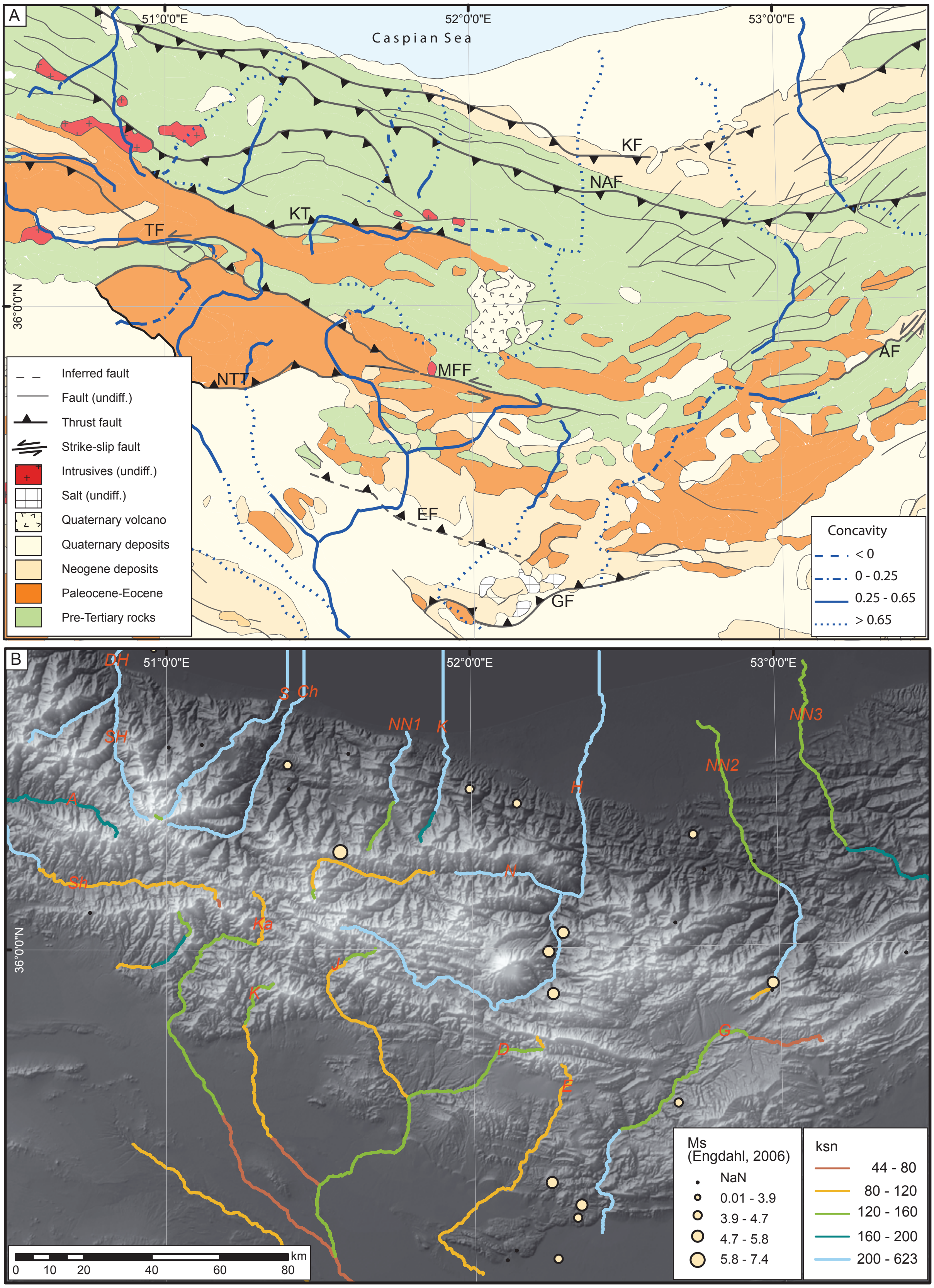

Figure 2.3: Stream profile analysis of the Central Alborz. (A) Concavity of major trunk streams superposed on simplified geological map (after Pollastro et al. (2000), main faults with sense of motion after Hessami & Jamali (2006). KF - Khazar Fault, NAF - North Alborz Fault, KT - Kandevan Thrust, TF - Taleghan Fault, MFF - Mosha Fasham Fault, NTT - North Tehran Thrust, EF - Eyvanakey Fault, GF - Garmsar Fault, AF - Astaneh Fault). (B) Normalized steepness indices and seismicity on SRTM-DEM, northern streams: DH - Do Hezar, SH - Se Hezar, S - Sardab, Ch - Chalus, NN1 - No Name 1, K - Kojoor, H - Haraz, NN2 - No Name 2, NN3 - No Name 3; transverse and south-draining streams: A - Alamut, Sh - Sharud, Ka - Karaj, K - Kan, J - Jajrud, D - Damavand, E - Eyvanakey, G - Garmsar.

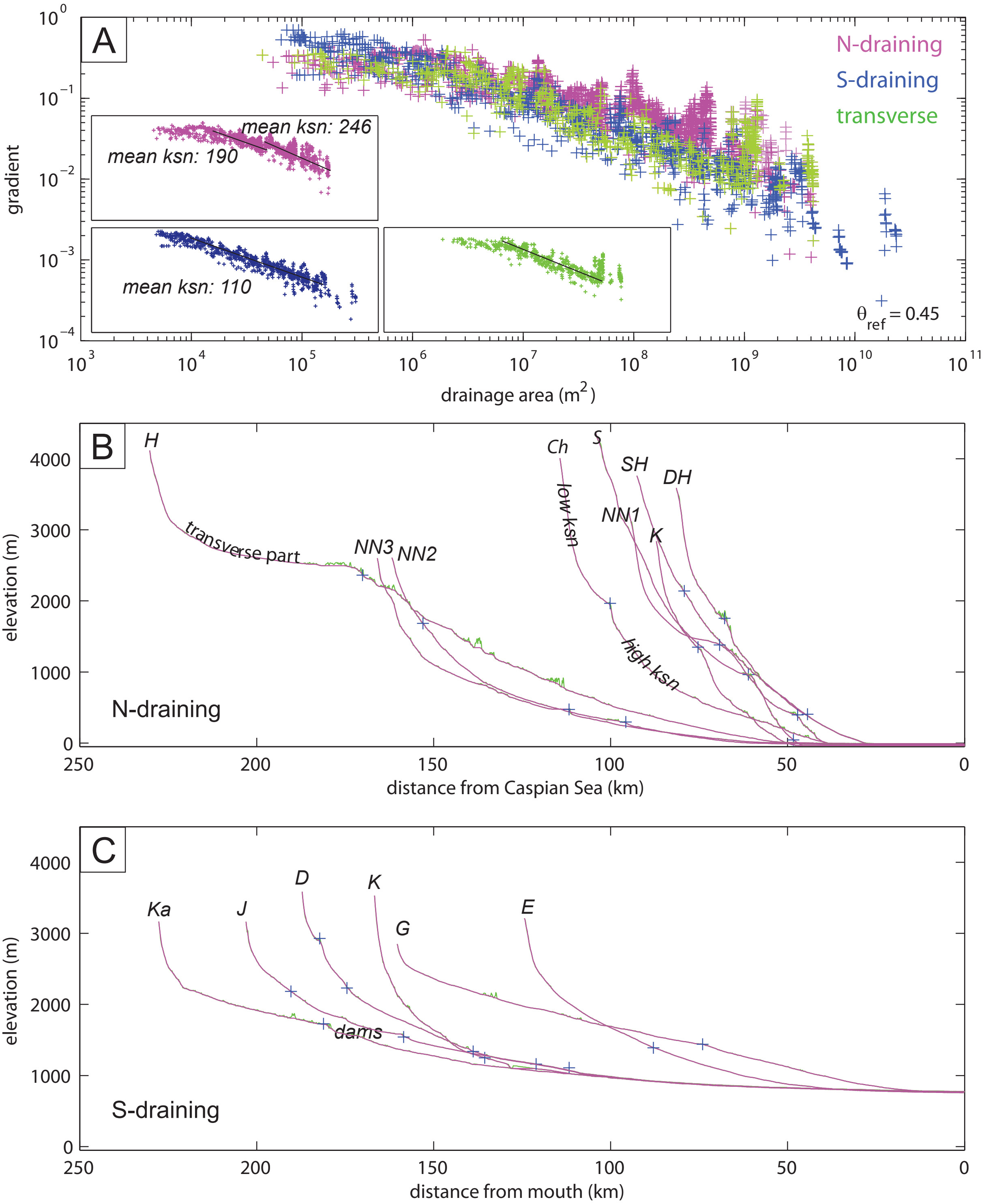

Figure 2.4: Slope-area plots, color-coded for N-, S- or transverse draining channels (A) and longitudinal profiles (B and C) of main trunk streams of the Central Alborz. Note the generally higher steepness of northern compared to transverse and southern streams. In addition, a pronounced knickpoint is separating zones of moderate and high steepness on N-draining channels (for illustration marked on the Chalus channel, Ch). Abbreviations of channel names as in Figure 2.3B. Crosses mark locations of knickpoints.

# Chapter 3

# Fault-kinematic and geomorphic observations along the North Tehran Thrust and Mosha-Fasham Fault, Alborz mountains Iran: implications for fault-system evolution and interaction in a changing tectonic regime

## 3.1 Introduction

Interaction of faults or their segments in tectonically active regions are observed on different temporal scales, ranging from rupture propagation in singular earthquake events (e.g., Stein et al., 1997; Hubert-Ferrari et al., 2000; Hartleb et al., 2002; Wesnousky, 2006) over decades to millions of years (e.g., Meyer et al., 1998; Peltzer et al., 2001; Barka et al., 2002; Anderson et al., 2003a,b; Armijo et al., 2003; Eberhart-Phillips et al., 2003; Bennett et al., 2004; Lin & Stein, 2004; Spotila & Anderson, 2004). A better knowledge of temporal aspects of faulting therefore is relevant for the evaluation of seismotectonic segments and associated landscape development that span the Quaternary and beyond.

Fault interaction is also observed at a range of spatial scales involving an alternation of slip rates on neighboring fault systems (Rockwell et al., 2000; Peltzer et al., 2001; Pollitz & Sacks, 2002; Friedrich et al., 2003; Bennett et al., 2004; Niemi et al., 2004; Dolan et al., 2007). Conversely, at the spatial scale of a single mountain front sustained faulting can occur over timescales of $10^4$ to $10^6$ years within discrete seismotectonic segments, apparently without interfering with adjacent segments (Arrowsmith et al., 1999; Strecker et al., 2003).

The effects of fault propagation also can be studied at various scales and are in the broadest sense compatible with each other, as well as with laboratory studies at various smaller scales or modeled results of joint propagation. The relative motion of the fracture (fault) surfaces (opening, sliding, or tearing mode) causes differences in the stress field near the tips, resulting in different styles of propagation (Pollard & Aydin, 1988; Pollard & Fletcher, 2005). However, the magnitudes of these stress components depend upon the fracture geometry away from the tipline and the loading conditions. Thus, faulting is a process that can involve several different physical mechanisms, which may differ depending upon the rock type and the tectonic setting (Pollard & Fletcher, 2005).

These relationships underscore the different levels in the complexity of fault development and the necessity to identify and evaluate spatiotemporal fault behavior. Faulting scenarios may become even more complex if a reorientation of the tectonic stress field triggers the reactivation of dip-slip faults as obliquely slipping or pure strike-slip faults (Strecker et al., 1990). Alternatively, deformation may be partitioned into a number of different faults, each with different kinematics and pronounced temporal variation (Sanderson & Marchini, 1984; Teyssier et al., 1995).

Fault linkage and subsequent interaction on the field-scale has been primarily studied in detail in extensional settings (e.g., Dawers et al., 1993; Armijo et al., 1996; Cowie et al., 1993, 2000; Densmore et al., 2003, 2007), and from the perspective of strike-slip partitioning and weak vs. strong fault behavior, particularly along the San Andreas Fault (e.g., Zoback et al., 1987; Teyssier and Tikoff, 1998; King et al., 2005), where fault-normal crustal compression parallel to the strike-slip fault is observed. Other natural examples are from segmented strike-slip faults, including geometric observations resulting from spacing or contractional or extensional overlaps (e.g., Bilham & King, 1989; Aydin & Schultz, 1990; Brankman & Aydin, 2004). Fault propagation has been detailed studied in areas of blind thrusts, where it results in the lateral growth of hanging wall anticlines with subsequent imprints in the landscape (e.g., Burbank et al., 1996; Jackson et al., 1996; Keller et al., 1998, 1999; Burbank et al., 1999; Jackson et al., 2002a). However, on a regional scale, the problem of fault interaction and the effects of a changed tectonic stress field on the kinematic evolution of faults in areas governed by shortening seems less well understood.

The Alborz mountains of Iran are a tectonically active range, where such fault interactions can be studied at the scale of range bounding faults, several tens of kilometers long. Two prominent faults along the southern border of the central Alborz mountains are the North Tehran Thrust (NTT), immediately north of Tehran, and the Mosha-Fasham Fault (MFF) to the east (Fig. 3.2). The kinematic relationship and interaction between these neighboring faults is an unresolved problem in the late Cenozoic evolution of this mountain range. An improved understanding of the nature of possible interaction between these faults is, however, crucial for the evaluation of regional tectonic activity, and the overall assessment of the evolution of fault systems in the Alborz range, which accommodate almost one third of the intracontinental deformation in Iran. GPS measurements revealed NNE-directed shortening with a rate of $5 \pm 2$ mm/yr (Vernant et al., 2004a,b). In addition, a range-wide shearing is observed at a rate of $4 \pm 2$ mm/yr, which is associated with left-lateral motion on E-W striking structures (Fig.3.1). In regions of low deformation rates, morphological indicators in the landscape might suggest important Quaternary tectonic activity along discrete faults, which would correspond to widely distributed deformation in space and time.

Along the North-Tehran Thrust, the relief increases to more than 3000 m over the Tehran plain, suggesting that the fault has accommodated significant amounts of strain or high strain rates in the Tehran region. The Mosha-Fasham Fault has been inferred to accommodate a significant amount of the observed lateral shearing in the range (Allen et al., 2003; Vernant et al., 2004a,b; Ashtari et al., 2005; Ritz et al., 2006a). The eastern fault termination of the NTT probably marks the junction with the MFF (Tchalenko, 1974; Allen et al., 2003). Here, the orientation of the E-W striking NTT agrees with similar striking thrusts and fold axes that are partly cut by the MFF farther east.

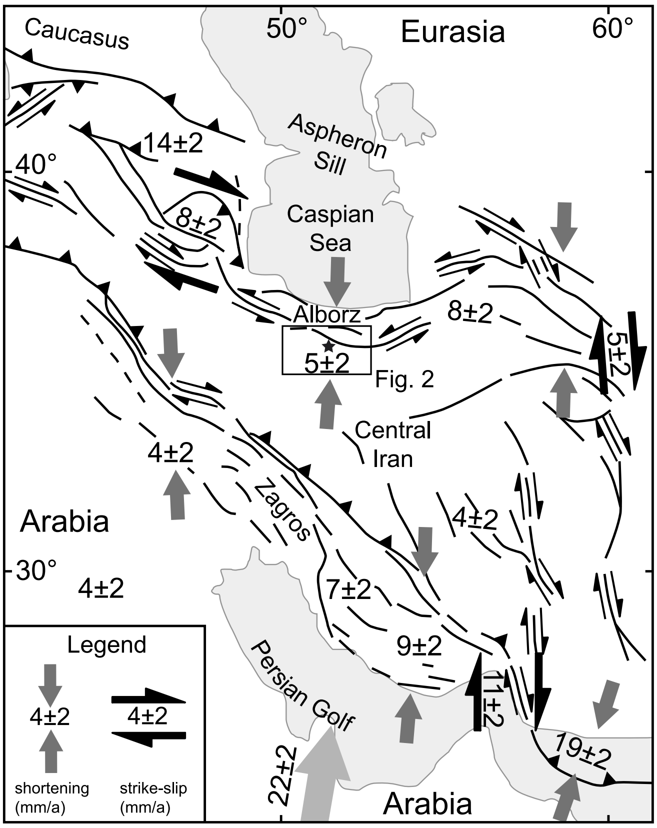

Figure 3.1: Simplified tectonic map of the Middle East with arrows showing sense of relative motion. Relative displacement in the central Alborz mountains occurs at rates of $5 \pm 2$ mm/a and $4 \pm 2$ mm/a for shortening and shearing, respectively (modified after Vernant et al., 2004a). The box indicates the study area in the south-central Alborz mountains Fig.4.2. Note the approximate location of Tehran (marked as star).

Several historical earthquakes are attributed to ruptures of different segments of the MFF that have affected this fault along its entire length (Tchalenko, 1974; Ambraseys & Melville, 1982; Berberian, 1983; Berberian & Yeats, 2001). In contrast, recent seismicity and manifestations of active faulting are limited to the eastern segment of the MFF, indicating sinistral motion. Interestingly, in the vicinity of both faults, instrumentally recorded earthquakes do not exceed magnitudes of 5.5 (Tchalenko, 1974). However, historical reports of damage in the vicinity indicate that M $> 7.0$ events may occur on these faults, suggesting that the instrumental record may not yet have recorded the large magnitude events that accommodate much of the relative motions in the area (Tchalenko, 1974; Ambraseys & Melville, 1982; Berberian, 1983; Berberian & Yeats, 2001).

It is not known whether or not this gap in seismicity may be associated with a change in the slip rate on adjacent faults, as observed in other tectonically active regions (e.g., Bennett et al., 2004). In the Alborz mountains this is a critical aspect, because the NTT apparently merges with the MFF in an area where the strike of the MFF changes, and where the boundary between recently active and apparently quiescent fault segments occurs.

In this study we characterize the style of deformation observed along the different fault segments of the MFF and NTT. Our field observations constrain the distribution of deformation within the southern Alborz mountains. Fault kinematics, structural data, and geomorphic observations indicate that the deformation field has changed over time. Using these data, we can reconstruct the history of deformation to infer how the development of deformation may be related to a changing stress field in this area. We document the kinematic evolution of the fault system and its link to the landscape development. Based on this information, we present different fault-kinematic scenarios and test their viability for the transition zone between the Mosha-Fasham Fault and the North Tehran Thrust.

## 3.2 Methods

Fault kinematic measurements were recorded mainly in the hanging wall along the different fault segments. The sense of movement was derived from kinematic indicators, such as Riedel shears or fibrous mineral steps of slickensides. The data were separated into discrete kinematic populations based on overprinting criteria. Concentrations of average P- and T-axes were determined, and P- and T-quadrants constructed to yield pseudo-fault plane solutions that are readily comparable with earthquake fault plane solutions (using FaultKin Linked Bingham distribution, Allmendinger, 2001).

We used detailed geomorphic observations to assess the landscape response to cumulative displacement and to address the issue of tectonic activity on Quaternary time scales. In addition, the mapping of offset geomorphic markers was supported by analysis of Corona and Aster satellite data, and airphotos at the scale of 1:40,000. Airphotos and 10m-DEM were made available to us by the National Cartographic Center (NCC), Iran. For limited areas, not fully covered by the NCC-DEM, we have used Shuttle Radar Topography Mission (SRTM) data with 90m resolution. From these data, we have calculated the topographic residuals, following a flow chart from Hilley et al. (1997).

## 3.3 Geologic and structural setting

The stratigraphic sequence of the southern central Alborz mountains is characterized by an up to 13-km-thick succession of Precambrian to Quaternary strata, deformed and uplifted during two main tectonic events (Assereto, 1966). A Cambrian to Middle Triassic platform sequence is interpreted to correspond to the northern rim of Gondwana (Kürsten, 1980). The oldest contractional event, the Cimmerian orogeny, started in Late Triassic after collision of

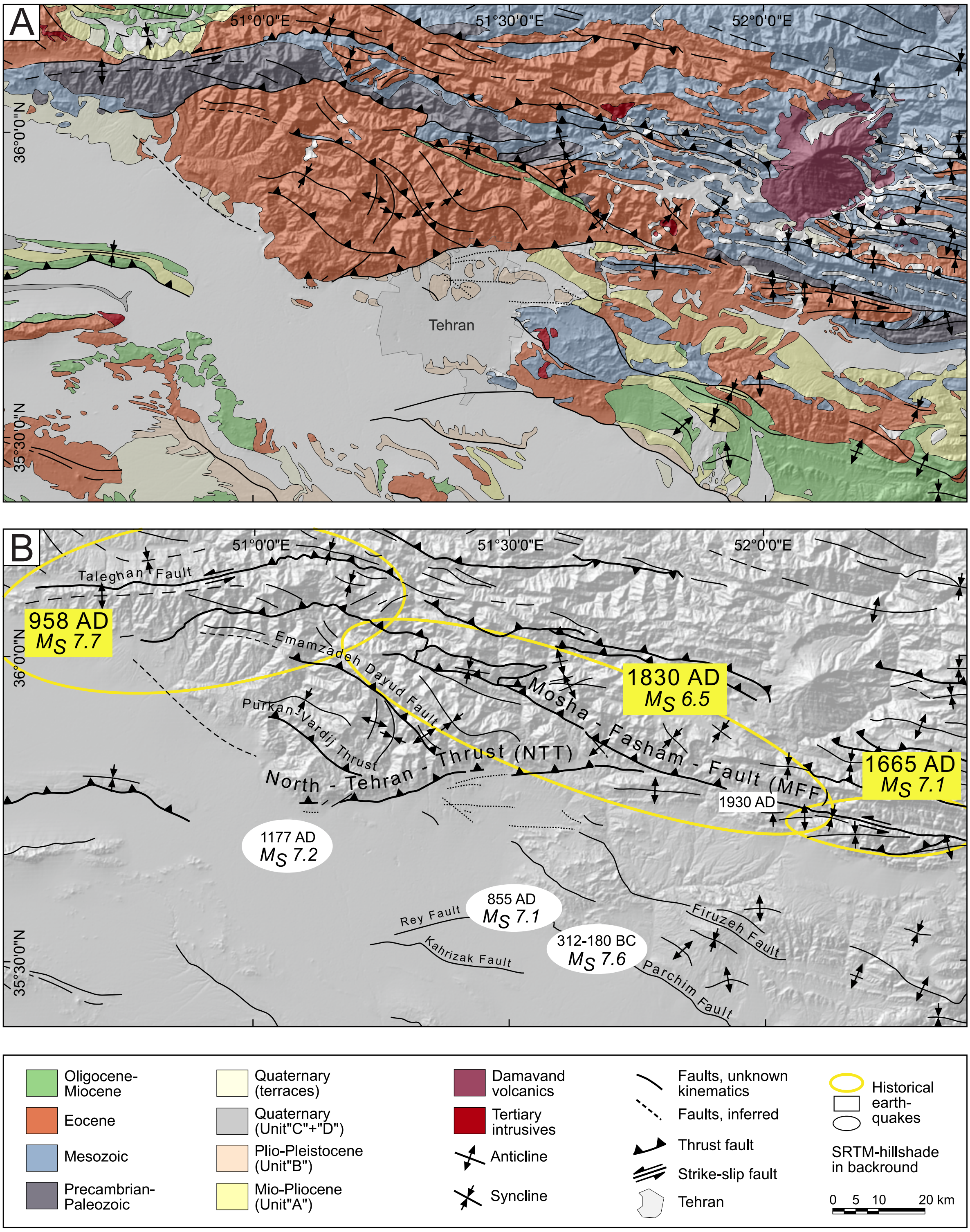

Figure 3.2: Simplified geology (A) and structural map (B) showing faults of interest and historical earthquakes (modified after Geological Map of Iran, 1:250,000 sheets Tehran, Saveh, Amol, and Qazvin-Rasht; historical earthquake data after Tchalenko (1974, rectangles), DeMartini et al. (1998, white ellipses), and Berberian & Yeats (1999, yellow ellipses).

the Iranian microplate with Eurasia and resulted in emerged areas and a regional unconformity, covered by the Shemshak Formation (Assereto, 1966; Kürsten, 1980; Davoudzadeh & Schmidt, 1984; Alavi, 1991, 1996; Stampfli & Borel, 2002). In the central Alborz however, the Cimmerian orogeny was associated with the late-stage formation of grabens (Zanchi et al., 2006). Cretaceous carbonate and volcanic rocks were deformed during contractional reactivation of these extensional structures. Paleocene conglomerates and limestones cover the folded strata (Assereto, 1966). A sequence of up to 5-km-thick Eocene volcanic rocks, volcanoclastic sediments, and shale (Karaj Formation) overly the deformed Cretaceous rocks and appear to have formed in an extensional back-arc setting (Guest et al., 2006b). Subsequent Oligocene to Miocene shortening caused progressive uplift, and was accompanied by concomitant erosion and sedimentation of fine-grained sandstones and marls (Red Formation). These processes are linked to the onset of the Arabia-Eurasia collision and started about 12 m.y. ago, inferred from accelerated exhumation rates in the Alborz range (Guest et al., 2006b).

The southern central foreland basin of the mountain belt comprises extensive alternating conglomerates, silt,and sandstone units (Hezardarreh Formation or Unit A). Based on sedimentary facies correlations with the foreland deposits of the Zagros mountains (Bakhtiari Formation) the inferred age is Late Mio-Pleistocene (Rieben, 1955). However, this might represent a simplification, since the Bakhtiari Formation represents diachronous deposits advancing towards the foreland rather than being a uniformly deposited sheet (Fakhari et al., 2008). This could also be the case for the Alborz mountains, where a recent study suggested a late Miocene age (7.5 to 6.2 Ma) for the Hezardarreh Formation exposed along the southern Alborz mountains (Ballato et al., 2008). This formation is in turn unconformably overlain by the Kahrizak Formation (Unit B), which comprises sand- and siltstones, and the Tehran Alluvium (Unit C), a laterized conglomerate (Rieben, 1955).

Based on thermochronologic data (Axen et al., 2001) and field observations, Allen et al. (2003) suggested a two-stage Neogene evolution of the Alborz mountains with (1) Miocene N-S directed shortening, accompanied by limited conjugate right- (western part) and left-lateral (eastern part) strike-slip faulting, and (2) Pliocene-Quaternary NE-SW directed shortening, accompanied by left-lateral strike-slip faulting along the entire length of the mountain range.

Interpretations of the geometry and kinematics of faulting in the Alborz mountains remain controversial (Priestley et al., 1994; Jackson et al., 2002b; Allen et al., 2003; Guest et al., 2006a). There appears to be general consensus about sinistral transpression with strain partitioning involving dip-slip shortening and strike-slip faulting. More than 30% of the shortening is associated with seismic activity, whose sense of motion indicates that shortening is partitioned into left-lateral strike slip and thrusting in the WNW-trending high Alborz range and reverse faulting with a left-lateral oblique component of motion at lower sectors (Priestley et al., 1994). In contrast, coeval with the transpressional deformation, the internal domain of the central Alborz mountains is characterized by recent transtension (Ritz et al., 2006a). Here, the geomorphic characteristics of the landscape traversed by the neighboring Taleghan, eastern Mosha-Fasham, and Firuzkuh faults documents left-lateral kinematics with a minor normal component. This kinematic system is compatible with a general strike-slip regime and a local change in the position of $\sigma_1$ from a regional horizontal position ($S_{Hmax}$) to a vertical one between the borders and the internal domain (Ritz et al., 2006a).

### 3.3.1 Mosha-Fasham Fault

The sigmoidal trace of the Mosha-Fasham Fault is $> 175$ km long and strikes E-W to WNW-ESE, with variable N-dips between 35° to 70° (Tchalenko, 1974; Allen et al., 2003). Its central part is characterized by a double-bend towards a northwest strike (Fig. 3.2), which accounts for approximately one third of the entire fault length. The MFF comprises three segments, a western (approximately west of 51° 20'E), an eastern (east of 52° E), and the central segment, located between them (Berberian & Yeats, 1999; Tchalenko, 1974). Importantly, the eastern tip of the MFF is close to the western termination of the active left-lateral (transtensional) Firuzkuh Fault (Ritz et al., 2006a; Allen et al., 2003), whereas the western tip is masked by Quaternary sediments. However, the entire western segment of the MFF strikes parallel to the active, left-transtensional Taleghan Fault (Ritz et al., 2006a)(Fig. 3.2B).

Deflected streams, offset channels, and fault planes with horizontal striations in the eastern and central-eastern fault sectors indicate left-lateral motion (Allen et al., 2003; Ritz et al., 2006a; Ashtari et al., 2005). In addition, thrust and reverse faults are observed, and juxtapose Cambrian with Eocene or Miocene strata. Early shortening at the MFF has been estimated to be on the order of 4 km (Allenbach, 1966; Steiger, 1966). Fault-plane striations, analyzed by Bachmanov et al. (2004), reveal faulting with dominant strike-slip in the eastern part and an equal degree of reverse and strike-slip motion in the central part. Despite these observations, several E-trending folds, aligned along and cut by the Mosha-Fasham Fault, indicate that a former dextral transpressional regime was superseded by sinistral strike-slip faulting. These observations emphasize the significance of the MFF as a long-lived structure which has accommodated shortening under changing stress regimes in the course of the convergence between Eurasia and Arabia.

Allen et al. (2003) calculated a maximum sinistral offset of $\sim 35$ km, based on piercing points in lower Paleozoic strata in the eastern and central-eastern segments, which would, assuming the beginning of left-lateral motion 5 Ma ago, correspond to a slip-rate of up to 7mm/a. However, Ritz et al. (2006a) calculate a sinistral slip rate of $2 \pm 0.1$ mm/a with a minor normal component. This transtension is in agreement with microseismicity recorded along the eastern Mosha-Fasham Fault, showing left-lateral strike-slip faulting associated with a normal components (Ashtari et al., 2005; Ritz et al., 2006a).

Limited data exist along the western segment, but kinematic indicators show reverse dip-slip to sinistrally oblique reverse faulting near the western terminus, and sinistral oblique-reverse motion near the eastern segment boundary (Guest et al., 2006a). In addition, Guest et al. (2006a) found minor synthetic faults with a reverse-dextral oblique sense of slip in the hanging wall of the MFF. However, based on syn-kinematic folding, foliations, and s-c fabrics, Moinabadi & Yassaghi (2007) infer a dominance of dip-slip faulting along the western segment.

Several destructive earthquakes occurred in the study area (Fig. 4.2B), attributed to slip along different segments of the MFF, and possibly motion on blind faults in the foreland (Ambraseys, 1974; Tchalenko, 1974; Ambraseys & Melville, 1982; Berberian, 1983; De Martini et al., 1998; Berberian & Yeats, 1999, 2001). The three largest damaging earthquakes along the MFF occurred 958, 1665, 1830, and 1930 AD. Damage of the 958 Taleghan-Ray earthquake is reported from an area of more than 200 km in diameter (Ambraseys & Melville, 1982). As the Taleghan and western Mosha faults are parallel structures, activity along the Taleghan Fault during the 958 AD earthquake may have been possible.

### 3.3.2 North Tehran Thrust

Here, we refer to the North Tehran Thrust (NTT) as the boundary fault between Karaj in the west and Niknam Deh in the east, where the Eocene rocks of the Alborz range are thrust over Neogene and Quaternary sediments of the Tehran embayment (Tchalenko, 1974, 1975; Berberian, 1983; Allen et al., 2003)(Fig. 3.2, for locations compare 3.3A).

The NTT is more than 60 km long, strikes E-W to ENE-WSW and is an oblique thrust or reverse fault with a left-lateral component of motion (Alavi, 1996). North of Tehran NW-striking folds and faults deflect older, N to NE-striking structures, inferred to result from earlier right-lateral motion along the NTT (Allen et al., 2003). The NTT fault zone comprises numerous sub-parallel, right-stepping en échelon segments, as well as NW-striking thrusts, the Purkan-Vardij Thrust (PVT) and the likewise striking Emamzadeh-Davud Fault (EDF) that merge with this fault (Tchalenko, 1974; Berberian & Yeats, 1999; Allen et al., 2003)(Fig. 3.2B).

The western segment (west of 51°15'E) comprises a ramp-flat geometry, following the limbs of a footwall anticline at the right bank of the river Kan (for location compare Fig. 3.3A). Two kilometers west of this location the fault trace becomes discontinuous. It is much more subtle and locally associated with NE- or E-striking thrusts (Tchalenko, 1974). Locally, vertically dipping Plio-Pleistocene sediments abut in fault contact horizontal to gently dipping Eocene tuffs.

The central-western segment, between 51°15'and 51°28'E, is characterized by thrusting and reverse faulting at an increasingly steeper fault plane towards east. This segment is itself subdivided into several en échelon faults (Tchalenko, 1974).

The central-eastern segment, between 51°28'and 51°34'E, however, is characterized by a broad zone of thrusting (Tchalenko, 1974). East of Lashgarak (for location compare Fig.

3.3A), the fault termination probably marks the junction with the MFF (Tchalenko, 1974; Allen et al., 2003; Bachmanov et al., 2004). This region is intensely folded, although the topography is much more subdued compared to that of surrounding regions. Here, the NTT strikes E-W, parallel to other thrusts and fold axes that merge with the MFF or are cut by it (Fig.3.2).

Faulting and folding of the piedmont south of the NTT suggests a shift of the deformation into the foreland. Deformation of the piedmont consists of four sub-parallel E-W oriented anticlines, involving the "A" Formation, which is unconformably overlain by almost horizontally bedded "B" Formation deposits (Engalenc, 1968). The folds are asymmetric, with steep northern limbs, which are partly overturned and developed into S-verging flexures and reverse faults (Tchalenko, 1974). In addition to these thrusts, NW-striking faults are observed in the central and western piedmont (Tchalenko, 1974).

## 3.4 Fault kinematic data

Different structural trends along the southern Alborz range can be identified that allow us to develop a relative faulting chronology, based on cross-cutting relationships, and the relative age of the involved units. In this section, we first discuss the macroscopic structures and subsequently present fault-slip data collected on major and minor faults. Combined, these data help unravel the kinematic history of the southern Alborz range.

In the NTT hanging wall, sub-parallel to obliquely oriented (Niknam Deh, west; Fig. 3.4A) fold axes are exposed. At the western and the eastern (Niknam Deh, east; Fig. 3.4B) tips of the NTT, NE-striking meso- to macroscale folds affect the Eocene Karaj Formation. In one case the folds are unconformably overlain by tilted, SE-ward dipping Plio-Pleistocene Unit A deposits.

ENE- to ESE-striking faulting with dominant dip-slip movement and occasional dextral and sinistral components is observed at the western segment of the MFF (Fig. 3.3B and C), but also affects the Karaj Formation and is linked with activity on the NTT (Fig. 3.5A, localities 2 and 4). In addition, NW- to N-striking faults with medium to high-angle dips were observed along the entire length of the NTT, generally affecting the Karaj and Miocene Red formations. In the western area, the offset pattern along these faults is consistent with either west-side down displacement or left-lateral motion (Fig. 3.5A, localities 1 and 3). Close to the eastern termination of the NTT, these faults are exposed in the NTT hanging wall and the MFF footwall, either displaying motion partitioned into strike-slip and dip-slip components or oblique kinematics resulting in associated flower structures.

In the eastern part of the study area approximately E-striking high-angle faults were observed that we term the Latyan fault zone. These faults affect mainly Unit A deposits (but more recent sediments cannot be excluded). Faulting has resulted in a cataclastic zone, up to 1-2 meters wide, with rotated clasts obliquely oriented and forming large shear bands.

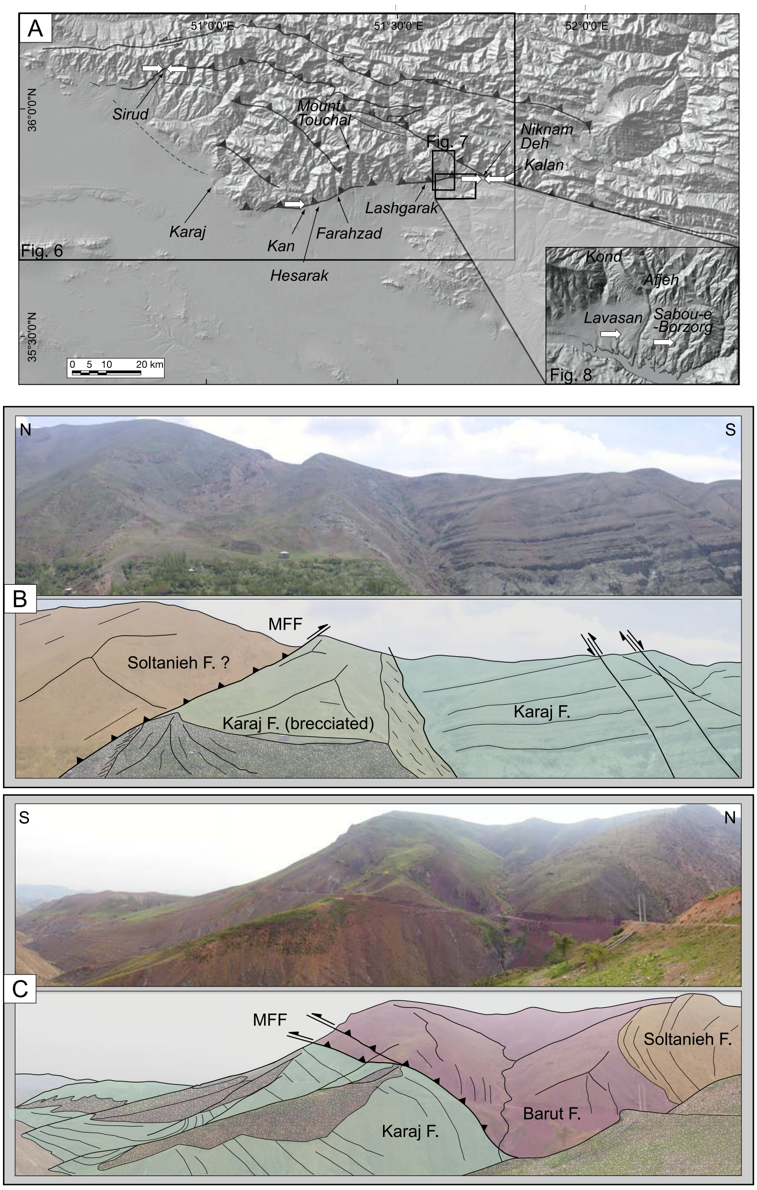

Figure 3.3: Overview map and field examples of folding and faulting associated with the western MFF fault segment. (A) Regional overview map showing main faults and location names as mentioned in the text. Boxes indicate following figures (inset is zoom of Fig. 8 box), while white arrows show locations of field photos (this figure B and C and Fig. 3.4) and point in view direction. (B) View towards E showing the MFF at Sirud (western segment). Here, the fault has thrust characteristics with Cambrian units juxtaposed against Eocene Karaj Formation. (C) View towards W showing the MFF between Sirud and Velijan (western segment). The overall impression of the fault geometry suggests thrusting, while fault-kinematic measurements indicate sinistral reactivation (compare Fig. 3.5B 23). Note the footwall syncline in the Karaj Formation (middle ridge), compatible with primary thrust kinematics.

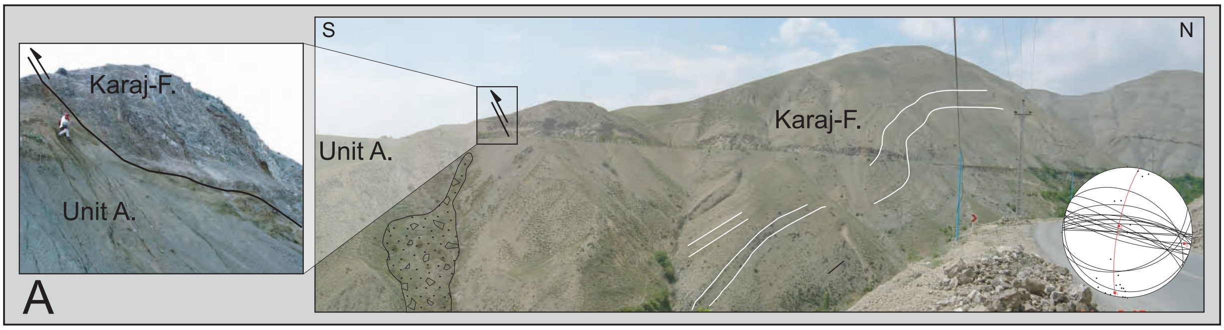
S
N
Karaj-F.
Unit A.
Karaj-F.
Unit A.
A


N
S
Karaj-F.
B


2m
C

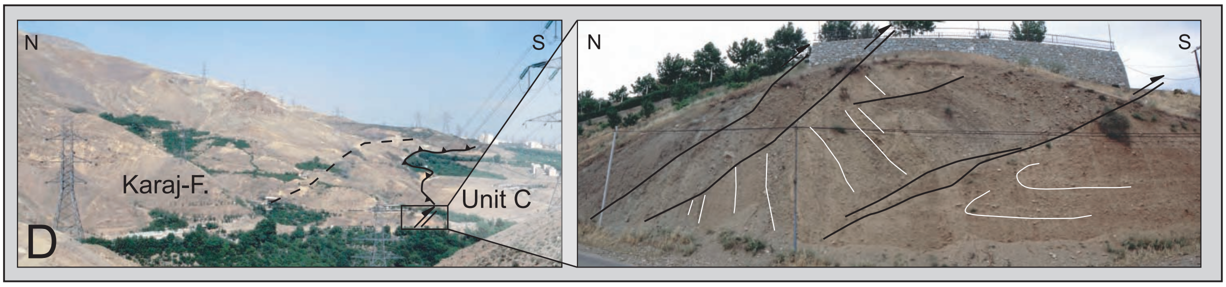
N
S
Karaj-F.
Unit C
D
N
S

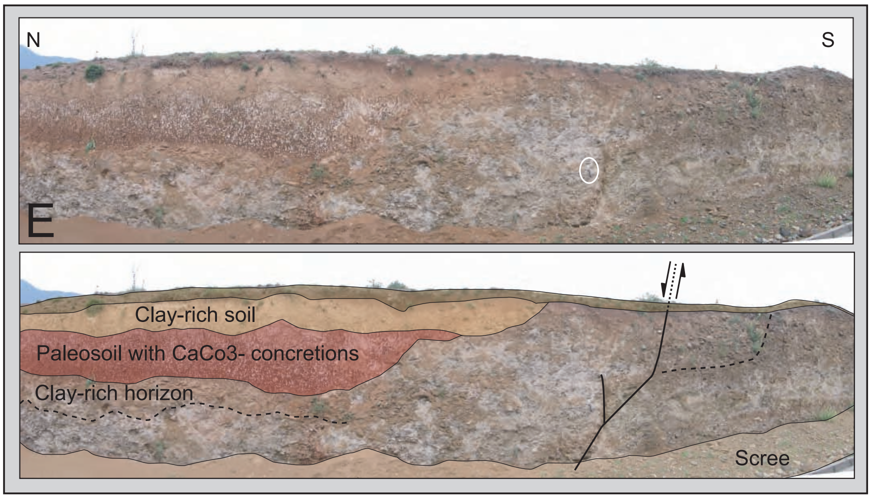
N
S
E
Clay-rich soil
Paleosoil with CaCo3- concretions
Clay-rich horizon
Scree

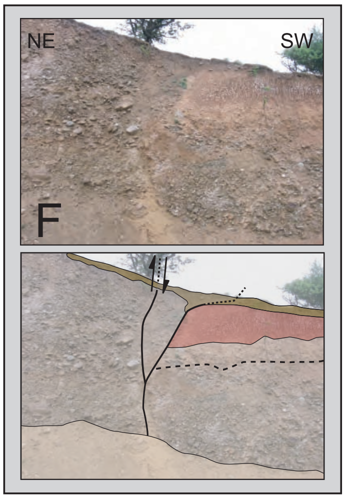
NE
SW
F

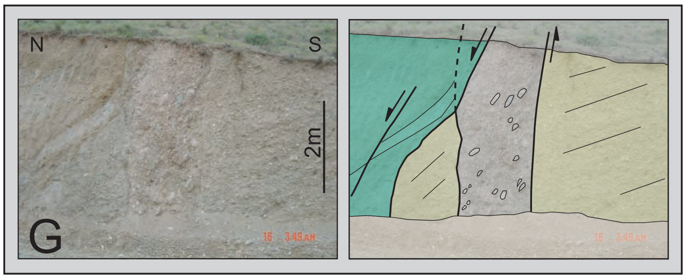
N
S
2m
G

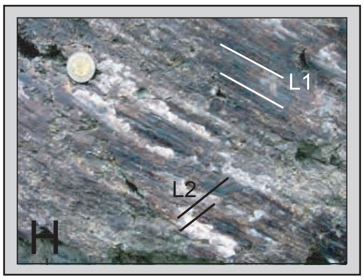
L1
L2
H

Figure 3.4: Field examples of folding and faulting associated with the NTT and MFF fault system. (A) NTT exposure west of Niknam Deh (see arrows at Niknam Deh in Fig. 3.3A for location). The fault trace shows a ramp-flat geometry and the hanging wall exhibits an alternation of synclines and anticlines with axes oblique to the NTT, but compatible with the present-day shortening direction. See inset stereoplot with the calculation of the fold axis from measurements of the fold limbs. White lines denote bedding in Karaj Formation rocks. Extensive slope debris below the fault trace indicates a cataclastic fault zone. Fault kinematic measurements in tectonized Quaternary river gravels show sinistral reactivation (compare Fig. 3.5B (locality F)). (B) Folding in the hanging wall of the NTT at Niknam Deh, just east of (A), white lines denote bedding, inset stereoplot for axis calculation; note that here the fold axis is not compatible with the present-day shortening direction. (C) Cataclastic shear zone in volcanic rocks of the Karaj Formation associated with the NTT near Farahzad. No sense of motion or timing of fault activity can be inferred. (D) NTT fault trace (black line with teeth) and possible subsidiary fault (dashed) at Kan (see arrow at Kan in Fig. 3.3A for location). This outcrop was previously studied by Tchalenko (1974, 1975) and shows thrusting of cataclastic Karaj Formation rocks over alluvial sediments (possibly Unit B) as well as internal deformation of alluvial units. (E) and (F) High-angle faulting in alluvial deposits at a roadcut in Lavasan (see arrow in inset in Fig. 3.3A), both outcrops are just some meters apart. The colorcoding of the soils is the same. Geological hammer for scale in white circle on (E), note the paleosoils as marker horizons for faulting. A flower structure geometry of the fault (here informal called Latyan fault) is inferred. The erosional terrace level corresponds to T4 in Fig. 3.8 and seems to postdate the faulting. (G) High angle, E-striking Latyan fault about 3 km east of (E) and (F) near Sabou-e-Bozorg (see arrow in inset in Fig. 3.3A). Erosional terrace level corresponds to T2 in Fig. 3.8. Rotated clasts indicate coarse shear bands in the fault zone, coherent with the drag of the bedding. However, horizontal striations in the fault gouge indicate strike-slip reactivation. (H) Example of reactivation of the MFF with two generations of oblique kinematic indicators; the older lineation (L1) is associated with slickensides and a polished surface, while superimposed are striated calcite fibers (L2).

The tectonized clasts and an offset paleosoil (Fig. 3.4G and 3.4E and F, respectively) show a vertical sense of movement, although limited sub-horizontal fault striations may indicate a strike-slip reactivation of this structure. In some cases these faults have flower-structure geometries, indicating oblique motion. The same set of faults also occurs occasionally in the Miocene Red Formation farther east where it is associated with motion along the MFF.

The youngest tectonic manifestations are N-striking thrust faults cutting alluvial deposits (from Unit A to Unit C) away from the range in the Tehran plain. These thrusts have been observed only in the western and central parts of the NTT footwall and either verge west- or eastward.

Our data and observations by other workers show that these structures are not compatible with one sustained kinematic regime. Instead, the kinematic analysis and our synthesis of macrostructures reveal two separate kinematic regimes that have influenced the NTT and MFF (Fig. 3.5 A and B). We infer that these regimes were controlled by a rotation of the shortening direction from an original NW-NNW to a neotectonic NE-NNE orientation. This may have resulted from a rotation of the direction of the greatest horizontal stress $S_{Hmax}$. These interpretations are based on Anderson's theory of faulting (Anderson, 1905, 1951), whereupon faults form at specific angles to the applied principle stresses and where one stress direction is vertical. However, this theory relates the orientation of faults to the stress field at the time of development. Once formed, the faults remain zones of weakness, which might be reactivated, even if the regional stress field is not optimally oriented. In this case, the state of stress does not control the orientation of the fault plane, but instead controls the slip vector, whose orientation depends on the stress tensor aspect ratio (e.g., Célétier, 1995). In addition to these complexities, we have to consider that even in small regions, the stress field may vary and become inhomogeneous. However, in our study area, faulting in both regimes has been accompanied by macroscale and mesoscale folding (compare insets in Fig. 3.5 A and B, respectively), which we think is another indicator for the rotation of the shortening direction and supports the applicability of Anderson's theory.

It is interesting, however that indicators of sinistral motion along the central segment of the MFF are rare. Such kinematics are instead often associated with E-striking subsidiary faults (e.g. Fig. 3.5B, localities 14, 17), partly with normal components, and with the similarly E-striking western MFF segment. These observations imply a strong influence of the fault geometries with respect to the accommodation of regional stresses resulting from the convergence between Arabia and Eurasia.

The earlier NW-oriented shortening episode is compatible with thrusting and dextral strike-slip kinematics on the MFF and NTT (Fig. 3.5 A). The Miocene marls of the Red Formation are the youngest units affected by this kinematic regime. Part of this deformation regime are conjugate low-angle NE- and WNW-striking dextral oblique thrusts, NE-striking thrusts, high-angle NW-striking left-lateral strike-slip faults, NNE-striking reverse faults, and NE-trending folds. This structural inventory is consistent with the macroscale dextral transpressional character of the MFF, as expressed by the alignment of ENE-striking thrusts and folds that are cut by the fault.

NE-shortening is associated with oblique thrusting along the central MFF and in its footwall, as well as sinistral strike-slip faulting on minor faults in the central MFF segment (Fig. 3.5 B). NW-striking reverse and thrust faults, and NNE-striking dextral strike-slip faults constitute the main inventory of the analyzed structures. In addition, WNW-trending folds, oblique to the strike of the NTT, are indicative of left-oblique reactivation of the NTT. NW-trending fold axes and macroscale tilting are also observed and attest to the regional accommodation of NE-directed shortening.

In addition to the orientations of the inferred compressive stresses our fault-kinematic data reveal limited examples of extensional pseudo-fault plane solutions (Fig. 3.5 C) with varying orientations of the tension axes. The data were recorded along the MFF and a subsidiary fault-branch as well as along the NTT in the junction area between both faults. In some cases, a combined data analysis, without extraction of the normal components reveals pseudo-fault plane solutions with left-oblique kinematics on W- to NW striking nodal planes (Fig. 3.5 C, localities 7, 14, 16, and 17).

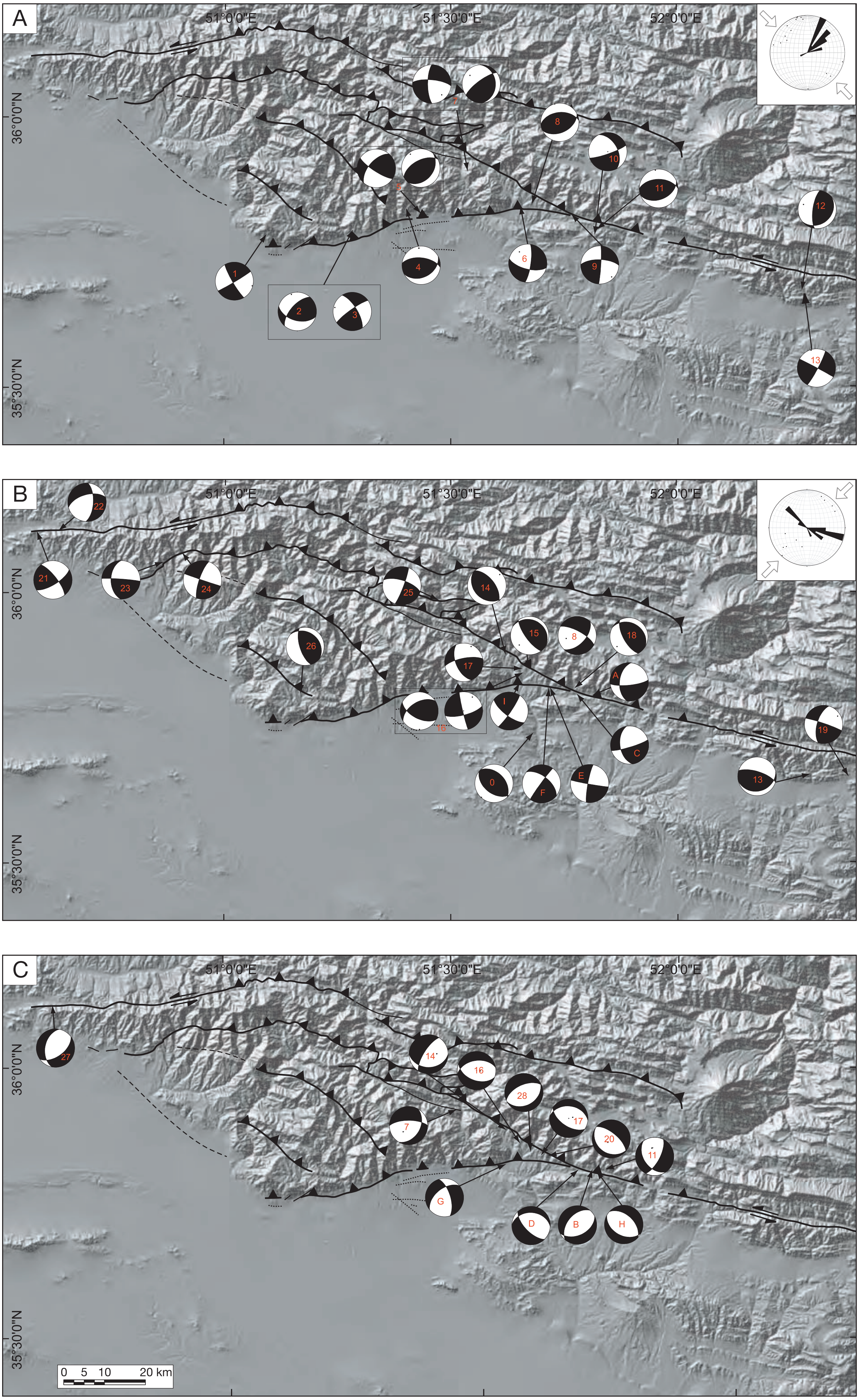
A
51°0'0"E
51°30'0"E
52°0'0"E
36°0'0"N
35°30'0"N
1
2
3
4
5
6
7
8
9
10
11
12
13
B
22
21
23
24
25
14
26
15
8
18
17
A
I
16
C
19
13
0
F
E
C
27
14
16
28
7
17
20
11
G
D
B
H
0 5 10 20 km

Figure 3.5: Pseudo fault-plane solutions of measured and sorted fault kinematic data, grouped according to their kinematic populations. The fault kinematic analysis reveals two faulting regimes for the NTT and MFF, controlled by a rotation of $S_{Hmax}$ from an original NW/NNW (A) direction to a NE/NNE orientation (B), note the inset scatter plots of calculated $\sigma_1$ poles and the rose diagrams of the measured mesoscale and calculated macroscale fold axes orientations. In addition, indications of extension were observed, without clear cross-cutting relationships for the measurements in bedrock (7, 14, 16), but demonstrating the youngest tectonic movement in the Quaternary outcrops (C). Fault kinematic raw data (strike, dip, rake and sense of movement; see Fig. A.1, appendix A) were analyzed using the Fault Kin program (Allmendinger, 2001).

The fault-kinematic analysis of the strained clasts and faults measured in the junction area of the NTT and MFF show recent left-lateral strike-slip and normal faulting (Fig. 3.5B and C, localities A to H). Since these data correspond to the youngest activity, they are in agreement with the geomorphic observations of a kinematic changeover from dip slip to systematically oblique faulting. This is also observed in Oligo-Miocene bedrock units, where the oldest, dextral-transpressional trend is superseded by a left-transtensional regime. However, the Quaternary faulting history is also very complex and reveals different extension directions. Good conditions for kinematic analysis and trench logging are found in the Kond and Afjeh valleys, and in Kalan. These outcrops show evidence for repeated abrupt offsets, as documented by the sedimentary wedges in the footwall and fissure fills along the fault, and clearly document Quaternary seismogenic activity.

## 3.5 Geomorphic observations

To characterize the distribution of relief in the vicinity of the faults as a proxy for deformation and uplift and to identify areas of young tectonism, we used morphometric and landform analysis of the investigated area.

### Morphometric analysis

Localized surface uplift or base-level lowering may result in increased channel slopes with higher erosion rates, and therefore increased relief of drainage basins relative to surrounding crests (Bürgmann et al., 1994; Merrits & Vincent, 1989). Residual relief maps, calculated as the difference between an envelope of the highest elevations and another envelope of the present-day drainage channels, therefore help outline sectors of high stream-incision rates, presumably associated with high rock uplift (Bürgmann et al., 1994; Hilley et al., 1997). However, the interplay between uplift and erosion is also influenced by differences in erodibilty of the material, e.g., rock type variations in the range, which might account for considerable differences in relief. The following calculations are based on the assumption of spatially uniform resistance of rock to erosion, but are less reliable where this condition is not satisfied. The rock type variability in the Eocene units of the study area is generally high, nevertheless, we think that differences in erodibility of these units are less significant, especially on the scale used for the morphometry. To be more precise, it is worth comparing the area between the NW-prolongation of the NTT and the Emamzadeh-Davud Fault (EDF) (Fig. 3.2), where a more than 5 km thick succession of these highly variable Eocene units is exposed. At this location the Karaj Formation comprises three different shale members, repeatedly alternating with tuffs, tuffaceous siltstones, limestones, and sandstones in places, but it does not exhibit any significant difference in residual relief. However, where such rock type variations are obvious and might correspond to the observed relief, we will indicate this possibility in the text.

The residual relief map of the NTT/MFF area exhibits two distinct spots and one elongated zone of high relief (Fig. 3.6B, dark blue areas). The elongated area is located between and aligned with the subvertical western segments of the Mosha-Fasham and Taleghan faults. This high is associated with outcrops of Precambrian to Paleozoic units, which comprise mainly dolomite, sandstone and limestone, and might be more resistant to erosion than the Mesozoic limestone and shales or the Eocene limestones, shales and volcanoclastic sediments. The remaining two zones of high topographic relief do not strikingly correspond to such strong resistant rock types. One of these spots is located immediately east of the outside corner of the MFF left bend, and accordingly, at the inside-corner of the Taleghan Fault left bend. However, the third high-relief zone is located around Mount Touchal, at the inside corner of the NTT and EDF (see Fig. 3.2A for geology and B for fault names). Here, in the immediate hanging wall of the EDF, the base of the Eocene units is exposed, which also comprise other lithologies, such as lava flows. These units are potentially more resistant. However, the top units of the Touchal, which corresponds to the location of the high residual relief, consist of an alternation of shale and tuffaceous siltstone, and are consequently more erodible.

To infer a relation of the relief in the NTT-hanging wall with the relief across the connecting faults (MFF, EDF, and PVT; see Fig. 3.2B for fault names), a topographic swath profile was calculated, approximately perpendicular to the NW-striking faults (Fig. 3.6C). In addition to a general eastward increase in elevation, the maximum elevation (upper line) consistently has the highest points in the hanging wall of the NW-striking faults. Interestingly, the mean elevation (middle line) drops in the MFF fault zone.

For about two-thirds of its length, the NTT fault trace constitutes the southern edge of the Alborz mountains. Towards the east, increasing footwall uplift alters this expression. Assuming that topographic relief correlates with cumulative offset (King et al., 1988; Stein et al., 1988; Bilham & King, 1989; Taboada et al., 1993), topographic along-strike profiles were calculated at different distances from the fault trace to characterize the long-term behavior of the NTT (Fig. 3.6D). All profiles show consistently two main steps in elevation, linked by a transition zone. Thus, the western segment may have accumulated less displacement than the central segment. Interestingly, a topographic outlier in the central NTT segment, which exhibits anomalously high topography, coincides with the termination of a prominent

WNW-trending anticline (Latyan structure after Dellenbach (1964)), but is also associated with a subtle right-bend of the NTT (Fig. 3.6D). This suggests interaction with the NW-ward growing anticline and related faults, which would plunge below the NTT. Towards the east, in the junction area, the topography is much more subdued without any significant differences among the four profiles. This might suggest less accumulated uplift, which could result from a kinematic changeover to dominant strike-slip motion. However, while this kind of analysis requires uniform resistance of rocks to erosion, we cannot exclude that in this easternmost segment, the effect is due to higher erodibility of the exposed shales. Overall, the segmentation of the NTT, as amplified in its distinguishable topographic expression, suggests semi-independent uplift histories.

Interestingly, the position of the Kan river also marks the position of the segment boundary between the western and central segments. Decreasing offsets towards the tips of the overlapping segments might have enhanced the ability of the river to cut through the more slowly rising mountain front. In contrast, catchments in the hanging wall of the rapidly rising central segment are rather steep and small. However, another possibility might be that an early Kan river was able to capture areas in the headwater, which allowed it to continue incising contemporaneous to uplift. In this case, the relief would rather reflect the drainage history than spatial gradients in rock uplift. At present, this cannot be excluded.

**Faulting and landform evolution in the NTT/MFF transition area**

Where the eastern branch of the NTT approaches the MFF, both faults show a change in strike direction. The MFF changes strike from WNW to NW, while the NTT has a subtle left bend. No small-scale offsets as indicators of motion during the most recent earthquakes were observed along the fault traces, but cumulative offsets reveal the long-term tectonic activity of both faults. For example, three sets of areally extensive Quaternary terraces occur in the footwall of the MFF and in the hanging wall of the NTT, which have no match beyond the fault (Fig. 3.7).

This clearly documents Quaternary thrusting along the NTT. The geomorphic surface T2, a gravel covered erosion surface, is sculpted into the folded Eocene to Miocene units that have been deformed during NE-directed shortening (Fig. 3.7B). A reconstruction of T2 surface remnants (Fig. 3.7C) reveals vertical displacement of $\sim$ 317 m relative to the local base level at the NTT. Assuming a Quaternary age of the surface, the offset implies a minimum slip rate on the NTT of 0.2 mm/yr. However, this rate could be several mm/yr, if the surface is only few hundred thousand years old.

Terraces in the hanging wall of the MFF are rare, but the fault trace is characterized by a pronounced step in topography. Channels crossing this structure are not deflected laterally, but recent faulting is manifested by a scarp of a young dip-slip splay fault of the MFF (Fig. 3.7A).

Distinct sinistral stream offsets of about 85 m characterize the eastern termination of the NTT, east of the area of thrusting (Fig. 3.8A). In addition, the deformation history of the

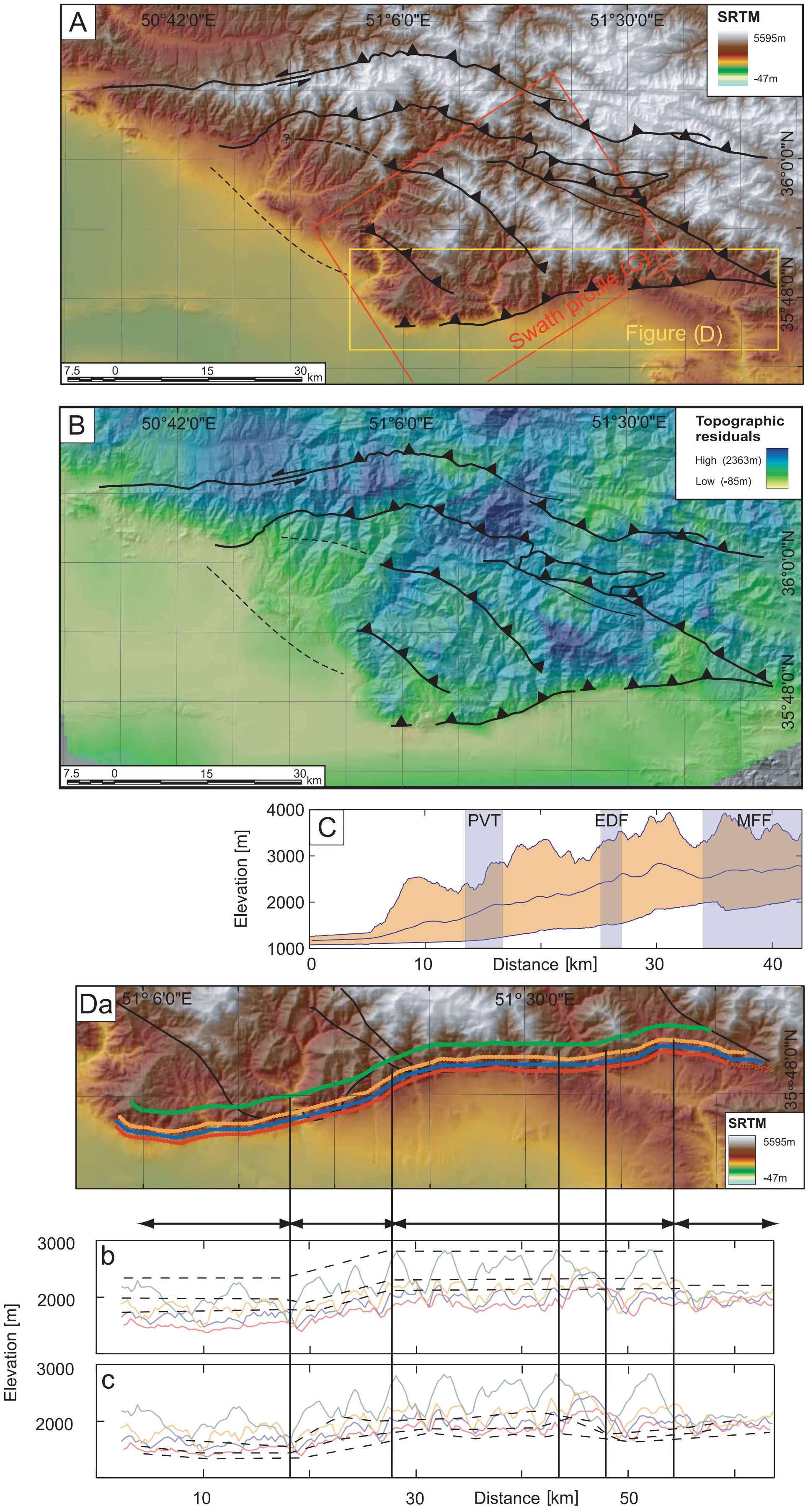
A
50°42'0"E
51°6'0"E
51°30'0"E
SRTM
5595m
-47m
36°0'0"N
35°48'0"N
Swath profile (C)
Figure (D)
7.5 0 15 30 km
B
50°42'0"E
51°6'0"E
51°30'0"E
Topographic residuals
High (2363m)
Low (-85m)
36°0'0"N
35°48'0"N
7.5 0 15 30 km
C
PVT
EDF
MFF
Elevation [m]
4000
3000
2000
1000
0
10
Distance [km]
30
40
Da
51°6'0"E
51°30'0"E
35°48'0"N
SRTM
5595m
-47m
b
c
Elevation [m]
3000
2000
3000
2000
10
30
Distance [km]
50

Figure 3.6: Topographic analysis, derived from DEM data. (A) Overview-DEM with main faults (for labels compare Fig.3.2B). Indicated are locations of following figures. (B) Topographic residuals of the study area, derived from SRTM data by subtracting a drainage-envelope from a ridge-crest envelope. The blue spots correspond to high incision and presumably, high-uplift zones. (C) Topographic swath profile across the NTT and perpendicular to its connecting faults (MFF, EDF, PVT; see Fig. 3.2B for fault names) showing the distribution of minimum, maximum and mean elevation. Note that the highest maximum elevation is always located in the hanging wall of these faults. (D) Topographic along-strike profiles in different intervals to the NTT-fault trace. (a) Location of the profiles on SRTM-DEM, color coding is equivalent to the profile lines in (b) and (c). Note also the locations of the connecting faults (MFF, EDF, and PVT). Dashed lines show manual interpolation along the highest peaks (b) or manual interpolation along the base level (c). Note the consistent segmentation in (b) and (c) as indicated by the black vertical lines.

NTT footwall may be revealed by tectono-geomorphic features, including four generations of abandoned surfaces (T1-T4). These terraces occur at increasingly lower elevations towards the west, which is in agreement with the decreasing degree of incision of the surfaces.

An E-W striking, almost vertical splay fault (Latyan Fault, Fig. 3.4G) offsets sediments of Plio-Pleistocene age (Unit A). The fault activity is postdated by terrace T4. This structure was originally a dip-slip fault with up to the south motion, as inferred from rotated clasts in the fault zone, a missing paleosol (Fig. 3.4 G, E, and F, respectively), and the deep incision of streams south of it (Fig. 3.8A). However, horizontal striations developed in a fault gouge also indicate strike-slip reactivation, and the en échelon alignment of map-scale extensional gashes that form sigmoidally shaped depressions (Fig. 3.8A, D) point toward sinistral shear. The extension direction inferred from these gashes is ENE-WSW, matching the present-day tectonic stress field.

## 3.6 Discussion and Conclusions

Applying Anderson's theory of faulting (Anderson, 1905, 1951), our fault kinematic study revealed an early dextral kinematic history for the NTT and the central MFF. In a few cases the dextral kinematic indicators clearly postdate earlier dip-slip reverse faulting. Miocene dextral strike-slip and oblique dextral reverse faulting along the MFF and NTT took place during NW-oriented shortening. The dextral kinematics are compatible with observations by Axen et al. (2001), and Zanchi et al. (2006) documented dextral transpression during NW-shortening. Partly refolded NE-trending fold axes in the hanging wall of the NTT observed by Allen et al. (2003), also support such a scenario. Hence, it is reasonable to infer that the E-W striking NTT is mechanically linked with the dextral transpressional alignment along the MFF (Fig. 4.2). However, the regional expression of this alignment is incompatible with the domal structure used in an early study by Allen et al. (2003) to estimate the maximum MFF offset. When restored, this structure would cross the MFF, instead being part of a former alignment. The high-uplift zone between the subvertical western segments of the

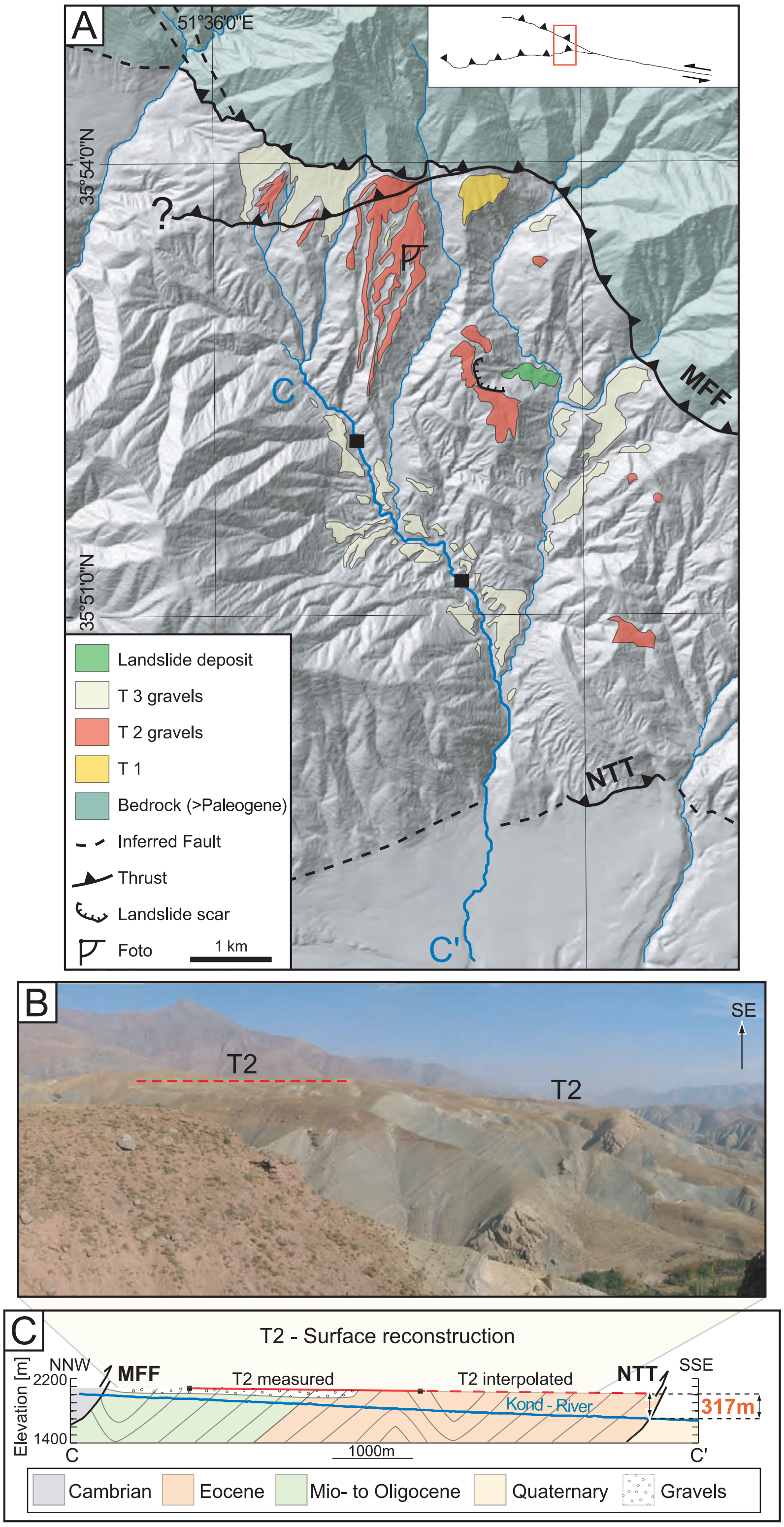
A
51°36'0"E
35°54'0"N
35°51'0"N
?
C
C'
MFF
NTT
Landslide deposit
T 3 gravels
T 2 gravels
T 1
Bedrock (>Paleogene)
Inferred Fault
Thrust
Landslide scar
Foto
1 km
B
T2
T2
SE
C
T2 - Surface reconstruction
NNW
MFF
T2 measured
T2 interpolated
NTT
SSE
Elevation [m]
2200
1400
Kond - River
317m
C
1000m
C'
Cambrian
Eocene
Mio- to Oligocene
Quaternary
Gravels

Figure 3.7: Geologic-geomorphic map of the Kond Valley in the NTT hanging wall and MFF footwall. (A) Three terrace systems occur in the NTT hanging wall (T1-T3), indicating repeated Quaternary uplift along this NTT segment. The MFF is characterized by a step in elevation. However, streams cross the MFF without deflection or offset. Recent faulting is manifested with a scarp at a young dip-slip splay fault of MFF. Inset: Figure location with respect to the MFF-NTT system. (B) Terrace T2, a very extensive, gravel-covered paleopediment, sculpted into folded and tilted Eocene to Miocene units. (C) Two terrace profiles, developed in dip-direction (the upper one from differential GPS measurements, the lower one from DEM) were extrapolated by linear best fit to their location above the recent Kond River (black dots in (A) and (C). These points in turn were extrapolated towards the NTT location. The reconstruction of terrace T2 revealed an uplift of about 317 m relative to the erosion base level at the NTT.

MFF and Taleghan fault, as observed from topographic residuals, also fits the alignment. The elongated area therefore might be related to uplift under the dextral transpressional regime.

Conversely, Allen et al. (2003) and Guest et al. (2006a) interpreted strike-slip faulting in this region with conjugate dextral and sinistral strike-slip movements during N-S shortening. The early dextral strike-slip regime was superseded by Pliocene NE-oriented shortening, which was associated with sinistral-oblique thrusting along the NTT and the central-western MFF, sinistral strike-slip motion on subsidiary faults in the central MFF segment, and folding and tilting of Eocene to Miocene units in the MFF footwall. This is compatible with observations in other areas of the central Alborz mountains (e.g., Allen et al., 2003; Axen et al., 2001; Guest et al., 2006a; Zanchi et al., 2006; Moinabadi & Yassaghi, 2007). The formation of gravel-covered erosion surfaces in these tilted units was accompanied by continued thrusting along the NTT. However, folding in the hanging wall and sinistral stream offsets indicate a left-oblique component or a Quaternary strike-slip reactivation of the eastern NTT segment, close to its termination. Here, the NTT has an approximate E-W strike, similar to the active, eastern sinistral MFF segment. It is therefore possible that the NTT is favorably oriented to accommodate overall shortening by sinistral strike-slip movement. In addition, the high residual relief in the inside corner of the NTT-EDF system and the topographic along-strike profiles of the NTT suggest that these segments have been not only active, but also very efficient in uplifting this block of the mountain front. Accommodation of left-lateral motion by the eastern NTT is also compatible with the sigmoidal-shaped en échelon tension gashes in the vicinity of the reactivated Latyan fault (Fig. 3.8). Farther west, the left-bending section of the NTT changes into a dip-slip fault, as indicated by uplifted fluvial terraces and a much more sinuous mountain front. In such a scenario the area west of the Afjeh river would constitute a horsetail termination of a sinistral strike-slip system, causing the opening of a small basin with successive lowering of the local base level of the NTT footwall towards the west (Fig. 3.8A-C).

The macroscale pattern of the MFF and the NTT, as part of a former dextral transpressional system, and the present-day sinistral regime observed at the eastern and central-

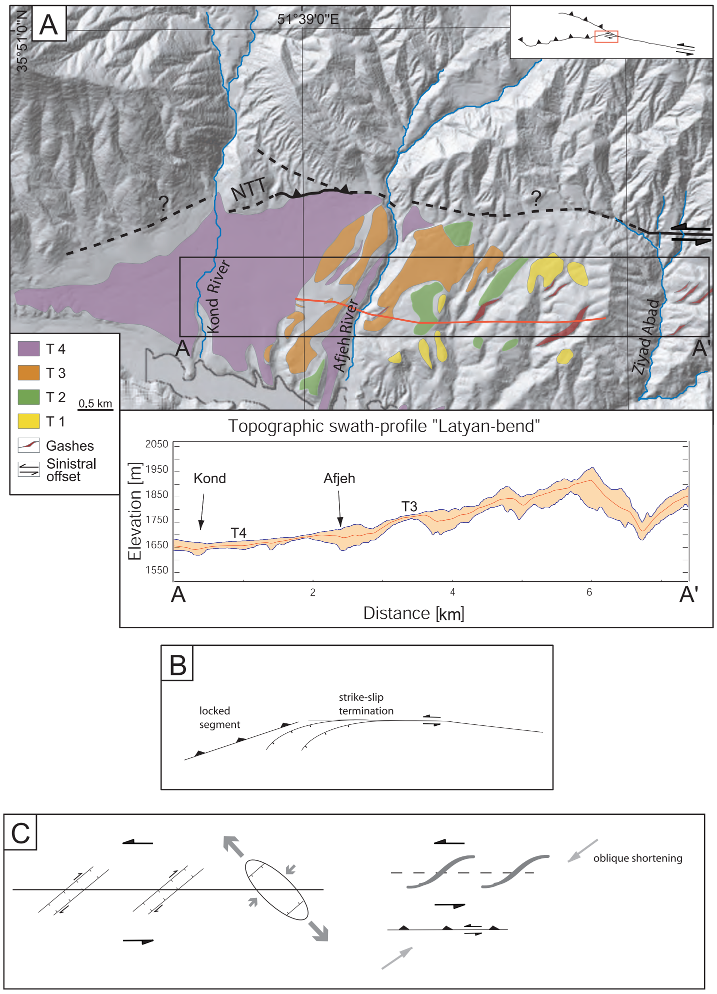

Figure 3.8: Eastern segment of NTT with footwall deformation: Left-lateral stream offsets are observed at the eastern termination of NTT (right middle in figure A), whereas the western prolongation is characterized by thrust-movement (compare Fig. 3.7). West of Kond the NTT fault trace is covered by recent sediment. Alternatively, the sinuosity of the mountain front may also rather indicate thrusting and widening of valley by lateral erosion. The footwall topography decreases (A and swath-inset), and the terraces become increasingly abandoned westward, indicating a pull-apart basin. This may result from the left bending of the fault or a horsetail-termination related strike-slip motion (B). Note S-shaped closed valleys, aligned along an E-W striking, vertical splay fault (middle of figure, compare Fig.3.4E-G), interpreted as en échelon aligned macroscale extensional gashes. The extensional direction, inferred from the tension gashes matches the neotectonic stress field (C - sketch after Burbank and Anderson (2001), where extension fractures are formed in response to a strike-slip shear couple), their sigmoidal shapes suggest sinistral shearing (D - sketch after Philip & Meghraoui (1983), with the creation of oblique grabens in response to shortening, which is oblique to the thrust front). Inset in (A): Figure location with respect to the MFF-NTT

| Feature | NW-compression | NE-compression | General description of the observed structure |
|---|---|---|---|
| **Topography** | high uplifted sectors between the western segments of MFF and Taleghan-Fault | high uplift zone at the inside corner of NTT-EDF | Topographic residuals as indicators of high-incision/high-uplift zones (Fig. 3.6B) |
| **Macroscale structures** | NE-trending folds, NE-striking thrusts, MFF-alignment | NW-trending folds, NW-striking thrusts, NW-tilted units | Two sets of large-scale folds (Fig.4.2); refolded folds |
| **Mesoscale structures** | conjugate low-angle NE- and WNW-striking dextral oblique thrusts; NE-striking thrusts; high-angle NW-striking left-lateral strike-slip faults; NNE-striking reverse faults, and NE-trending folds | oblique thrusting along the central MFF and in its footwall, as well as sinistral strike-slip faulting on minor faults in the central MFF segment; NW-striking reverse and thrust faults, and NNE-striking dextral strike-slip faults | fold axes, directly measured in the field or calculated from measurements of the limbs (see inset in Fig. 3.4A, B); measured fault-kinematic data based on striations and slickensides (Fig. 3.5) |
| **Quaternary offsets** | no obvious signal | offset terraces in NTT hanging wall, offset streams at eastern-most NTT | gravel covered erosion surface, sculpted into folded Eocene to Miocene units; channels at the NTT are offset or deflected left-laterally (Fig. 3.7 and 3.8) |

Table 3.1: Synopsis of simple and composite landscape and structural compartments in the south-central Alborz

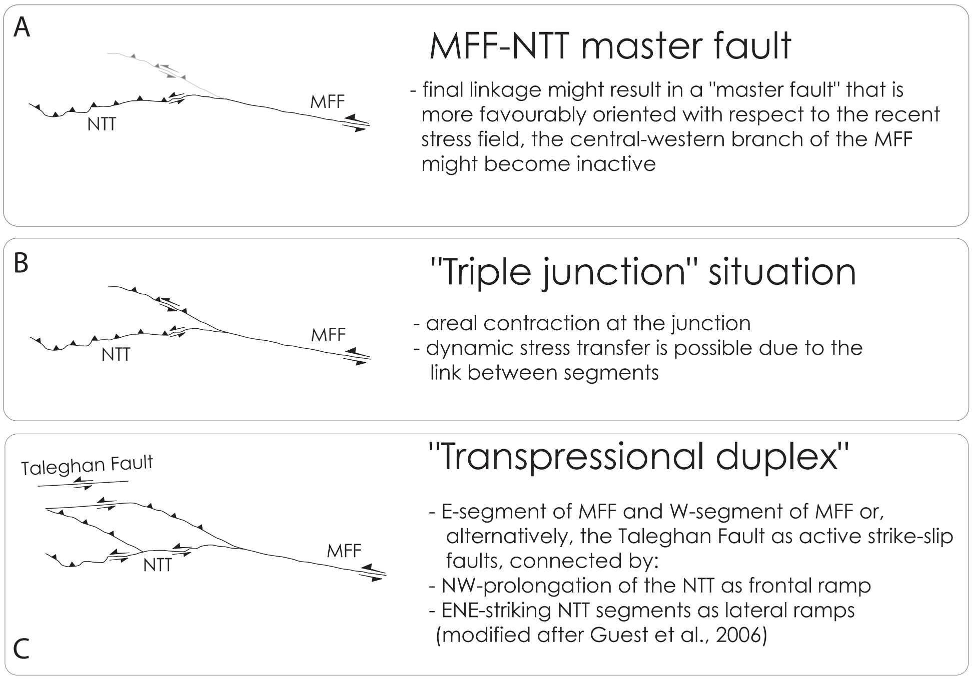

Figure 3.9: Three possible scenarios depicting fault interaction of this area: (A) The NTT-eastern MFF system could represent a master fault, (B) the connection of the faults could be comparable to a triple junction, and (C) the faults could form part of a transpressional duplex

eastern MFF and along the eastern NTT, all suggest mechanical linkage, and therefore kinematic interaction of both fault systems. Our observations allow for three possible scenarios of fault interaction in this area (Fig. 3.9).

### 3.6.1 Master-fault scenario

First, the MFF-NTT system could represent a master fault resulting from eastward propagation of the North Tehran Thrust, which may have eventually reached the Mosha-Fasham Fault (Fig. 3.9A). This linkage created a longer master fault that increasingly accommodated more displacement. At present, such a structure would take up all of the strain in the deforming area. In contrast, the previously important western and central-western MFF branches would therefore fall within a stress shadow and would have become inactive. Analogous progressive linkage processes have been recorded by field observations elsewhere (Gupta et al., 1998; Gupta & Scholz, 2000) and by numerical modeling (Cowie et al., 1993).

The most obvious argument for a master-fault scenario is the lack of geomorphic indicators for Holocene faulting along the central-western segment of the MFF, whereas such indicators exist for the adjacent NTT. Moreover, the observed left-lateral kinematics of the easternmost NTT strand follows a similar motion of the MFF, and the affected NTT branch has approximately the same strike as the eastern MFF. It is therefore reasonable to assume that the NTT is more favorably orientated to accommodate sinistral shearing under the present-day stress field than the NW-trending central MFF branch. In addition, the NTT-

EDF bounded area of presumed high-uplift may indicate more active block movement there than along the central MFF. However, several observations are incompatible with an inactive central-western MFF branch. First, even if the main present-day seismic activity is observed at the eastern MFF branch, individual small events are also recorded along the central MFF and between the western Taleghan and MFF segments (Ashtari et al., 2005). Second, historical earthquakes have affected different segments of the MFF as a whole. In particular, the destructive earthquake from 958 AD was probably associated with ruptures of the western MFF segment (Tchalenko, 1974; Ambraseys & Melville, 1982; Berberian, 1983; Berberian & Yeats, 2001). These destructive earthquakes did not leave a significant geomorphic mark, as it would be expected for repeated historical ruptures. Nevertheless, the pronounced break in the topography and moreover the paleo-pediment in the Kond Valley (Fig. 3.7) imply that the mountain front, which is bounded by the central-western MFF, has been active during Quaternary time.

### 3.6.2 Triple-junction scenario

In a second possible scenario, the active fault systems correspond to a situation comparable to a triple junction (Fig. 3.9B). Here, fault interaction and stress transfer would result in shortening or extension in adjacent areas. Dynamic stress transfer is possible due to the link between segments.

The triple-junction scenario, in its simplest form the intercept of the NTT, the eastern MFF, and the central-western MFF, would allow for coeval deformation along both, the NTT and the MFF. It also could account for the different kinematics of the MFF at the NW-bend. The triple junction concept, originally developed to test whether the geometric configuration of three plates is stable or not (e.g., McKenzie & Morgan, 1969), was also used to analyze fault junctions (e.g., Peltzer & Tapponnier, 1988; Spotila & Anderson, 2004; Raterman et al., 2007). Since a slip rate is to date only available for the eastern MFF segment, the fault-junction analysis is limited to the geometric aspect. Overall, the geometry of the MFF-NTT junction is in a stable condition. However, simple motion diagrams of the fault system cannot fully account for the observed late Neogene to Quaternary kinematics (Fig. 3.10). Assuming three rigid blocks between the faults, we have first inferred the central-western MFF as thrust, the NTT as left-oblique thrust, and solved for the eastern MFF to compare the diagram with the long-term deformation signal, which we suggest to be coherent with the geomorphic signature. The resultant vector for the eastern MFF segment is longest, but would correspond to thrusting with only a minor component of sinistral motion. To increase the strike-slip fraction here, while the geometries of the other fault segments are kept, the shortening at the central-western MFF segment has to become significantly smaller. Therefore, with the observed kinematics coeval activity of all three faults is difficult to reconcile. However, the diagram suggests that the highest slip rates should occur on the

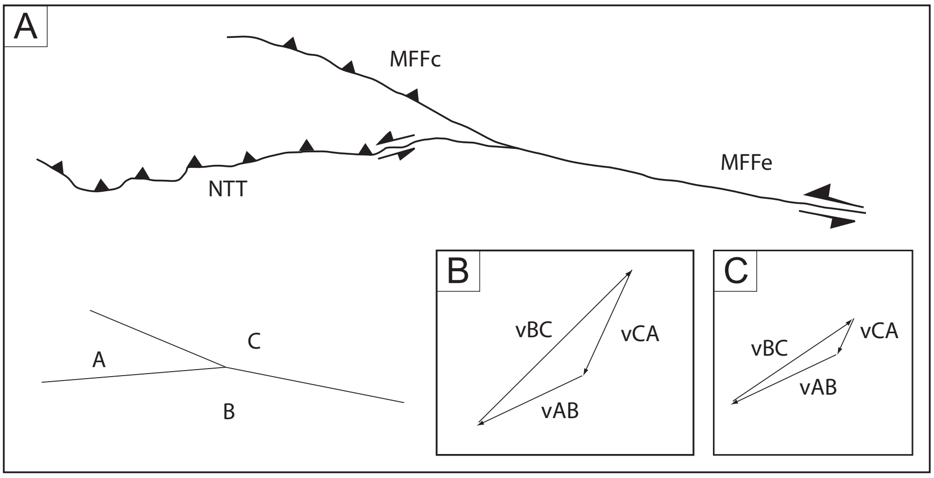

Figure 3.10: Simple motion diagram to explain the MFF-MFF-NTT fault junction. (A) Simplified fault segment geometry as observed in the field with indication of thrusting along the central MFF segment, and left-oblique thrusting at the NTT. (B) The simple motion diagram shows that the resultant vector for the eastern MFF is the longest. This means that this segment would experience the highest rate, coherent to what is observed in the present-day seismicity. However, the direction of motion indicates a primary thrusting with only a minor component of sinistral motion. To increase the strike-slip component here, the shortening at the central-western MFF segment has to become significantly smaller (C).

eastern MFF segment. Slip would become distributed over the branching faults, which is a reasonable assumption for the studied area.

### 3.6.3 Transpressional duplex scenario

In the third alternative, the MFF and NTT form an integral part of a transpressional duplex (Fig. 3.9C). In this case, which is modified from the model of Guest et al. (2006a), the eastern and western segments of the MFF correspond to active strike-slip faults, connected by a NW prolongation of the NTT as frontal ramp, and ENE-striking NTT segments that form lateral ramps. This model could reconcile the different kinematic styles along the MFF. Accordingly, the dominant kinematics of the NTT segments must be left-lateral motion.

Under the present-day stress field, a transpressional duplex would transfer the left-lateral to oblique-reverse motion along the MFF in order to accommodate shortening in this part of the mountain range. The model therefore accounts for the observed sinistral motion along the eastern MFF branch and the kinematic change towards thrusting or left-oblique thrusting in the central and western segments, respectively. Within such a duplex structure, the elevated topography north of Tehran would be created by westward thrusting along the NW-striking central MFF-segment and similarly- striking, parallel thrusts in the footwall. Active frontal ramps in this system are the EDF, the PVT, and the NW prolongation of the NTT. The EDF is, together with the NTT, responsible for the high residual relief of the Touchal block. The fact that the NW-striking PVT and EDF are observed only in the hanging wall of the NTT and do not cut the fault, suggests either kinematic linkage of these faults with the NTT or that the NTT movement postdates any activity along the PVT and EDF. However, the northwestern prolongation of the NTT is characterized by a very sinuous range front, indicative of strong lateral erosion into the hanging wall, and therefore low degree of tectonic activity (e.g., Bull, 2007).

The NTT and the western MFF do not constitute sinistral tear faults to connect the frontal ramps, even if the present-day stress field would allow for dominant left-lateral kinematics. Instead, the kinematic regime along the NTT is characterized by oblique thrusting or reverse faulting. The fault dip is rather steep and the wide fault zone in the hanging wall strikes parallel to the NTT and documents S-directed, rather than W-directed, movement. The NTT segments therefore may represent lateral ramps and the steep fault dip might eventually flatten with depth. The along-strike topographic profiles of the NTT also reveal a semi-independent deformation history, which might be coupled with deformation along the NW-striking thrusts in the hanging wall. However, the central NTT segment, which accommodated the highest amount of deformation, starts already in the footwall of the EDF (Fig.3.6).

Taken together, our data show that a transpressional duplex system was not the first-order structure at the onset of the evolution of this part of the mountain range. Instead, the duplex is a young structure, probably associated with the changeover from regional NW- to NE-shortening. The inherited topography and uplift history might be responsible for this modification. The en échelon array of the NTT might have favored the development of thrust sheets under the recent stress field. This scenario is in agreement with the fact that such a clear linkage with the NW-striking faults is not observable for the western MFF segment, which suggests that these faults, starting from the NTT, might propagate northwestward. The transpressional duplex therefore is in a nascent stage. The distribution of the residual relief, which often corresponds to areas of highest uplift (e.g., Bürgmann et al., 1994), suggests that the Touchal block, which is thrust along the EDF and bounded by the central and eastern NTT-segments, as well as the central-western MFF, was uplifted most effectively. In this context, the sinistral changeover at the easternmost NTT is indicative of a jump of the deformation front onto this block.

In conclusion, our data suggest an early mechanical linkage of the NTT and MFF fault systems during a former dextral transpressional stage under NW-directed shortening. This regime, however, was superseded by Pliocene to Recent NE-oriented shortening. Resulting from this reorganization, the NTT and MFF were reactivated and incorporated into a nascent transpressional duplex. This system has prevailed for a significant duration of deformation. However, the youngest period is characterized by an extensional regime, which might invert the observed structure. Importantly, this system has not yet erased the topographic signal of the transpressional arrangement.

# Chapter 4

# Differentiating simple and composite tectonic landscapes using numerical fault-slip modeling.

## 4.1 Introduction

The evolution of topography in tectonically active regions is mainly driven incrementally by repeated slip during earthquake ruptures (e.g., King et al., 1988; Stein et al., 1988; Bilham & King, 1989; Taboada et al., 1993; Hetzel et al., 2004; Meigs et al., 2008). Fault scaling laws suggest a systematic relationship between relief of the resulting geologic structure (mountain, ridge, basin) and the slip distribution along the responsible faults (e.g., Scholz, 1982; Cowie et al., 1993; Dawers et al., 1993; Dawers & Anders, 1995; Ellis & Dunlap, 1988). A constant ratio between accumulated displacement and fault length (for similar rock types and simple fault geometries), and therefore systematic changes of relief in the along-strike direction can be expected (e.g., Taboada et al., 1993; Hetzel et al., 2004; Densmore et al., 2005). However, for regions with reactivated faults, Walsh et al. (2002) suggest that the fault length is rapidly established and fault growth is dominated by accumulating displacement. Pre-existing crustal faults may localize strain, and fault lengths may therefore be largely inherited from the underlying zone of weakness (e.g., Hilley et al., 2005). As a result, these faults will rapidly acquire displacement-length scaling properties after reactivation, consistent with previously established fault-growth trends (Walsh et al., 2002).

The long-term deformation field and the topographic expression of protracted faulting are further influenced by the 3D geometry of the responsible faults, their segmentation, maturity, and their interactions (e.g., Bilham & King, 1989), resulting in interference and complex superposition of single-fault displacement fields (e.g., Cowie et al., 1993; Dawers et al., 1993; Cowie et al., 2000; Walsh et al., 2002; Manighetti et al., 2009). The specific uplift pattern of mechanically interacting faults helps understand how regional fault arrays accommodate strain. Thus, it is important to consider fault interaction when assessing tectonic landforms, particularly if such landforms are being used to characterize the degree of tectonic activity of a region.

The spatial topographic evolution of small (km-scale) geological structures can be approximated by repeated coseismic deformation (e.g., Taboada et al., 1993), which might be modeled using simple elastic dislocation models (Okada, 1992). However, the full earthquake cycle includes interseismic motions and buoyancy forces exerted on the uplifted or subsided crust, which counteract but do not balance the seismic deformation (e.g., King et al., 1988). Therefore, together with loading and unloading due to sedimentation and erosion, the growth and width of larger geological structures are further influenced by interseismic deformation when stresses are relaxed at depth and isostatic equilibrium is restored (e.g., King et al., 1988).

Various studies have focused on numerical modeling of fault interactions at different time scales in order to reveal the state of Coulomb stress changes during or after earthquakes (e.g., Reasenberg & Simpson, 1992; Stein et al., 1997; Hardebeck et al., 1998; Anderson et al., 2003b; Lin & Stein, 2004). Others aimed to compare modeled with geologically derived slip rates in order to derive the most mechanically viable tectonic boundary conditions (e.g., Cooke & Kameda, 2002; Griffith & Cooke, 2005; Cooke & Marshall, 2006). In addition, uplift patterns and topography have been used to model the geometry of the responsible interacting faults, even in complex structural settings with different fault geometries and sense of slip (e.g., Taboada et al., 1993; Meigs et al., 2008).

When analyzing recent and past kinematic styles, however, it has to be considered that faults represent weak, long-lived crustal discontinuities. These faults are often reactivated in a wide range of deviatoric stress states and orientations and their associated landforms might thus not simply reflect the current ambient crustal stresses. Thus, inherited topography, unrelated to the current tectonic conditions, can be expected. If fault-related landforms are being used to characterize the level of tectonic activity, this may lead to erroneous assessments.

This important problem of different tectonic histories and landforms constitutes the basis for our investigation of simple and composite tectonic landscapes in compressive settings. Here, we define simple landscapes as those environments which have developed during sustained tectonic conditions, including incipient faults and their landforms. Plate kinematic reorganization or changes in the far-field tectonic stress may result in rotations of the direction of maximum horizontal stress through time. This will generate new faults and associated landforms, but it will also cause the continuation of activity along pre-existing faults and further growth of already generated landforms under the new tectonic boundary conditions. Consequently, such regions constitute composite landscapes that contain topography inherited from previous conditions, and are inconsistent with the regional present-day stress field and kinematic setting. Differentiating between simple and composite landscapes is thus a major challenge in understanding long-term fault histories and represents a first-order problem in correctly assessing and interpreting landscape evolution in tectonically active regions.

The south-central Alborz mountains of northern Iran are an excellent example of such a composite landscape, having evolved under the influence of different stress regimes (Fig. 4.1). Fault kinematic analysis of major and minor faults in this area has revealed early NW-directed compression (that is, the orientation of the maximum horizontal compression or $S_{Hmax}$) associated with dextral oblique thrusting. This was superseded by active NE-oriented compression, which caused thrusting and sinistral strike-slip faulting (Landgraf et al., 2009). This neotectonic activity has resulted in fault reactivation and the formation of a nascent transpressional duplex adjacent to the city of Tehran (e.g., Guest et al., 2006a; Landgraf et al., 2009). Despite considerable Quaternary faulting and the growth of topography between the Tehran plain and the Alborz mountains, the spatial distribution of recent seismicity is disparate (e.g., Ashtari et al., 2005). Such behavior is consistent with slowly deforming, wide intraplate regions, where long recurrence intervals between earthquakes are expected (e.g., Friedrich et al., 2003). Therefore, short-term indicators of tectonic conditions such as space-geodetic techniques (GPS, InSAR) and instrumentally recorded seismicity have not yet measured complete deformation cycles and provide insufficient datasets to understand the present-day and long-term tectonic characteristics of the region (e.g., Friedrich et al., 2003).

In order to differentiate between composite and simple landscapes, we use numerical fault interaction modeling of freely slipping faults driven by incrementally changing horizontal stress directions. The computed surface displacement fields provide a synoptic overview of simple landscapes. Accordingly, a composite landscape in this modeling setup combines simple landscapes which correspond to different boundary conditions over time. Assuming that elevated stresses due to the slip become permanent, the vertical displacement of the model corresponds to areas of fault-driven rock uplift and subsidence. Those real landscape elements which are not reproduced by the modeling are expected to represent topography inherited from previous different boundary conditions. Therefore, comparison of the landscape metrics with results from modeling using different directions of $S_{Hmax}$ helps to untangle the composite topography and reveal long-term effects of tectonic activity in influencing landscape evolution. We compare the respective model results with topographic residuals, calculated from a Digital Elevation Model (DEM) based on Shuttle Radar Topography Mission (SRTM) data, and discuss agreements and differences of the results with respect to the viability of boundary conditions and long-term tectonic significance of topographic characteristics.

## 4.2 Study area

The Alborz Mountains accommodate about one-third of the Arabian-Eurasian convergence (e.g., Priestley et al., 1994; Berberian & Yeats, 1999; Jackson et al., 2002b)(Fig. 4.1). Space geodetic measurements in Iran suggest NNE-directed shortening at a rate of $22 \pm 2$ mm/a relative to an Eurasian reference frame, of which $6 \pm 2$ mm/a are apparently accommodated across the Alborz mountains (Vernant et al., 2004a,b; Masson et al., 2007). In addition to the NNE-directed shortening component, range-wide left-lateral shearing at a rate of $4 \pm 2$ mm/a is observed, because the adjacent South Caspian basin moves northwestward relative to an Eurasian reference frame at a rate of $6 \pm 2$ mm/a (Vernant et al., 2004b). Masson et al. (2007) have calculated principal horizontal axes of the geodetic strain rate tensor using the GPS velocity field. Thus, the direction of maximum shortening in the study area is oriented N20E, similar to large areas in Iran. In contrast, stress inversions from focal mechanisms result in a maximum horizontal stress direction of about N45E for the central Alborz mountains (Heidbach et al., 2008). Furthermore, earthquake focal mechanisms display strain partitioning involving dip-slip and strike-slip faulting (Priestley et al., 1994; Jackson et al., 2002b)(Fig. 4.1).

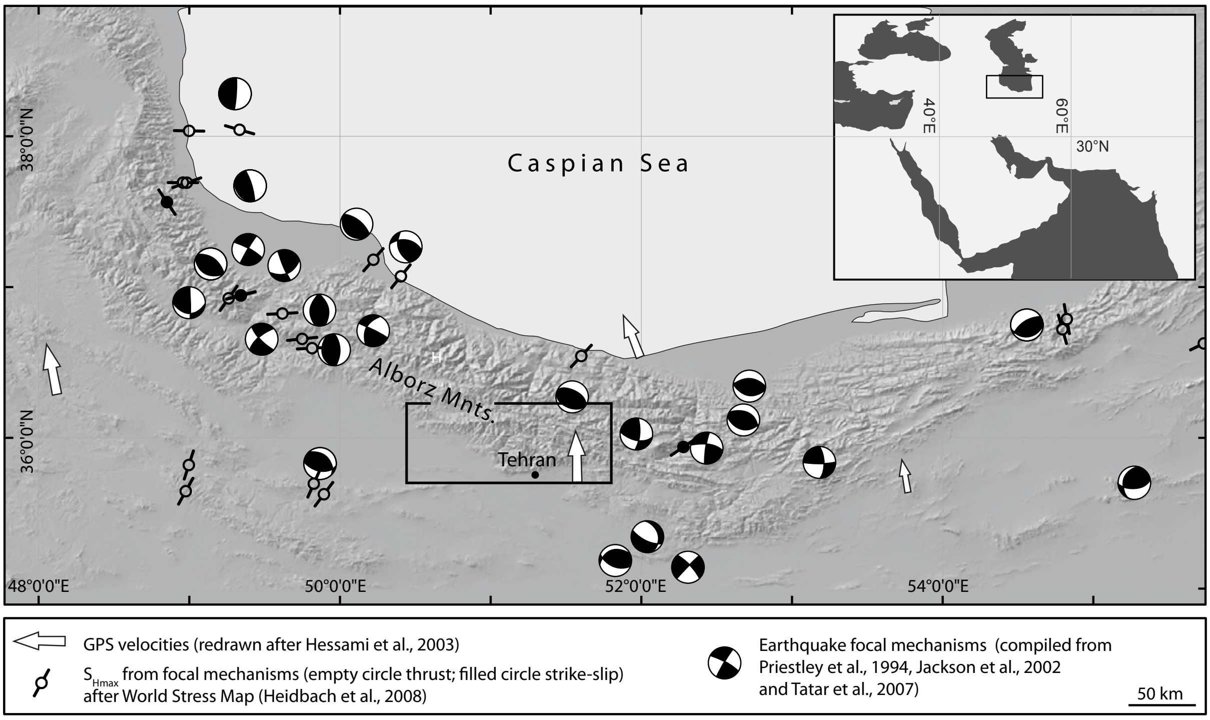

Figure 4.1: Overview of Alborz mountains. SRTM hillshade model with compilations of $SH_{max}$-directions, GPS motion, and earthquake focal mechanisms. Box denotes study area. White arrows show GPS-derived senses of relative motion (1999-2001, relative to stable Eurasia) (Hessami & Jamali, 2006); note the variation in $SH_{max}$-direction in different parts of the mountain belt, inconsistent with general N- to NNE- motion of Iran relative to Eurasia. Inset, map of Middle East with box showing location of Fig. 4.2.

The majority of earthquakes in the central and eastern Alborz mountains occur at depths above 15 km (Engdahl et al., 2006). The main shock of the most recent M6.2 Baladeh earthquake of 2004 (36.27N, 51.575E) had a thrust mechanism, with a slip vector trend of 036°±10°, but aftershocks had strike-slip as well as thrust mechanisms (Tatar et al., 2007).

The main faults investigated in this modeling study are the seismically active Mosha-Fasham and Taleghan faults (MFF and TF), as well as the North Tehran Thrust (NTT). Rare seismicity is recorded at the NTT (Fig. 4.2), but there is ample evidence for pronounced Quaternary activity (e.g., Landgraf et al., 2009). Microseismicity in this region seems to be limited to the eastern MFF segment (Ashtari et al., 2005). In contrast, historical seismicity data suggest events with magnitudes larger than 7 for this region (Ambraseys, 1974; Ambraseys & Melville, 1982; Berberian & Yeats, 1999, 2001).

Faults in the Alborz mountains record a complicated kinematic history. The early history of the MFF was dominated by normal faulting in the Late Triassic, followed by Tertiary contractile reactivation (Zanchi et al., 2006). Faults in this region often show reactivation under changing maximum horizontal stress directions (Allen et al., 2003; Ritz et al., 2006a; Guest et al., 2006a,b; Landgraf et al., 2009). During Tertiary mountain building, these faults were ultimately incorporated into a nascent sinistral-transpressional duplex (Guest et al., 2006a; Landgraf et al., 2009). This duplex system transfers motion from the eastern sector of the Mosha-Fasham Fault toward its western branch and/or the parallel Taleghan fault branch. It incorporates four NW-striking frontal ramps: the prolongation of the North Tehran Thrust (NTT/NW), the Purkan-Vardij Thrust (PVT), the Emamzadeh Davud Fault (EDF), and the central segment of the Mosha-Fasham Fault (Fig. 4.2B). These frontal ramps do not cut the North Tehran Thrust, but join it. In the overall geometry of the mountain range, the NTT segments act as lateral ramps rather than as tear faults (Landgraf et al., 2009). The Quaternary history along the NTT has been dominated by thrusting, although it has been recently superseded by sinistral transtension along the easternmost segment, which is compatible with the character of the MFF and western Taleghan faults (Ritz et al., 2006a). This similarity of young transtension prompted us to posit that this segment of the NTT might be favorably oriented with respect to the present-day stress field to accommodate N-S directed, collision-related deformation (Landgraf et al., 2009).

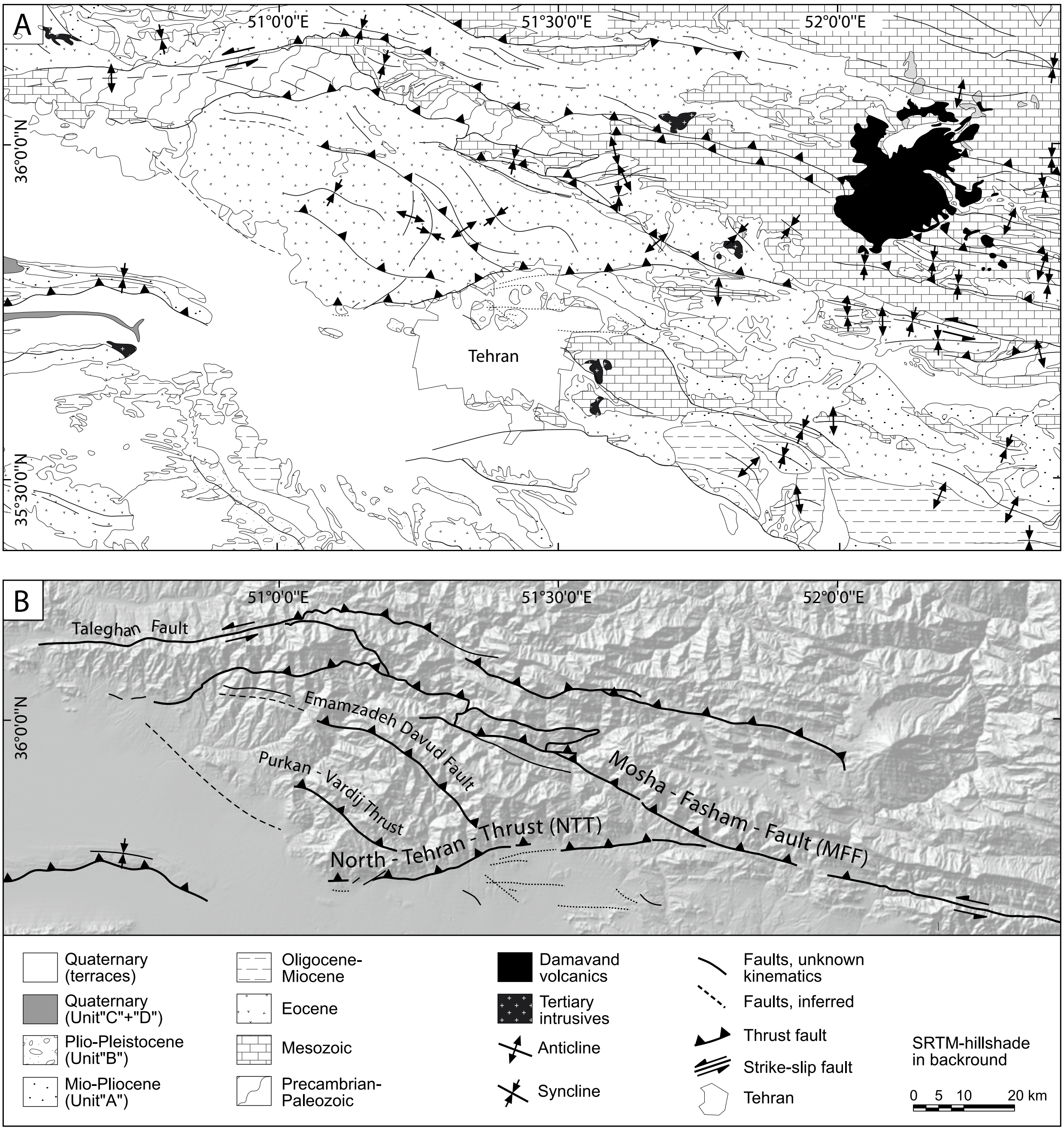

Figure 4.2: Simplified geological (A) and structural maps (B) showing faults of interest (simplified after Landgraf et al. (2009) and modified after Geological Map of Iran, 1:250,000 sheets Tehran, Saveh, Amol, and Qazvin-Rasht. Basin fill in the vicinity of the Damavand volcano are not shown for simplicity.

## 4.3 Methods

### 4.3.1 Model assumptions and model characteristics

We have used numerical simulations to investigate the long-term response (e.g., the vertical displacement field) of sustained mechanical interaction and remote loading of the faults in the greater Tehran area. No subsurface information is available for these faults and the few earthquakes (Ashtari et al., 2005) are not sufficient to characterize the fault geometries at depth. To incorporate the faults into the model, we have used our own field measurements (strike and dip) and published geological cross sections (Guest et al., 2006a,b), with additional information from Allen et al. (2003) and Zanchi et al. (2006)(Fault data table; Fig. B.1, appendix B).

The simplified, rectangular faults were implemented in an elastic half-space, which was constantly loaded by a sustained stress tensor, thus simulating the regional stress field at a given time. Numerous studies have shown that faults are non-planar, self-similar and rough surfaces over a wide range of scales (e.g., Power & Tullis, 1991; Renard et al., 2006; Sagy et al., 2007). Fault geometric complexity (such as fault bends and steps) affects the seismic behavior of the respective faults (Wesnousky, 1988; Stirling et al., 1996; Ben-Zion, 2008). To account for these facts, we divided the modeled faults into 2x2 km patches. These patches were then offset normal to the main fault plane and patch orientation was adjusted to reproduce an approximately closed, self-similar, non-planar fault surface (Fig. 4.3) using the method described by Power & Tullis (1991) and used by Zielke & Arrowsmith (2007).

No additional slip was introduced; the boundary conditions are stress derived and act along each fault. The faults are thus allowed to slip freely in response to the applied shear stress. Slip along each fault changes the state of stress in the surrounding medium (the half-space), and therefore the net tractions along all other faults that were defined. These elements release stress and transfer it to one another via in-plane slip using the analytical expressions from Okada (1992) for rectangular faults. Interaction between adjacent faults and segments increasingly contributes to the final displacement field. In reality, this would imply that the results do not represent the vertical displacement of one single earthquake, but rather the displacements after sequences of earthquake events. The displacement results from one “system-level interaction cycle” between the faults under sustained boundary conditions.

The model works iteratively, relaxing the resolved stresses until the tractions along each patch fall below a threshold of 0.001 MPa. When the interaction is finished, the slip at each patch is used to displace the observation plane at the half-space free surface (simulating the topography) following Okada’s formulation of the Green’s functions (Okada, 1992). No friction is applied to the faults. We suggest that this is valid for three reasons: first, we do not model specific earthquakes in "real time", as we are interested in the final displacement, integrated over several earthquake cycles. Second, we compare our results with long-term

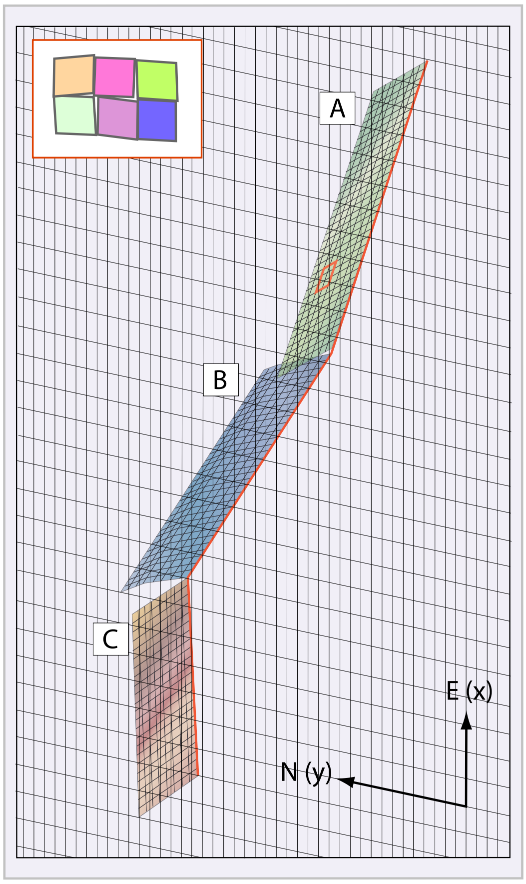

Figure 4.3: Conceptual figure to illustrate the fault geometry in the model. Rectangular faults are subdivided into segments (A-C), simulating real fault segments or changes in fault geometry. Segments are further subdivided into patches of equal size, which release stress and transfer it to one another (Okada, 1992). To reproduce more realistic behavior, a roughness was imposed on all faults, as shown in the inset (representative to red rectangle in segment A). In this study the horizontal observation plane, indicated in gray with grid, is located at the surface. Note also the changing downward connectivity between the inclined fault segments. Here, the double bending geometry (surface fault trace marked in red) and different segment dip results in convergence between segments A and B, and in divergence with possibly less connectivity between segments B and C, respectively. This fault configuration is identical to the implementation of the Mosha-Fasham Fault.

displacements. Long-term fault interaction might result in fault unclamping and weakening, and thus nearly frictionless behavior (e.g., Parsons, 2002). Third, we do not have reliable information about the strength of the modeled faults. Incorporating friction, therefore, would not add information, but rather increase uncertainties.

However, there is a disadvantage when modeling rectangular faults. Their connection at depth either results in divergence or convergence of the segments (Fig. 4.3). Divergence might result in insufficient connectivity and therefore interaction, whereas convergence can result in overlap and collision of the segments. In this boundary element approach, such collisions may result in mathematical singularities. To overcome this problem, the program tests for possible collision patch-wise and inhibits interaction between overlapping patches.

The model provides tectonic forcing without any feedbacks to isostatic adjustment or surface processes and thus considers cumulative coseismic deformation only (e.g., King et al., 1988; Stein et al., 1988; Taboada et al., 1993). Although in tectonic settings with dip-slip fault environments the observed vertical relief is not automatically equal to the vertical displacement due to slip at depth, it should represent a significant fraction of it (Stein et al., 1988; Hetzel et al., 2004). Therefore, for this qualitative study and first-order exercise, consideration of coseismic deformation alone is sufficient.

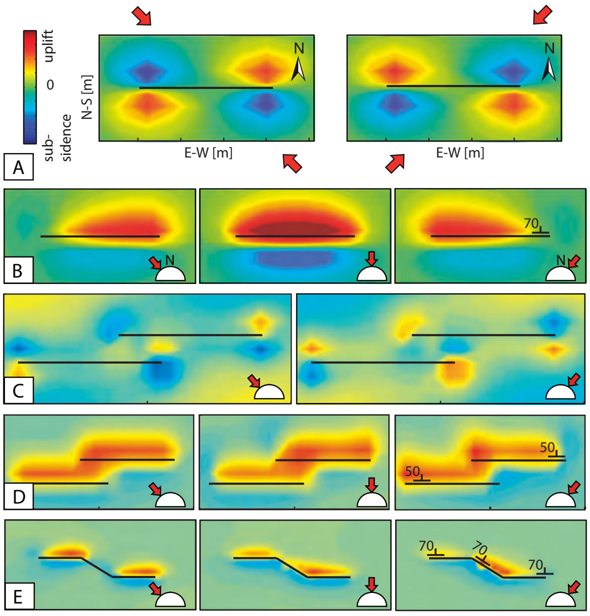

Figure 4.4: Map view of vertical displacement field of simplified fault arrays, calculated for a surficial horizontal observation plane. Red arrows indicate applied $S_{Hmax}$. In all panels left figure is subjected to NW-, right figure to NE-, and middle figure to N-directed compression with relative magnitudes of 1 for $S_{Hmax}$ and 0.2 for both $S_v$ and $S_{hmin}$, respectively. Positive displacement values (red) correspond to uplift, negative values (blue) are the result of subsidence. For non-vertical faults, orientation is marked by attitude symbols in the right figures.

### 4.3.2 Illustrations of fault (slip) interaction modeling

Below we illustrate the modeling effects on simplified fault models. We will use the terms uplift for positive and subsidence for negative vertical displacement in the modeled data. The model's initial simplicity enables the reader to better understand and build intuition about the parameters that control uplift patterns for different faults. Based on this understanding, the analysis will become more complex. This heuristic approach does not provide a definite answer, but rather identifies the effects of parameter changes.

Figures 4.4 A-E are in map view and show the vertical displacement field, calculated at a horizontal surface observation plane. The faults are loaded by a regional stress tensor where the maximum horizontal stress ($S_{Hmax}$, relative magnitude of 1) is compressional and either NW-, NE-, or N-directed. The vertical ($S_v$) and least horizontal ($S_{hmin}$) stresses are equal in relative magnitude (0.2), which is compatible with a transpressional environment. Additional scenarios, revealing the effects of changing differential stress and thus of settings that promote either strike-slip or thrust faulting, can be found in the data repository. Figure 4.4A represents a scenario with an E-W striking, vertical fault. The antisymmetric uplift pattern in response to oblique loading is controlled by the finite fault length. It is a strike-slip fault. However, the uplift pattern and the absolute values in different fault areas shift, if the fault is not vertical (Fig. 4.4B). In the case where the E-W striking fault dips 70° to the north, the fault acts as a ramp which promotes oblique thrusting. This different character is even more pronounced if the model contains more than one fault or segments with different geometry. Figure 4.4C shows two left-stepping, vertical fault segments. NW-oriented compression causes uplift in the overlap, whereas NE-oriented compression results in subsidence between the segments, such as pull-apart basins. As a result of the relatively large segment overlap with respect to separation, two centers of uplift or subsidence, respectively, are generated close to the end of the segments. This is in agreement with observations from geological structures in comparable natural settings (e.g., Deng et al., 1986). If the stepping fault segments are not vertical, the pattern of deformation is different and less sensitive to changes in the compression direction (Fig. 4.4D). Here, the left-stepping fault segments both dip 50° to the north. Despite the different direction of compression, equally distributed uplift along strike as result of predominant thrusting dominates in all three cases with slightly higher uplift associated with the northern fault. All three scenarios produce uplift in the segment overlap, whereby under NE-directed compression the total amount of uplift is less and a sharp gradient to subsidence is produced at the eastern end of the overlap. However, changes in differential stress can alter these expressions (StepOver.pdf, Data repository). Apparently, contractional step-overs of inclined faults (in this case left-stepping with NW- and N-compression) are less sensitive to changes in differential stress, despite the case where a "pure" strike-slip setting is imposed. The different parameters that promote thrusting (non-vertical geometry, contractional step-over, vertical stress close in amount to least horizontal stress) thus complement or amplify each other. Conversely, an extensional step-over (here left-stepping under NE-directed compression) in this transpressional environment is more sensitive to changes in the differential stress. The strike-slip component apparently emerges due to the balancing effects between the extensional step-over geometry and the thrust-promoting parameters (Fig. B.3, appendix B). Finally, figure 4.4E represents a double-bending fault, comprised of two 70° north-dipping segments, linked by a 70° northeast-dipping segment. The maximum uplift is located at the "inside corner". This geometry is most favorably oriented to accommodate N- or NE-directed compression, i.e. the resulting displacement is highest, while under NW-compression, there is only minor subsidence along the connecting fault (Fig. B.4, appendix B). In addition, the northward dip of the fault segments amplifies uplift in the northeastern corner, while the antisymmetric southeastern corner experiences (with a lower total amount) subsidence.

### 4.3.3 Processing of DEM data and data analysis

To compare the computed surface displacements with topography and areas of high rock-uplift rates, we have calculated topographic residuals and applied different correlation methods. The residual relief map was produced using SRTM data with a spatial resolution of 90 m, following the work flow of Hilley et al. (1997). Accordingly, the main drainage network is calculated and interpolated to a surface (lower envelope). From the inverted DEM a ridge network or upper envelope surface is constructed. Subsequently, the lower surface is subtracted from the upper envelope surface. In the eastern part of the study area, but inside the boundary of the fault interaction model, the 5671 m high Damavand volcano presents a non-tectonic topographic feature. Leaving this high peak in our calculations of the topographic residuals would cause an unrealistic distortion of the ridge envelope and residuals. However, the eastern branch of the seismically active Mosha-Fasham Fault is located south of this volcano. We therefore use this fault in the interaction model (e.g., Fig. 5C), but compare only the effects to the west of the volcano. Hence, all datasets were cut to the areal extent of the residual map (Fig. 5D). We compare different sets of raster arrays: DEM data (SRTM, 90 m spatial resolution), the topographic residual relief map ($\sim$ 500 m resolution), and finally, the vertical displacement fields computed from the fault interaction (2000 m resolution). Therefore, we have resampled all datasets to a common resolution of 1000 m and applied a low-pass filter via a 2D-moving average window of $8 \times 8$ pixels. For comparison, we normalized the rasters. Because the models not only show uplift, but also subsidence, and therefore negative values, we have introduced two cases for the normalization. The first case (Condition 1) considers both relative subsidence and uplift, i.e. prior to the normalization, we have subtracted the minimum value from all pixels. However, in the second case (Condition 2), we do not consider subsidence and only compare the uplift component. Thus, all negative values were set to zero prior to normalization. Finally, to compare the model results with the topographic metrics we have transposed the matrices into vectors, as the first value of the following row was added to the last value of the previous, respectively. Thus, we used bivariate analysis to understand the (pixel by pixel) relationship between the variables. This involves compiling bivariate scatter plots and calculating Pearson's linear product-moment correlation coefficient, which is sensitive to various disturbances in the bivariate data set (e.g., Trauth, 2007). A correlation coefficient of 1 represents a perfect linear correlation, i.e. an increase in modeled uplift with increasing topographic residuals, while a coefficient of 0 suggests no correlation. Pearson's correlation coefficient does not distinguish spatial coincidence, but rather describes the overall agreement between datasets. To reveal how models and topographic metrics are spatially correlated, we have calculated the difference between DEM and topographic residuals, as well as between the models and topographic residuals. These differences have been squared, so there is no discrimination between positive or negative differences, respectively.

### 4.3.4 Comparison of the modeled and real landscapes

Areas of presumably high rock-uplift rates were identified based on different premises. In tectonically active mountain ranges, about 80-90 % of relief is typically contained in the characteristics of fluvial bedrock channels (e.g., Whipple et al., 1999). High localized tectonic rock-uplift rates require that fluvial channels adjust. Whereas the biggest rivers might have the potential to erode efficiently and incise, the tributary channels and hillslopes are less efficient and are left behind. This consequently results in an increase in channel steepness and ridge crest to valley bottom relief (Figure 4.5A, (e.g., Whipple et al., 1999; Kirby et al., 2007)). Topographic residuals can help visualize such effects (e.g., Stearns, 1967; Bullard & Lettis, 1993; Bürgmann et al., 1994; Hilley et al., 1997; Hilley & Arrowsmith, 2000). Large differences between the upper and lower envelopes correspond to high topographic residuals, and presumably to areas of high uplift-rates (or base-level fall). Conversely, small differences with low topographic residuals correspond to areas where tributaries and hillslopes keep pace with the inferred lower tectonic forcing rates and/or are able to erode efficiently (Figure 4.5B) (e.g., Bürgmann et al., 1994; Hilley et al., 1997). The interplay between uplift and erosion is certainly influenced by differences in erodibility of the material (e.g., rock type variations in the range) which might account for considerable differences in relief and which would render this metric less reliable (e.g., Tucker & Slingerland, 1996; Whipple & Tucker, 1999; Whipple et al., 2000; Hilley et al., 2004). Our study is based on the assumption of spatially uniform resistance of rock to erosion, but this issue is addressed further in the discussion. Qualitative comparison between the residual map and the vertical displacement field derived from the fault interaction model (FIMoz) should be appropriate to highlight areas which undergo high fault-related rock-uplift under present-day boundary conditions, thus corresponding to the associated "simple landscape" (compare Table 4.1). The same information might also be expected from the DEM itself, if the mountain building process is the result of one sustained kinematic regime and a maintained direction of $S_{Hmax}$. In contrast, the DEM is the topographic result of previous and present-day faulting, isostasy, and erosion, and so might be more appropriate for comparison with fault interaction models which are derived from stress states assumed to represent previous conditions. High elevation areas in the DEM which do not correspond to high topographic residuals are more likely to represent inherited topography. Likewise, DEM areas of relatively low elevation might correspond to previously subsiding areas, which now might be filled with sediment. Thus, the DEM potentially constitutes elements of the composite landscape, and therefore will also be used for comparison with the model results. Inherited topography might not necessarily correspond to high topographic residuals. Under certain circumstances, however, rapid response of the drainage network to rock-uplift changes might result in the formation of permanent hanging valleys (e.g., Crosby et al., 2007), which thus preserves inherited topography together with locally high topographic residuals. To account for the differing degree of agreement between the datasets in the individual scenarios (Table 4.1), we have used several methods for comparison.

## 4.4 Results

### 4.4.1 Present-day boundary conditions

Figure 4.5C shows the vertical displacement of the model, driven by a regional stress tensor calculated from the GPS-derived strain rate and direction (Masson et al., 2007)(Equations B.1-B.4, appendix B). This displacement is compared with the topographic residuals (Fig. 4.5D, right). Assuming that the shortening direction corresponds to the direction of maximum horizontal compression, this model represents the recent boundary conditions and

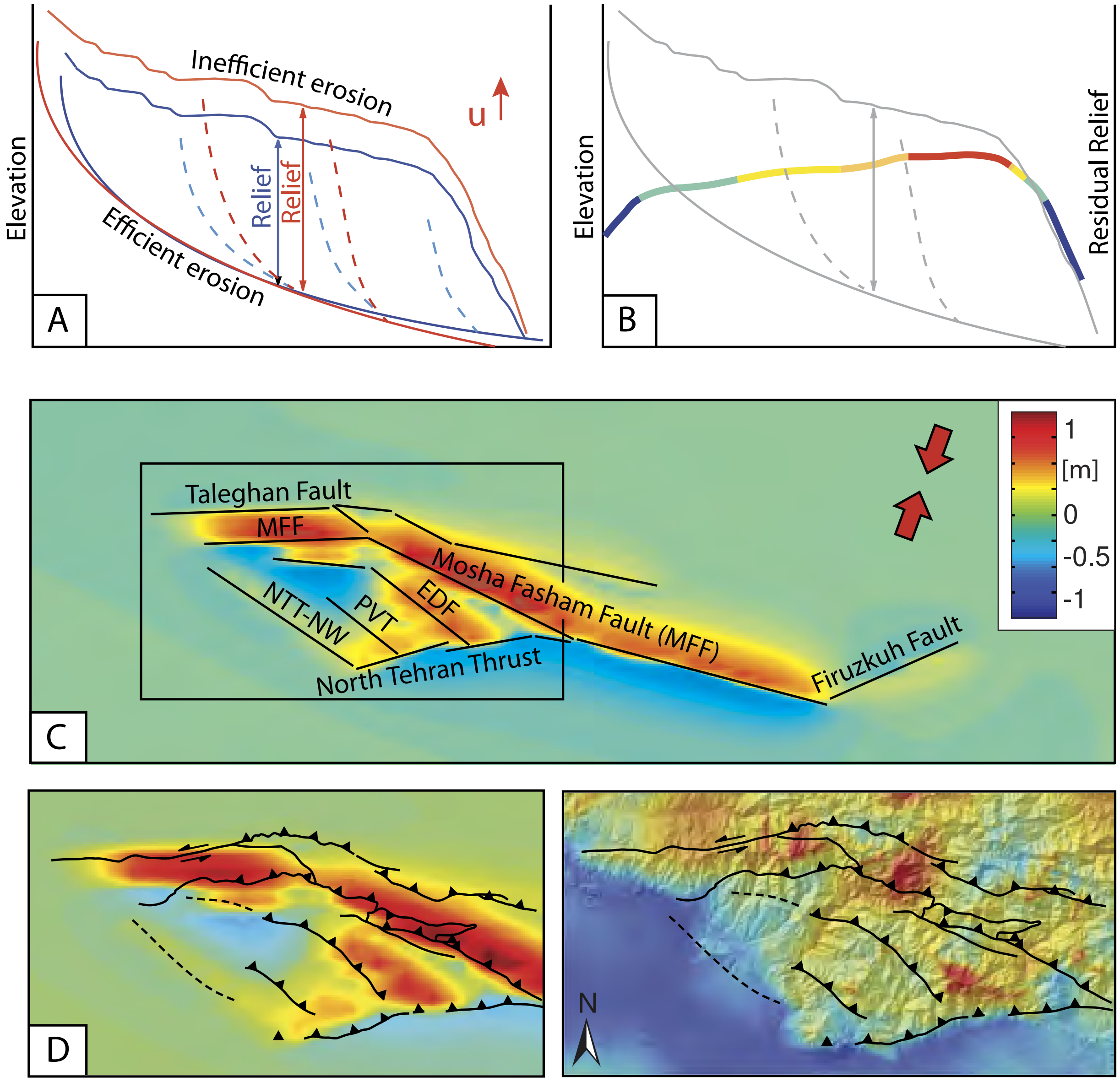

Figure 4.5: Criteria and metrics to compare modeled and real landscape. (A) Relief information in bedrock channels relative to adjacent ridgelines (modified after Whipple et al. (1999)); blue: initial situation, red: after rock-uplift. The large trunk channels might be efficient enough to erode and downcut, while response of tributary channels and slopes lag behind. The main channels steepen, redistributing and increasing relief. (B) 2D-version of topographic residuals after induced rock-uplift (color as in D, with red for high and blue for small residuals, respectively). High topographic residuals occur where difference between rock uplift and efficient erosion is largest. (C) Map view of simplified fault array for which interaction was calculated, using regional stress orientation calculated from strain after Masson et al. (2007). Colors as in Figure 4.4. Abbreviations of fault names are: PVT, Purkan-Vardij-Thrust; EDF, Emamzadeh Davud Fault; NTT-NW, North Tehran Thrust-NW prolongation; note en echelon array of the NTT fault (for fault geometry data see Fig. B.1, appendix B). Interaction was calculated using all displayed faults, but comparison is limited to the area inside black frame. (D) Comparison of modeled data (left, same as C) and topographic residuals of central Alborz mountains (right, stretched by standard deviation), superposed on SRTM-based hillshade. This model corresponds to the recent boundary conditions (i.e., N20E-oriented compression) and highlights areas of probable active rock uplift. Visual inspection reveals considerable agreement between both data sets.

**(A) Expectations for correlation (simple landscape)**

| **Model** | **Topographic residuals** | **DEM** |
|---|---|---|
| Subsidence | high residuals | low elevation |
| No offset | low residuals | low elevation |
| Uplift | high residuals | high elevation |

**(B) Expectations for correlation (inherited topography)**

| **Model** | **Topographic residuals** | **DEM** |
|---|---|---|
| Subsidence (inherited) | low residuals | low elevation |
| No offset (inherited) | low residuals | low elevation |
| Uplift (inherited) | low residuals | high elevation |

**(C) Normalization using Condition 1**

| **Model** | **Topographic residuals** | **DEM** |
|---|---|---|
| Subsidence | low residuals | low elevation |
| No offset | moderate residuals | moderate elevation |
| Uplift | high residuals | high elevation |

**(D) Normalization using Condition 2**

| **Model** | **Topographic residuals** | **DEM** |
|---|---|---|
| Subsidence | lowest residuals | lowest elevation |
| No offset | lowest residuals | lowest elevation |
| small Uplift | low residuals | low elevation |
| moderate Uplift | moderate residuals | moderate elevation |
| high Uplift | high residuals | high elevation |

Table 4.1: Table showing parameters used to compare modeled and real data. (A) Active subsidence (local base level fall) and uplift are supposed to show high topographic residuals, but low and high elevations in the DEM, respectively. In contrast, inherited topography (B) would show high residuals only in the case of low transience, if permanent hanging valleys would have been produced. Otherwise, inherited topography may correspond to low residuals, but again low and high elevations in the DEM, respectively. (C) Using Condition 1 subsidence would be compared with low residuals and low elevation. Good correlation of these parameters would thus highlight inherited subsidence. Otherwise, bad correlation shows that subsidence cannot be compared sufficiently. Good correlation between uplift and the topographic parameters, however, would rather depict present-day conditions. (D) Using Condition 2, the subsidence signal is suppressed in favor of uplift which is more differentiated, but also highlighting the present-day conditions. Thus, inherited uplift is best reflected by differences between topographic residuals and high elevations in the DEM.

therefore should highlight areas of active rock uplift and high topographic residuals. There is considerable agreement between the main structures of both data sets. This is especially true between the MFF and Taleghan fault (the Taleghan range; for locations see Fig. 4.6) and between the NTT and EDF (Mount Touchal). However, the maximum residual relief is located immediately east of the outside corner of the MFF left bend, and accordingly the inside corner of the Taleghan Fault left bend (Mount Bajdan, Fig. 4.6). This area has no obvious equivalent of high uplift in the model. Instead, fault-related uplift there is distributed along the entire central MFF segment.

### 4.4.2 Changing boundary conditions

Adopting the results of a fault-kinematic study which showed that the central Alborz mountains experienced a change in the direction of maximum horizontal compression from a previous NW to a neotectonic NNE direction (Landgraf et al., 2009), we have modeled the uplift pattern for $S_{Hmax}$-directions from W to E. For NW-direction of $S_{Hmax}$, we have used a simplified fault array without the frontal ramps of the duplex. The results are shown in Fig. 4.6 with increments of 20° (results at 5° increments are given in Fig. B.5 and B.6, appendix B). In the upper panel, the normalized DEM and topographic residual map are shown in the same color scheme.

All areas of high topographic residuals can be modeled using the implemented fault array under different directions of $S_{Hmax}$. The Taleghan range will always exhibit uplift, except for dominantly east-west compression. This is because the western Taleghan and Mosha-Fasham faults are favorably oriented to accommodate NW- to NE-directed compression (Fig. 4.6A-F). Furthermore, the opposing dip of the subvertical faults support an effective uplift of the range. Along the NTT, however, NW-directed compression favors uplift along the western segment (Fig. 4.6A-D), which is less steep than the central and eastern segments (60° vs. 75°). Uplift along the central segment starts to become more prominent after rotating the direction of $S_{Hmax}$ to N and NNE and incorporating the EDF as a frontal ramp (Fig. 4.6 D and E). In this case, Mount Touchal is located in the acute "inside corner" between these faults, which supports uplift (compare Fig. 4.4D). In contrast, the slight right bend of the MFF as another inside corner, but with an obtuse angle, experiences more distributed uplift. The NTT-PVT, and NTT-NTT/NW corners, however, are less effective at generating uplift. This may result from the shallow dip (between 20° and 35°) of the NW-striking ramps (see Fig. B.1, appendix B). The required range of orientations of compression to cause uplift of Mount Touchal is rather narrow. Subjected to N40E-directed compression, the summit still experiences uplift, but the maximum has shifted towards NW. Maximum uplift at Mount Bajdan is accomplished at N50E-directed compression (see Fig. B.2, appendix B), but uplift will be more localized there if the $S_{Hmax}$-direction becomes more oblique (Fig. 4.6F-G and Fig. B.5 and B.6, appendix B).

The spatially most extensive uplift is generated under N- to NE-directed compression (Fig. 4.6D-F). The highest mean displacement is achieved at a $S_{Hmax}$-direction of N25E, whereas the maximum local uplift occurs at N50E-directed compression and corresponds to the location of Mount Bajdan (Fig. B.2, appendix B).

The fault model configurations also cause certain areas to subside. However, besides the plains and drainage channels, there are no associated basins in the DEM, but locally extensive Pliocene to Quaternary deposits exist, which might have filled accommodation space (Fig. 4.2A). NW-compression leads to subsidence SW of the Taleghan range and to a lesser degree in the footwall of the central MFF segment. Incorporation of the frontal ramps under N- to NE-directed compression subsequently results in uplift in the MFF central footwall, in combination with a narrow piggyback basin. In addition, significant subsidence takes place south of the Taleghan range, slightly west of the center of the model. This corresponds to areas of relatively subdued topography in the DEM and high topographic residuals.

### 4.4.3 Correlation between model and topographic metrics

We have calculated the squared spatial difference between DEM and topographic residuals, as well as between the models and topographic residuals (Fig. 4.6, right column). Red areas correspond to accordance between the data. DEM and topographic residuals differ most in the NE where the DEM has its highest elevation, but the corresponding relief is small. This area could possibly reflect inherited topography, but does not show significant uplift in the models. Areas which repeatedly vary between the residuals and all models are the outermost NE sector (outside of the fault array) and the area north of the Taleghan fault (edge effect).

We find considerable spatial coincidence in the model with a N300E compression direction (Fig. 4.6A). The areas of modeled uplift correlate with high residual relief, and subsiding areas correlate well with low residuals. This is also evident in Fig. 4.7, where the data are less scattered than in other scenarios. However, this model is spatially inconsistent with high residual relief at Mount Bajdan and at the western segment of the NTT. Further NW- to NE-compression progressively accentuates central subsidence between the western MFF, the evolving NTT-NW prolongation, and the EDF. This effect is also expressed by a kink in the correlation plots (Fig. 4.7). For "Condition 1"-models, which contain subsidence information, pixels with normalized vertical displacement below a value of approximately 0.4 do not correlate, whereas uplifted areas (values greater than 0.4) correlate well without pronounced scatter. However, in "Condition 2"-models (ignoring subsidence), the same kink is only suppressed to lower displacement values of about 0.2, suggesting that even areas of minor uplift do not correlate (see Fig. B.7 and B.8, appendix B). Comparing these observations with Table 4.1 (Panels C and D), we find that scenarios modeled under N300E to N20E-directed compression might reflect inherited subsidence.

The highest correlation coefficient between models and residuals is achieved with a $S_{Hmax}$

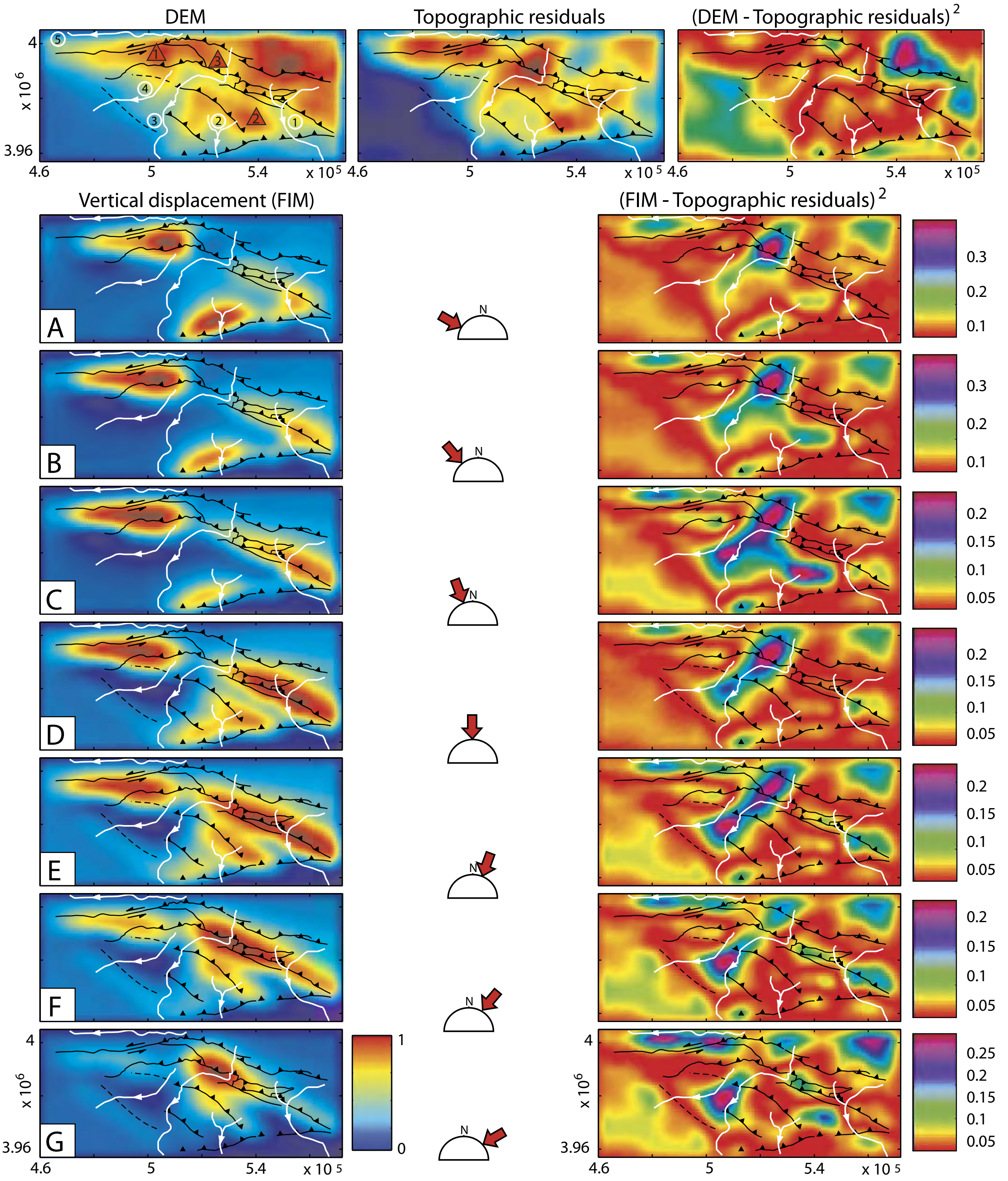

Figure 4.6: Filtered and normalized data sets and their differences; upper panel, normalized DEM (left), topographic residuals (middle), and squared differences between DEM and topographic residuals (right). Normalized DEM compares to a real range of topography between 1333m and 4123m, topographic residuals range from 0 to 1554 m. Red triangles on DEM correspond to presumable high-uplift rate areas, which are (1) Taleghan range, (2) Mount Touchal, and (3) Mount Bajdan (after Moinabadi & Yassaghi (2007)), respectively; circled numbers correspond to rivers (1) Jajrud, (2) Kan, (3) Karaj, (4) Kordanrud, and (5) Taleghanrud. X- and Y-scale are in meters, corresponding to UTM, Zone 39N. Panels A-G show normalized vertical displacement fields (left column) for different compression directions with varying azimuthal steps of 20°, calculated using Condition1 (Color schemes with red showing uplift and blue showing subsidence) and their squared differences from topographic residuals (right column) to visualize spatial variability. Middle column illustrates orientation of maximum horizontal compression. Note simplified fault array for NW compression models (A-C), based on the assumption that frontal ramps of the transpressional duplex have evolved subsequent to a stress-field reorganization. Main rivers (white) and faults (black) are superposed for illustration.

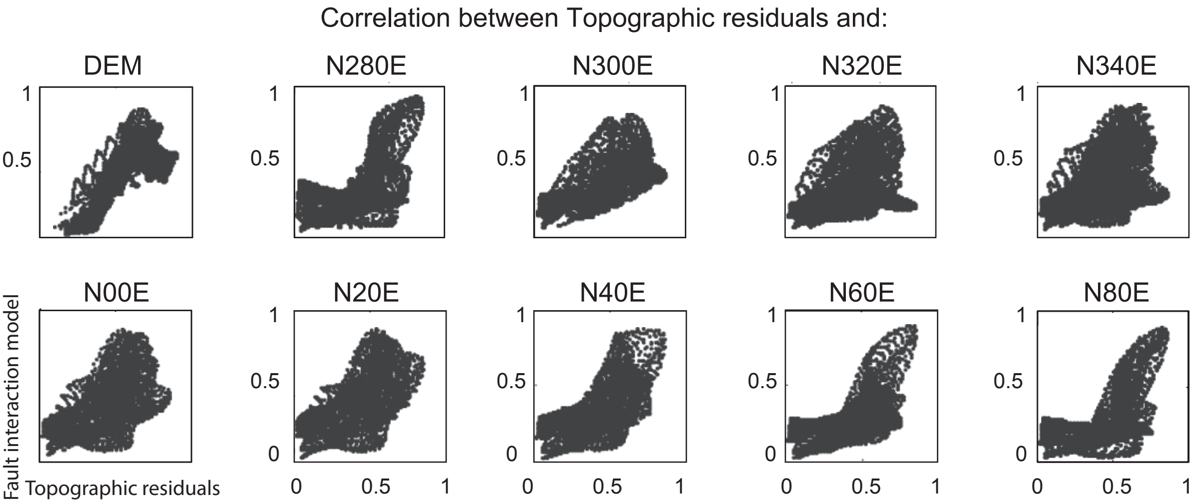

Figure 4.7: Correlation between topographic residuals (x-axis) and fault interaction models (y-axis), normalized respectively. Azimuth of compression direction is shown on top of figures, respectively. Fault interaction models were normalized using "Condition 1". Each data point comprises one compared pixel. In general, majority of data pixels correlates, i.e. pixels with high topographic residuals match with pixels of high modeled uplift. Kink in models with oblique compression direction indicate that pixels with low values (subsidence) do not correlate well with areas of low topographic residuals. In contrast, uplifted model areas correlate well with high topographic residuals and scatter less. Upper left graph shows correlation between topographic residuals and real data (DEM).

direction oriented between N15E and N45E (Fig. 4.8). Interestingly, DEM and residuals generally agree (i.e. show the same trend) for "Condition 1", except for compression at N40E and increasing obliquity. These datasets do not agree in the uplift of Mount Bajdan (Fig. 4.6, upper right). The DEM correlates better with N- to NNE-loaded models. There is less agreement between DEM and residuals in "Condition 2" models, which only compare the uplifted areas. Here, topographic residuals always correlate better than the DEM, but the correlation is more variable between the different scenarios, depicting even better the highest correlation of NNE- to NE-directed compression scenarios.

## 4.5 Landscape evolution in the South-central Alborz Mountains

### 4.5.1 High topographic residuals - all about high rock-uplift rate?

The interplay between uplift and erosion is influenced by differences in erodibility of the material, particularly rock type variations in the range, which might account for considerable differences in relief and that are unrelated to tectonism. The residual relief map exhibits two distinct sites and one elongated zone of high residuals (Fig. 4.5 and 4.6, upper panel, triangles 1 to 3). The Taleghan range (triangle 1) is associated with outcrops of Precam-

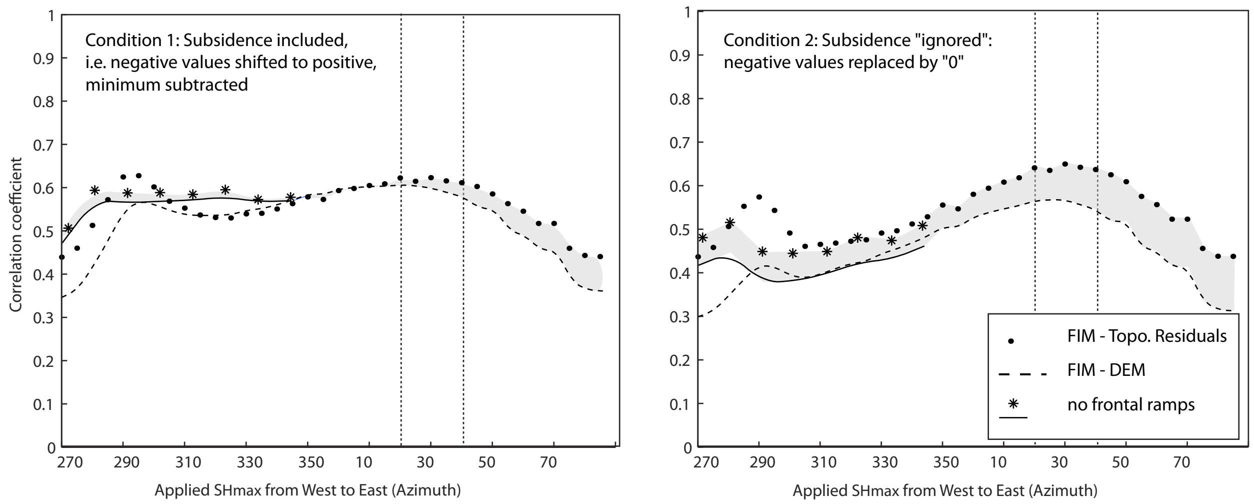

Figure 4.8: Pixel-wise derived Pearson's linear correlation coefficient between topographic metrics and vertical displacement field of fault interaction models for "Condition 1" (left) and "Condition 2" (right). Dots denote correlation coefficient between topographic residuals and models, while dashed line shows coefficients between DEM and models, respectively. We assume that the transpressional duplex evolved under present-day conditions, while a previous fault configuration under NW-compression probably lacked NW-striking frontal ramps. Thus, additional models were calculated without a NW continuation of the NTT, the PVT, and EDF and used for the correlations (stars and solid line). Vertical lines depict best correlations between models and topographic metrics. Shading indicates differences in correlation between topographic residuals and models and DEM and models, respectively.

brian to Paleozoic units (compare Fig. 4.2A). These rock types include mainly dolomite, sandstone, quartzite, and limestone which are more resistant to erosion and weathering in this environment than the Mesozoic limestone and shales or the Eocene volcanoclastic assemblage. On the other hand, the appearance of the older units at surface indicates that a substantial amount of rock-uplift and exhumation has already occurred. This was probably accommodated by slip along the subvertical, converging E-W striking faults, which are expected to accommodate strain and repeated fault reactivation under NW- to NE compression (Fig. 4.6A-E). Uplift of the Taleghan range is amplified by a basement-cored hanging wall anticline in the eastern part of the MFF western segment and towards SW progressively younger break back thrust sheets in the western part (Yassaghi & Madanipour, 2008). These observations underscore the importance of the western MFF as a long-lived fault with a high total displacement and protracted deformation history.

The second high-relief area (Mount Touchal, triangle 2 in Fig. 4.6, upper panel) is located at the inside corner of the NTT and EDF, in Eocene volcanoclastic units. Although the rock type variability in this about 7 km thick succession (Amini & Emami, 1993) is generally high, the spatial differences in erodibility are not significant at the km-scale used for the morphometry (Landgraf et al., 2009). For example, between the NW-prolongation of the NTT and the EDF (compare Fig. 4.2), a succession of three different shale members, repeatedly alternating with tuffs, tuffaceous siltstones, limestones, and sandstones, is exposed without exhibiting any significant difference in residual relief. Mount Touchal itself is in a synclinal position, but in the immediate inside corner between NTT and EDF, the oldest and deepest section of the Eocene sequence is exposed, likewise indicating substantial rock-uplift and exhumation. Comparing Fig. 4.6D-E and Fig. 4.4E, it is obvious that this fault configuration in an inside-corner position promotes such uplift. However, only N- to NNE-compression directions, compatible with the direction of present-day motion of Iranian crust relative to Eurasia, produce such a pronounced uplift. Furthermore, the effects of the NTT segmentation are more pronounced under NNE-directed shortening, which might have enabled the Kan river to cut through the range (Fig. 4.6D and E, river 2).

The third high-relief area (Mount Bajdan, triangle 3 in Fig. 4.6, upper panel) broadly coincides with the area characterized by the belt of Paleozoic to Precambrian units, exposed between the Taleghan and Mosha-Fasham faults. Locally, however, the area coincides with NE-trending syn- and anticlines in Mesozoic to Eocene units (cf. Fig. 4.2). These units are probably less resistant to erosion than the Paleozoic rocks, suggesting that tectonic uplift may be the reason for these high topographic residuals. In addition, fast uplift of Mount Bajdan might explain the bending of the Karaj river (Fig. 4.6, river 3) at exactly this location, while the river is otherwise antecedent and flows straight through the other frontal ramps. Guest et al. (2006b) showed that the duplex region was already tectonically active before 7 Ma (Fig. 4.9A). The youngest age in their thermochronology coincides with Mount Bajdan which might be another indicator for high rock-uplift rates there. However, to cause uplift in this part of the fault array, the orientation of the maximum horizontal compression direction should be highly oblique with respect to the range (at least N40E, compare Fig. 4.6G and Fig. B.5 and B.6, appendix B).

### 4.5.2 3-D displacement in the duplex array

To further test other deformation scenarios and their consistency with respect to the overall fault motion, we have calculated the horizontal displacement field for the cases of NNE- and NE-compression (Fig. 4.9 A and B). Combined with the vertical displacement, we can compare the relative motion with the observed sense of motion along the main faults. Model A, which is loaded with NE-compression, reveals the largest horizontal displacement with predominant sinistral strike-slip motion along the eastern MFF and western Taleghan fault. To a certain degree this is in agreement with the results of geomorphic, paleoseismologic (Allen et al., 2003; Ritz et al., 2006a), and microseismicity (Ashtari et al., 2005) studies. However, the model shows that the hanging wall of the eastern MFF segment also experiences uplift, which is incompatible with the present-day transtension (Ritz et al., 2006a). The western and central (NW-striking) MFF segments reveal minor left-oblique motion, consistent with fault-kinematic data (Guest et al., 2006a; Landgraf et al., 2009). However, Moinabadi & Yassaghi (2007) documented primarily dip-slip motion for the MFF in the Mount Bajdan area.

Motion along the NTT does not show significant horizontal and only limited vertical motion in model A. In model B, which is loaded by NNE-directed compression, uplift along the NTT is amplified. In this case, the central NTT and MFF segments experience some degree of dextrally oblique motion which is incompatible with observed neotectonic left-lateral motion. Interestingly, we have measured dextral-oblique fault-kinematic indicators along the central MFF segment and along the NTT (Landgraf et al., 2009). However, rather than being related to a local geometric phenomenon, these observations probably represent previous conditions of NW-compression along this fault. This interpretation is supported by rare cross-cutting relationships of young sinistral-oblique kinematic indicators overprinted on dextral-oblique fault striations (e.g., Landgraf et al., 2009) and regional-scale observations of previous dextral motion in the Alborz mountains (e.g., Axen et al., 2001; Zanchi et al., 2006; Yassaghi & Madanipour, 2008).

Thus, assuming that the combination of horizontal and vertical displacements is comparable to fault-kinematic indicators measured along the fault zones, model A is more consistent with the present-day conditions than model B. Comparing the loading conditions for this model with regional GPS-derived velocities, this scenario would account for the NW-motion of the South Caspian basin relative to stable Eurasia and Central Iran and result in range-wide left-lateral shearing in the Alborz mountains (Vernant et al., 2004b). If, however, the separate models together reflect slip partitioning of the present-day plate motion, the appropriate scenario should be a combination of both models. To simulate this scenario (model C), we forced left-lateral slip onto the eastern MFF segment in addition to the regional NNE-compression, which loads the entire fault array (Fig. 4.9 C). Similar to model B, this scenario allows uplift at Mount Touchal and the Taleghan range, whereas along the central MFF segment the maximum is slightly shifted towards Mount Bajdan in the NW. In model C, the central MFF segment experiences left-oblique thrusting, with a higher dip-slip ratio in the western part. Both, the western MFF and TF show left-lateral motion, but at the MFF dip-slip faulting is superposed. The NTT would undergo primarily dip-slip motion, but the relative horizontal vectors in the foot- and hanging walls, respectively, suggest a left-lateral component. In this case, the amount of vertical motion on the NTT is lower than that on the central MFF segment. However, using regional stress, calculated from strain after Masson et al. (2007) (with magnitudes for 1000 yrs of tectonic loading), approximately 6 m of additional left-lateral slip at the eastern MFF segment is needed to invert the horizontal displacement at the central segment from right- to left-oblique motion. This amount of slip is about three times larger than the observed Pleistocene slip rate of approximately 2 mm/a for the eastern MFF or the assumed coseismic average displacement of 1.20 m (M7.1) with an associated mean maximum recurrence interval of 620 years (Ritz et al., 2003, 2006a). However, the strain rates, calculated from GPS (Masson et al., 2007) only account for the horizontal components. If converting to stress, the vertical stress will become $\sigma 3$ and promote thrusting, a condition which might not reflect the actual three-dimensional stress field of the region.

## 4.6 Implications for the tectonic evolution of the Alborz range

The existence of distinct zones of high rock-uplift rates which require different maximum horizontal compression directions is characteristic of a composite landscape with a complex tectonic history. The location of uplift is directly related to the geometry of the fault array in each stress regime. The Taleghan range shows equally high modeled uplift in a wide range of $S_{Hmax}$-directions. Otherwise, conformity between topography, residual relief, and modeled rock uplift is high within a narrow ratio of compression orientations with respect to the chosen fault array. The highest coefficient of correlation between model and topographic metrics is achieved with a compression direction oriented between N15E and N55E (Fig. 4.8). Within this range of compressional stress orientations, the distribution of topography is still composite after our definition, i.e. other areas are uplifted during NNE- than NE-directed compression. Therefore, on a small spatial scale (i.e. the transpressional duplex array), and intermediate temporal scale (the duration of at least several earthquake cycles) our study suggests that the local stress field might be inhomogeneous and the growth of fault-related topography in the central Alborz mountains is partitioned. The transpressional duplex is shortened in a NNE-direction, while the MFF is able to maintain a predominant left-lateral motion. This has further implications for the tectonic characteristics of this area. How can such focused strike-slip motion be explained along the designated faults in an overall compressive setting? Common explanations for such a case include low-friction strike-slip faults, upper crustal response to oblique slip on deep-seated faults or shear zones, or upward propagation of oblique shear from depth (e.g., King et al., 2005). The MFF is a compressionally reactivated normal fault involving basement rocks (Zanchi et al., 2006; Yassaghi & Madanipour, 2008; Landgraf et al., 2009). Therefore, the steep geometry of this inherited fault might be prone to accommodate lateral shearing. Despite the general structure of the Alborz mountains as a doubly verging orogen, which may be comparable to a large-scale positive flower structure (e.g., Allen et al., 2003), there is no single through-going or central strike-slip fault. Hollingsworth et al. (2008) suggested that the extrusion of the South Caspian block, which began about 10 m.y. ago in the the Kopeh Dagh, is accommodated by the Sharud fault system in the eastern Alborz. According to Nowroozi (1976, 1979) the Sharud fault system includes a branch north of Tehran, probably corresponding to the MFF. This underscores the significance of the MFF as a major fault, accommodating westward extrusion.

In addition, coeval shortening and lateral shearing in the Alborz mountains might also suggest that the magnitudes of the vertical and least horizontal stresses are nearly similar

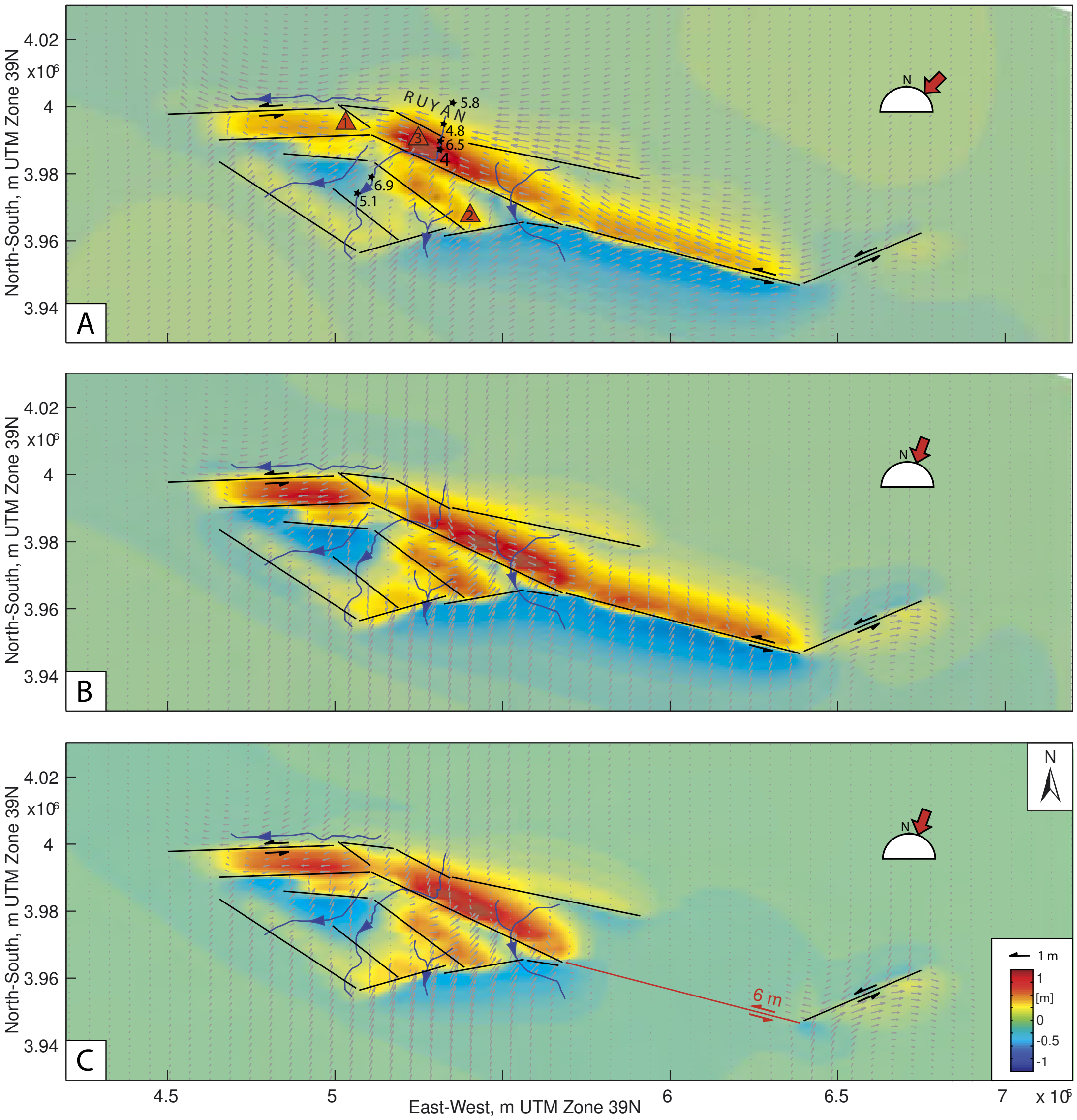

Figure 4.9: Figure showing the XY-displacement field (gray arrows) overlain on vertical displacement calculated for a surficial horizontal observation plane. To compare it with fault kinematic indicators, both displacement fields must be combined. Overlain are the common faults, summits, and rivers (compare Fig. 4.6). (A) Scenario with N45E-oriented regional compression. Highest uplift occurs at Mount Bajdan. Stars along the Karaj river mark apatite U-Th/He data from Guest et al. (2006b) in Ma. Errors are stated to be ±0.5 Ma, respectively. Note the youngest age of 4 Ma, spatially coincident with the location of Mount Bajdan. (B) Scenario with N20E-oriented regional compression. Here, the oblique orientation of the central MFF segment relative to the largest horizontal compression direction would cause dextral-oblique motion along this part of the fault. Even the central NTT segment would experience some degree of dextral oblique motion. (C) Scenario with N20E-oriented regional compression using the stress magnitudes from strain after Masson et al. (2007) after 1000 years of tectonic loading and 6 m left-lateral slip on the eastern MFF segment. In this scenario, we load the model with a regional stress field, comparable to plate motion, but in addition force the eastern MFF segment to slip with left-lateral motion. The resultant displacement field shows how topography of the central MFF hanging wall will be slightly advected towards west, while the horizontal motion is in agreement with fault kinematic data, i.e., left-oblique motion.

and perturbations are likely. Locally, topographic loading and unloading might thus alter the tectonic stress field, causing migration of deformation to other faults (e.g., Hilley et al., 2005) or a switch between a thrusting and a strike-slip regime (e.g., Cowgill et al., 2004). The latter scenario was described from the Akato Tagh bend along the Altyn Tagh fault (Cowgill et al., 2004). There, the highest topography occurred at two nodes in the inside corners of a restraining bend and thus apparently led to a conversion of thrust- to strike-slip dominated deformation. In our study area, Mt. Damavand volcano might be responsible for exerting significant vertical loading stress in the hanging wall of the eastern MFF segment (Fig. 4.2), and therefore promote conditions conducive to strike-slip faulting. A simple calculation of the loading-induced normal and shear stresses in the adjacent volume (Fig. B.10, appendix B) shows that Mt. Damavand comprises a significant additional load. About one third of the vertical stress (20 MPa) is still available at 10 km depth (approx. locking depth of the underlying fault), which is about an order of magnitude less than the assumed prevailing lithostatic stress of about 250 MPa at this depth. However, the additional amount of differential stress ($\sigma_1 - \sigma_3$) that is caused by the volcano, which may ultimately control slip behavior of the adjacent faults, reaches its maximum (about 12 MPa) at about 2 km depth. At 10 km depth about 5MPa additional differential stress is still available (Fig. B.10, appendix B). Hampel et al. (2009) showed for Scandinavia and the Basin and Range Province that loading and reloading resulting from glacial and pluvial cycles, respectively, can have a significant impact on the slip rates of the incorporated faults. According to the calculations of these authors the magnitudes of differential stress that can alter the fault slip behavior is approximately 5-10 MPa (at 2 km depth), thus similar or less than the Damavand effect.

Previous NW-directed compression also incorporated the MFF within a dextral transpressional system with an en échelon array of syn- and anticlines, which are cut by the fault and which caused additional vertical loading stresses in the foot- and hanging walls. In addition, in the southern Alborz mountains the propagation of deformation into the foreland began at about 9 Ma (Ballato et al., 2008). However, several studies have shown that the change to left transpression in the Alborz might have occurred already as early as 10 Ma ago (e.g., Hollingsworth et al., 2008; Ballato et al., 2010a), while an additional switch to left transtension in this internal domain is of Pleistocene age (Ritz et al., 2006a). Topographic loading and an increase in the gravitational potential in the hanging wall of the NTT, however, may rather cause faulting to migrate into the foreland, evidenced by folding and faulting observed in Quaternary alluvium (e.g., Abbassi & Farbod, 2009). Whether these effects are sufficiently strong to alter the stress regime remains unclear, but these considerations highlight the need for an improved model with the possibility to include topographic loading.

## 4.7 Composite landscapes - implications and perspectives

The goal of this study is to differentiate composite and simple landscapes, i.e. to separate landscape elements that are inherited from previous tectonic boundary conditions from those developed in the current stress and deformation regime. Changing plate configurations and interaction can cause regional changes in stress magnitudes and principle stress directions. From various regions in the world and different tectonic settings it is known that the evolution of orogens or rifts can be accompanied by rotation of the principle stresses and that inherited fault arrays related to a tensional stress field can be inverted and uplifted, even over geologically short periods of time (e.g., Golombek et al., 1983; Strecker et al., 1990; Bosworth & Strecker, 1997; Strecker & Marrett, 1999; Schumacher, 2002; Cortez et al., 2005; Mora et al., 2006). Preexisting, inherited faults may thus influence later reactivation and the loci of deformation and uplift (e.g., Schumacher, 2002; Hilley et al., 2005; Mora et al., 2006). Our study shows that arrays of linked faults or faults with pronounced bends or step-overs have distinct offset patterns and are particularly sensitive to detection of changes in the regional tectonic stress field. However, not all structures in fault arrays are useful to provide information of such changes. In the Alborz mountains, we found that non-vertical E-W faults are less sensitive to changing boundary conditions. They are in a “tectonic steady state”, favorably oriented to accommodate the entire range of NW- to NE-directed compression, without significant changes in resulting uplift pattern. Good indicators of composite topography, however, are array “inside corners” in the hanging wall. These correspond to junction or intersection areas of fault arrays, whose bisecting line is approximately aligned with the $S_{Hmax}$-direction.

The approach of fault interaction modeling to understand composite landscapes can be effectively extended to various tectonic settings and problems. Rift settings for instance might be applicable to compare modeled subsidence with real basin fill which helps differentiate “negative composite topography”. Schumacher (2002) compared isopach maps of different temporal intervals with in-situ measurements of inherited faults in the Upper Rhinegraben, to show how rotations in the $S_{Hmax}$-direction shifted depositional centers and how the inherited faults have influenced the rift evolution.

Reactivation of inherited structures under changing boundary conditions can have important impacts on landscape response. In the northwestern Argentine Andes, for instance, Strecker & Marrett (1999) performed a fault-kinematic study and showed that transfer faults between thrusts, which originally constituted local subdued topography, guided the course of antecedent rivers. After a regional rotation of the shortening direction (Marrett et al., 1994), however, such transfer areas experienced uplift, and maintenance of the river gradient required progressively deeper incision, resulting in precipitous local topographic relief, often associated with lateral erosion and pronounced repeated landslide activity.

These observations also lead to another important consideration that has to be taken into account, which involves landscape response time. Our approach assumes that despite changed boundary conditions and possible long sustenance of the new regime there is still a previous landscape signal left in the topography. How long do we expect the inherited topography to maintain its original characteristics? The above mentioned examples showed changes in the stress state and associated kinematic regime that occurred on the order of millions to hundreds of thousands of years (e.g., Strecker et al., 1990; Bosworth & Strecker, 1997; Schumacher, 2002). For the Alborz mountains, the change from dextral to sinistral transpression had most likely occurred by 9 Ma, while NNE- and NE-directed compression are compatible with present-day conditions. On the other hand, Ellis et al. (1999) showed that landscape response times (time to reach equilibrium between lithospheric deformation and erosional processes) in semi-arid normal faulting environments are on the order of several $10^5$ to 1 million years. Consequently, after $10^6$ years little may be left in the landscape that tells about prior conditions. However, in their experiments, the initial conditions did not vary. Hence, it would be interesting to see if response times would be significantly longer after boundary conditions have changed. Occurrences of relict landscapes or fluvial hanging valleys in different regions of the world argue for transient landscape signals that can be visible even after millions of years, seemingly decoupled from equilibrated younger regions (e.g., Clark et al., 2005, 2006; Crosby et al., 2007). Thus, in attempts to model the interplay between lithospheric deformation and superposed surface processes considering composite landscapes is an important issue for future studies.

## 4.8 Conclusions

Our numerical fault interaction modeling has shown that it is possible to unravel the composite landscape of the south-central Alborz mountains to a certain degree. Generally, the modeling revealed that “inside corners” between faults or segments are particularly indicative of specific boundary conditions. If erodibility is regionally equal, topographic residual maps can be used to compare modeled uplift with presumably high rock-uplift rate areas. High positive correlation between these areas reflect the actively deforming (simple) landscape elements. High modeled uplift which has no equivalent in the residual map might correspond to inherited topography, especially, if these regions show high elevations in the DEM.

In the Alborz mountains, distinct zones of inferred high uplift rate are associated with slip along interacting faults in the duplex array but require different compression directions. The faults bounding the Taleghan range, an area of high elevation and high uplift rate, are favorably oriented to undergo reactivation under NW- to NE-directed compression. This area therefore is limited as a landscape indicator for ongoing tectonism or for differentiating between simple and composite topography. Two other areas, although generated by the same fault configuration, require slightly different $S_{Hmax}$-directions to evolve. We interpret those areas as the result of slip partitioning. The MFF as a long-lived, steep fault is able to maintain predominant left-lateral motion which is significant in transferring extrusion-related motion of the South Caspian block to the west, while in general, the range (at the dimension of the fault array) is shortened in a NNE-direction.

Fault interaction modeling to understand composite landscapes can be effectively extended to various tectonic settings and problems. How far beyond the present-day such composite landscapes might persist will to a large extent depend on the rates of surface processes and probably on the magnitude of the change in boundary conditions. This, however, is an important issue to consider when expanding this approach to other study areas. As a fast synoptic overview, numerical fault interaction modeling can help to better understand the tectonic landscape evolution, especially in tectonically complex settings with repeated reactivation of faults or fault arrays.

# Chapter 5

# Quaternary deformation in the Tehran plain deduced from $^{10}Be$ and $^{36}Cl$ depth profiles of alluvial geomorphic surfaces

## 5.1 Introduction

The use of terrestrial cosmogenic nuclides (TCN) in dating unconsolidated alluvial deposits in a variety of depositional environments has enriched our ability to date the history of sedimentary processes and associated landforms for the Quaternary Period and beyond (e.g., Lal, 1991; Biermann et al., 1995; Gosse & Phillips, 2001; Cockburn & Summerfield, 2004). This method bridges the time scales of radiocarbon, luminescence, $^{40}Ar/^{39}Ar$ or U-series dating, which cover either shorter or much longer time spans. In particular, in those environments where organic matter is not available for radiocarbon dating due to poor preservation potential or arid conditions not conducive to the formation of large quantities of organic material, TCN dating has become an important chronometer. The build-up of *in situ* cosmogenic nuclides at surface and at depth results from interactions of neutrons and muons of secondary cosmic rays with specific target elements in minerals. The build-up depends on exposure duration as well as denudation rate affecting the surface. Among these production processes, spallation by high-energy neutrons is the dominant production reaction for most TCN, followed by negative-muon capture, and low-energy neutron capture (e.g., Gosse & Phillips, 2001). However, there are several problems inherent to the method of TCN dating of alluvial deposits. These include a complex pre-exposure history (inheritance), soil mixing, post-depositional erosion, and burial (e.g., Gosse & Phillips, 2001), all of which affect the accumulated nuclide concentration. In order to obtain meaningful age information under these circumstances it is important to devise measures to reduce such uncertainties by implementing sampling strategies that allow for separate estimates of post-depositional effects. This includes detailed geological and stratigraphic observations of the sampled geomorphic surfaces (e.g., shape or estimates of riser diffusion are required to evaluate local erosional components). Furthermore, in order to calibrate the surface samples for inheritance and to exclude subsequent vertical rearrangement of clasts in a targeted profile, it is necessary to collect depth profiles of approximately 3 meters with several amalgamated samples taken at systematic intervals (e.g., Anderson et al., 1996; Repka et al., 1997). TCN concentrations from deeper parts of the profile should approximately reflect inheritance. Using two TCNs with different half-lives or combining a stable with an unstable nuclide are possibilities to evaluate erosional effects and the exposure history. Commonly, $^{10}Be$ and $^{26}Al$ or $^{10}Be$ and a stable TCN as $^{21}Ne$ have been successfully applied to alleviate this problem (e.g., Klein et al., 1986; Graf et al., 1991; Lal, 1991; Biermann et al., 1999; Granger & Muzikar, 2001; Kober et al., 2007). Another approach involves the use of $^{36}Cl$ data with the $^{10}Be$ system (e.g., Phillips et al., 1997, 2009). Yet an additional alternative is to directly determine the erosion rate from depth profiles (e.g., Wolkowinsky & Granger, 2004; Siame et al., 2004; Schaller et al., 2004; Lal, 2005, 2006; Schaller et al., 2009; Braucher et al., 2009). The profile shape is characteristic for a specific site and nuclide production rate or sum of production pathways (e.g., Gosse & Phillips, 2001). While an undisturbed profile of a spallation-dominated nuclide such as $^{10}Be$ will exponentially decrease with depth (e.g., Lal, 1991) due to the exponential attenuation of cosmic rays with depth, erosion of overlying rock will cause steepening of such a profile. However, the depth profile of $^{36}Cl$ can be more complicated due to the complexity of the additional production reaction by low-energy capture on the target trace element Cl (e.g., Liu et al., 1994; Phillips et al., 2001; Schimmelpfennig et al., 2009). Fitting the profile data by using $Chi^2$ minimizing can simultaneously solve for exposure time and denudation (e.g., Siame et al., 2004; Ritz et al., 2006b; Braucher et al., 2009). If these pre- and post-depositional parameters are considered thoroughly, the TCN method can be applied to date geomorphic surfaces in various geological settings, even if these environments have experienced complex geomorphic histories involving erosion and deposition.

Geomorphic surfaces, such as fluvial and marine terraces or gravel-covered pediments in tectonically active regions can be very helpful in defining the degree of ongoing tectonic deformation, because these features are either originally flat lying or gently inclined, and thus constitute ideal reference horizons that reflect the degree of activity for a given region (e.g., Bloom et al., 1974; Strecker et al., 1989; Thorson, 1989; Avouac & Peltzer, 1993; Avouac et al., 1993; Marshall & Anderson, 1995; Strecker et al., 2003; Melnick et al., 2006, 2009). Episodic vertical tectonic movements or the combination of vertical movements and depositional/erosional overprints may lead to a staircase morphology of such landforms. Consequently, if these multi-generation landforms can be dated, tectonic deformation rates can be determined and spatiotemporal trends in fault activity can be evaluated. Although TCN dating is often the method of choice in such environments, and despite the fact that measurements of cosmogenic nuclide concentrations are increasingly accurate and robust due to improvements in accelerator mass spectrometry, their interpretation may be erroneous.

Ongoing debates focus on the correct use of this method (e.g., Perg et al., 2001; Brown & Bourlès, 2002a; Brown et al., 2002b; Perg et al., 2002; Brown et al., 2005; Chevalier et al., 2005a,b; Meriaux et al., 2004, 2005; Cowgill, 2007). This controversy is based on the observation that TCN-derived fault-slip rates on time scales of $10^3$ to $10^5$ years may differ significantly from rates determined for decadal to centennial time scales that were derived from GPS measurements or paleoseismology. It has been argued that such discrepancies might be rooted in pre- and post-depositional processes on TCN-dated surfaces, i.e., sedimentary and erosive processes, respectively (e.g., Brown et al., 2002b, 2005; Chevalier et al., 2005a,b). Clearly, if such processes are not adequately taken into consideration through improved sampling protocols and rigorous interpretation, the cosmogenic radionuclide analysis of alluvial surface samples might yield erroneous results. If such dates are being used to characterize fault-slip rates or to highlight regional events of aggradation and incision, the error might propagate into the evaluation of tectonic activity and could affect hazard assessment of earthquakes and related phenomena.

In this study, we systematically sampled and studied depth profiles and boulders of gravel-covered pediments and fluvial terraces in the Tehran plain south of the tectonically active Alborz mountains in north-central Iran. Space geodetic measurements in Iran suggest NNE-directed shortening at 6 ± 2 mm/a, apparently accommodated across the Alborz mountains, plus range-wide left lateral shearing at a rate of 4 ± 2 mm/a , because the adjacent South Caspian basin moves northwestward at a rate of 6 ± 2 mm/a, all relative to an Eurasian reference frame (e.g., Vernant et al., 2004b). The Tehran plain is separated from the Alborz mountains by the ENE-striking North Tehran Thrust (NTT) and hosts the Tehran metropolitan area. The Tehran plain is part of the south-central Alborz foreland, but deviates from the general northwest trend of the mountain front-foreland couple in this part of the range. The present-day topography of the Tehran plain reflects the interplay of tectonism, deposition, and pronounced phases of lateral erosion associated with the formation of pediments. However, protracted Quaternary deformation has been occurring in this region. Abbassi & Farbod (2009) have recently revised earlier studies (e.g., Tchalenko, 1974, 1975; Berberian, 1983) and interpreted folded foreland sectors in the context of a foreberg (e.g., Bayasgalan et al., 1999). The timing of this structural development is tenuous, because age correlations are based on surfaces in the SE of Iran. Here, we take advantage of the structural observations of these authors and our own structural fieldwork and combine them with additional geomorphic observations and our TCN dating of alluvial and strath terraces (Fig. 5.1). One age is derived by optically stimulated luminescence (OSL) and gives an additional constraint on the timing of deposition in the Tehran plain. The present analysis shows that the two oldest recognized phases of alluviation, subsequent erosion, and faulting, which affect units A and B, predate Late Pleistocene time. The oldest dated surface is the Saboo erosional surface of 195 ka. In the Tehran plain surface samples alone are insufficient to yield unambiguous age information to characterize the age of geomorphic surfaces. Fitting of the depth profiles separately by $Chi^2$ minimizing and/or the two-nuclide approach yields a much higher rate of denudation than expected. In some cases, surface concentrations are in "steady-state" (i.e. production and radioactive decay of the TCN are in equilibrium) when applying the calculated denudation rate and can only yield effective ages. Abandoned terraces that probably correspond to incision after deposition of unit C show Late Pleistocene ages along the Kan River in the west and the Jajrud River in the east. Pulses of Holocene incision have been observed at the Afjeh valley entrance and are probably related to repeated earthquake ruptures. Those events have resulted in the formation of strath terraces and the development of a bedrock channel near the eastern tip of the NTT, but they might have ruptured the entire length of this fault. Nevertheless, although the manifestations of ongoing deformation along the NTT are scarce, numerous faults and deformed Quaternary units in its footwall and in the Tehran plain unambiguously demonstrate that this region is tectonically active, although perhaps not on time scales spanning the ultimate millennia.

## 5.2 Methods

### 5.2.1 Sampling

Except in one case, where we sampled boulders (Rahad Abad site, Fig. 5.1C) and bedrock strath terraces (Afjeh, Fig. 5.1D), amalgamated alluvial samples were collected in depth profiles. We sampled in up to 3-m-deep holes of about 1 m diameter on laterally extensive, virtually non-shielded, sparsely vegetated surfaces. The source areas for the pediment and terrace gravels (Fig. 5.1A, B, E, and F) constitute intermediate volcanic and volcanoclastic rocks, limestone, and limited amounts of siltstone.

For a representative contribution of the variable lithologies inside the source rock of the catchments providing gravels to these different generations of geomorphic surfaces, we sampled hundreds of pea-sized clasts (amalgamated samples), where available. In addition, we collected larger clasts and/or material in the sand size fraction, if pea-sized material amounts seemed insufficient. At one site (Rahad Abad), we have used the $^{10}Be$ and $^{26}Al$ nuclide pair from purified quartz of large boulders. At another site (Saboo, Fig. 5.1E), we sampled three different particle sizes (profiles). Here, we scraped all material in steps of about 30 cm from approximately 10-cm-thick layers, including matrix and small clasts (A-profile), from which we used the sand-sized fraction. In addition, we collected cobbles and small boulders, if available (B-profile), and finally sampled clasts from the pit wall (C-profile).

### 5.2.2 Preparation and Analysis

For each sample, a representative bulk subsample was kept to measure the sediment density and to assess the chemical composition of the amalgamated sample. This is especially

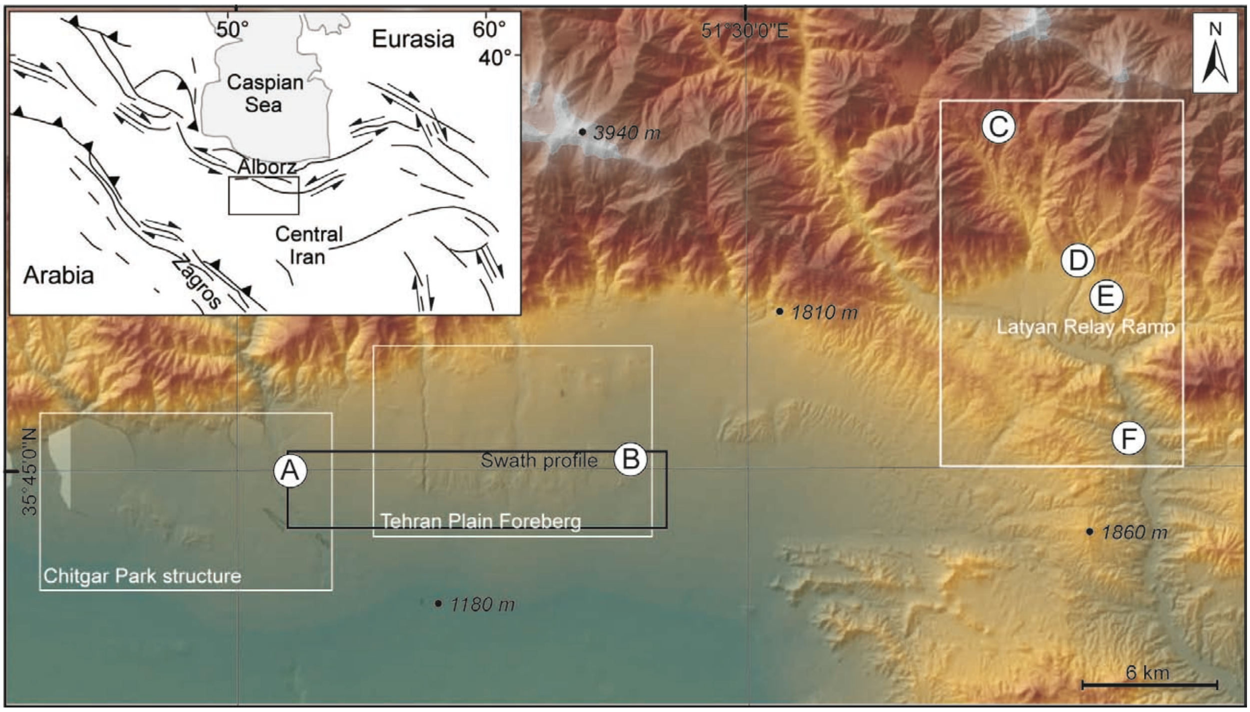

Figure 5.1: Study sites in the south-central Alborz mountains. Inset shows regional tectonic setting. Map base is 10-m hillshade and SRTM DEM. Sample locations are denoted by circled letters. Boxes mark areas discussed. (A) Kan site, fluvial terrace, $^{10}Be$ depth profile; (B) fluvial/alluvial terrace at the Tehran National Library, $^{10}Be$ depth profile; (C) high pediment surface at Rahad Abad, $^{10}Be$ and $^{26}Al$ ($^{36}Cl$) of boulders; (D) bedrock (strath) terraces at Afjeh valley entrance, $^{36}Cl$, (E) paleopediment at Saboo Bozorg, $^{10}Be$ and $^{36}Cl$ depth profiles; (F) Jajrud, fluvial terraces, $^{10}Be$ and $^{36}Cl$ depth profiles.

important for evaluating the thermal neutron field in the rock, because $^{36}Cl$ is not only produced by spallation from calcium, but may also be produced by thermal neutron caption from $^{35}Cl$ (e.g., Stone et al., 1998; Schimmelpfennig et al., 2009). Samples were first crushed in a jaw crusher and a disk mill. Subsequently, the samples were sieved to 125-500 $\mu m$ to ensure that grain boundaries are exposed to leaching (e.g., Stone et al., 1996). Where high material loss occurred during quartz separation, we increased the fraction to 700 $\mu m$ (Merchel et al., 2008). Because of the highly variable and polymictic composition of the samples, we focused on the nuclides $^{10}Be$ and $^{36}Cl$ derived from quartz or calcite, respectively. Mineral separation included magnetic separation using a Frantz magnetic separator. At this step a representative aliquot was selected from some samples by quartering up to 20-30 $g$. This material was subsequently pulverized in an agate mill for X-ray diffraction and X-ray fluorescence measurements. The X-ray diffraction revealed that the non-magnetic fraction generally comprised a mixture of varying amounts of calcite, quartz, and different feldspars. The treatment of the samples, including grinding, leaching and chemical extraction of chlorine by precipitation of silver chloride, was performed following the methodology of Stone et al. (1996) at the CEREGE facility (CNRS, Aix-en-Provence). At two sites, we used both nuclides $^{10}Be$ and $^{36}Cl$ from the same set of amalgamated clasts. This involved first of all extracting $^{36}Cl$ from calcite (e.g., Stone et al., 1996), which was dissolved from a pre-treated mixture of calcite, quartz, and feldspar. After decanting the calcite-bearing solution, the silicate residual was used for further quartz purification and chemical $^{10}Be$ extraction. This approach is new (Merchel et al., 2010) and allows simultaneous detection of $^{10}Be$ and $^{36}Cl$ from samples which underwent the same burial history, but did not necessarily experience identical pre-depositional events. With the exception of one site (Afjeh), where we extracted chlorine from plagioclase, we used the calcite protocol of chlorine extraction (Stone et al., 1996). Because this procedure is generally applied for limestone, i.e., for samples of approximately 100% $CaCO_3$ content (or 40% Ca), the application of this technique for calcite/silicate mixtures requires certain pre-examinations and adjustments. First of all, the percentage of calcite in the mineral separate has to be known. We determined this by either X-ray fluorescence of the representative aliquot or by total dissolution of 1 g sample with concentrated $HNO_3$. By testing both methods on three samples we found that reasonably similar results can be produced within less than or about 5% (Table C.11, appendix C). Therefore, the laborious step of using X-ray fluorescence might not be necessary. The results were used to upscale the amount of initial weight and to downscale the amount of acid used for the leaching steps and total dissolution, particularly to avoid that all available calcite is already dissolved during the leaching steps. However, a low percentage of calcite distributed in the silicate mixture requires special handling. It is inevitable to carefully agitate the sample in our approach. Calcite might be capped with silicate and remain shielded from the acid, and the dissolution reactions sometimes are delayed. In order to avoid and test for chlorine loss, we added the acid in small increments and analyzed three samples with replicates, which show very good agreement (compare samples 13-1-4a, 23-1-0B, and 23-1-4b).

The $^{36}Cl$ and chlorine concentrations were determined for all samples by isotope-dilution accelerator mass spectrometry (ID-AMS) at the Lawrence Livermore National Laboratory‘s CAMS, Berkeley, CA (Southon et al., 1992). Results are based on a calibration with KN500 material. The concentrations of the blank was two orders of magnitude lower than that of the samples and replicates were within less than 5%. Cosmogenic $^{10}Be$ samples were processed following standard procedures described by Brown et al. (1991) and concentrations were determined at the French accelerator mass spectrometry facility ASTER (CEREGE, Aix-en-Provence) (Arnold et al., 2010). All values are calibrated by the original NIST SRM 4325 material. Unless otherwise stated, all ASTER $^{10}Be$ results are traceable to this material with an assigned value of $(2.79\pm0.03)\times10^{-11}$ and the corresponding half-life of $(1.387\pm0.012)\times10^{6}$ a (Korschinek et al., 2010; Chmeleff et al., 2010). The surface exposure ages were estimated to site-specific latitude and altitude using scaling functions of Stone et al. (2000) and a spallation surface production rate at sea level, high latitude (SLHL) of 4.5 at/g/yr.

## 5.3 Structural and morphological expression of deformation in the Tehran Plain

In this section, prominent tectono-geomorphic phenomena of the Tehran plain and adjacent sectors of the NTT are described and analyzed regarding their structural and geomorphic evolution. At the end of every subsection, TCN sampling locations are described in the geomorphic context in order to ultimately provide a temporal framework of the neotectonic evolution of the Tehran plain. Detailed studies have been performed by several workers to differentiate the alluvial deposits in the Tehran plain and other regions in Iran (e.g., Rieben, 1955, 1966; Vita-Finzi, 1969). The sedimentary units in the Tehran plain comprise Miocene (?) to Pleistocene (?) strata of alternating conglomerate, silt and sandstone (Hezardarreh Formation or unit A after Rieben, 1955). These units are in turn unconformably overlain by the heterogeneous Kahrizak Formation (unit B), which comprises sand- and siltstones, the Tehran Alluvium (unit C), a laterized conglomerate of inferred Holocene age, and undifferentiated recent alluvium (unit D). Vita-Finzi (1969) further subdivided unit C into the older Tehran alluvium, generally constituting conglomeratic fan or bajada deposits, and a younger, better-sorted channel-fill unit, known as the Khorramabad Formation. Generally, these units are associated with terraces, i.e. the oldest units occur on remnants of former transportation surfaces at high elevations, whereas the younger units occur at successively lower elevations. Geophysical prospecting and drilling have revealed up to 250 m of Quaternary gravel below the Tehran metropolitan area (Bassir, 1971). The occurrence of these deposits in the Tehran plain is dictated by the existence of previously uplifted fluvial terraces, which acted as barriers and sediment traps. The thickness of Quaternary deposits increases dramatically southwards from about 50 m to more than 200 m over a distance of 1.5 km. The elevations of terraces, alluvial fans and paleo-pediments and their variable degree of dissection help distinguish different generations of geomorphic surfaces. Accordingly, satellite and airphoto mapping, as well as field inspection have revealed four main geomorphic surfaces in the Tehran plain (Fig. 5.5, 5.8 and 5.16). A structural east-west trend is clearly recognizable in slope-aspect relationships of these surfaces (Fig. 5.2).

The extensive bajada comprises slopes inclined less than 10% which dip towards South. This surface records 700 m of N-S elevation difference across a distance of 20 km. Steeper slopes which correspond to uplifted and older surfaces show a much higher fraction of southeast orientations. This aspect is mainly associated with surfaces to the north, where deformation is parallel to the NTT. While folding plays a significant role in the Tehran plain, the lack of northward-inclined hillslopes indicates that sediment accumulation rates exceed rates of deformation and uplift.

The westernmost structure, here informally called the Chitgar Park structure, strikes northwest, approximately parallel with the mountain front to the west and east of the Tehran plain (e.g., Fig. 5.1A and 5.6). A similarly striking structure separates the easternmost

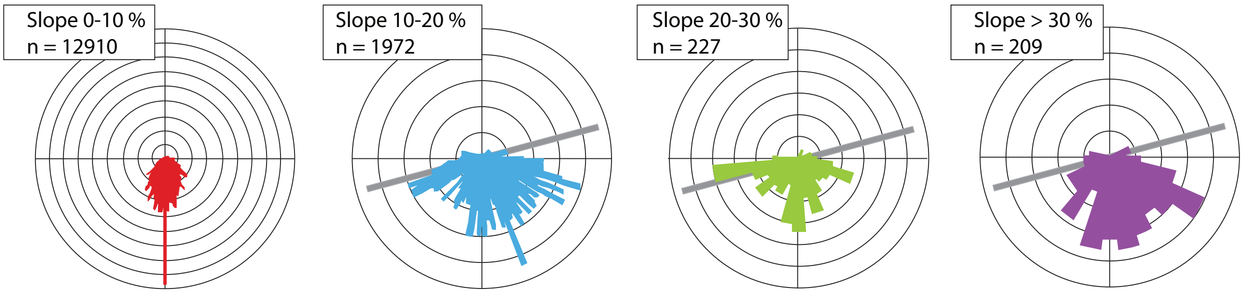

Figure 5.2: Slope-aspect relationships for surfaces in the Tehran plain, calculated from 90 m SRTM data using MICRODEM-tool. Note different scaling (up to 2 magnitudes of difference) of the graphs. The area used for the calculation corresponds with the Tehran plain foreberg (white box in Fig. 5.1), and an additional sector, approximately 1.5 km toward the east. Gray line corresponds to the strike of NTT.

basin from the main foreland. This sub-basin, here called the Latyan basin (Landgraf et al., 2009), is internally deformed and has the topographic expression of a relay ramp (Fig. 5.1C). The deformation pattern in the alluvium close to the mountain front generally follows the strike of the NTT, thus mirroring a genetic relationship. Farther south, however, patches of uplifted alluvial terraces are east-west aligned and thus at an acute angle with respect to the NTT (Fig. 5.1B). The responsible structure for this uplift is interpreted to be a transpressional “foreberg”, accommodating part of the oblique motion related to the Arabian-Eurasian collision (e.g., Abbassi & Farbod, 2009). The orientation of the drainage network is orthogonal to this structure. Rivers sourced in hinterland basins exit the mountain front obliquely, flow transversely southward, and are antecedent in the “foreberg”. Interestingly, hinterland catchments are located in the hanging wall to the NTT and show elongation in the N-S direction. They are thus oblique to the mountain front and the range-bounding fault. This might indicate that some important structural feature has been established with an approximately E-W trend, contemporaneously with activity at the NTT, but prior to the growth of the foreberg. In the following, we will describe the main structures and their morphological expression and discuss their deformation history based on our new TCN-derived ages.

### 5.3.1 Chitgar Park structure

Abbassi & Farbod (2009) interpreted the Chitgar Park structure as an exception from other folds in the Tehran plain, associated with internal faulting without folding. However, the morphology and internal geometry of this structure characterizes it as a S-verging fault-propagation fold. A steeper forelimb in the south suggests that the responsible fault is north-dipping (Fig. 5.3A, for location of the cross-section see Fig. 5.5A). Furthermore, the folded units show decreasing dips upsection, indicating syndepositional forelimb rotation. Bedrock is exposed in the hinge zone, which is virtually vertical and highly sheared. It probably belongs to the latest members of the Eocene volcanoclastic Karaj Formation, which grade either into Upper Eocene Kond Formation or Miocene Red Formation. Shearing is localized in gypsum and marl-bearing units. Locally, granodioritic boulders occur in wide cataclastic zones with biotite-bearing stretching lineations on clayey planes. Granodiorite is exposed in the Karaj catchment to the NW, which is probably the source of the alluvial/fluvial sediments of the Hezardarreh Formation, which in turn overlie gypsum and marls and constitute the principle units of the southern limb (Fig. 5.3A and c to e). Dips of the Hezardarreh Formation pass from vertical near the hinge to 21° SW where the sediments are separated by an erosional unconformity from the overlying alluvial Kahrizak Formation (Fig. 5.3A and d). This implies that a large part of fault activity took place during deposition of the Hezardarreh Formation. However, the Kahrizak Formation, which is exposed on both limbs, is still inclined. The dip is steeper on the southern limb, while the northern limb of the Kahrizak Formation dips only gently north and forms a buttress unconformity on the vertical Karaj Formation (Fig. 5.3A and b). However, given the general southward transportation of the alluvial fan sediments, this documents considerable deformation also during this period. The northern limb has undergone brittle extensional deformation as documented by obliquely oriented horst and graben (Fig. 5.3A, site a). Based on these observations, we suggest a trishear folding interpretation for the Chitgar Park structure. Thus, the box in Fig. 5.4A corresponds to the exposed and highly deformed hinge zone and part of the southern limb (bedrock and Hezardarreh Formation). During a period of quiescence, erosion might have removed part of the backlimb and to a lesser degree the forelimb. The vertical bedrock might have a higher resistance to erosion, which could be responsible for its preservation. The present-day course of the Karaj River south of the Chitgar Park structure might also indicate that a lesser amount of Hezardarreh Formation sediments were deposited to the north compared to the south of the structure. Another phase of sediment accumulation above the erosional unconformity took place, which outpaced the deformation (Fig. 5.4 B). Subsequently, further faulting caused continued folding of the sediments (Fig. 5.4 C), followed by renewed erosion (Fig. 5.4 D).

The Chitgar Park structure lies between two adjacent alluvial fans of the Vardij valley to the west and the Kan valley to the east. These fans are currently incised by both rivers, which are laterally diverted (Fig. 5.5). Furthermore, abandoned channels of similar orientation as the recent drainages, but located closer to the structure on the east and west, attest to lateral advection and incision through time. This may indicate lateral propagation of the fault at depth. The Chitgar Park structure constitutes two uplifted segments, separated by a windgap (*WG* in Fig. 5.5D). As indicated by the dashed line, the windgap seems to be level with the Kan alluvial fan, indicating that it was coeval with fan accumulation. Thus, dating of the Kan alluvial fan allows determination of a reference datum for abandonment and subsequent deformation of the former river channel. Due to rural development, however, it is not possible to date directly the fan surface directly. Instead, we use the TCN-derived age of the neighboring left-bank Kan river terrace (Fig. 5.5B, marked by star). We deem

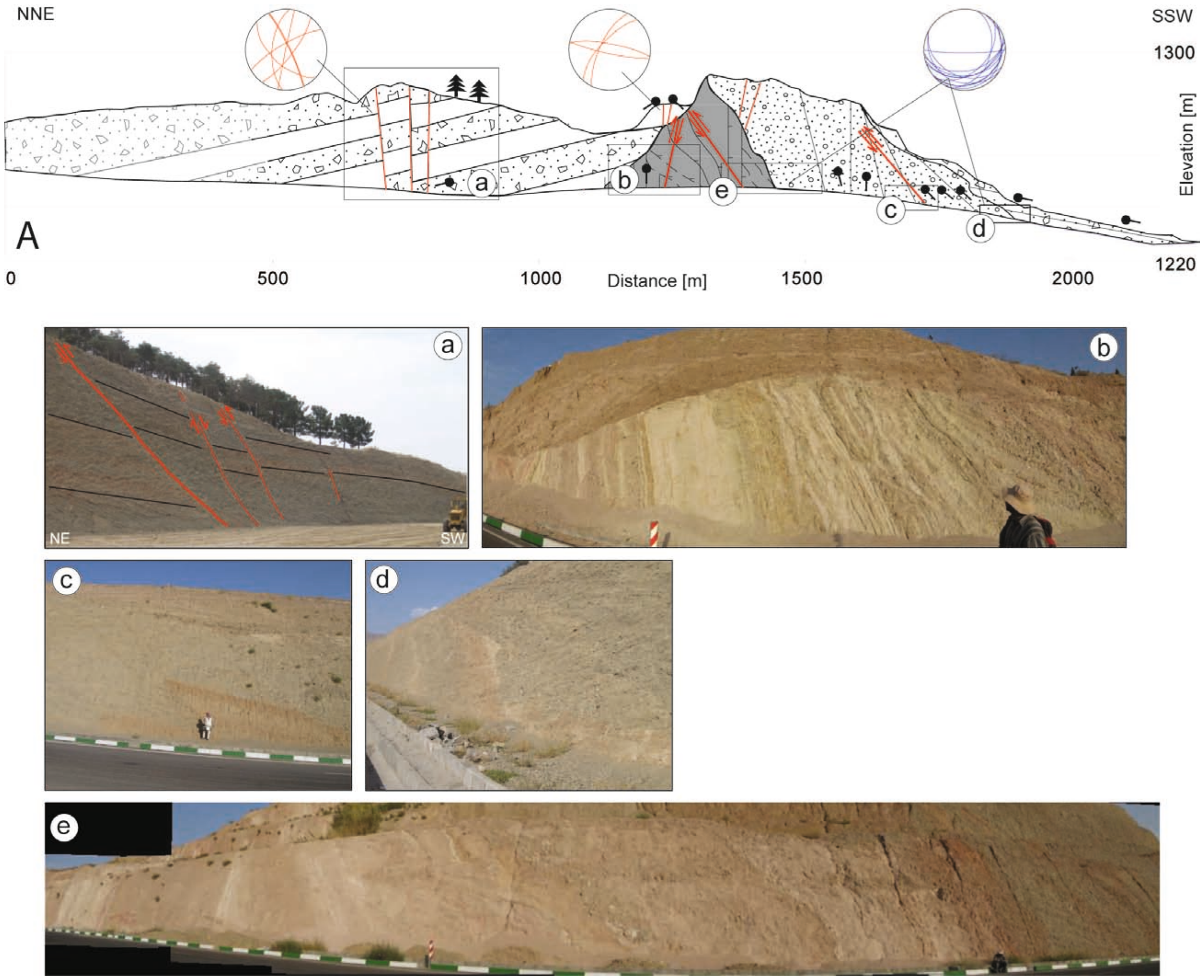

Figure 5.3: Cross-section across the Chitgar Park structure. Photos document style of deformation. Bedrock (in gray, upper stages of Karaj Formation and Kond- or Red formations in unconformity) highly sheared and fractured is slightly discordant overlain by alluvium of the Hezardarreh Formation (unit A) in the south, and in buttress unconformity with unit B in the north (b and e). The backlimb is gently dipping and records extensional faulting (a), while the forelimb units (unit A) pinch out (see stereoplot with bedding in blue) and are associated with internal thrusting. (c) in turn, these units are unconformably overlain by unit B (d).

this valid, because smoothness and degree of incision or erosion are equally developed on both surfaces, indicating a similar geomorphic history. However, while their appearance is similar, topographic across-cone profiles at three distances from the fan apex (Fig. 5.6) show that river terraces at 1.5 and 3 km from the mountain front are at a higher level than the fan surface and elevation is continuously increasing towards the east. This indicates that the Kan embankment is not directly nested in the fan surface, but rather constitutes a separate river terrace. The left-bank terrace is furthermore influenced by alluvial fan activity from the east, which currently results in sediment transport toward the SW (Fig. 5.6). This interpretation is further supported by the occurrence of a debris flow unit above the otherwise fluvial intercalations in the soil profile.

Sampling took place at the left bank of the Kan river, approximately 2.5 km downstream

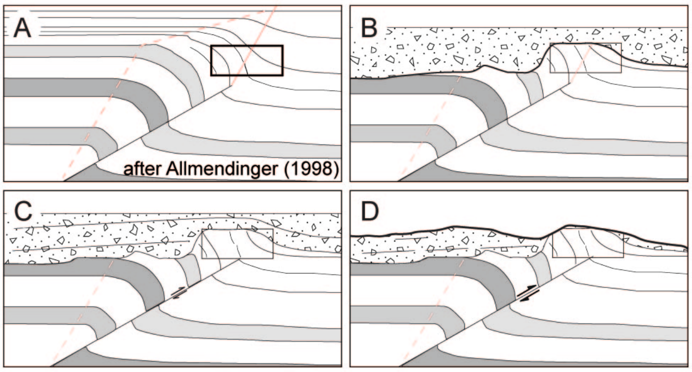

Figure 5.4: Simplified sketch to illustrate possible deformation history at the Chitgar Park structure based on outcrop patterns of deformed rocks and unconformities. (A) Trishear folding allows forelimb rotation; Box indicates part of the highly deformed, steep limb above the fault tip, which might correspond to the oldest exposed units, ranging from vertical strata of the Karaj Formation to increasingly less steep unit A sediments at the Chitgar Park structure; (B) possibly, the vertical dip of the bedrock units caused higher resistance to erosion, an erosional unconformity was established (thick black line), and the area was subsequently covered by alluvial deposits. (C) Further deformation caused tilting of the younger deposits in the forelimb and to lesser degree in the backlimb. (D) Continued uplift and subsequent erosion have further shaped the structure into the present-day condition (compare Fig. 5.3).

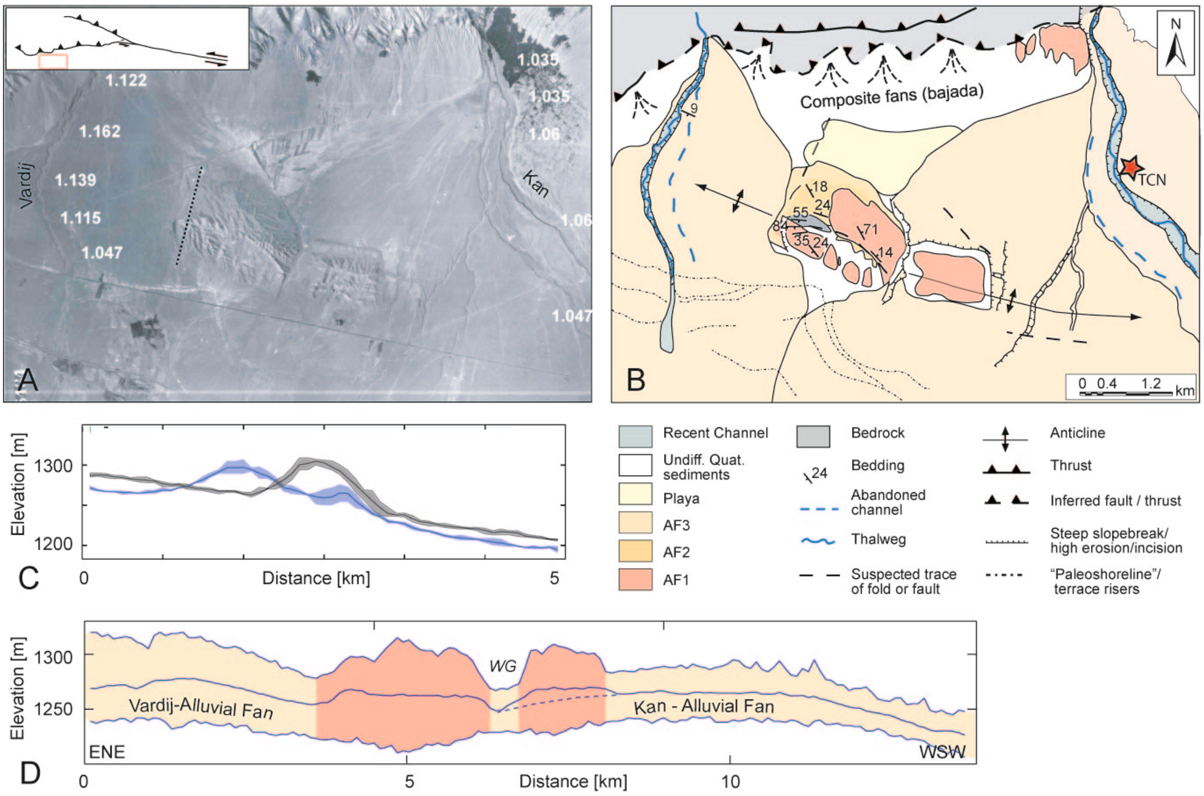

Figure 5.5: (A and B) Tectonic geomorphology of the region of the Chitgar Park structure between the Vardij and Kan rivers. Both channels are diverted around this structure. Channel sinuosity values are plotted in white in (A). Dashed line depicts cross-section (Fig. 5.3) and box outlines a windgap. Inset in A shows location of the structure relative to the North Tehran Thrust and Mosha Fasham Fault. (C) Narrow swath profiles (showing minimum, mean and maximum elevation) crossing the terraces (D) Swath profile across the Chitgar Park structure

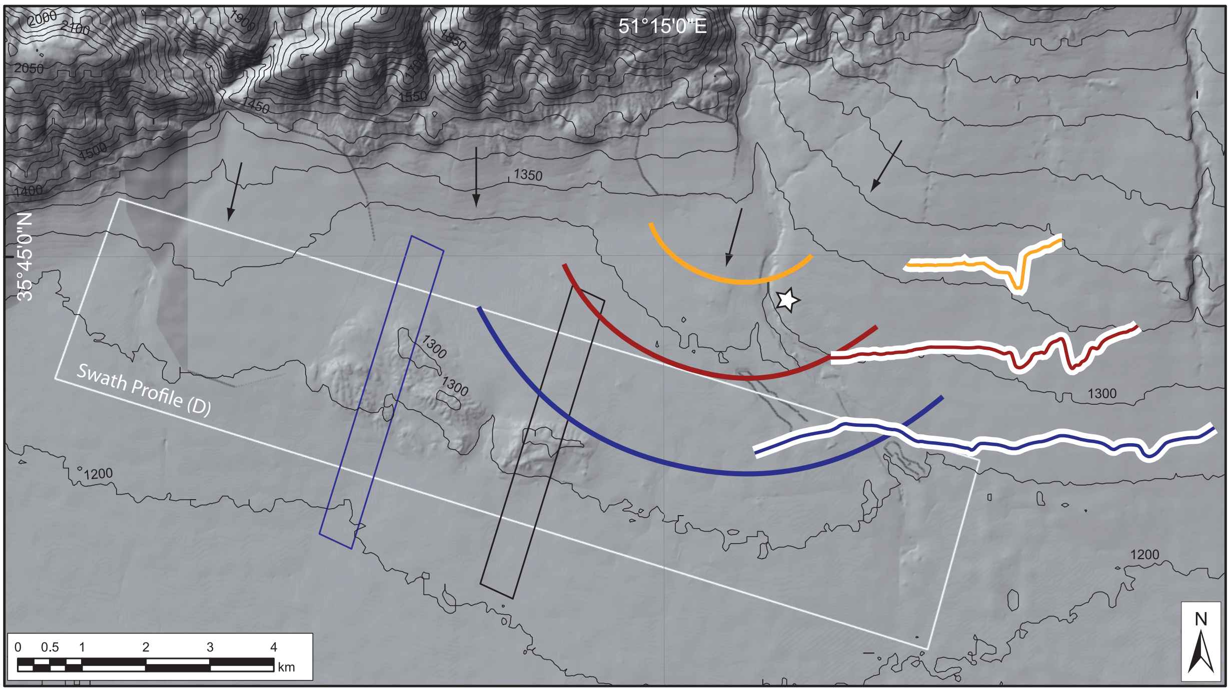

Figure 5.6: Overview of Chitgar Park structure on 10 m hillshade DEM with superposed 50 m contour lines. Boxes depict locations of along-strike swath profile (white, Fig. 5.5D) and perpendicular swaths (blue and black, Fig. 5.5C). Concentric lines depict the Kan alluvial fan at 1.5 (yellow), 3 (red), and 4.5 km (blue) from the apex (see Fig. 5.5B). Topographic profiles were calculated from the 10 m DEM and are plotted to the right. Note how topography rises to the east of the (Kan) River. Black arrows denote slope aspect.

Figure 5.7: Extensive fluvial/alluvial fan terrace along the River Kan. View to the east, across the floodplain of the Kan River towards the terrace.

of the mountain front. The surface is smooth, without any local relief, laterally extensive, and only sparsely vegetated (Fig. 5.7). Amalgamated clast samples have been collected in a 3-m deep test pit and at the surface. Surface samples comprised two different clast sizes, which are pea-sized clasts and pebbles, respectively, which were analyzed separately. Depth samples comprised pea-sized clasts. A lithological description has been logged for the test pit (Fig. 5.19E). As reference for inheritance, amalgamated pea-sized clasts from the recent Kan channel have been collected and analyzed additionally.

### 5.3.2 Tehran plain "foreberg" structure

Forebergs constitute rows of low hills at a certain distance from a fault-bounded mountain front and show evidence for thrusting and strike-slip faulting with variable ratios (e.g., Bayasgalan et al., 1999). The Tehran plain foreberg constitutes a S-verging fault-propagation fold with a steeper forelimb in the south, suggesting that the responsible fault is north-dipping. The dips of the folded units decrease southward, i.e., upsection, indicating forelimb rotation. The associated fault might be the Tarasht fault, recognized by Abbassi & Farbod (2009) on air photos. This fault may reach the surface south of the uplifted terraces in some places and is blind in others. Backthrusts (such as the Mahmudieh Thrust or Davudieh Fault according to Tchalenko (1974, 1975) and Berberian (1983) occur at different scales and form local push-up structures, but presently reach the surface only locally (see Fig. 5.11 for location). Evidence for left-lateral strike-slip faulting inside the foreberg is rare, but exists in the Abbassabad hills (e.g., Abbassi & Farbod, 2009), where a few ridges and drainages have accrued a cumulative offset of approximately 200 meters. Some outcrops show signs of transpressional deformation (Fig. 5.9 A and B), manifested in half-flower structures. Oblique shortening is furthermore accommodated by a set of én-echelon, left-stepping and southeast-dipping thrusts, known as the Bagh-e-Feyz and Television faults (Tchalenko, 1974, 1975; Berberian, 1983), which probably root into the Tarasht fault (Figure 5.11).

The folding and associated uplift has caused the formation of a set of approximately E-W aligned, uplifted terraces, which are partly separated by incision. The anticlinal axis exhibits a small left step-over, connected by an oblique ramp. However, assuming that topography reflects the cumulative, long-term displacement pattern, the trend of the topographic swath profile (Fig. 5.10) suggests that the folds are kinematically linked and a possible previous slip-deficit has regained. The main anticlinal axis, where highest uplift has been achieved, is clearly visible in the geomorphology (Fig. 5.8), due to the pronounced parallel incision pattern and some concave slope breaks in the abandoned alluvial fans. This incision, which kept pace with the uplift, has affected the alluvial units A and B. However, the unit B alluvium is largely subhorizontal and overlies the tilted unit A unconformably (Fig. 5.9 C). Nevertheless, terrace tops can reach 40 to 60 m above the local surrounding alluvium, which is incised by 15-20 m. The terraces have parabolic shapes, indicating that diffusion processes have been taking place, concurrent with or subsequently to uplift. However, recent incision, cut into alluvial unit C, and partly into unit B, is characterized by rather sharp convex slope breaks. Four rivers with catchments in the hinterland drain the structure. Three of them are crossing the terraces antecedently (Punak, Darakeh, and Velenjak rivers), while the Darband river is slightly bending around the easternmost uplifted terrace. Thus, uplift along the Tehran foreberg seems to control the base level of the greater Tehran plain, such that river incision stops along the southern front, and modern alluvial-fan sediments are deposited here (Fig. 5.8). This in turn is one of the most striking indicators for Quaternary

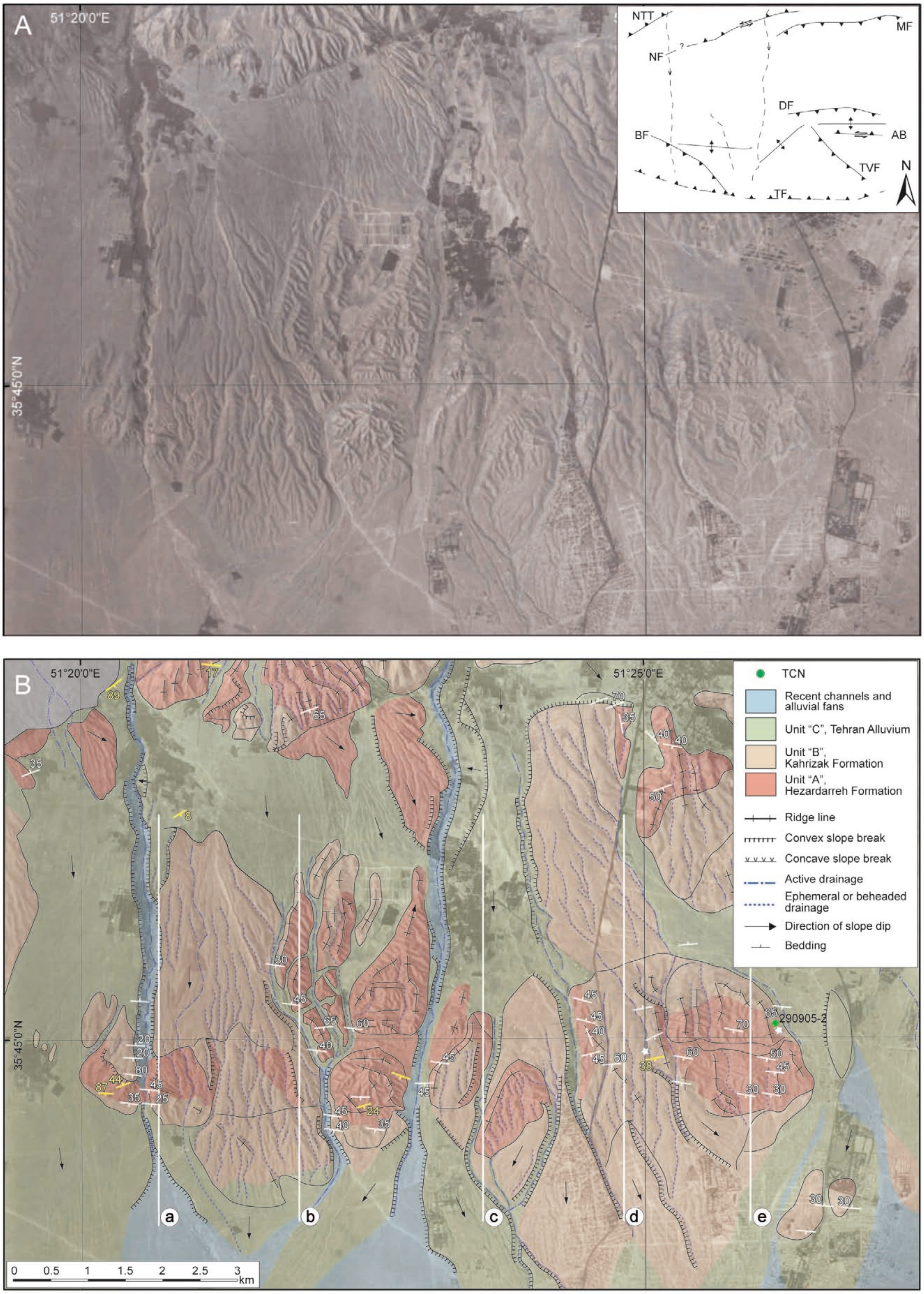
A
51°20'0"E
35°45'0"N
NTT
NF
MF
DF
AB
BF
TVF
TF
N
B
51°20'0"E
51°25'0"E
35°45'0"N
TCN
Recent channels and alluvial fans
Unit "C", Tehran Alluvium
Unit "B", Kahrizak Formation
Unit "A", Hezardarreh Formation
Ridge line
Convex slope break
Concave slope break
Active drainage
Ephemeral or beheaded drainage
Direction of slope dip
Bedding
290905-2
a
b
c
d
e
0 0.5 1 1.5 2 2.5 3 km

Figure 5.8: Geomorphological air photo mapping of the Greater Tehran area. (A) Air photo from 1955, inset shows inferred fault configuration, abbreviations as follow: NTT North Tehran Thrust, NF Niavaran Fault, MF Mamudieh Fault, DF Davudieh Fault, BF Bagh-e-Feyz Fault, AB Abbassabad hills and fault, TVF Television Fault, TF Tarasht Fault. (B) Geomorphic and lithological interpretation and additional information. Bedding in white is redrawn after Engalenc (1968), while symbols in yellow indicate measurements, obtained in this study. White lines correspond to topographic profiles in Fig. 5.10B. Stars depict sites of field descriptions of Fig. 5.9.

deformation along this structure. Urban development of the Tehran megacity covered most of the younger, less dissected alluvial fan formations. Few of the uplifted terraces, however, are less occupied and are virtually unaffected by construction, which makes these areas targets for TCN-dating. We sampled the top surface of a terrace at the Abbassabad hills, next to the Tehran National Library (green circle in Fig. 5.8), which exhibits subhorizontal unit B sediments in unconformity on southward-tilted unit A alluvium (Fig. 5.9C and 5.12). The terrace is extensive, but has a pronounced parabolic shape, suggesting considerable surface denudation. Due to clay-enrichment in the surface horizons, very few clasts have been found there. Amalgamated clast samples were collected in a 3-m deep test pit, and a lithological profile was schematically logged (Fig. 5.19B).

### 5.3.3 Latyan basin relay-ramp and deformation features east of Tehran

The Latyan basin is an exception in the Tehran plain. Separated from the main plain by a very pronounced, NW-trending anticline, i.e., the Latyan anticline after Dellenbach (1964), this area forms a small intermontane basin, which is drained by the Jajrud river. The basin constitutes both the northern limb of the Latyan anticline as well as the footwall of the North Tehran and Mosha-Fasham faults. The basin is in a crucial position, because here the North Tehran fault develops a slight left-bending geometry and changes its character from dominantly left-lateral strike-slip to oblique dip-slip motion. The area east of Tehran has been described in detail by Landgraf et al. (2009). The basin area is currently undergoing left-transtension. Here, we will take advantage of this work and add geomorphological observations and age control. To better understand the deformation history, we have sampled for both TCN or OSL dating. From north to south, we sampled boulders of an uplifted paleo-pediment in the Kond valley (hanging wall of NTT, Fig. 5.1C), a fluvial terrace remnant in the immediate hanging wall of the NTT in the Afjeh valley entrance, two strath terraces incised by a bedrock channel at the same location in the Afjeh valley entrance (Fig. 5.1D), a paleosurface developed in the Latyan basin (NTT footwall, Fig. 5.1E), and two fluvial terraces of the Jajrud, which are nested in the Latyan anticline downstream of the basin (Fig. 5.1F). Both the Kond and Afjeh rivers are tributaries of the Jajrud river and are currently incising the Latyan basin.

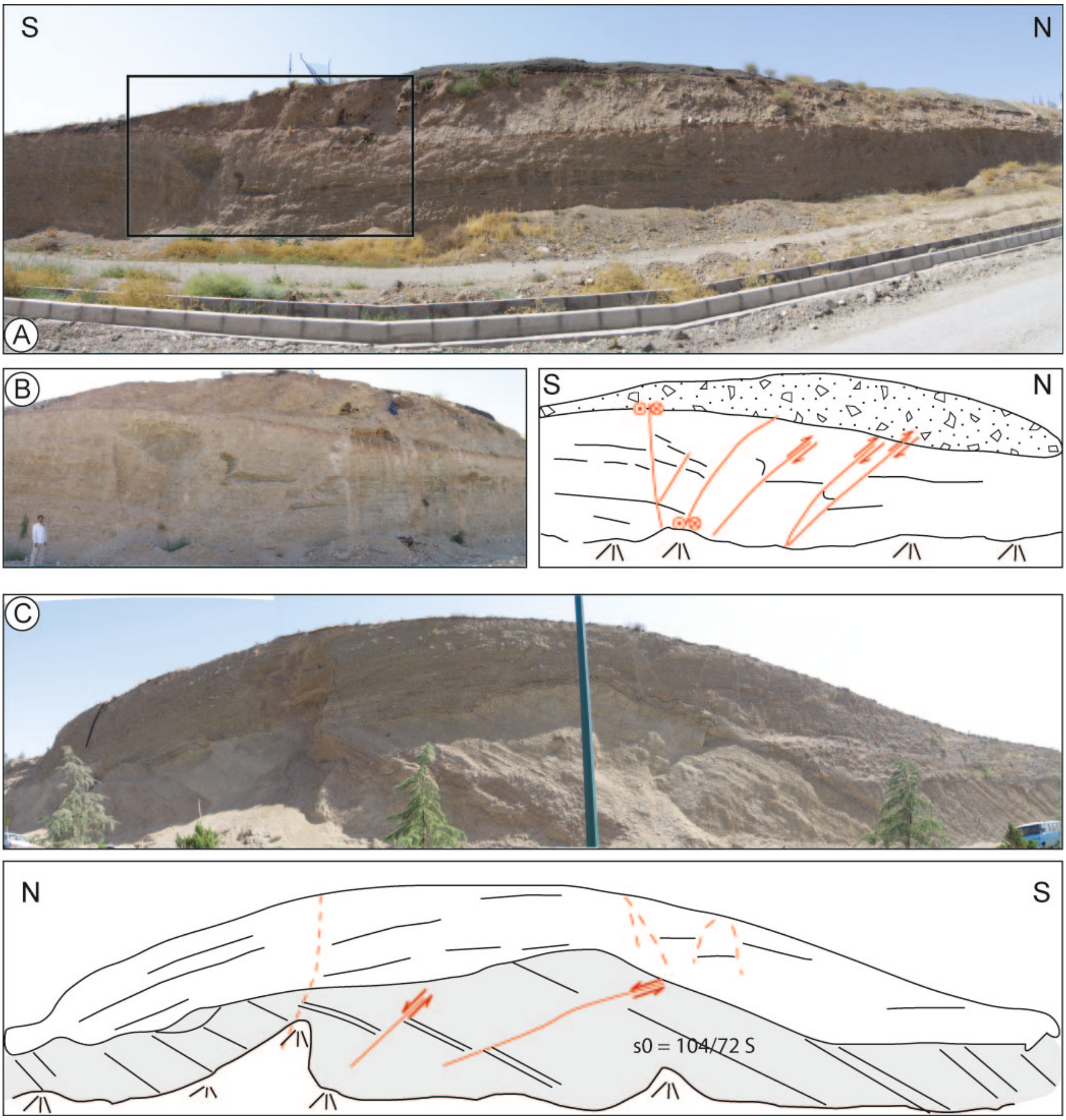

Figure 5.9: Examples of internal deformation in the foreberg structure. (A and B) Half flower structure developed as result of left-transpressional deformation due to oblique shortening; (B) is a zoom of rectangle shown in A, for location see star at 51.25 ∘) longitude in Fig. 5.8B. This deformation might be related to the East-West fault (after Tchalenko (1974, 1975) and Berberian (1983)) and is probably the continuation of the left-lateral (transpressional) fault, which offsets the Abassabad hills (Abbassi & Farbod, 2009). (C) Cut in the Abbassabad hills next to the National Library. This outcrop belongs to one of the highest uplifted terraces. Note the steep southward-dipping unit A sediments, which are in buttress unconformity and overlain by unit B sediments. Limited faulting and fracturing deform the sediments of unit B. Location is close to the sampling locality (star and green circle in Fig. 5.8B.)

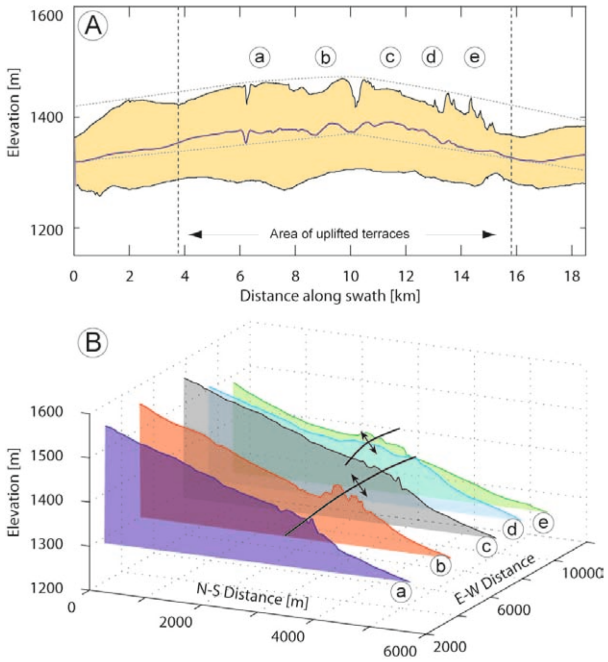

Figure 5.10: Topography of the foreberg. (A) Topographic swath profile, showing maximum, mean, and minimum elevation across the terraces (see Fig. 5.1 for area). Despite the left step-over of the anticlines, the topography suggests one throughgoing displacement profile, with highest cumulative displacement in the center. Note small letters for location of topographic cross-sections. (B) Parallel topographic cross-sections (for location see Fig. 5.8B). The alignment of uplifted terraces with step-over morphology in the east is clearly visible. Note the lower elevation of the northern termination of profiles d and e, which might be related to obliquity of the profiles with respect to the mountain front and thus the greater distance of those profiles from the sediment source.

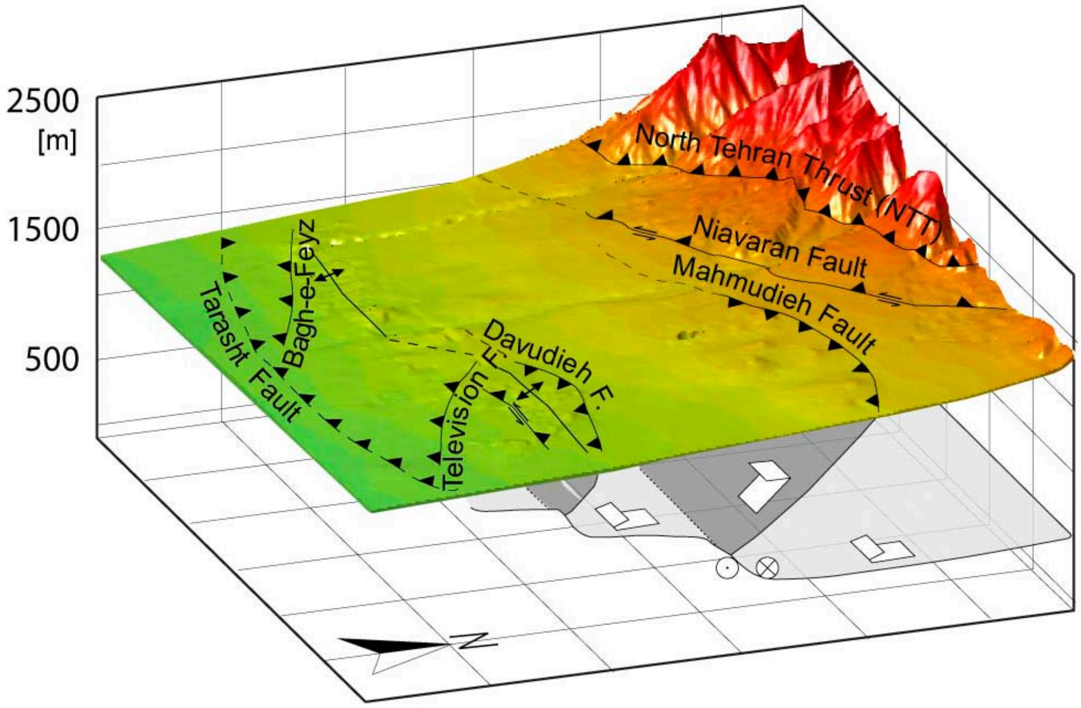

Figure 5.11: 3D-view of the main structures of the foreberg area. The Tehran plain foreland undergoes transpressional deformation with folding, thrusting, and left-lateral strike-slip faulting or oblique faulting. The responsible fault is inferred to dip towards the north and might be connected at depth with the North Tehran Thrust and/or the Niavaran fault.

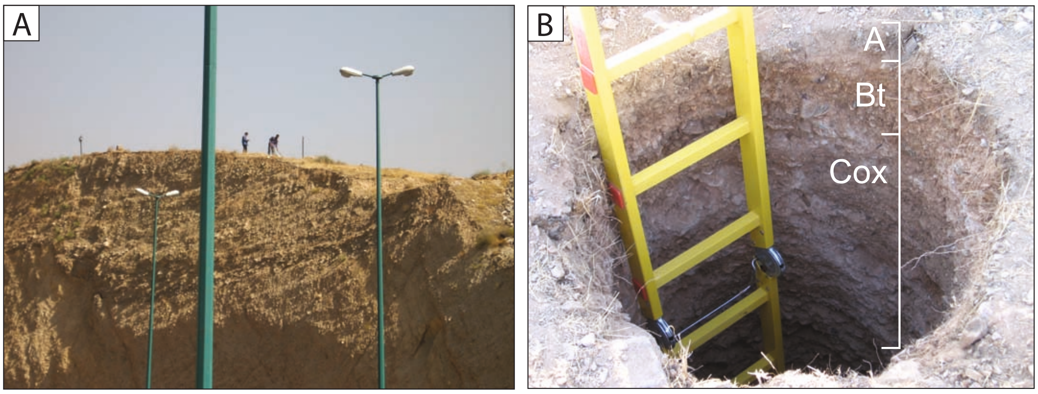

Figure 5.12: Uplifted terrace level at the National Library in Tehran. (A) View to the east onto a road cut of the sampling location. This terrace is highly dissected. Note the faulted lower part and sharp unconformity between the steeply inclined lower beds and subhorizontal upper part. Note also the parabolic shape of the terrace, suggesting significant surface denudation. (B) Upper part of sampling pit.

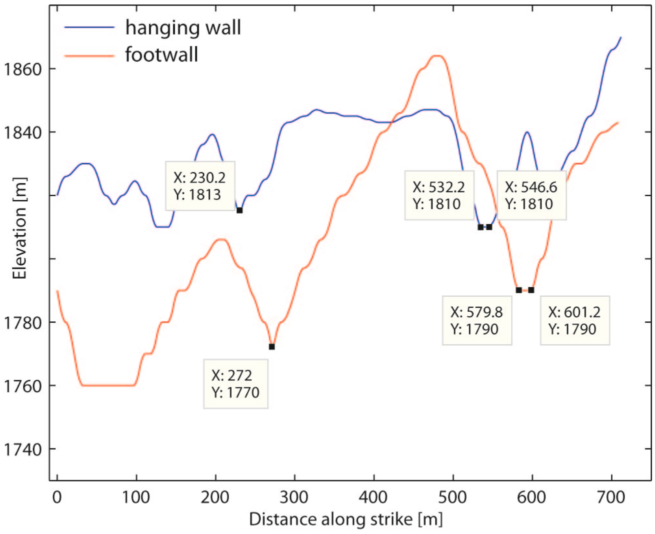

Figure 5.13: Topographic profiles (10-m DEM) of hanging wall and footwall, calculated parallel to the NTT. Two streams that cross the fault are left-laterally offset by a cumulative amount of about 42 and 54 m, respectively. The channel bed of the right offset channel is substantially wider, thus the 54 meters are considered as a maximum bound. The profile location spatially coincides with the strike-slip arrow symbols of Fig. 5.16(-inset).

### Paleo-pediment in the Kond Valley at Rahad Abad

The paleo-pediment, a gravel-covered erosion surface (Fig. 5.14), sculpted into folded and tilted Eocene to Miocene units, has been incised by about 317 m with respect to the local base level at the NTT (Landgraf et al., 2009). This indicates significant dip-slip motion along this fault. The paleo-pediment abuts the rising mountains along the Mosha-Fasham fault (MFF), suggesting that it was the active mountain front at the time of deposition. Thus, dating of the abandonment of the paleo-pediment allows estimation of the timing of incision, which might be related to focused tectonism along the NTT. The gravels covering the pediment surface are recycled monomictic deposits of the Paleocene (?) Fajan conglomerate (Assereto, 1966), comprising sandstone, quartzite, limestone, and dolomite.

We sampled boulders of more than 1 m in diameter (Fig. 5.14) and analyzed them for cosmogenic $^{10}Be$ and $^{26}Al$. In this case inheritance may be negligible, because of a very short transportation pathway.

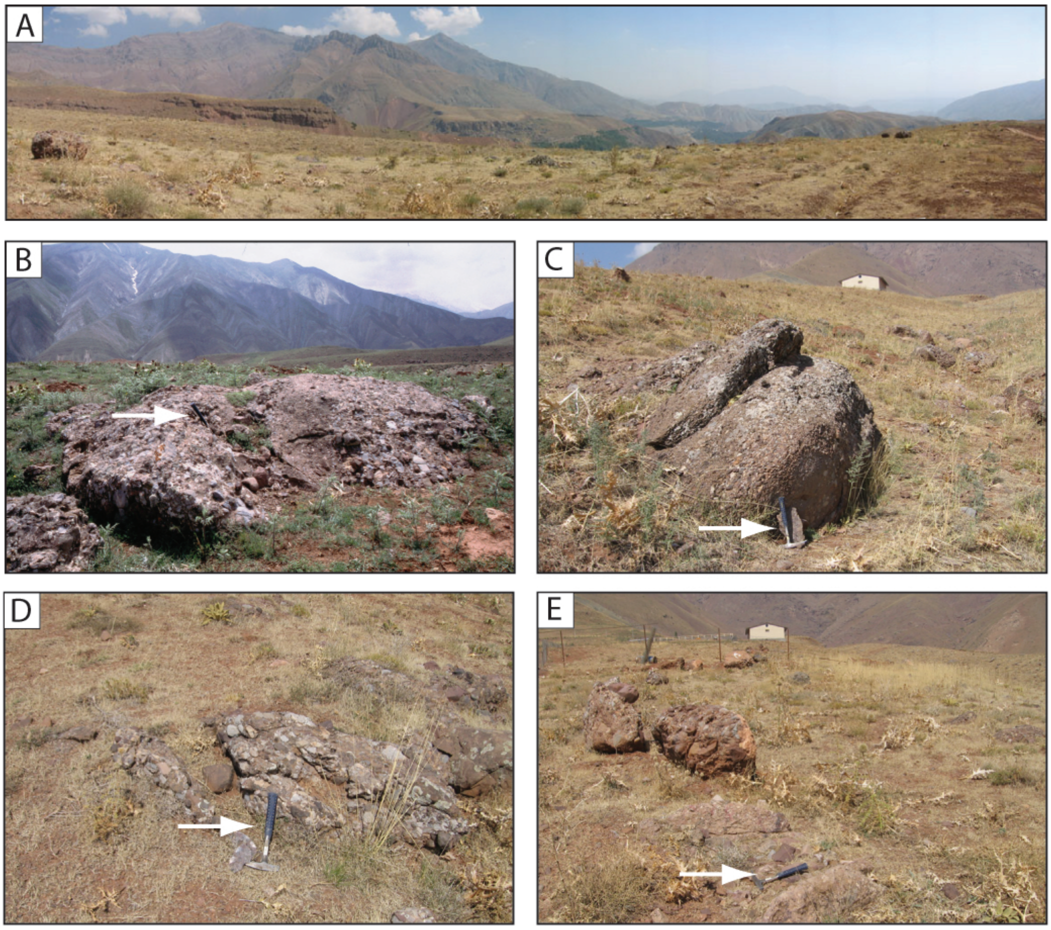

Figure 5.14: (A) Extensive abandoned gravel-covered pediment surface at Rahad Abad (about 25 km NE of Tehran), view ENE. Note the scattered rounded boulders. (B to E) Boulder samples, hammer for scale on all photos (white arrows). Note the different height of boulder burial. (B) Sample 16-6 was collected from the surface of a boulder more than 2 m in diameter, with a surface elevated more than 60 cm above the ground. (D) Sample 29-1-3 and (E) Sample 29-1-4 are partially embedded in the soil; (C) Sample 29-1-2; here, a 2-cm-thick slab that was spalled off and collected at hammer location, thus partly self-shielded. This boulder is furthermore located in a gentle depression.

### Fluvial and bedrock (strath) terraces at Afjeh valley entrance (east of Tehran)

Discontinuous remnants of a fluvial terrace are exposed along the Afjeh valley. At the valley entrance, this terrace abuts pervasively fractured bedrock and records repeated transtensional deformation, manifested in striated clasts and clay, as well as fanning colluvial wedges with decreasing dip angles upsection (Fig. 5.15E). Downstream of this fault zone, an undeformed sand lens was sampled for OSL dating. Samples (26-2-1 and 26-2-2) were taken at the same height about 50 cm below a 50 cm-thick debris flow unit and about seven meters below the terrace surface. Given the relatively steep southward dip of the strata, even more sediment could have been deposited before terrace abandonment. After incising through this terrace, the Afjeh channel began incising a dioritic sill, which has produced a spectacular bedrock channel. Two strath terraces formed at about 5 and 1.70 m above the recent channel

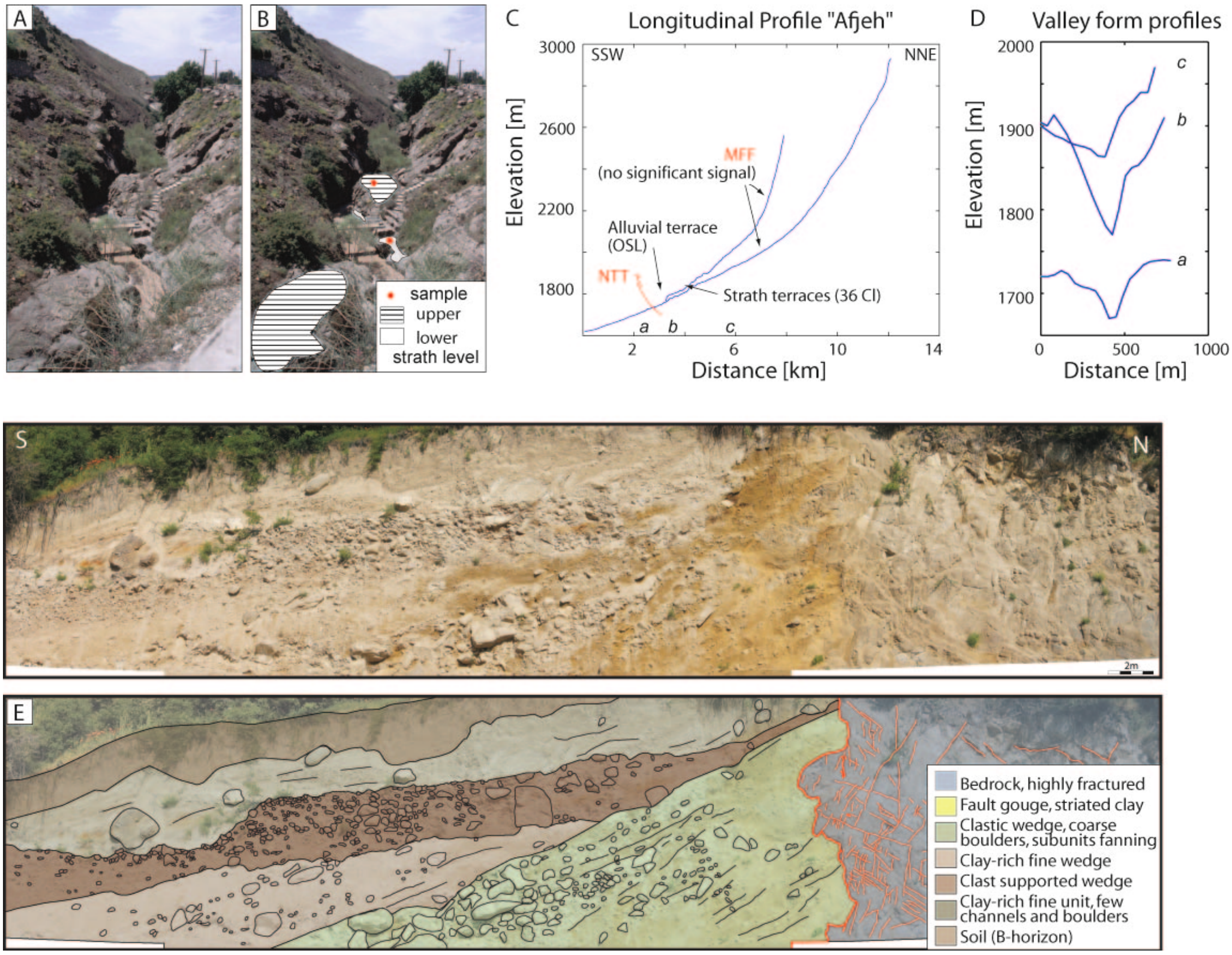

Figure 5.15: Bedrock channel incision of the Afjeh River in a dioritic dyke. (A and B) Overview with two strath levels (sketched on B), view towards south. Colored sectors show upper strath surface (patched) and lower strath surface (white) with sampling locations (star). Water table (spring 2005) is about 80 cm above the channel bed. (C) Longitudinal river profile with knickpoint, where the bedrock channels have developed. (D) Across-valley profiles (a to c) in foot and hanging walls of NTT. Note the narrow valley at the mountain front and valley widening in the hanging wall farther upstream. Profile locations are labeled in (C). (E) Quaternary normal faulting in alluvial-fan deposits at the Afjeh valley entrance, view towards W. Karaj Formation (gray) is pervasively fractured (red lines). The north dipping low-angle fractures are associated with dip-slip reverse motion. The subvertical fractures are associated with strike-slip and dip-slip normal motion (northern block up). The wedge geometry (note decreasing strata dip-angles) of the sedimentary units suggests a complex interplay between repeated earthquakes and footwall erosion.

(Fig. 5.15 A, B). These strath surfaces were sampled and plagioclase was separated for TCN dating using $^{36}Cl$. This transient incision event also coincides with a knickpoint in the Afjeh longitudinal profile (Fig. 5.15 C).

### Paleo-pediment at Saboo-e-Bozorg (east of Tehran)

Four generations of abandoned surfaces, at increasingly lower elevations and decreasing degree of incision towards the west characterize the Latyan basin (Landgraf et al., 2009). The lowest surface is inferred to correlate with the fluvial terrace in the hanging wall of the NTT at the Afjeh valley entrance, which was dated by OSL. Furthermore, it is striking that the surfaces (from old to young) dip mostly towards the southwest, while the drainages are transverse and more or less north-south directed (Fig. 5.16A, B). The southwest dip of the surfaces does not necessarily coincide with strike and dip of the underlying strata, suggesting repeated deformation under changing tectonic boundary conditions. While the western drainages are connected to the hinterland, the central and eastern drainages have their catchments in the uplifted basin itself, and hinterland drainages are deflected. The two higher paleo-surfaces were thus tapped from the foreland and beheaded from hinterland contributing areas. An east-west striking, vertical splay fault dissects the basin. This fault was originally a dip-slip fault, but was reactivated as a left-lateral strike-slip fault (Landgraf et al., 2009). It is interesting to note that boulders derived from the Fajan conglomerate stick out from the highest surface and the ridge crest developed in unit A. However, those boulders, while generally more than a meter in diameter, occur only as isolated individuals. This could suggest that they might have been transported from the paleo-pediment, in which case they could be significantly younger. Today, outcrops of the Fajan conglomerate can be found in the hanging wall of the Mosha-Fasham Fault, but also in the Latyan anticline, south of the basin. Another, yet more instructive occurrence of such boulders can be found in a beheaded channel between the Kond valley and the dioritic sill (Fig. 5.16B). The drainage area of this channel is exclusively in the diorite and Eocene shale units and is very small. However, the trace of the boulders seems to lead to a windgap towards the Kond valley. This suggests that there has been a previous connectivity with the Kond valley and thus to the paleo-pediment at Rahad Abad, before the channel was diverted and started to incise the much less erodible bedrock. Alternatively, both channels might have been active at the same time. In any case, connectivity must have existed after deposition of the youngest terrace, because the conglomerate-bearing channel is slightly incised into it.

A structural model explaining the Latyan basin thus needs to incorporate these observations. Such a model must include the oblique-normal faulting along the NTT, westward rejuvenation of the embedded surfaces, and their pronounced southwestern dip. Here, we present three models, which can alternatively satisfy those observations (Fig. 5.16a to c). The first model (a) has been proposed by Landgraf et al. (2009). The horsetail termination of predominantly strike-slip motion along the NTT causes footwall extension with opening of small graben, displacing Quaternary units. Several deeply incised channels, steep slope breaks, or paleo-valleys, sometimes internally drained, seem to reflect such graben structures. However, structural evidence for normal faulting has been observed along the mountain front rather than inside the Latyan basin. Alternatively, the Latyan basin could comprise a relay, or strike-slip ramp (e.g., Peacock & Sanderson, 1991, 1995; Densmore et al., 2003; Di Bucci et al., 2006) between an inboard fault (NTT) and an outboard fault (Latyan fault after Landgraf et al. (2009), Fig. 5.16b). The zone of overlap and separation, i.e., the relay zone, would comprise the Latyan basin. The bedding here is re-oriented in order to accommodate the component of vertical displacement between the faults. Thus, the geometry of the in-

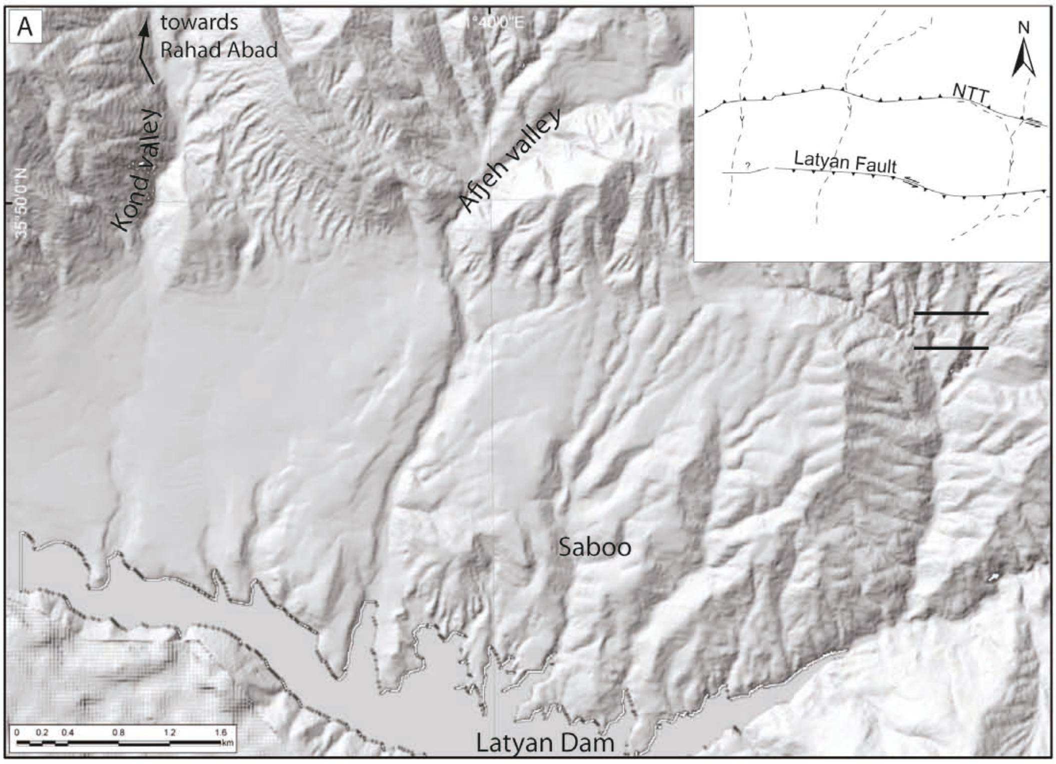
A
towards
Rahad Abad
Kond valley
Afjeh valley
35°50'0"N
1°40'0"E
Saboo
Latyan Dam
0 0.2 0.4 0.8 1.2 1.6 km
N
NTT
?
Latyan Fault

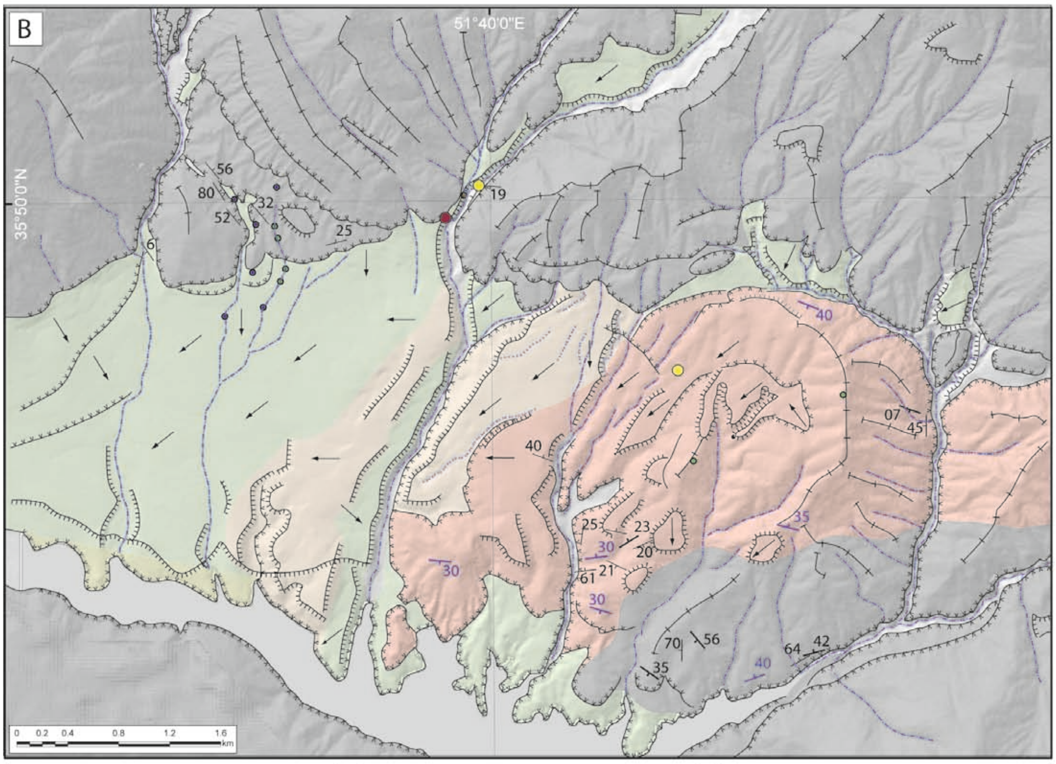
B
51°40'0"E
35°50'0"N
56
80
52
32
25
6
19
40
07
45
40
35
25
23
30
20
61
21
30
30
70
56
35
64
42
40
0 0.2 0.4 0.8 1.2 1.6 km

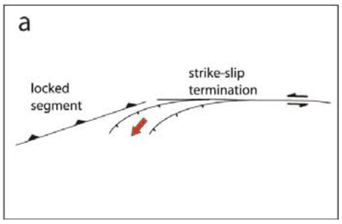
a
locked segment
strike-slip termination

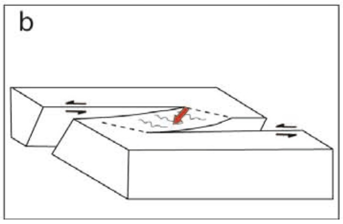
b

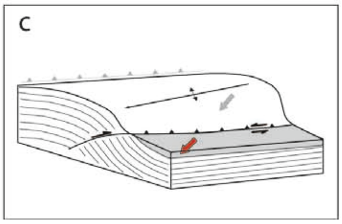
c

Figure 5.16: Geomorphic mapping of the Latyan basin and surroundings and structural models. (A) Hillshade from 10m-DEM with labels of localities; inset: fault configuration for the same frame, dashed lines correspond to major rivers. Black horizontal lines depict locations of topographic profiles of Fig. 5.13. (B) Geomorphic mapping (legend as 5.8). Yellow circles depict TCN samples and red circle OSL samples; green circles are locations of Fajan conglomerate boulders as redeposited on the Rahad Abad paleo-pediment; blue circles are locations of polymictic pebbles, with provenance from the Kond or Afjeh valleys, which represent terrace remnants and/or beheaded channels. This area thus probably repesents a wind gap between the Kond valley and the Latyan basin. (a) Model, explaining the Latyan basin as result of a horsetail termination of predominantly strike-slip motion along the NTT, after Landgraf et al. (2009). (b) Strike-slip (or relay) ramp between NTT and Latyan fault causes reorientation and southwestward inclination of the Latyan basin. (c) Westward plunging hanging-wall anticline related to NTT motion underlies the basin. The position above the southern limb and the deformation gradient from east to west causes southwestward inclination of the Latyan basin surfaces.

corporated faults would result in the observed southwestern dip of the surfaces between the fault tips. In the third model the Latyan basin is the southern limb of a westward plunging anticline, a hanging-wall anticline, related to motion along the NTT. This model could also explain the southwestern inclination of the basin slopes and the wedging of sedimentary units in the Afjeh valley, which then could reflect forelimb rotation.

The four low-relief surfaces observed in the Latyan basin are erosional surfaces, carved into the underlying strata of different alluvial units (Fig. 5.16B). As such, they represent markers of the former regional base level. Thus, while the erosion surfaces themselves must have formed during periods of protracted tectonic quiescence, their current position and age can help determine when and at which rates subsequent tilting and uplift above the present-day base level has occurred.

We sampled the second-highest pediment surface near Saboo-e-Bozorg for TCN depth-profiles of the nuclides $^{36}Cl$ and $^{10}Be$ (Fig. 5.17). This, as well as the highest surface is beheaded from hinterland drainages, which are deflected eastward around the Latyan "ramp structure". The surface is extensive, has a low relief and sparse vegetation. Presently cultivated areas were avoided. Agricultural activity in this area is limited to tree plantations and soil cultivation generally only affects the uppermost 30 cm.

### Jajrud, fluvial terraces (east of Tehran)

This site comprises a virtually undeformed Quaternary fluvial terrace system of the Jajrud river, about five kilometers downstream of the Latyan basin. Terrace conglomerates are onlapping onto tilted alluvial deposits of inferred Mio-Pliocene age (unit A) and are inset in the E-W trending Latyan anticline (compare Fig. 5.18 A). The upper terrace is incised by about 81 m, the lower by about 49 m. From their geomorphic expression, the equal diffusion, and the virtual lack of an onlap in the perpendicular profile, we interpret the lower terrace to be a strath of the upper terrace. The ages of these terraces can be used to determine the

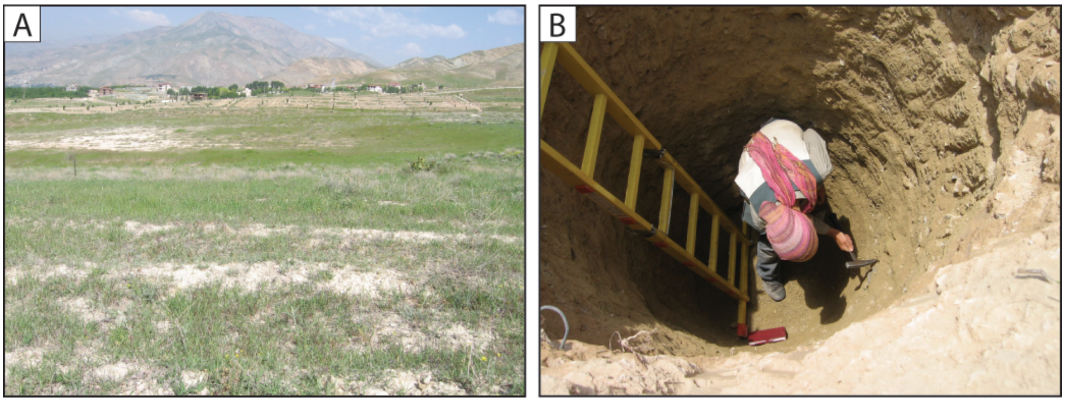

Figure 5.17: Extensive and moderately dissected pediment surface at Saboo. (A) NW-view from sampling pit across surface. Note the sparse vegetation. (B) Sampling pit (3 m deep and approximately 2 m in diameter). Profiles were sampled for different grain/clast sizes for $^{10}Be$ and $^{36}Cl$ analysis.

timing of incision by the Jajrud river, which in turn can be compared with the upstream rates of tributary incision by the Kond and Afjeh channels. Furthermore, because the subhorizontal terraces are nested inside the Latyan anticline, this structure has not been folded significantly after abandonment of these terraces.

Both terraces constitute flat, low-relief surfaces with sparse vegetation and virtually no shielding. Riser diffusion between the upper and lower surface can be observed, but is limited in extent. We have avoided this area when sampling the lower terrace. We have sampled both terraces for TCN depth-profiles of the nuclides $^{36}Cl$ and $^{10}Be$ (Fig. 5.18).

## 5.4 Dating results

In all cases, where we obtained data from surface samples and depth profiles their concentrations were offset significantly, with lower surface concentrations compared to the extrapolated depth profiles (Fig. 5.19). This suggests that processes that influence the nuclide concentrations, such as erosion, shielding, or pre-exposure, might differ between surface and depth samples. Additionally, soil mixing may have disturbed the concentrations in the upper part of the profile, including the surface sample. In order to understand nuclide-accumulation during time and the effect of erosion on the calculated exposure age, we first used the site-specific production rate to calculate the theoretical nuclide concentrations over time for a range of erosion rates (Fig. 5.20 and 5.21). We then used Chi$^2$-inversion to search for the minimum misfit between a theoretical and the real profile for a range of exposure ages and erosion rates (Ritz et al., 2006b), and Chi$^2$-minimizing (e.g., Siame et al., 2004; Ritz et al., 2006b; Braucher et al., 2009) to fit the profiles (allowing exposure age, erosion rate, and inheritance as unknown variables).

The $^{10}Be$ profile from the Kan river site shows a significant break between the surface sample concentrations and the depth samples (Fig. 5.19E). There is no possible solution to fit all the samples together. Because the lithologic profile shows a debris flow deposit above

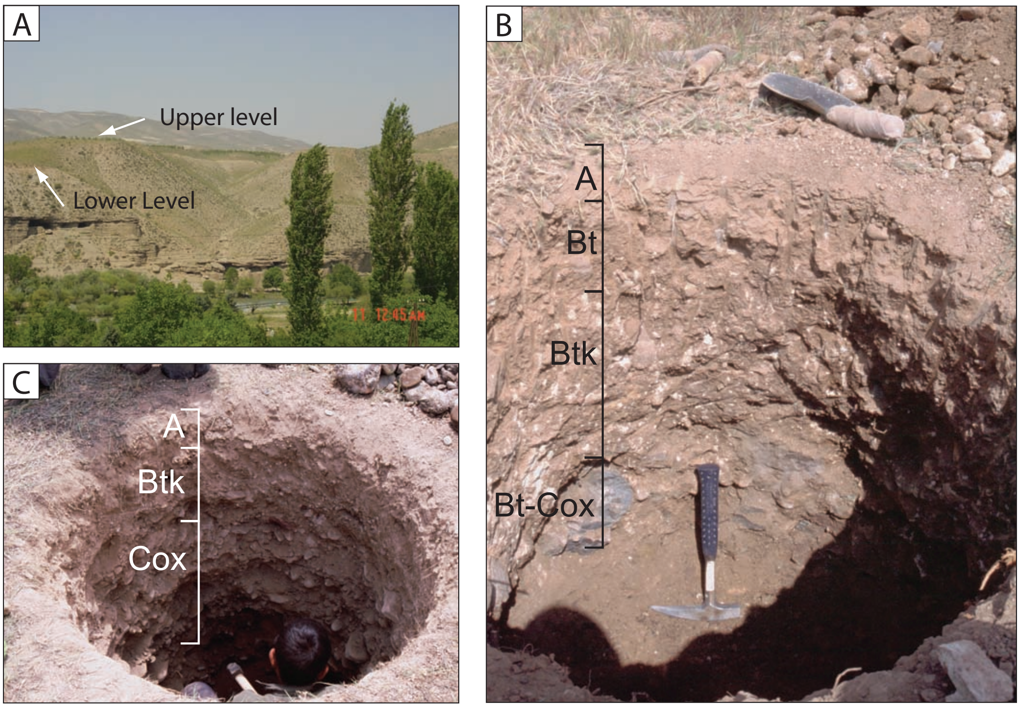

Figure 5.18: (A) Fluvial terraces of Jajrud river, view towards WSW. Lower level is interpreted to be a strath of the upper level. (B) View into sample pit of the lower terrace. Note the reddish, clay-rich soil and white pedogenic carbonate nodules. Soil was so consolidated that workers stopped digging at a depth of one meter. (C) Upper part of sample pit of the upper terrace. Profile shows less matrix and higher clast content. Pedogenic carbonate is also present.

the fluvial intercalations at about 1 m depth, which coincides with the uppermost depth profile sample, we have considered the surface sample as belonging to a second (younger) deposit and fit the remaining depth-samples by Chi$^2$-minimizing. The Chi$^2$-inversion reveals a minimum misfit at 275 ka and about 3 m/Ma erosion (Fig. 5.22). The resulting Chi$^2$-minimizing solution reveals a best fit at an age of 266 ka, with 2.8 m/Ma erosion, and no inheritance (Chi$^2$ 1.03), in good agreement with the inversion (Table C.10). Changing inheritance to the value measured in the recent Kan channel and solving for age and erosion, degrades the misfit to 5.4 and changes the exposure age to 135.3 ka without erosion. The surface samples reveal zero-erosion ages of 25.1 ± 1.9 (pea-sized clasts) and 31.1 ± 2.9 ka (pebbles), respectively (Table C.4).

The $^{10}Be$ depth profile of the National Library site reveals a step between samples 29-2-5 and 29-2-6, i.e., between 1.20 m and 1.50 m depth. Nuclide concentrations follow an exponential decrease from top to 1.20 m depth, then increase at 1.50 m, and decrease again exponentially towards the bottom of the profile. While no lithologic change was recognized in the profile (Fig. 5.19B), the concentrations could be interpreted as two deposits. Alternatively, the lower samples have higher inherited concentrations. The Chi$^2$-inversion shows a vertical trend, parallel to the time axes, suggesting steady-state conditions (Ritz et al., 2006b) at an erosion rate of about 20 m/Ma for the one-deposit scenario (Fig. 5.22). We thus calculated the maximum denudation rate and effective age after Lal (1991), which are

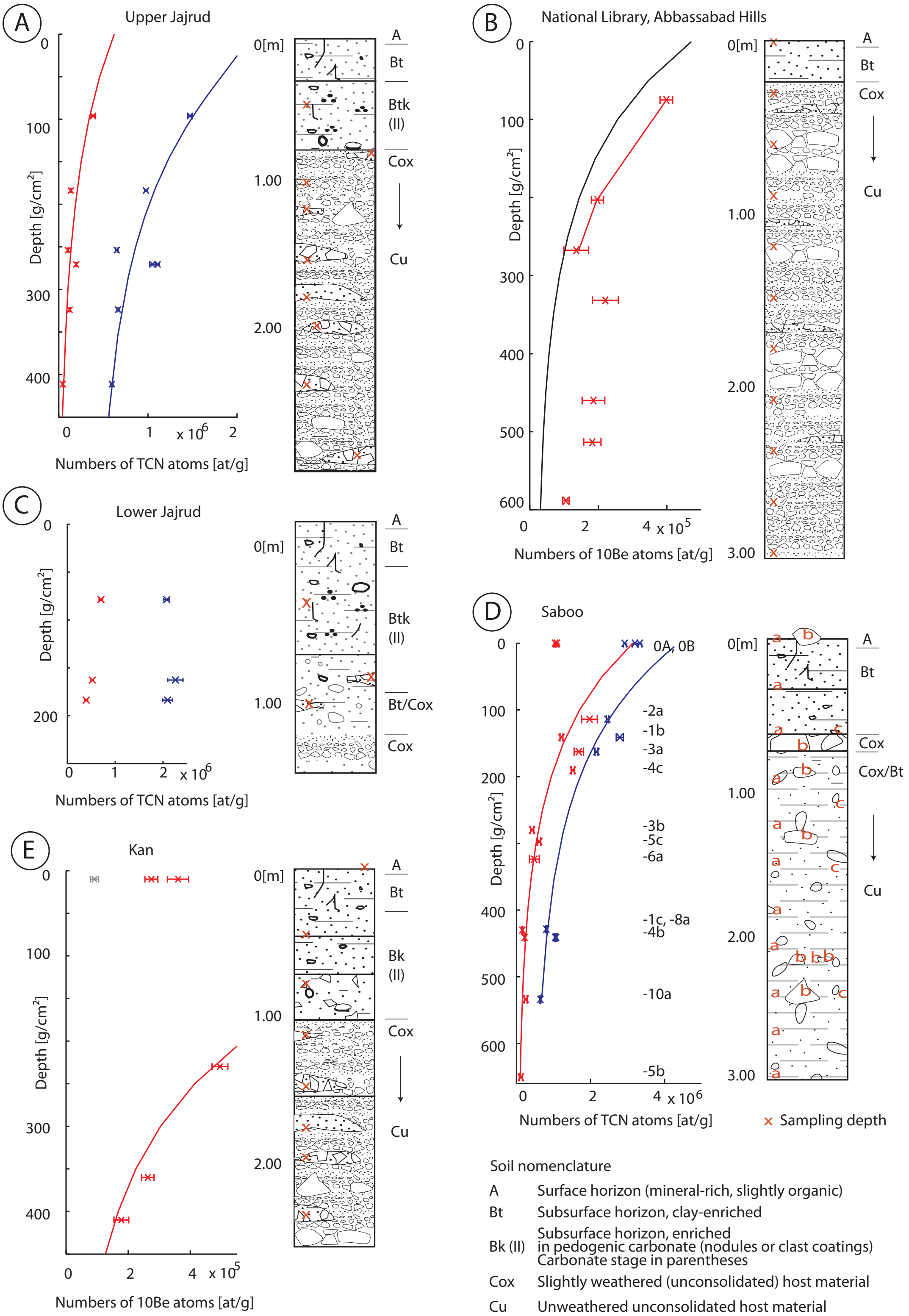

Soil nomenclature

| | |
|---|---|
| A | Surface horizon (mineral-rich, slightly organic) |
| Bt | Subsurface horizon, clay-enriched |
| Bk (II) | Subsurface horizon, enriched in pedogenic carbonate (nodules or clast coatings) Carbonate stage in parentheses |
| Cox | Slightly weathered (unconsolidated) host material |
| Cu | Unweathered unconsolidated host material |

Figure 5.19: Fitted depth profiles, soil-profile descriptions (A-E) and corresponding shielding plots (a to e). $^{36}$Cl data are plotted in blue and $^{10}$Be data in red. (A) Jajrud, upper terrace. $^{36}$Cl and $^{10}$Be data with theoretical profiles of the best-fit solution. (B) National Library, Tehran. $^{10}$Be data. This terrace is in steady state; black profile corresponds to minimum age with corresponding erosion rate. Note that despite lack of visible lithological changes, the depth profile could also be interpreted in terms of two deposits (uppermost fitted). (C) Jajrud, lower terrace, interpreted to be strath of upper Jajrud (A, compare also Fig. 5.18 A). All samples and both nuclides have a higher concentration than the upper Jajrud profile. (D) Saboo. $^{36}$Cl and $^{10}$Be data of different sampling strategies. A-profile contains sand-size fraction, including matrix, but also small clasts. B-profile corresponds to separately sampled cobbles and small boulders, and C-profile corresponds to pea- to pebble-sized clasts. Note offset between surface samples and profile fits. (E) Kan. $^{10}$Be data and fit. Note the offset between surface samples (red) and profile fit. Gray "surface" age corresponds to active channel and might reflect effects of inherited nuclide concentration. Note also the significant change in the soil-profile with transition between fluvial intercalations and alluvial/debris-flow deposits on top.

21.2 m/Ma and 96.4 ka, respectively (Table C.10). When modeling the two-deposit scenario, the best fit of the upper (younger) deposit results in an age of 173.2 ka with an associated erosion rate of 15.2 m/Ma. With these conditions, the concentrations are already saturated (Fig. 5.20D).

The boulder samples from Rahad Abad reveal apparent (zero erosion) ages between about 14 and 64 ka using $^{10}$Be, and between 14 and 57 ka using $^{26}$Al (Table C.4). The spread of ages might suggest that post-depositional processes play a significant role. The associated maximum denudation rates for the boulders are between 11 m/Ma for the oldest and 53 m/Ma for the youngest boulder (Table C.9). Comparing these results with the theoretical nuclide accumulation for the Rahad Abad site (Fig. 5.20A and B), all of the samples have reached saturated concentrations. Thus, we calculated the effective ages after Lal (1991), which are 258.5, 116.4, 110.7, and 53.8 ka, respectively (Table C.9). Moreover, the calculated erosion island diagram reveals a complex exposure history for this site(Fig. 5.20 B).

Optically stimulated luminescence dating on quartz grains from the Afjeh alluvial terrace was carried out at the Sheffield Centre for International Drylands Research (SCIDR) luminescence laboratory. The two samples from a silt layer approximately seven meters below the top of the terrace yield ages of 36.7 ± 4 ka and 30.5 ± 1.9 ka, respectively. The exposure times of the strath terraces cut into the dioritic sill have been determined with $^{36}Cl$ in plagioclase. They revealed Holocene ages of 3.3 ± 0.4 ka for the 5 m-high terrace and 1.6 ± 0.2 ka for the 1.70 m-high terrace.

The second highest erosional surface on the Latyan ramp at Saboo has a minimum misfit at 200 ka, when plotting all $^{10}Be$ data from the three profiles together. This best-fit age is achieved without inheritance and with only limited (0.29 m/Ma) denudation (Fig. 5.22). The Chi$^2$-minimizing, allowing also to solve for inheritance, revealed a similar result, with an age of 195.1 ka and neither erosion or inheritance (Chi$^2$ of 257, Table C.10). The Chi$^2$-

inversion of the $^{36}Cl$ profile shows a vertical trend parallel to the time-axis, thus indicating steady-state concentrations. However, the misfit decreases when incorporating inheritance, but ages and erosion rates vary beyond control and show no correlation with the $^{10}Be$ age. While it is possible that both nuclides, whose source is an amalgamated sample, provide different inheritance, the shorter half-life of $^{36}Cl$ and the variability in the ages lead us to accept the steady-state condition of the $^{36}Cl$ profile.

Finally, the Jajrud terraces are somewhat problematic. The Chi$^2$-inversion of the $^{10}Be$ profile from the upper terrace reveals an age of about 135 ka, without inheritance, but a high erosion rate of about 23 m/Ma (Fig. 5.22). Comparing this with the theoretical accumulation (Fig. 5.20 E, dotted lines), such high erosion will bring $^{10}Be$-concentrations into saturation already after about 100 ka. The Chi$^2$-inversion, however, shows a distinct minimum. Furthermore, Chi$^2$-minimizing reveals an exposure age of about 40.2 ka, without denudation and some inherited concentration of 15,319 atms/g (Table C.10). The Chi$^2$-inversion of the $^{36}Cl$ profile shows a vertical trend parallel to the time-axis, thus indicating steady-state concentrations. However, solutions for about 40 ka exist with reasonable Chi$^2$ values. The concentrations of both nuclides of the lower terrace (only three samples) are significantly higher than at the upper terrace. Even the lowest sample at 1-m depth, still yields a concentration, slightly higher than the uppermost sample of the upper terrace (see discussion). Chi$^2$-inversion shows steady state for $^{10}Be$, but yields an age of 55 ka for $^{36}Cl$. These are unreasonable solutions, because $^{36}Cl$ has the shorter half-life and reaches steady-state earlier. However, solving for exhumation age, erosion rate, and inheritance using Chi$^2$-minimizing a solution exists with no erosion, small inherited concentration and about 60 ka of exposure for $^{10}Be$ and no erosion, small inheritance, and 70 ka for $^{36}Cl$ (Table C.10). While it might be arbitrary to accept the Chi$^2$-minimizing solution for the lower, but the inversion-solution for the upper terrace, this scenario would provide a meaningful result considering stratigraphy and concentrations. In this case, the lower terrace might be "shielded" from wind deflation by its position below the upper terrace.

## 5.5 Discussion

In the following section, we first discuss factors possibly influencing the ambiguity of the TCN results at some sites, as the varying erosion rates and exposure ages using different nuclides, as well as the observed offsets between surface samples and depth profiles. We will focus this discussion in the light of geomorphic factors as well as the context of analytical factors and sample chemistry. This is followed by a general discussion about the application of the dating results for the Tehran plain and implications for the deformation history and landscape evolution.

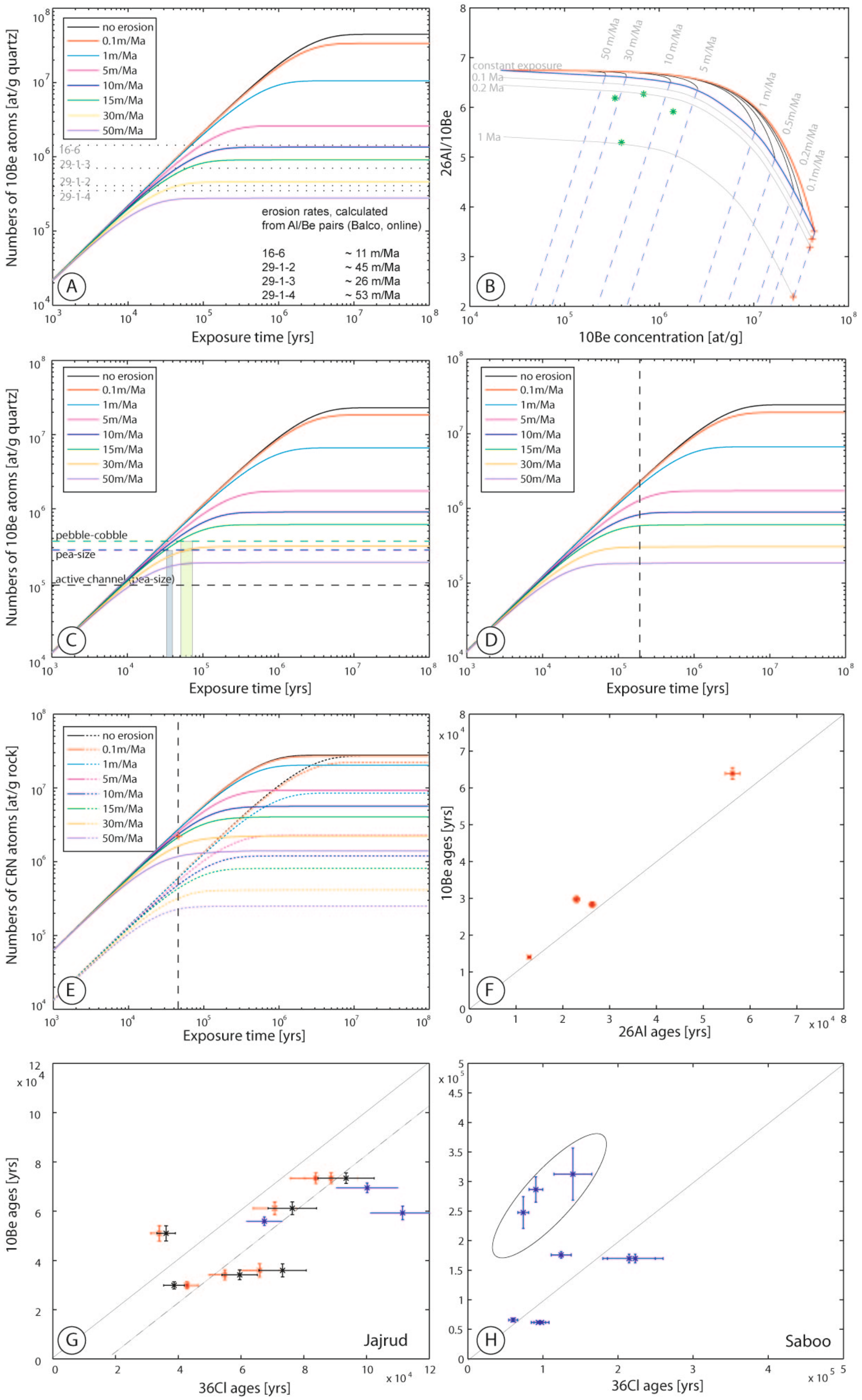
A
Numbers of 10Be atoms [at/g quartz]
Exposure time [yrs]
no erosion
0.1m/Ma
1m/Ma
5m/Ma
10m/Ma
15m/Ma
30m/Ma
50m/Ma
16-6
29-1-3
29-1-2
29-1-4
erosion rates, calculated
from Al/Be pairs (Balco, online)
16-6 ~ 11 m/Ma
29-1-2 ~ 45 m/Ma
29-1-3 ~ 26 m/Ma
29-1-4 ~ 53 m/Ma
B
26Al/10Be
10Be concentration [at/g]
constant exposure
0.1 Ma
0.2 Ma
1 Ma
50 m/Ma
30 m/Ma
10 m/Ma
5 m/Ma
1 m/Ma
0.5m/Ma
0.2m/Ma
0.1m/Ma
C
pebble-cobble
pea-size
active channel (pea-size)
D
E
Numbers of CRN atoms [at/g rock]
F
10Be ages [yrs]
26Al ages [yrs]
G
Jajrud
36Cl ages [yrs]
H
Saboo

Figure 5.20: Effect of erosion and burial on exposure at different sites. (A) Theoretical $^{10}$Be accumulation with time and different erosion rates at Rahad Abad site. Higher erosion rates result in earlier saturation with lower concentrations. Horizontal lines show Be concentration of boulder samples. Comparison with erosion rates calculated from $^{26}$Al/$^{10}$Be pairs (Balco et al., 2008) shows that virtually all samples have reached steady state. (B) Erosion-island plot of the $^{26}$Al/$^{10}$Be pairs at Rahad Abad. All ratios plot below the simple erosion island, suggesting temporal burial for a period longer than 0.2 million years. The lowest ratio, however, rather corresponds to an erosional spalling event. (C) Theoretical $^{10}$Be accumulation at Kan site. Horizontal lines show Be concentration of amalgamated pea-sized and cobble samples, and of the active channel. Assuming a mean erosion rate between 15 and 20 m/Ma, this concentration corresponds to ages of 30-40 or 50-70 ka, respectively, as indicated by the rectangles. (D) Theoretical $^{10}$Be accumulation at the National Library site in Tehran. No surface sample is available, but the vertical line shows minimum age as calculated from the depth profile. The nuclide concentrations on this terrace have reached steady state. (E) Theoretical $^{10}$Be (dotted) and $^{36}$Cl (solid) accumulation at Jajrud (upper terrace). The $^{36}$Cl concentrations are dependent on composition. Here, we calculated based on the composition of the uppermost sample (13-1-1). However, with the exception of 13-1-3 composition does not vary significantly. Red star and cross denote calculated surface concentration of $^{36}$Cl and $^{10}$Be, respectively. (F) Comparison between (apparent) $^{26}$Al and $^{10}$Be zero erosion ages at Rahad Abad. The diagonal solid line indicates complete agreement between ages. (G) Comparison between (apparent) $^{36}$Cl and $^{10}$Be zero erosion ages at Jajrud (red and black for upper Jajrud, corresponding to leached and bulk chemistry, respectively, and blue for lower Jajrud terrace). (H) Zero erosion ages at Saboo. Ellipse corresponds to A-profile (sand-size) and is offset. Profile follows a steeper trend than the concordance line, while samples from B-profile and surface are closer to agreement between ages. See Tables C.3 and C.4 for zero erosion ages.

### 5.5.1 Discussion of the TCN results

#### Geomorphological factors

To better understand our new data in the geomorphological context, we calculated the Chi$^2$-inversion of the depth profiles, plots of the (apparent) zero-erosion ages of the different isotope pairs, as well as erosion island diagrams (Figs. 5.20 F-H, 5.22, 5.23, and 5.24).

We performed the Chi$^2$-inversion (e.g., Ritz et al., 2006b) of the depth profiles to test the significance of one model or profile fit versus another. Because of the large scatter of depth samples with respect to the theoretical model, their variable analytical error, and generally small sample numbers with respect to unknown parameters, i.e., exposure age, erosion, and inheritance, the Chi$^2$ values are generally very high and the significance of the results is statistically hard to ascertain. Because the $^{36}$Cl concentrations are in saturation, maximum denudation rates can be calculated (e.g., Gosse & Phillips, 2001) and are 9.14 m/Ma for Saboo, and 19.7 m/Ma for Upper Jajrud. The relatively high denudation rate for Jajrud roughly agrees with the rate derived from the $^{10}$Be inversion of the same profile, which is 22.86 m/Ma. It is also compatible with the rate derived from the steady-state $^{10}$Be-profile of the National Library site, which is 20.3 m/Ma (Fig. 5.22). For Saboo, however, there is a discrepancy between the denudation rate derived from the $^{36}$Cl (9.14 m/Ma) and $^{10}$Be (0.29 m/Ma) nuclides, respectively. This is visible in the profile fit, but also in the single nuclide

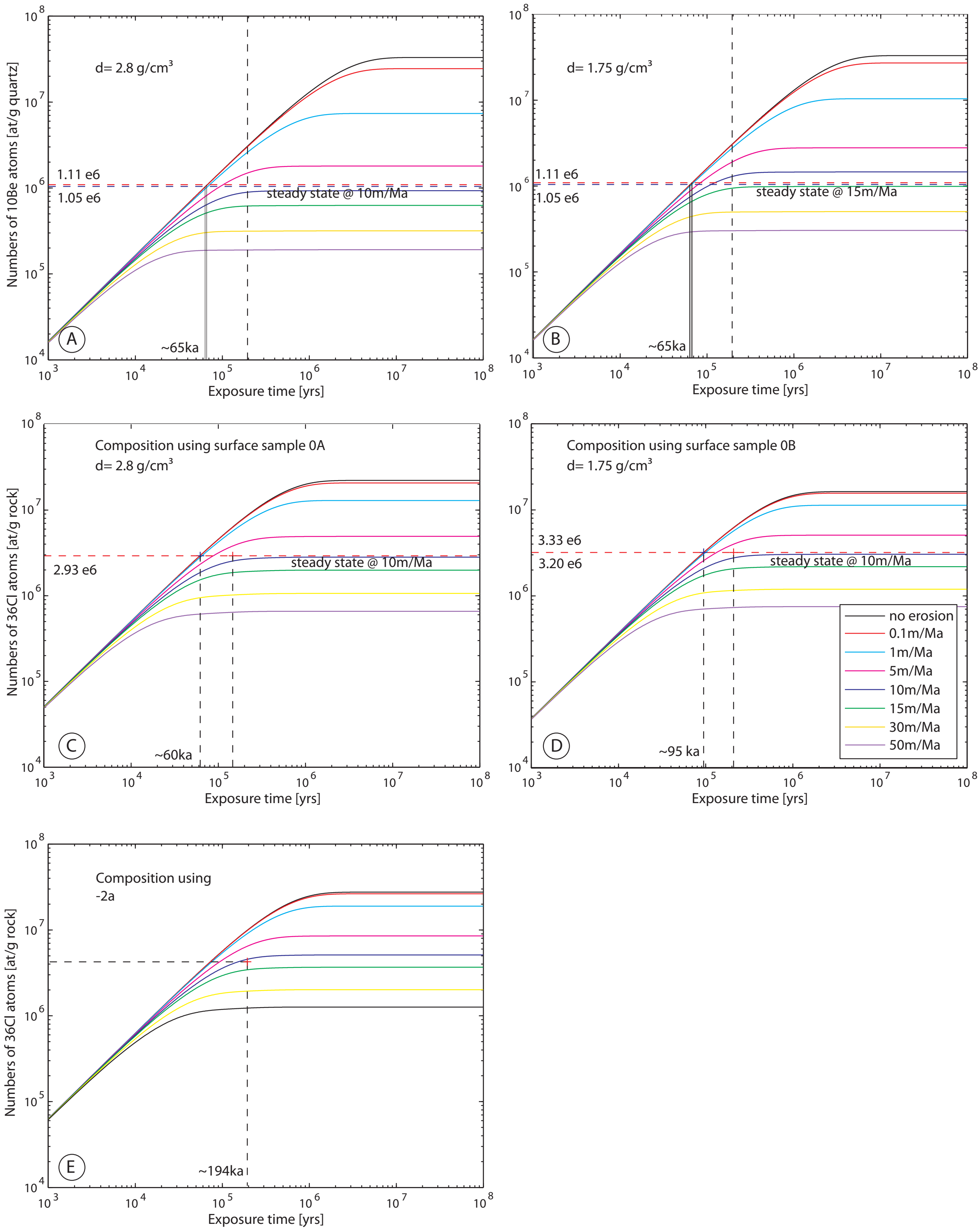
A
d= 2.8 g/cm³
1.11 e6
1.05 e6
steady state @ 10m/Ma
~65ka
Numbers of 10Be atoms [at/g quartz]
Exposure time [yrs]
B
d= 1.75 g/cm³
1.11 e6
1.05 e6
steady state @ 15m/Ma
~65ka
Exposure time [yrs]
C
Composition using surface sample 0A
d= 2.8 g/cm³
2.93 e6
steady state @ 10m/Ma
~60ka
Numbers of 36Cl atoms [at/g rock]
Exposure time [yrs]
D
Composition using surface sample 0B
d= 1.75 g/cm³
3.33 e6
3.20 e6
steady state @ 10m/Ma
~95 ka
Exposure time [yrs]
no erosion
0.1m/Ma
1m/Ma
5m/Ma
10m/Ma
15m/Ma
30m/Ma
50m/Ma
E
Composition using
-2a
~194ka
Numbers of 36Cl atoms [at/g rock]
Exposure time [yrs]
10^3
10^4
10^5
10^6
10^7
10^8

Figure 5.21: Effect of erosion and burial on exposure ages at Saboo. (A and B) Theoretical $^{10}$Be accumulation through time, with different erosion rates, and different densities of surface samples 0A (cobbles) and 0B (pea-size to pebbles), respectively. For colors see legend in (5.21D). Concentration lines of surface samples show zero erosion ages between 60 and 70 ka, but steady state at 10 and 15 m/Ma (15 m/Ma corresponds to the $^{36}$Cl depth profile fit). (C and D) Theoretical $^{36}$Cl accumulation, considering different density and composition of the same samples as (A and B). Here, zero erosion age of 0A agrees with the Be age, while 0B (incl. replicate) reveals an older Cl age. Both samples are in steady state at 15 m/Ma. (E) Theoretical $^{36}$Cl accumulation for the A-Profile, using composition of sample -2a (Standard deviation of composition-dependent production between samples of this profile is about 3%). Profile fit by chi$^2$-minimizing yielded an exposure time of 177 ka and 15 m/Ma erosion (marked as red star) Note that this position is also very close to steady state.

derived maximum denudation rates of the respective samples (Table C.9). This denudation, however, is considered to be the result of a post-depositional process, i.e. the (steady) removal of fine material from the terrace surface. Thus, all clasts of one amalgamated sample from a certain depth should be subjected to the same denudation, averaged over the sample's residence time inside one nuclide attenuation length, but unaffected by different lithology and cosmogenic nuclides. Because chlorine reaches saturation earlier than beryllium, this is generally considered as being advantageous in two-nuclide studies, i.e. the nuclide in saturation reveals the erosion rate, which then allows one to calculate the exact exposure age of the non-saturated nuclide as a function of the erosion rate (e.g., Gosse & Phillips, 2001). However, applying the higher erosion rate to the beryllium profile and solving for an exposure age will result in an age of about 1.4 Ma, but at a much higher misfit (about 850 instead of 250). Because with higher erosion, the shape of the profile steepens, the theoretical profile fits reasonably well the lower half of the data, but fails to fit the upper half.

What causes these discrepancies? Comparing the trend of zero-erosion ages (Fig. 5.20 G and H) might help understand this issue. If all nuclide-producing processes are considered, and no post-depositional processes occur, the apparent ages of the samples, assuming zero erosion, should be 1:1 and thus plot on the diagonal. If chlorine is in steady-state its concentration is supposed to be relatively smaller than that of beryllium, which is still accumulating. The $^{36}$Cl/$^{10}$Be ratio gets smaller and the zero erosion ages should be offset from the diagonal towards older $^{10}$Be ages. This, however, is only observed for the Saboo-A-profile (the sand-size fraction, ellipse in Fig. 5.20H). Instead, the other Saboo samples (B-profile) generally scatter around the diagonal. The Jajrud samples, however, show a systematic offset towards older chlorine ages, a direction consistent with the effect of post-depositional erosion (e.g., Phillips et al., 1997). The high offset of about 20,000 years, however, might suggest that additional processes need to be considered. Different inheritance between the lithologies, i.e., a higher inheritance of calcite-bearing clasts in this case, but also of some samples inside of one profile could be the reason.

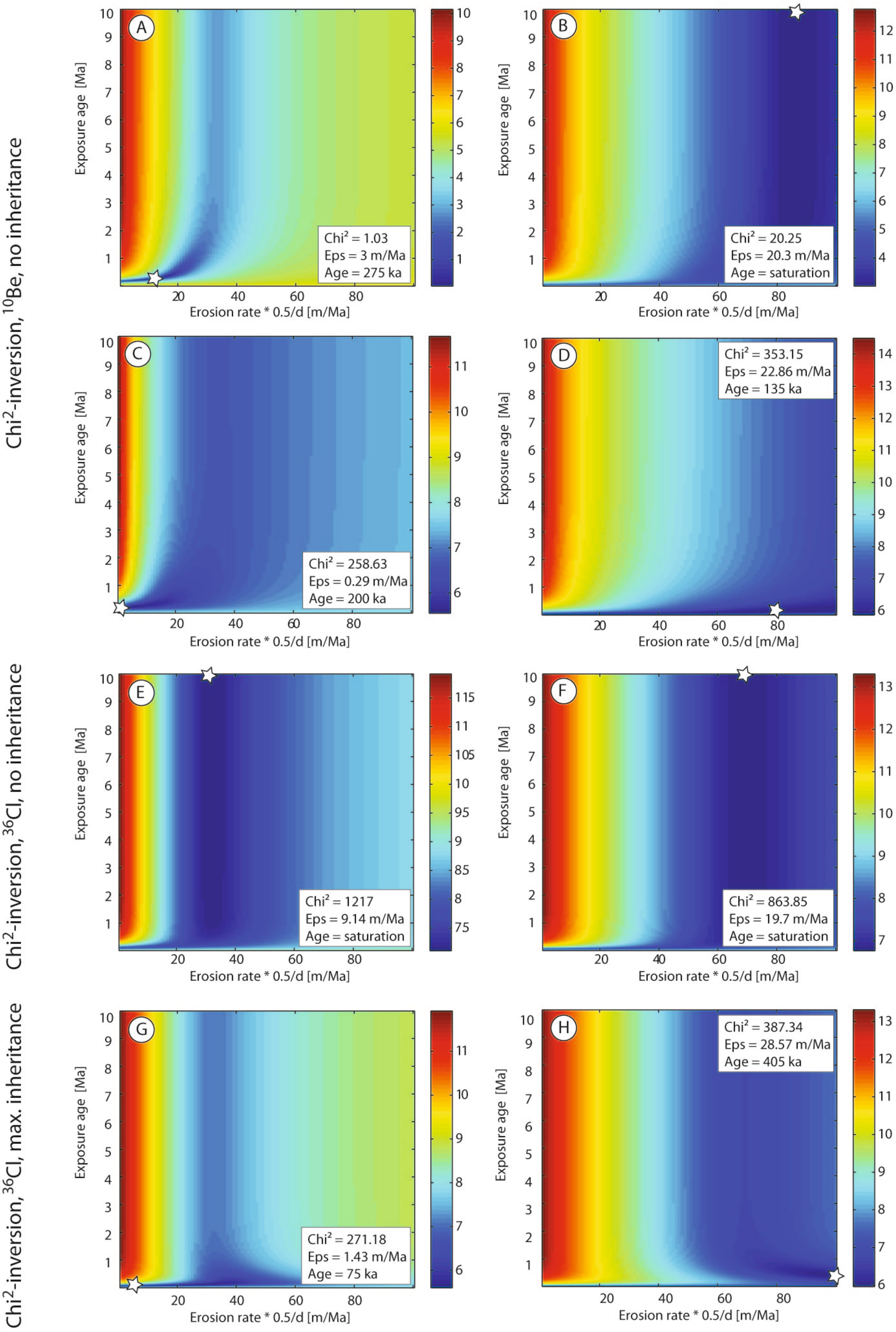
Chi$^2$-inversion, $^{10}$Be, no inheritance
Chi$^2$-inversion, $^{36}$Cl, no inheritance
Chi$^2$-inversion, $^{36}$Cl, max. inheritance
A
Chi$^2$ = 1.03
Eps = 3 m/Ma
Age = 275 ka
B
Chi$^2$ = 20.25
Eps = 20.3 m/Ma
Age = saturation
C
Chi$^2$ = 258.63
Eps = 0.29 m/Ma
Age = 200 ka
D
Chi$^2$ = 353.15
Eps = 22.86 m/Ma
Age = 135 ka
E
Chi$^2$ = 1217
Eps = 9.14 m/Ma
Age = saturation
F
Chi$^2$ = 863.85
Eps = 19.7 m/Ma
Age = saturation
G
Chi$^2$ = 271.18
Eps = 1.43 m/Ma
Age = 75 ka
H
Chi$^2$ = 387.34
Eps = 28.57 m/Ma
Age = 405 ka
Exposure age [Ma]
Erosion rate * 0.5/d [m/Ma]
1 2 3 4 5 6 7 8 9 10
20 40 60 80

Figure 5.22: Results of Chi$^2$-inversion. Star depicts minimum misfit. Eps is erosion rate in m/Ma. (A to D) $^{10}$Be, assuming no inheritance. Chi$^2$ measure of misfit becomes larger when adding inheritance. (A) Kan site. (B) National Library site. The vertical trend parallel to the time axes reflects steady state conditions. (C) Saboo site. (D) Upper Jajrud site. (E and F) Inversion results for $^{36}$Cl, assuming no inheritance. Both profiles reveal saturation and steady-state conditions. (E) Saboo. (F) Upper Jajrud. (G, H) The misfit becomes smaller when applying inheritance to the $^{36}$Cl inversion. Maximum inheritance was assumed to correspond to the concentration of the deepest depth profile sample, which is at three meters for Saboo (G) and at 2.30 m at Upper Jajrud site (H).

While erosion results in a lower nuclide accumulation rate for spallogenic nuclides (because the area of highest production at the surface is continuously detached), for $^{36}$Cl, depending on the rate of erosion, this could result in a higher accumulation rate at the surface, because the thermal neutron production has a maximum at a density-corrected depth of about 40 g/$cm^2$ (Liu et al., 1994). Differences in the bulk chemistry between the samples at different depth might result in different depths and magnitudes of maximum neutron production. Due to the non-spallogenic production pathways of $^{36}$Cl, the usage of this nuclide together with a spallogenic nuclide as $^{10}$Be can help determine both exposure age and erosion rate and to distinguish between simple and complex exposure histories (e.g., Lal, 1991; Liu et al., 1994; Phillips et al., 1997). Erosion island diagrams are used to discriminate such processes. Samples that plot between the zero-erosion line and the saturation line, which is the connection of endpoints of individual erosion rates before steady-state, are assumed to exhibit a simple exposure history with steady or no erosion (e.g., Klein et al., 1986; Kober et al., 2007). However, the usage of chlorine together with beryllium might have a disadvantage at higher exposure ages or lower erosion rates, because ratios at steady-state are reached earlier.

The erosion island plots of the $^{36}$Cl/$^{10}$Be ratios show a simple exposure history for Jajrud (Fig. 5.23), with three samples plotting close to the saturation line and between 10 and 30 m/Ma of erosion, bracketing the erosion rates derived from the Chi$^2$-inversion. Some samples plot in the "forbidden" zone above the saturation line, thus exhibiting some unexpected high nuclide ratios. This might be related to problems in sample preparation or measurement, although we do not deem this likely. It is intriguing that despite the problems with some of the depth samples at Upper Jajrud, the trend of deviation of all concentrations with depth is consistent for both nuclides, i.e., samples that exhibit a lower or higher $^{36}$Cl concentration than expected for their certain position also reveal lower or higher $^{10}$Be concentrations, respectively (Table C.1). Thus, for Jajrud, the physical conditions that the samples were exposed to might have been the same. On the other hand, a different chlorine concentration could also exclusively be related to a different chemical composition and thus production rate, because it is very sensitive to the target element concentration in the sample, but still reveal the expected position in the erosion island or the expected age, because when calculating

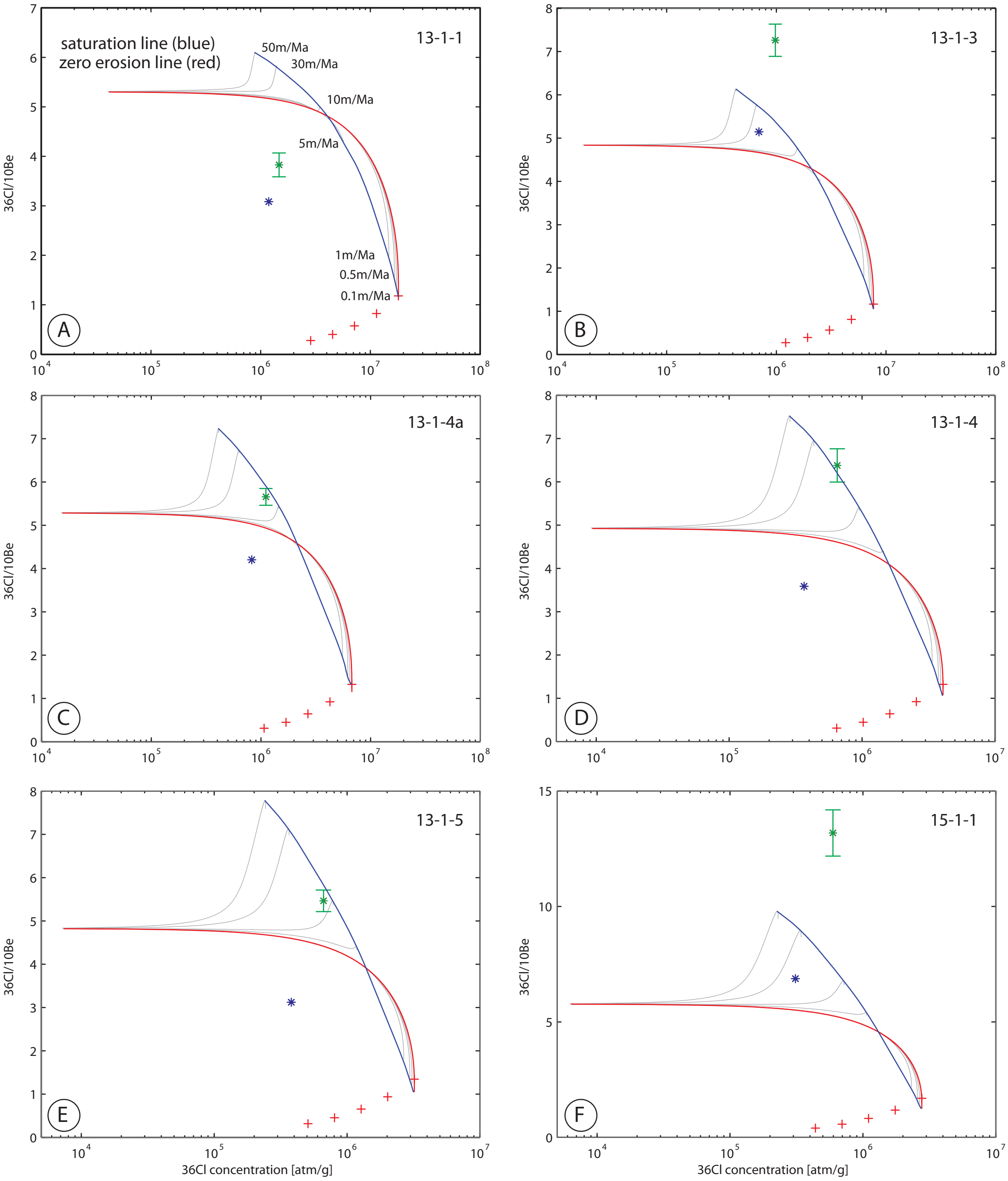

Figure 5.23: Erosion island plot of the $^{36}$Cl/$^{10}$Be pairs at Jajrud (Upper terrace), calculated with site-specific production rates and associated compositions (Cl). Depth increases from (A) to (F). Note the different scales for some of the plots. Shapes and position of the erosion islands vary in response to the varying contribution of the different production pathways for each composition and depth. Green star depicts the data, blue star has inheritance subtracted.

exposure ages, the sample composition is accounted for. Sample 13-1-3, for instance, revealed a much lower amount of total CaO, which results in a lower $^{36}$Cl production rate by spallation of Ca and thus a lower total $^{36}$Cl concentration (Table C.8). However, in the erosion island plot, this will certainly span a different island and thus account for chemistry effects. This sample, however, shows a deviating trend between leached and bulk-chemistry derived zero-erosion ages (Table C.3). This might indicate that there is an inherent analytical problem, i.e., the bulk sample does not sufficiently reflect the real chemistry of the amalgamated sample. The "buried" age of the uppermost Jajrud sample might be related to soil formation and mixing (Fig. 5.19).

The erosion island plots show a complex exposure history for Saboo (Fig. 5.24). Low isotopic ratios at Saboo that plot below the erosion island could be either explained by burial or episodic rapid erosion (e.g., Gosse & Phillips, 2001; Kober et al., 2007). Inheritance may also lead to low ratios, especially, if the calcium-bearing source lithology has a different pre-exposure history than the quartz-bearing lithology. The Chi$^2$-inversion of the beryllium profile reveals that inheritance does not play a role either. Chlorine inheritance cannot be easily determined from the deepest depth-profile sample, because muonic production outpaces spallation at depth, thus significant post-depositional production might be responsible for higher concentrations at depth. The very extensive, gently sloping terrace surface in turn argues against widespread erosion events. Furthermore, depositional events, which might correspond to shielding horizons, cannot be recognized in the soil profile nor are there any disturbances in the TCN-profiles. However, Fig. 5.16 A and B demonstrate that topography rises to the northeast of the sampling site at Saboo. This area is characterized by several incised gullies and small channels, some of them having developed into windgaps after abandonment of their northern sources. Possibly, episodic sheet flow has accompanied the evolution of this topographic gradient, which might have caused episodic burial and erosion. If the duration of burial can be determined from geomorphic or other independent estimates, the corresponding processes (pre-exposure, burial, post-emergence exposure) provide the minimum total exposure duration (e.g., Gosse & Phillips, 2001). In the case of Saboo, none of these processes can be unambiguously distinguished. Thus, the corresponding age has to be considered as a minimum age, but it could be significantly underestimated.

The zero erosion-age plot of the Rahad Abad site indicates offsets of the results from the diagonal towards the longer-lived nuclide, and probably reflects the isotopic steady-state conditions of the boulders (Fig. 5.20 F). While the sampled boulders are themselves sufficiently large in diameter and very resistent to erosion, some of them are embedded in the soil, having only the upper part exposed (Fig. 5.14). Previous burial, as indicated by the erosion island plot (Fig. 5.20 B), might thus have affected these boulders. The sample with the lowest ratio, however, rather reflects erosional spalling as shown by spheroidal weathering with individual spalled off sections reaching 2 cm in thickness. This scenario

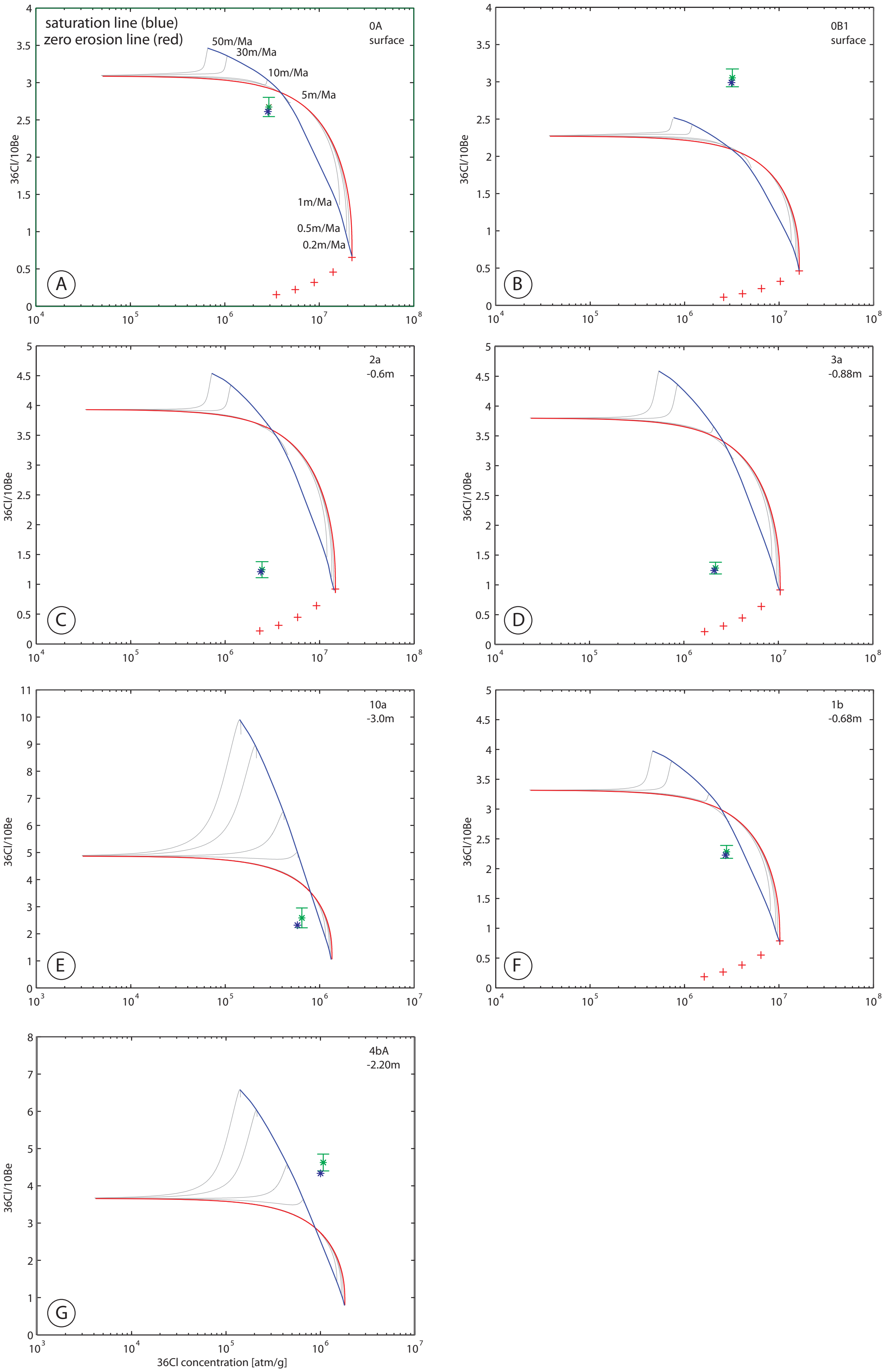
saturation line (blue)
zero erosion line (red)
50m/Ma
30m/Ma
10m/Ma
5m/Ma
1m/Ma
0.5m/Ma
0.2m/Ma
0A
surface
A
0B1
surface
B
2a
-0.6m
C
3a
-0.88m
D
10a
-3.0m
E
1b
-0.68m
F
4bA
-2.20m
G
36Cl/10Be
36Cl concentration [atm/g]
$10^3$
$10^4$
$10^5$
$10^6$
$10^7$
$10^8$

Figure 5.24: Erosion island plot of the $^{36}$Cl/$^{10}$Be pairs at Saboo, calculated with site-specific production rates and associated compositions (Cl). Depth increases from (A/B) to (E) and from (F) to (G/H). Note the different scales for some of the plots. Shapes and position of the erosion islands vary in response to the varying contribution of the different production pathways for each composition and depth. Green star depicts the data, blue star has inheritance subtracted.

thus is comparable with observations from the Mongolian Gurvan Bogd mountains (Ritz et al., 2006b). These authors described the evolution of a fan surface from an original bar-and-swale morphology, covered by boulder fields, towards a flat, but deeply incised surface with less (and finally no) boulders, suggesting that the boulder erosion rate approached the rate at which fine material is removed. At Rahad Abad, there are still a few boulders with unaffected cores that were sampled for our analysis. Thus, considering the burial episode, the calculated effective ages could be significantly underestimated.

### Influence of chemistry

To evaluate the possible influence of analytical uncertainties resulting from sample chemistry, we tabulated the$^{36}$Cl production pathways and coefficients of production (Tables C.5, C.7, and C.8) and compared the contrasts in $^{36}$Cl production and corresponding (apparent) age resulting from leached versus bulk subsample chemistry, as well as from different assumed total Chlorine amounts (Tables C.3, C.4, and C.6).

It is particularly important to evaluate the thermal neutron field at the sample location, because $^{36}Cl$ is not only produced by spallation from calcium, but may also be produced by thermal neutron capture from $^{35}Cl$ (e.g., Stone et al., 1998; Schimmelpfennig et al., 2009). The thermal neutron field in the rock is controlled by the bulk composition it traverses. For this reason, a representative subsample was kept for chemical analysis. For the Saboo and Lower Jajrud sites, this subsample was selected after mineral separation, before the total dissolution. However, elements which decelerate the neutrons of the cosmic ray, as for instance iron, could have been separated out, and thus the neutron field might be underestimated. To avoid this, we took additional bulk subsamples from the Upper Jajrud site. However, this effect will be significant only at high amounts of $^{35}Cl$. The amount of $^{35}Cl$ in the target sample is calculated by isotope dilution. Because of the varying steps of prior mineral separation, the real amount in the bulk material could be higher. To account for that, we calculated the apparent ages using the Cl amount from the target fraction, and compared the results with ages, calculated from the double amount of the target, as well as with arbitrary amounts of 200 and 500 ppm, respectively.

Chlorine values in the target fraction of our samples are generally low. At Saboo they are below 20 ppm, reaching 109 ppm at Upper Jajrud. Calcite spallation is the dominant process. Even assuming much higher $^{35}Cl$-values of 500 ppm will change the apparent ages only by less than 5% (Table C.6). In contrast, the apparent chlorine age differs by up to 11%, if using bulk instead of leached chemistry (Table C.3). This is especially intriguing, when comparing the replicates of sample 13-1-4a. The samples share the same bulk chemistry (same subsample). The replicate was taken after mineral separation, before the start of the protocol for chlorine chemistry. The concentrations of the replicates and the associated zero-erosion ages vary by about 5.6%. This variation, however, is added on to the deviation from the bulk-chemistry sample so that this deviation is 5% for 13-1-4aA, but 11% for 13-1-4aB. For Jajrud, the difference in bulk chemistry results in an about 3% higher spallation fraction in production (Table C.8). Significant differences, however, occur in the thermal neutron production, which is actually up to 30% lower when using bulk-chemistry. Such differences in chemistry will definitively span a different island in the erosion-island diagram. This should be kept in mind when interpreting results from Saboo, which is based on leached chemistry, but fortunately, has very low chlorine contents. Generally, the position of the erosion island shifts towards lower ratios on the y-axis and higher concentrations on the x-axis, when using the leached chemistry. Although speculative, moving the Saboo-islands virtually into the opposite direction might bring some samples, which are only slightly below (0A, 10a, 1b) into the island (Fig. 5.24).

Considering these effects of chemistry on the total $Cl^{36}$ production, additional uncertainties may arise for the Chi$^2$-inversion and solving for the entire $Cl^{36}$ depth profile. As described earlier, in this approach measured concentrations are compared with theoretical, site-specific concentrations. The profile fitting, however, was calculated for one specific chemistry, i.e., that of sample 13-1-1 at Jajrud, and -2a at Saboo, assuming that the samples do not differ significantly. That this is not implicitly true can be seen in Table C.12. Here, the theoretical concentrations per depth were calculated for one fixed exhumation scenario (46 ka exposure, 285,000 at/g inheritance, and 23 m/Ma erosion). Tables C.7 and C.8 show the effects of chemistry and depth on the production pathways. When considering a surface location (0 m depth), differences reflect chemistry only. It is intriguing that for the Upper Jajrud site, samples with significant lower percentage of spallation correspond to those samples which plot outside the erosion island diagrams. For Saboo, however, this effect seems to be less important.

Finally, even, if the chlorine system has the more complicated production mechanisms, problems might also be inherent to the $Be^{10}$ system in our study area. For the Saboo A-profile for instance, analytical uncertainties are much larger for $Be^{10}$ than for $Cl^{36}$, which is related to very small sample amounts. Furthermore, except for Rahad Abad, the quartz sources in the study area are microcrystalline tuffs and chert, which could have been subjected to the recoil effect.

## 5.5.2 Implications for Quaternary deformation in the Tehran plain

### Regional correlation of Late Pleistocene deposition and incision

The dichotomy of ages at Kan, with an older age at depth, but younger ages at the surface, has several implications for this area. First, the surface ages (25.1 ± 1.9 ka for pea-sized clasts and 31.1 ± 2.9 ka for pebbles) are reliable and the age of terrace abandonment might be correlatable with the age of sediment deposition at Afjeh, derived from OSL (36.7 ± 4 ka and 30.5 ± 1.9 ka). Both of these surfaces have comparable geomorphic patterns, such as smoothness and a low degree of dissection. With these characteristics, we have assigned these surfaces to the third terrace, cut into unit C sediments (Tehran Alluvium, Figs. 5.5, 5.16). This is furthermore the same surface of the piedmont alluvial plain, which forms the base for Tehran, and which is incised by only a few larger rivers. Unit C deposits from the Khorramabad area, about 350 km southwest of Tehran, yielded paleolithic instruments, revealing ages between 32.5 thousand and 38 thousand radiocarbon years (Vita-Finzi, 1969). Those artifacts, however, have been found at the base of the Unit C sediments. Although those data are based on distant outcrops, their ages are comparable with the depositional age at Afjeh. Yet another outcrop northwest of Tehran yielded two artifacts and gave possible ages of 46.9 to 50.6 ka (Rieben, 1955; Vita-Finzi, 1969). However, our data from the Kan surface suggest that renewed incision started shortly after about 30 ka in the northern Tehran plain. Based on first occupation on the Tehran alluvium, which is assumed to date to about 4 thousand years BC, Vita-Finzi (1969) argue that sedimentation of unit C continued until about this time. Renewed archeological excavations that took place at sites south of Tehran near Ray and on the Jajrud alluvial fan, near Varamin, have revealed buried Late Neolithic sites with calibrated radiocarbon ages between 5.3 thousand years BC to 4.6 thousand years BC (Fazeli et al., 2004; Gillmore et al., 2007). This might suggest that terrace abandonment in the northern Tehran plain did not coincide with the end of the sedimentation phase, but might be entirely structurally controlled. While sedimentation continued, accumulation has been shifted southward. For the Kan site, this in turn indicates late Pleistocene deformation along the Chitgar Park structure, as also indicated by the Chitgar windgap.

Furthermore, the depth profile age of 275 ka implies that the base level at this site cannot have changed significantly during middle to late Pleistocene time, allowing incision, subsequent refilling with deposition of the Kan alluvial fan and re-incision. Such a scenario probably extends continuous deformation along the Chitgar Park structure, which could keep pace with incision, back into middle Pleistocene time. Considering the highly tilted unit A and moderately tilted unit B sediments in the forelimb, this structure reveals a long-term tectonic history, probably spanning the entire Quaternary. However, it should be noted that immediately upstream of the Kan River mouth, massive landslide deposits are currently incised. In this context, a transient blockage of the Kan River at the valley exit and subsequent outburst of the accumulated sediment could alternatively explain the deposition of an extended alluvial fan next to the entrenched river bed, similar to the effects of missing fan-head incision described by Dühnforth et al. (2007).

### Incision, paleo-earthquakes, and fault slip rates

Incision rates can be calculated for the Kan and Jajrud rivers, including their tributaries Kond and Afjeh. Because we have measured the positions mainly with a handheld GPS, we will add an uncertainty of ± 5 m for the Kan, Jajrud, and the Afjeh fluvial terraces, and ± 0.5 m for the measured upper, and ± 0.2 m for the lower strath terraces at Afjeh.

The Kan River has incised into the 25 to 31 ka-old terrace by 19 ± 5 m, resulting in an incision rate of between 0.61 ± 0.17 and 0.76 ± 0.21 mm/a. Considering the (oldest) effective age of 258.5 ka for the Rahad Abad boulders and the calculated 317 m of incision of the Kond River (Landgraf et al., 2009), the corresponding long-term maximum incision rate is about 1.23 mm/a. At Afjeh, three rates for different late Pleistocene and Holocene surfaces can be calculated. The OSL-dated fluvial terrace has been incised by about 24 m. Assuming incision started immediately after deposition, the OSL-derived ages reveal average minimum incision rates of between 0.65 ± 0.15 and 0.79 ± 0.17 mm/a. However, we consider these to minima because the incision might have started later. The Jajrud terraces reveal incision rates for the late Pleistocene between 0.6 ± 0.04 mm/a for the upper terrace and about 0.7 to 0.82 mm/a for the lower terrace. The incision rates derived from late Pleistocene fluvial terraces are thus comparable within the error limits at the Kan, Jajrud, and Afjeh rivers. While we argue for some tectonic control on the Kan incision, the close agreement of incision at disparate locations may however be driven by either regional base-level fall or additional tectonic activity farther south.

Indeed, three topographic features, south of the Tehran Plain in the Central Iranian Plateau, have traditionally been interpreted to represent active faults, accommodating part of the Arabian-Eurasian deformation (e.g., Ambraseys & Melville, 1982; Berberian, 1983). However, Nazari et al. (2010) showed that morphologic features reminiscent of fault scarps are undeformed risers related to shorelines of an ancient lake. These risers are correlatable with other shoreline remnants farther east and suggest the existence of an extensive lake similar to the proportions of Lake Aral that once covered the Great Kavir desert probably until the late Holocene time (Nazari et al., 2010). The ultimate regression of such a lake would have caused a substantial regional lowering of the base-level. However, while this lowering must have affected the late Holocene incision rate, it is too young to have caused the start of incision after the late Pleistocene phase of sediment accumulation.

From terrace abandonment at Kan, Afjeh, and Jajrud, we calculate a mean "background" incision of 0.7 mm/a. Based on our observations from the bedrock channels at the Afjeh site, Holocene incision is apparently pulsed and temporary increased to 1.52 ± 0.27 and 1.07 ± 0.2 mm/a, respectively. These pulses might be fault controlled and are probably related to motion along the easternmost branch of the NTT. For the youngest pulse, reflected in the 1.70-m-high strath, this would roughly correspond to 0.58 m of fault-controlled incision during the ultimate 1.6 ka. We consider this to be a minimum amount, because the actual incision rate of the Afjeh tributary might be smaller than the background incision rate of the Jajrud River, which has a much larger catchment and currently incises alluvium, which is easier to erode than the resistent bedrock (diorite) at Afjeh. Fault inclination and obliquity of motion would result in an increase of the total offset in this environment. However, while fault kinematic indicators suggest a strike-slip component, small-scale channel offset or deflections have not been observed at Afjeh, implying that the dip-slip component dominates and the strike-slip has been accommodated on nearby faults. This raises the question of whether the pulsed incision might result from a single earthquake that this part of the fault accommodated. The trace of the NTT is irregular in places and reflects a segmentation in an array of en-échelon fault segments, with a total length of about 65 km along the mountain front. From displacement-length scaling relationships, maximum displacement may be between 2.1 and 2.95 m, using a reverse-fault and all-fault scenario, respectively, for an event that ruptures the entire length of the fault (Wells & Coppersmith, 1994). Due to the position about 11 km away from the fault tip and assuming typical bow-shaped displacement variations along faults, substantially less displacement per earthquake might be expected at Afjeh (average displacement between 0.92 and 1.46 m after Wells & Coppersmith (1994)). However, considering fault interaction between NTT and MFF (Landgraf et al., 2009), it is reasonable that slip from the eastern MFF segment has been transferred onto the NTT. Thus, at the Afjeh location, higher average slip is reasonable. Thus, the 0.58 m (as average displacement) could be explained by one single event, which would constitute a moment magnitude between 6.6 and 6.7 for a reverse-fault and all-fault relationship, respectively (Wells & Coppersmith, 1994). The timing for this youngest pulse of incision corresponds to 418 AD (195 - 641 AD within uncertainty). The earthquake catalogue does not list an event around that time, however, earthquake notes are rare for the pre-Islamic period in Iran (Ambraseys & Melville, 1982). Strong historic events have been recorded later for the study area, such as 855-856 AD, 958 AD, 1177 AD, reaching estimated surface magnitude equivalents of up to 7.7 (e.g., Ambraseys & Melville, 1982; Berberian, 1983; Berberian & Yeats, 1999, 2001).

Consequently, if we consider the lower strath to correspond to one big earthquake, the upper strath might reflect older events. However, a higher amount of slip would have been accommodated in about the same time, i.e., 2.1 m in only 1.7 ka. Assuming only one event of 2.1 m average displacement, this would constitute a moment magnitude between 6.7 and 7.2 (reverse-fault and all-fault), thus reaching the maximum expected moment magnitude for a surface-rupture length of 65 km on a reverse fault, i.e. 7.2 (Wells & Coppersmith, 1994). While no indicators of multiple events (additional strath levels) have been observed, the 2.1 m displacement may correspond to two or more events. If we consider the two strath levels indicating two single events, the recurrence interval between these two entire-length ruptures would be 1.7 ka and the elapsed time since the last event would correspond to 1.6 ka.

The main faults to which the paleo-earthquakes have been attributed, are the MFF, the Taleghan Fault north of the MFF, and the NTT. Furthermore, these faults are probably mechanically linked in a transpressional duplex system and share a common deformation history (e.g., Landgraf et al., 2009). Since the Pleistocene, the internal domain of the Alborz mountains, including the eastern Mosha-Fasham and Taleghan faults, has been undergoing left transtension (Ritz et al., 2006a; Nazari et al., 2009). Here, paleoseismological studies spatially bracket the Afjeh study site. For the Taleghan Fault, Nazari et al. (2009) observed two to three events of inferred magnitudes $M_w \geq 7$ in the last 5420 years. Coseismic vertical displacement during these events have been measured to be between 0.94 and 1.86 m and elapsed times since the last big event may have been between 3529 and 1599 years. Thus, this timing encapsulates the ages of both strath terraces at Afjeh and underscores the importance of this site for further paleoseismological investigations. In this context, it is especially important to understand the fault motion along the NTT. While the bedrock channel incision reflects a major component of dip-slip motion, fault striae also indicate (previous?) lateral motion. Furthermore, the offset streams that cross the NTT to the east of Afjeh are sinistrally offset by a cumulative amount of about 42 and 54 m, respectively (Fig. 5.13 and 5.16). These streams are crossing a longitudinal valley and are incised into a terrace remnant, which has equivalents about 1.5 km farther west and which might be correlatable with the fluvial terrace remnant at Afjeh, about 4 km west of this site. Thus, we use the OSL-derived age to calculate a late Pleistocene horizontal slip-rate for this part of the NTT, which is between 1.14 ± 0.3 mm/a for the older age and the western channel, and 1.79 ± 0.35 mm/a for the eastern, erosionally widened channel and the younger age. This rate is quite reasonable, considering a slip rate of about 2 mm/a for the eastern Mosha-Fasham fault and 0.6 to 1.6 mm/a along the Taleghan fault to the northwest. However, the predominant strike-slip component along the NTT ceases westward, allowing transition into the transtensional deformation of the Latyan basin.

### Implications for timing of distributed active faulting in the Latyan basin

The 195-ka-old surface at Saboo is the oldest, directly dated surface in the Tehran plain, but the erosion-island diagram indicates that it has been buried and must be even older. Its evolution is crucial for the understanding of the Latyan basin and the distribution of faulting in this part of the Tehran Plain. The surface is at approximately the same elevation as the much younger terrace remnants to the north, which have been described in the previous paragraph and which are separated from each other by a topographic high. This high is the present-day drainage divide and might be the sediment source for the burial. In this case, it has been uplifted prior to 200 ka. West of the Saboo surface and the drainage divide, a water gap exists at which a deeply incised channel of the NTT footwall abuts the erosionally unaffected deposits of the longitudinal valley along the trace of the NTT (Fig. 5.16). Farther west, a windgap and another watergap follow, indicating substantial drainage reorganization and probably footwall uplift along the NTT. Furthermore, there is another step in incision aligned along the Latyan fault, indicating that the abandoned surfaces constitute paleo-divides, which may now be consumed by headward incision and subsequent erosion. Such a scenario is partly compatible with modeling results of landscape evolution processes at extensional relay ramps (Densmore et al., 2003). In fact this setting is close to the model scenario where static (non-propagating) en-échelon fault geometries have been used. Limited time of development caused only incipient stream capture. Displacement along the faults has caused catchment incision and fan propagation. The overall slope of the relay is fault-parallel, with a slight tilt towards the Latyan fault tip. The drainage divide has migrated, allowing some relay drainage to flow around the Latyan fault. A secondary drainage divide is currently developing between the relay drainages. Catchments aligned on the Latyan fault experience higher rates of base level fall, which might result in headward incision (e.g., Densmore et al., 2003). Such a stage could be followed by capture with subsequent drainage of the relay from hinterland sources. This stage, predicted in the model, however, has not evolved in the Latyan basin. While in the experiments both faults evolve at the same time, our study area is influenced by inherited faults and topography. Nevertheless, some landscape proxies are intriguingly similar to those expected for such a relay scenario and the age of the Saboo surface indicates that this style of footwall deformation is older than 200 ka.

## 5.6 Conclusions

Ongoing deformation in the south-central Alborz foreland is related to the Arabia-Eurasian collision, and is thus influenced by the northward motion of Iranian crust and northwestward motion of the South Caspian basin in a stable Eurasian reference frame, respectively (e.g., Vernant et al., 2004b). This results in oblique motion along the main structures in the Tehran plain, with fault-propagation folding along major faults, limited strike-slip motion and en-echelon arrays of second-order upper plate thrusts. While the Tehran Plain records Quaternary deformation, the majority of faulting took place in the early stages of the Quaternary and before. The present analysis clearly shows that the two oldest recognized phases of alluviation, subsequent erosion, and faulting, which affect units A and B, occurred prior to the late Pleistocene. The rate of erosion is generally higher than expected, bringing Be concentrations into saturation already between 200 and 300 ka. The oldest dated surface is the Saboo erosional surface of 195 ka, while others show effective ages of up to about 258.5 ka (Rahad Abad). Abandoned terraces that probably correspond to incision after deposition of unit C have late Pleistocene ages along the Kan River in the west and the Jajrud River in the east. This allows us to infer a “background” incision rate and to relate increased pulses of Holocene incision to repeated earthquake ruptures. Those events have resulted in the formation of strath terraces and the development of a bedrock channel near the eastern tip of the NTT, but they might have ruptured the entire length of this fault. Whether the entire NTT is active, or deformation is distributed across several parallel faults or interacting fault arrays, is currently under debate (e.g., Abbassi & Farbod, 2009; Landgraf et al., 2009). Nevertheless, this study shows Holocene deformation in the eastern Tehran Plain and infers Late Pleistocene deformation for the central and western Tehran plain. While urban development in Tehran increasingly covers the active fault traces, the obvious indicators of paleo-earthquakes and ongoing deformation during the last millennia attest to the threat that those faults and their related structures carry for the megacity.

# Chapter 6

# Conclusions

The combination of geomorphic and stratigraphic indicators of Quaternary tectonic activity along the North Tehran Thrust and the present-day distribution of seismicity, exclusively clustered along the eastern segment of the tectonically active Mosha-Fasham Fault (MFF), has been the starting point of this thesis. The spatially limited occurrence of seismicity contrasts with noted historical earthquakes that ruptured segments along the entire length of the MFF (e.g., Ambraseys, 1974; Ambraseys & Melville, 1982; Berberian & Yeats, 1999, 2001). This setting thus constitutes an important problem in continental tectonics and intraplate deformation characteristics. One dilemma is that such local seismicity in a mid-continent setting could represent long-lasting aftershocks of a previous large earthquake rather than being the precursor of a coming event (Stein & Liu, 2009). Aftershocks can be damaging in the short-term and thus their damage potential should not be underestimated. In the long-term, however, relying on currently seismically active zones to predict the locations of future large earthquakes may result in erroneous hazard assessment elsewhere (Stein & Liu, 2009). For the study area, this problem has important consequences. The North Tehran Thrust (NTT), which is seismically virtually inactive, merges with the MFF at a geometric complexity, i.e., where the MFF bends from a WNW to NW-strike. The NTT constitutes the southern boundary fault of the Alborz mountains and delimits the Tehran megacity to the north. Thus, interaction between the eastern branch of the MFF and the NTT poses a considerable threat to Tehran, the Iranian capital with more than 13 million inhabitants. In this study, I investigated key areas of the south-central Alborz mountains and the foreland in the Tehran Plain. The combined use of fault-kinematic analysis, morphometry, numerical fault-interaction modeling, and dating of geomorphic surfaces using cosmogenic radionuclides allowed me to unravel the complexity of this intraplate setting on various spatial and temporal scales.

First, I have shown that fault interaction between the Mosha-Fasham Fault and the North Tehran Thrust plays a significant role in the long-term evolution of this part of the mountain range. Furthermore, fault kinematics, macroscopic structural data, and geomorphic observations indicate that the deformation field has changed over time. This is in line with the results of other studies in this area (e.g., Axen et al., 2001; Allen et al., 2003; Zanchi et al., 2006; Morley et al., 2009). Fault kinematic analysis of major and minor faults in this area has revealed early NW-directed shortening associated with dextrally oblique thrusting. This is in agreement with the orientation of the axes of macro-scale to meso-scale folding. The data suggest an early mechanical linkage of the NTT and MFF fault systems during the earlier dextral transpressional stage. This regime, however, was superseded by Pliocene to Recent NE-oriented shortening, which caused thrusting and sinistral strike-slip faulting. Large-scale folds have been refolded in this regime and new meso-and macro-scale folds have evolved. This reorganization is inferred to have resulted from a rotation in the direction of $S_{Hmax}$. Resulting from this reorganization, the NTT and MFF were reactivated and incorporated into a nascent transpressional duplex, which is compatible with a model suggested by Guest et al. (2006a). The duplex transports left-lateral motion from the eastern towards the western branch of the MFF, and possibly the parallel Taleghan Fault. This deformation is distributed across four frontal ramps, i.e., the central segment of the MFF, the Emamzadeh-Davud Fault, the Purkan-Vardij Thrust and the NW-prolongation of the NTT. The east-west striking NTT-segments constitute lateral ramps and are characterized by left-oblique motion. Currently, the central-eastern NTT segment is undergoing high strain, but the western segment experiences lower strain rates, thus highlighting the quasi-segmentation of the fault.

Secondly, I have assessed the role of the duplex geometry for landscape evolution. The transpressional duplex has prevailed for a long duration of deformation processes. Consequently, this structure has significantly affected the landscape evolution in this part of the range, which in turn implies that fault interaction dominates the growth of topography and relief distribution in such a complex setting. Using FIMoz (Zielke & Arrowsmith, 2006), a numerical program to model such fault interaction, I have shown that two of three distinctive features characterizing present-day topography and relief in the study area are directly related to their location inside the duplex array, when applying current tectonic boundary conditions. Thus, high rock uplift is linked to fault interaction between the eastern MFF and NTT and between the western MFF and the Taleghan Fault. The underlying concept for this analysis is that the growth of topography starts with repeated earthquakes, that displacement-length relationships control the growth of the associated faults and their corresponding topographic features, and that interacting faults or fault complexities influence the slip distribution, and thus topography. In simplified models, ignoring isostasy and subsequent erosion, I have compared the vertical displacement field, resulting from one interaction cycle (including effects as stress triggering) with real topographic metrics as topography and topographic residuals (a measure of local relief), which have been calculated from a SRTM DEM. The close agreement between model results and DEM-derived metrics is intriguing and underscores the importance of fault interaction in intraplate settings. This finding is important for our understanding of intraplate faults as complex systems.

Third, using fault-related landform evolution is a standard procedure to define the degree of tectonic activity, but this may result in erroneous assessment if tectonic boundary conditions have changed through time. In order to account for inherited topography and possible misconceptions of fault activity, I have used a new general concept of landscape compartments, i.e., simple and composite landscapes. I define simple landscapes as those environments which have developed during sustained tectonic conditions, including incipient faults and their landforms. Rotations of the shortening direction through time will generate new faults and associated landforms. In addition, such a changeover to new conditions will also cause the continuation of activity along pre-existing structures. Consequently, such regions with changing tectonic boundary conditions constitute composite landscapes that contain topography inherited from previous conditions. Numerical fault-interaction modeling using different tectonic boundary conditions yields synoptic snapshots of artificial topography that can be compared with the real topographic metrics, and thus helps decipher the relationships between tectonic boundary conditions, structural evolution and landform development. In general, the modeling approach shows that arrays of linked faults or faults with pronounced bends or step-overs have distinct offset patterns and are particularly sensitive to detection of changes in the regional tectonic stress field. However, not all structures in fault arrays are useful to provide information of such changes. Good indicators of composite topography are array "inside corners" in the hanging wall of faults. These correspond to junction or intersection areas of fault arrays, whose bisecting line is approximately aligned with the $S_{Hmax}$ direction. However, in the Alborz mountains, I found that E-W striking faults are less sensitive to changing boundary conditions. They are in a "tectonic steady state", favorably oriented to accommodate the entire range of NW- to NE-directed compression, without significant changes in resulting uplift pattern. On the other hand, these faults (western MFF and Taleghan Fault) show the highest total displacement, as reflected by basement involvement, which might indicate sustained faulting under changing boundary conditions as suggested by the models.

The success of such an approach and the detection of inherited topography largely depends on landscape response times. For the Alborz mountains it is currently under debate whether the present-day, predominantly left-lateral motion is Pleistocene in age or if it was already established 9-10 Ma ago (Ritz et al., 2006a; Hollingsworth et al., 2008; Shabanian et al., 2009; Nazari et al., 2009; Ritz, 2009; Siame et al., 2009; Hollingsworth et al., 2009; Ballato et al., 2010a). The arguments of Ritz et al. (2006a) and Nazari et al. (2009) are partly based on geomorphologic observations for the onset of left transtension in the internal domain of the Alborz. My study shows that much of the topography is linked to pronounced left transpression, which predates the youngest signal of left transtension. Importantly, this transtensional system has not yet erased the topographic signal of the earlier transpressional tectonic setting. It is therefore reasonable that both arguments are valid, i.e., an early change from predominant dextral to sinistral motion around 9-10 Ma ago and a subsequent changeover to transtension, which is Pleistocene in age. Thus, while the Alborz mountains and their foreland constitute a complex tectonic landscape, it might not be the most ideal setting to test the otherwise promising new approach that I have chosen.

Fourth, in order to quantify deformation patterns, I investigated the timing of Quaternary deformation and landscape evolution in the Tehran Plain using TCN dating. This analysis clearly shows that the two oldest recognized phases of alluviation, subsequent erosion, and faulting, which affect units A and B, predate late Pleistocene time. The rate of erosion is generally higher than expected, bringing Be concentrations into saturation already in 200 ka and 300 ka. The oldest dated surface age is the Saboo erosional surface of 195 ka. Other surfaces have effective ages of up to about 259 ka (Rahad Abad). Abandoned terrace ages that probably correspond to incision, subsequent to deposition of Unit C, have late Pleistocene ages along the Kan River in the west and the Jajrud River in the east. This allows me to infer a mean "background" incision rate of 0.7 mm/a and to relate increased pulses of Holocene incision to repeated earthquake ruptures. The corresponding vertical offset has been calculated to be 0.58 m, and 2.10 m, respectively. If assuming one earthquake per offset and rupture of the entire NTT, the associated moment magnitudes are 6.74 and 7.19, respectively. These events have resulted in the formation of strath terraces and the development of a bedrock channel near the eastern tip of the NTT, but they might have ruptured the entire length of this fault. However, considering the fault interaction between NTT and MFF, it is reasonable that slip from the eastern MFF segment has been transferred onto the NTT. Thus, at the Afjeh location higher average slip is reasonable. If the entire NTT is active or if deformation is distributed across several parallel faults or interacting fault arrays is currently under debate (e.g., Abbassi & Farbod, 2009; Landgraf et al., 2009). Nevertheless, my study documents Holocene deformation in the eastern Tehran Plain and it is suggested that late Pleistocene deformation has taken place in the central and western Tehran plain. While urban development in Tehran increasingly covers the active fault traces, the obvious indicators of paleo-earthquakes in the last millennia attest to the threat that those faults and their related structures pose for the megacity.

Fifth, I also worked on methodological development of the TCN dating of geomorphic surfaces with highly variable and generally low amounts of quartz-bearing or calcite-bearing source lithologies. I separated the two radionuclides $^{10}Be$ and $^{36}Cl$ out of the same amalgamated depth profile samples. This involved first of all extracting $^{36}Cl$ from calcite (e.g., Stone et al. 1996), which was dissolved from a pre-treated mixture of calcite, quartz, and feldspar. After decanting the calcite-bearing solution, the silicate residual was used for further quartz purification and chemical $^{10}Be$ extraction. This approach is new (Merchel et al., 2010) and allows simultaneous detection of $^{10}Be$ and $^{36}Cl$ from samples which underwent the same burial history, but did not necessarily experience identical pre-depositional events. The data show that both profiles, derived from $^{36}Cl$ are in isotopic saturation. However, with the advantage of the two-nuclide approach on the terrace profiles and the calculation of erosion island diagrams, I could infer a simple exposure history for Jajrud and complex exposure with a period of burial for the Saboo site. $Chi^2$ inversion to solve simultaneously for exposure time and erosion has also yielded inconsistent erosion between the nuclides, inferring that the processes responsible for nuclide production at depth might still not be sufficiently understood.

In sum, my study has shed new light on this complex area of intraplate deformation. The Mosha-Fasham Fault and the North Tehran Thrust are mechanically linked. This is a long-term, but also a short-term phenomenon. The spatial occurrence of higher strain accommodation in this complex fault system is related to the geometry and interaction between the involved faults. The consistency between the modeled results of one interaction cycle and the real topographic metrics suggests that if temporal quiescence of some faults or fault segments happens on the scale of several earthquake cycles, the resulting slip deficit is regained over time. Thus, analyses on an intermediate timescale are needed to overcome this dilemma and to better understand the present-day situation in the study area. Paleoseismology at a high spatial sampling density and additional dating approaches could help. However, the advanced urbanization and land use in this metropolitan area hampers such activities.

# Appendix A

# (to Chapter 3)

to: **Fault-kinematic and geomorphic observations along the North Tehran Thrust and Mosha Fasham Fault, Alborz mountains Iran: implications for fault-system evolution and interaction in a changing tectonic regime (Chapter 3)**

## Abstract and Acknowledgements

**Abstract** Neighboring faults can interact, potentially link up and grow, and consequently increase the seismic and related natural hazards in their vicinity. Despite evidence of Quaternary faulting, the kinematic relationships between the neighboring Mosha Fasham Fault (MFF) and the North Tehran Thrust (NTT) and their temporal evolution in the Alborz mountains are not well understood. The ENE-striking NTT is a frontal thrust that delimits the Alborz mountains to the south with a 2000 m topographic front with respect to the proximal Tehran plain. However, no large instrumentally recorded earthquakes have been attributed to that fault. In contrast, the sigmoidally shaped MFF is a major strike-slip fault, located within the Alborz mountains. Sinistral motion along the eastern part of the MFF is corroborated by microseismicity and fault kinematic analysis, which documents recent transtensional deformation associated with NNE-SSW oriented shortening. To better understand the activity of these faults on different time scales, we combined fault-kinematic analysis and geomorphic observations, to infer the kinematic history of these structures. Our fault kinematic study reveals an early dextral shear for the NTT and the central MFF, responsible for dextral strike-slip and oblique reverse faulting during NW-oriented shortening. This deformation regime was superseded by NE-oriented shortening, associated with sinistral-oblique thrusting along the NTT and the central-western MFF, sinistral strike-slip motion along subsidiary faults in the central MFF segment, and folding and tilting of Eocene to Miocene units in the MFF footwall. Continued thrusting along the NTT took place during the Quaternary. However, folding in the hanging wall and sinistral stream-offsets indicate a left-oblique component and Quaternary strike-slip reactivation of the eastern NTT-segment, close to its termination. This complex history of faulting under different stress directions has resulted in a composite landscape with inherited topographic signatures. Our study shows that the topography of the hanging wall of the NTT reflects a segmentation into sectors with semi-independent uplift histories. Areas of high topographic residuals and apparent high uplift underscore the fault kinematics. Combined, our data suggest an early mechanical linkage of the NTT and MFF fault systems during a former dextral transpressional stage, caused by NW-compression. During NE-oriented shortening, the NTT and MFF were reactivated and incorporated into a nascent transpressional duplex. The youngest manifestation of motion in this system is sinistral transtension. However, this deformation is not observed everywhere and has not yet resulted in topographic inversion.

**Acknowledgements** This work was funded by the German Research Council (DFG project

STR 373/19 − 1 and funds from the DFG Leibnitz Award to M. Strecker). We greatly appreciate logistical help from the Tehran Building and Housing Research Center. In particular, we would like to thank A.H. Heidarinejad, T. Parhizkar, and A.H. Mirzaei for their encouragement. We wish to thank Y. Djamour, M. Shakeri, and M. Hekmatnia for their logistical GPS support, and B. Fabian for her help with the illustrations. Our interpretations have benefited from discussions with J. Jackson, J.-F. Ritz and J.R. Arrowsmith. Special thank to Prof. G. Hilley and an anonymous reviewer as well as the editor Dr. Y. Ben-Zion for very helpful and constructive comments.

# Fault kinematic data

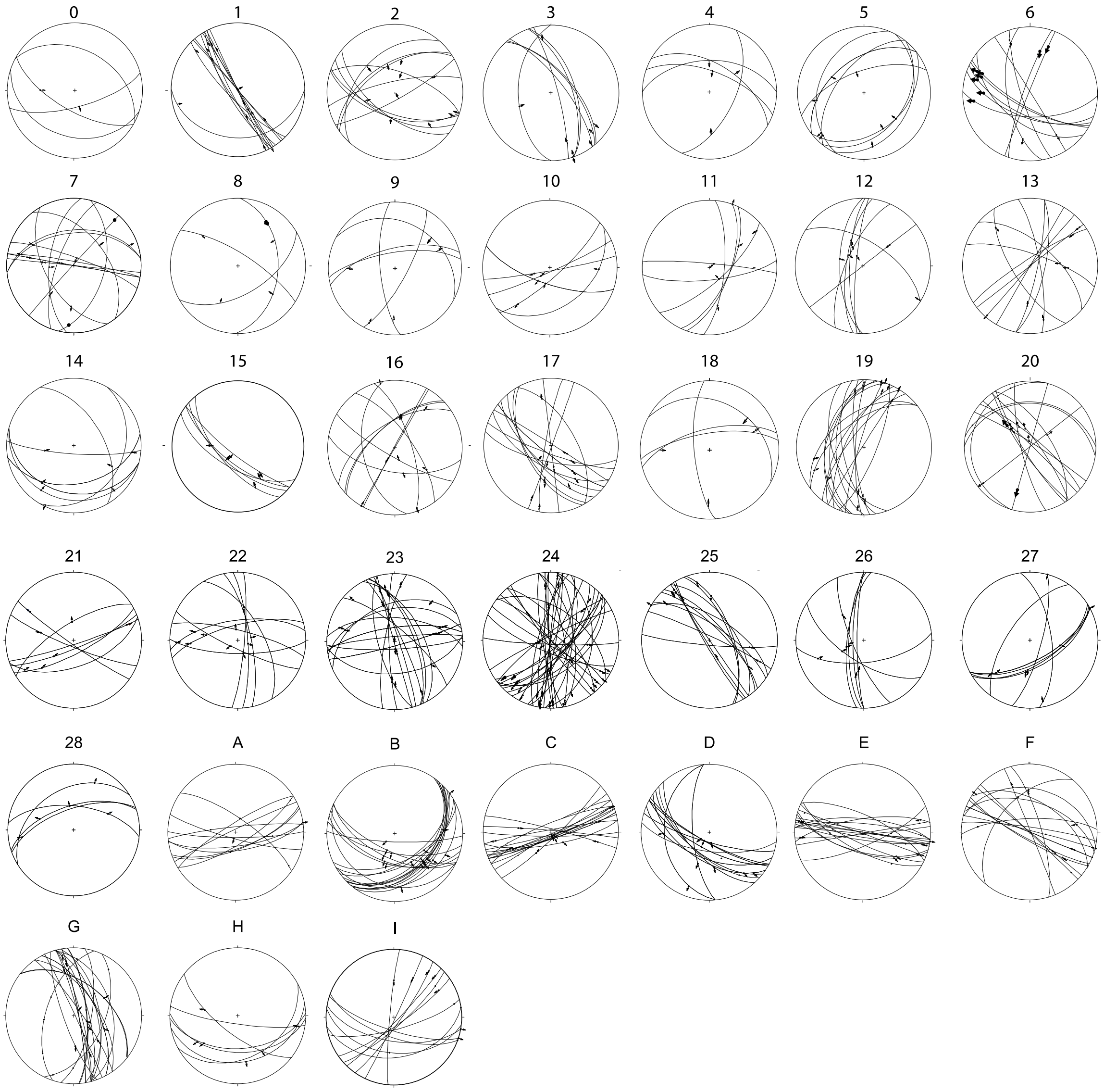

Figure A.1: Raw fault kinematic data collected along the MFF, NTT, and adjacent faults.

# Appendix B

# (to Chapter 4)

to: **Differentiating simple and composite tectonic landscapes using numerical fault-slip modeling (Chapter 4)**.

# Abstract and Acknowledgements

**Abstract** We define that simple landscapes are related to protracted tectonic conditions. Composite landscapes contain topographic elements that cannot be explained by motion along currently active faults and most likely result from changes in the tectonic regime. Landforms are often used to assess the spatial distribution and magnitude of tectonic displacements. Inherited topography, unrelated to the current tectonic conditions, may however lead to erroneous assessments of present-day tectonic activity. Differentiating between simple and composite landscapes in these environments is thus an important approach to overcome such predicaments. We use numerical simulations to determine the vertical displacement field, caused by mechanically interacting faults that are subjected to a uniform tectonic stress field. While progressively rotating the axis of maximum horizontal stress ($S_{Hmax}$) in a structural model setup, we produce a synoptic overview of simple landscapes and compare them with topographic features of a real composite landscape in the south-central Alborz mountains of Iran. Topographic residuals calculated from Digital Elevation Models (DEMs), reveal distinct zones of inferred high rock-uplift rates in the south-central Alborz. Certain areas of high elevation and rock-uplift rates can only be reproduced under a restricted range of $S_{Hmax}$-directions. The long-lived, steep Mosha Fasham Fault is able to maintain a predominant left-lateral motion under NE-directed $S_{Hmax}$, while in general, the fault array is shortened in NNE-direction. The faults bounding the Taleghan range are less indicative of changes in $S_{Hmax}$-direction. This area of presumably inherited topography is favorably oriented to undergo reactivation under a wide range of NW- to NE-directed compression.

**Acknowledgements** This work was funded by the DFG Leibniz Award to M. Strecker and a grant funded by the German Research Council (STR 373/19 – 1 to M. Strecker and A. Friedrich) and the German Academic Exchange Service (DAAD-D/07/42739). We wish to thank Birgit Fabian for her help with the drawings. We have benefited from discussions with G. Hilley, M. Trauth, F. Krüger, M. Ohrberger, and S. Hainzl.

# Using strain rate and direction to calculate regional stressing rate tensor

$$\sigma_{ij} = 2 * \mu * \varepsilon_{ij} + \lambda * \varepsilon_{kk} * \delta_{ij} \tag{B.1}$$

with:
$\mu$ = shear modulus, $\lambda$ = Lamé constant (both assumed to be $\sim$ 30GPa in crust, Poisson body)
$\varepsilon_{kk} = strainrate = \varepsilon_{11} + \varepsilon_{22} + \varepsilon_{33}$

and:
$\varepsilon_{11} = 5 * 10^{-8}/yr(N20E)$ and $\varepsilon_{33} = 1 * 10^{-8}/yr(N110E)$ (Masson et al., 2007), we calculate

$$\sigma_{11} = 2 * \mu * \varepsilon_{11} + \lambda * (\varepsilon_{11} + \varepsilon_{22} + \varepsilon_{33}) \tag{B.2}$$

$$\sigma_{22} = \lambda * (\varepsilon_{11} + \varepsilon_{22} + \varepsilon_{33}) \tag{B.3}$$

$$\sigma_{33} = 2 * \mu * \varepsilon_{33} + \lambda * (\varepsilon_{11} + \varepsilon_{22} + \varepsilon_{33}) \tag{B.4}$$

$\sigma_{11}(N20E)$ = 4800Pa/y or 4.8 MPa after 1000yr (assumed Recurrence Interval for large earthquakes)
$\sigma_{22}(vertical)$ = 1800Pa/yor 1.8 MPa / kyr
$\sigma_{33}(N110E)$ = 2400Pa/yor 2.4 MPa / kyr

Fault data and sketch of the parameters that define a fault (redrawn after FIMoz Manual)

| | **x_center (fault plane)** | **y_center (fault plane)** | **z_center (fault plane)** | **Azimuth** | **dip** | **Fault length** | **Fault Width** | **z** | **# l** | **# w** |
|---|---|---|---|---|---|---|---|---|---|---|
| | [m] | [m] | [m] | [deg] | [deg] | [m] | [m] | [m] | | |
| MFFeast | 606565 | 3957109 | -6100 | 285 | 70 | 71600 | 12770 | 12000 | 36 | 6 |
| MFFe-deep | 607311 | 3959894 | -13600 | 285 | 65 | 71600 | 3310 | 3000 | 36 | 2 |
| MFFcentral | 543381 | 3980832 | -4600 | 296 | 55 | 63000 | 10987 | 9000 | 32 | 5 |
| MFFc-deep | 545376 | 3984921 | -12100 | 296 | 65 | 63000 | 6620 | 6000 | 32 | 3 |
| MFFwest | 490924 | 3993182 | -6100 | 268 | 70 | 45000 | 12770 | 12000 | 23 | 6 |
| MFFw-deep | 490823 | 3996064 | -13600 | 268 | 65 | 45000 | 3310 | 3000 | 23 | 2 |
| Firuzkuh F. | 659430 | 3954034 | -6100 | 66 | 80 | 38000 | 12185 | 12000 | 19 | 6 |
| NTT NW | 492073 | 3974556 | -2100 | 304 | 20 | 49000 | 11695 | 4000 | 25 | 6 |
| PVT | 516699 | 3968333 | -2100 | 309 | 25 | 23000 | 9465 | 4000 | 12 | 5 |
| PVT deep | 522993 | 3976106 | -8100 | 309 | 35 | 23000 | 13948 | 8000 | 12 | 7 |
| EDF | 528633 | 3974730 | -6100 | 308 | 60 | 33753 | 13856 | 12000 | 17 | 7 |
| EDF deep | 531540 | 3978451 | -13600 | 308 | 50 | 33753 | 3916 | 3000 | 17 | 2 |
| EDF west | 500302 | 3988451 | -6100 | 275 | 60 | 25000 | 13856 | 12000 | 13 | 7 |
| EDF w-deep | 500714 | 3993156 | -13600 | 275 | 50 | 25000 | 3916 | 3000 | 13 | 2 |
| Taleghan-MFF | 508492 | 3997320 | -6100 | 121 | 88 | 12121 | 12007 | 12000 | 6 | 6 |
| Taleghan-east | 565609 | 3985013 | -6100 | 282 | 85 | 56818 | 12046 | 12000 | 28 | 6 |
| Taleghan-central-e | 529254 | 3994959 | -6100 | 299 | 85 | 18182 | 12046 | 12000 | 9 | 6 |
| Taleghan-central-w | 512564 | 4000521 | -6100 | 277 | 85 | 15909 | 12046 | 12000 | 8 | 6 |
| Taleghan-west | 478018 | 3998475 | -6100 | 88 | 85 | 49242 | 12046 | 12000 | 25 | 6 |
| NTT-west | 522045 | 3962830 | -6100 | 254 | 60 | 28244 | 13856 | 12000 | 14 | 7 |
| NTT-center | 547221 | 3965583 | -6100 | 260 | 75 | 24000 | 12423 | 12000 | 12 | 6 |
| NTT-east | 564751 | 3965588 | -6100 | 279 | 75 | 9600 | 12423 | 12000 | 5 | 6 |

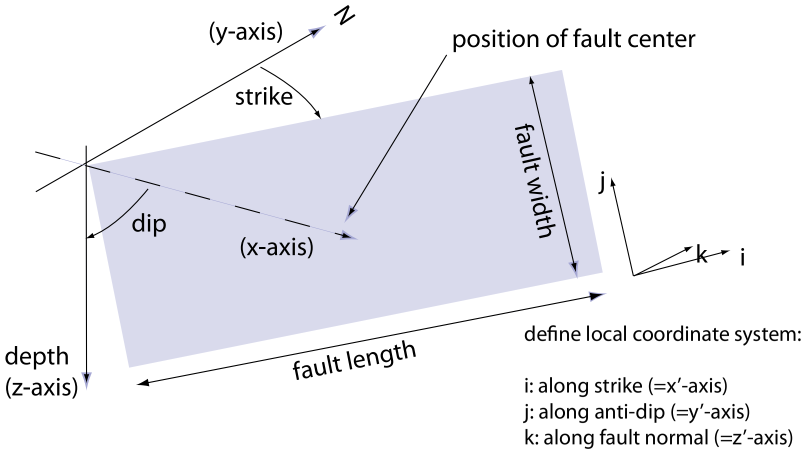

Figure B.1: Geometry and model parameters of the implemented faults, according to FIMoz requirements (cf. sketch below). Abbreviations of names are: MFF-Mosha-Fasham Fault, NTT-North Tehran Thrust, NTT NW -Northwest prolongation of NTT, PVT-Purkan-Vardij Thrust, EDF-Emamzadeh-Davud Fault; e-east, c-central, w-west segment, respectively. If fault segments change dip towards depth, the associated fault segment name has the annex "deep". Fault segments are defined according to their central coordinates; here, the numbers for x and y represent UTM coordinates (Zone 39N). The depth across which the fault segments extend is z, i.e. the eastern MFF, for instance, is assumed to cross a seismogenic layer of 15 km, while at 12 km depth the dip is changing from 70° to 65°N. "♯ l" and "♯ w" are numbers of subdivision patches along length and width of the fault segment, respectively.

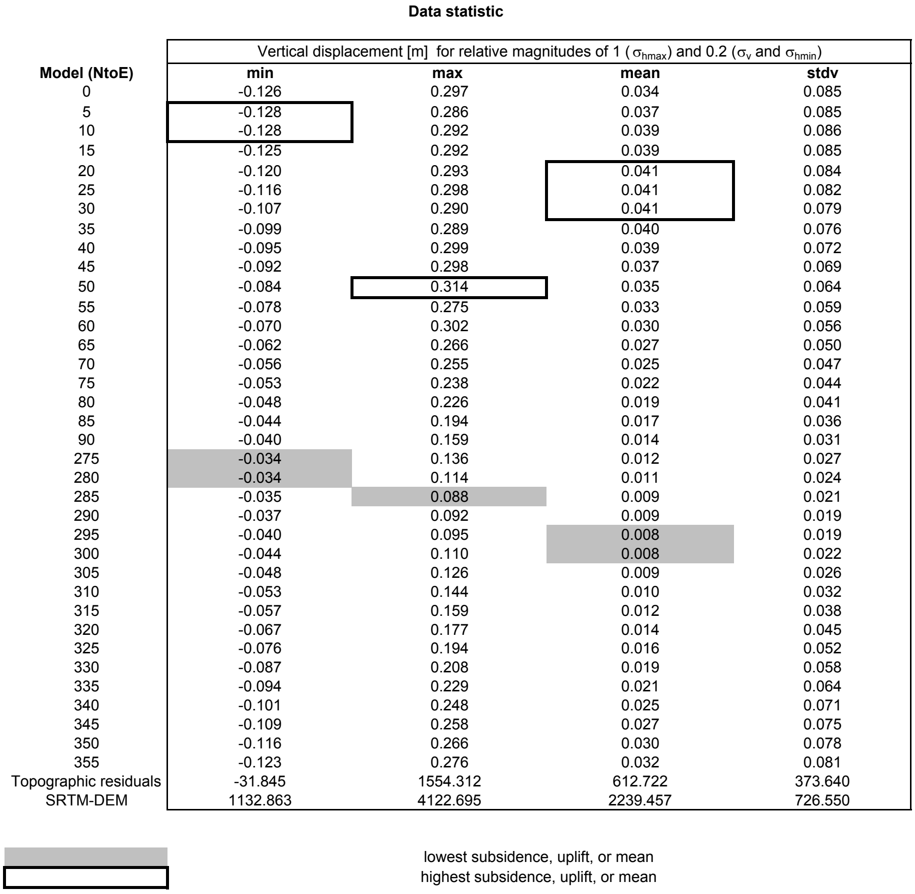

**Data statistic**

| **Model (NtoE)** | Vertical displacement [m] for relative magnitudes of 1 ($\sigma_{hmax}$) and 0.2 ($\sigma_v$ and $\sigma_{hmin}$) | | | |
|---|---|---|---|---|
| | **min** | **max** | **mean** | **stdv** |
| 0 | -0.126 | 0.297 | 0.034 | 0.085 |
| 5 | -0.128 | 0.286 | 0.037 | 0.085 |
| 10 | -0.128 | 0.292 | 0.039 | 0.086 |
| 15 | -0.125 | 0.292 | 0.039 | 0.085 |
| 20 | -0.120 | 0.293 | 0.041 | 0.084 |
| 25 | -0.116 | 0.298 | 0.041 | 0.082 |
| 30 | -0.107 | 0.290 | 0.041 | 0.079 |
| 35 | -0.099 | 0.289 | 0.040 | 0.076 |
| 40 | -0.095 | 0.299 | 0.039 | 0.072 |
| 45 | -0.092 | 0.298 | 0.037 | 0.069 |
| 50 | -0.084 | 0.314 | 0.035 | 0.064 |
| 55 | -0.078 | 0.275 | 0.033 | 0.059 |
| 60 | -0.070 | 0.302 | 0.030 | 0.056 |
| 65 | -0.062 | 0.266 | 0.027 | 0.050 |
| 70 | -0.056 | 0.255 | 0.025 | 0.047 |
| 75 | -0.053 | 0.238 | 0.022 | 0.044 |
| 80 | -0.048 | 0.226 | 0.019 | 0.041 |
| 85 | -0.044 | 0.194 | 0.017 | 0.036 |
| 90 | -0.040 | 0.159 | 0.014 | 0.031 |
| 275 | -0.034 | 0.136 | 0.012 | 0.027 |
| 280 | -0.034 | 0.114 | 0.011 | 0.024 |
| 285 | -0.035 | 0.088 | 0.009 | 0.021 |
| 290 | -0.037 | 0.092 | 0.009 | 0.019 |
| 295 | -0.040 | 0.095 | 0.008 | 0.019 |
| 300 | -0.044 | 0.110 | 0.008 | 0.022 |
| 305 | -0.048 | 0.126 | 0.009 | 0.026 |
| 310 | -0.053 | 0.144 | 0.010 | 0.032 |
| 315 | -0.057 | 0.159 | 0.012 | 0.038 |
| 320 | -0.067 | 0.177 | 0.014 | 0.045 |
| 325 | -0.076 | 0.194 | 0.016 | 0.052 |
| 330 | -0.087 | 0.208 | 0.019 | 0.058 |
| 335 | -0.094 | 0.229 | 0.021 | 0.064 |
| 340 | -0.101 | 0.248 | 0.025 | 0.071 |
| 345 | -0.109 | 0.258 | 0.027 | 0.075 |
| 350 | -0.116 | 0.266 | 0.030 | 0.078 |
| 355 | -0.123 | 0.276 | 0.032 | 0.081 |
| Topographic residuals | -31.845 | 1554.312 | 612.722 | 373.640 |
| SRTM-DEM | 1132.863 | 4122.695 | 2239.457 | 726.550 |

▨ lowest subsidence, uplift, or mean
☐ highest subsidence, uplift, or mean

Figure B.2: Minimum and maximum vertical displacement as well as mean and standard deviation of the separate models prior to their normalization. The absolute values are relatively small because the models have been loaded with small relative stress magnitudes. Highest subsidence is achieved with maximum horizontal compression direction of N5E to N10E, while highest uplift is reached with maximum horizontal compression direction of N50E and corresponds to the Mount Bajdan area. In contrast, the models N20E to N30E yield the highest mean. Comparing with Fig. B7, these models show the most extensive uplift by area.

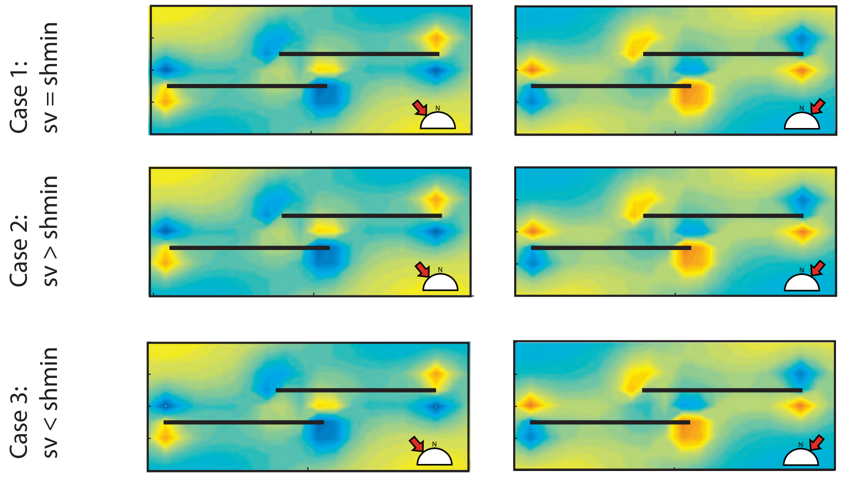

Step over with vertical fault segments

*Case1:*
*allows strike-slip &*
*thrusting*

*Case2:*
*promotes strike-slip*

*Case3:*
*promotes thrusting*

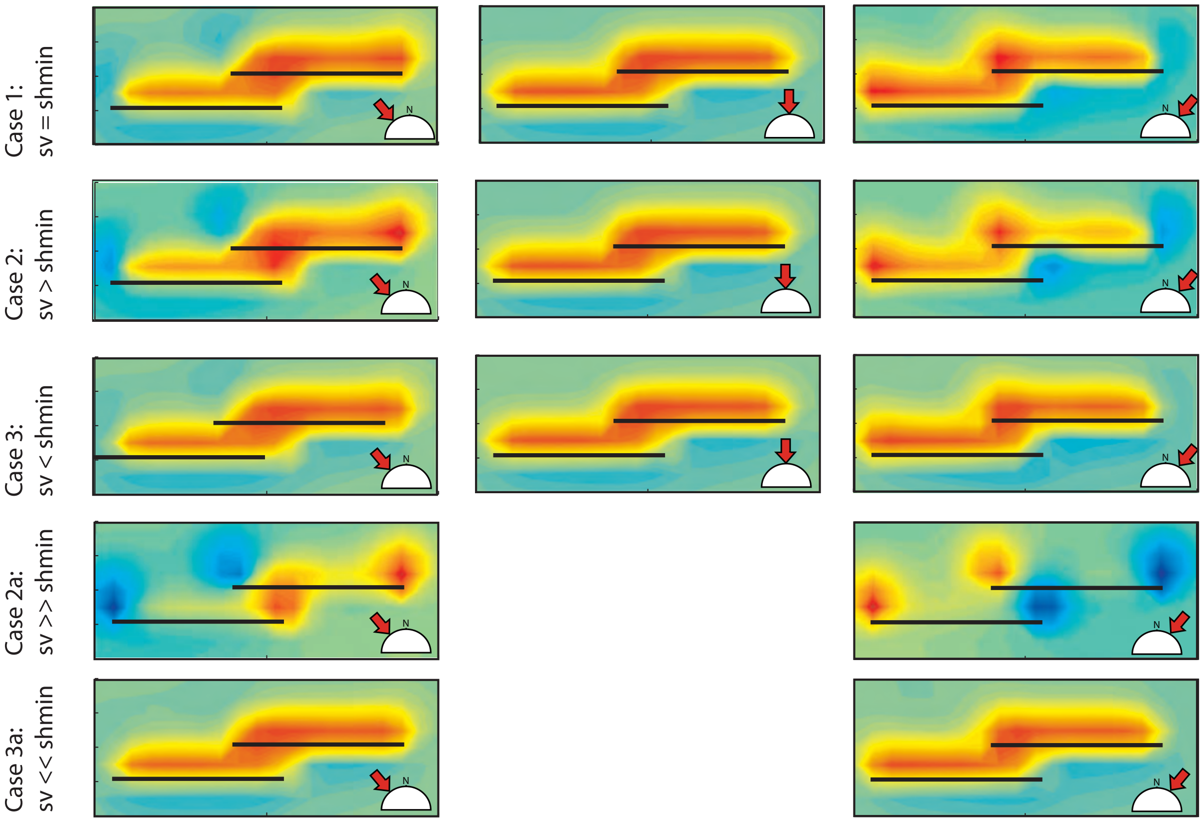

Step over with segments, dipping 50°N

| | *Case1:* | *Case2:* | *Case3:* | *Case2a:* | *Case3a:* |
|---|---|---|---|---|---|
| SHmax | 1 | 1 | 1 | 1 | 1 |
| Sv | 0.2 | 0.3 | 0.1 | 0.5 | 0.1 |
| Shmin | 0.2 | 0.1 | 0.3 | 0.1 | 0.5 |

Figure B.3: Results of different loading directions and magnitudes of differential stress on a left-stepping step-over array. Magnitudes for the different cases are given in the table below the figure. As in comparable figures of the main paper, the inset shows the loading direction ($S_{Hmax}$), while red colors show uplift and blue colors subsidence, respectively. In Case 1, the magnitudes for vertical and least horizontal stress are similar. Thus, this scenario should represent a transpressional environment, which allows both thrusting and strike-slip faulting. In this scenario, the geometry of the faults and their orientation relative to the shortening direction dominates the results. In contrast, Case 2 and 2a represent settings which promote strike-slip, while Case3 and 3a rather promote thrusting. As visible in the upper figures, changes in differential stress magnitudes has no effect on the displacement in the vertical step-over array. In contrast, along an N-dipping fault array, while generally widespread uplift is the dominant result, the focus of uplift is changing between the different scenarios. Moreover, while NW-directed compression would generally produce uplift in the segment overlap, the effects of changes in differential stress are even more pronounced between the different scenarios of NE-directed compression, where geometry related subsidence between the segments is competing with the uplift resulting from the northward dip of the faults.

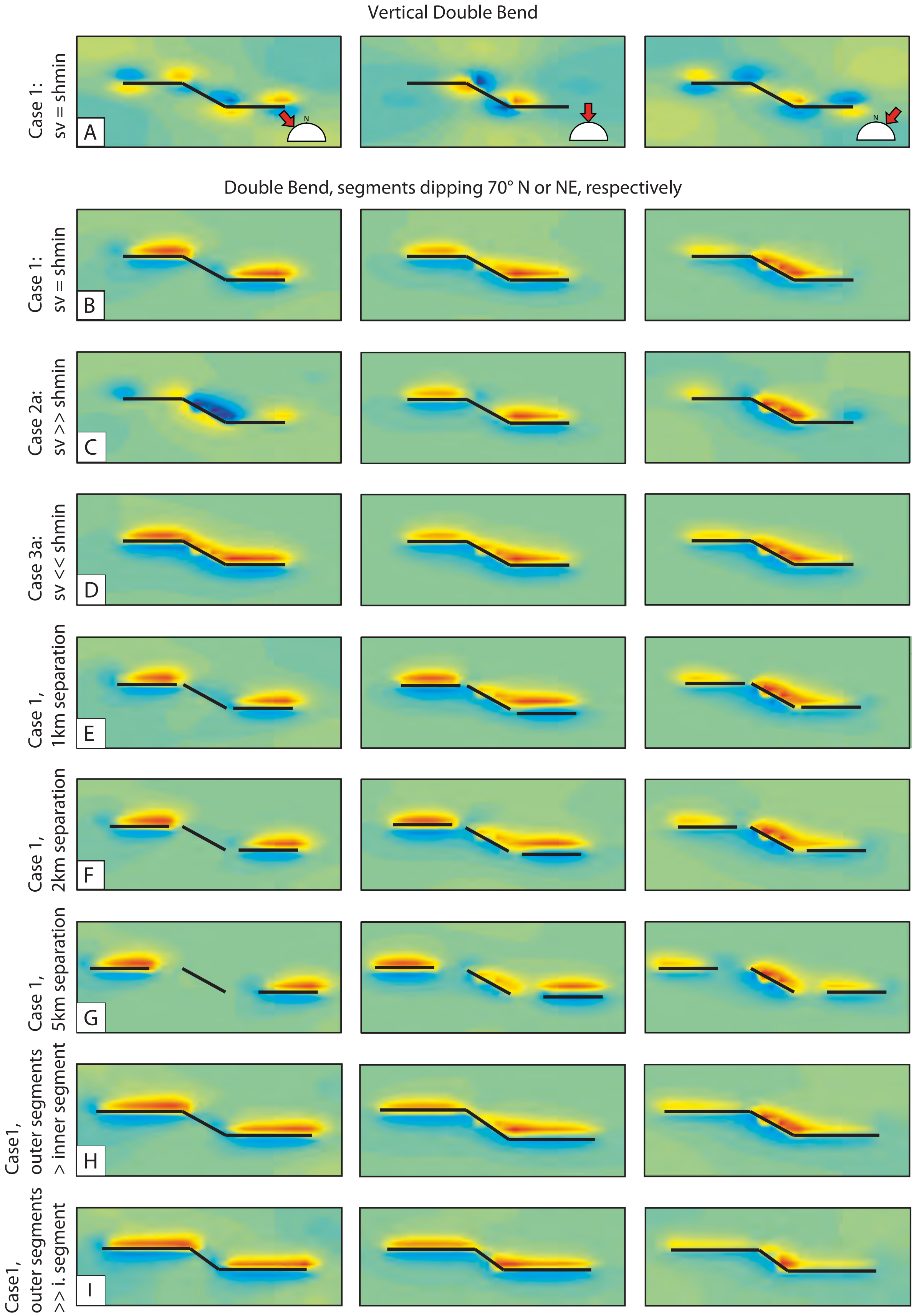
Vertical Double Bend
Case 1:
sv = shmin
A
N
N
Double Bend, segments dipping 70° N or NE, respectively
Case 1:
sv = shmin
B
Case 2a:
sv >> shmin
C
Case 3a:
sv << shmin
D
Case 1,
1km separation
E
Case 1,
2km separation
F
Case 1,
5km separation
G
Case1,
outer segments
> inner segment
H
Case1,
outer segments
>> i. segment
I

Figure B.4: Results of different loading directions and magnitudes of differential stress on a double-bend array. The effects of linkage versus separation (B, E-G), and different length ratios (B, H-I) between the segments are investigated. Definition of the cases and color coding are comparable to Figure B3: Case 2a promotes strike-slip, while Case 3a promotes thrusting. Panel A shows the effects of a transpressional setting on a vertical double-bend. Uplift is focused in the "inset corner" of the segments relative to the compression direction (middle and right column). NW-directed compression yields subsidence in the same corner, which is related to the dextral motion at the E-W striking segments, while the middle segment, which strikes parallel to the compression direction, will not alter the displacement field. If the fault segments are not vertical, the amount of uplift increases and the distribution is strongly related to the geometry of the double-bend with respect to the compression direction. Separation between the segments changes the uplift distribution slightly. While 1 and 2 km separation have only minor effects, a 5 km separation between the segments shows basically vertical displacement of the single segments without obvious evidence of interaction. Uplift patterns also change with different length ratios between the segments: a high outer/inner segment ratio cause more pronounced focus of uplift in the "inside corner" for NE-directed compression, which is otherwise a more pronounced result of N-directed compression.

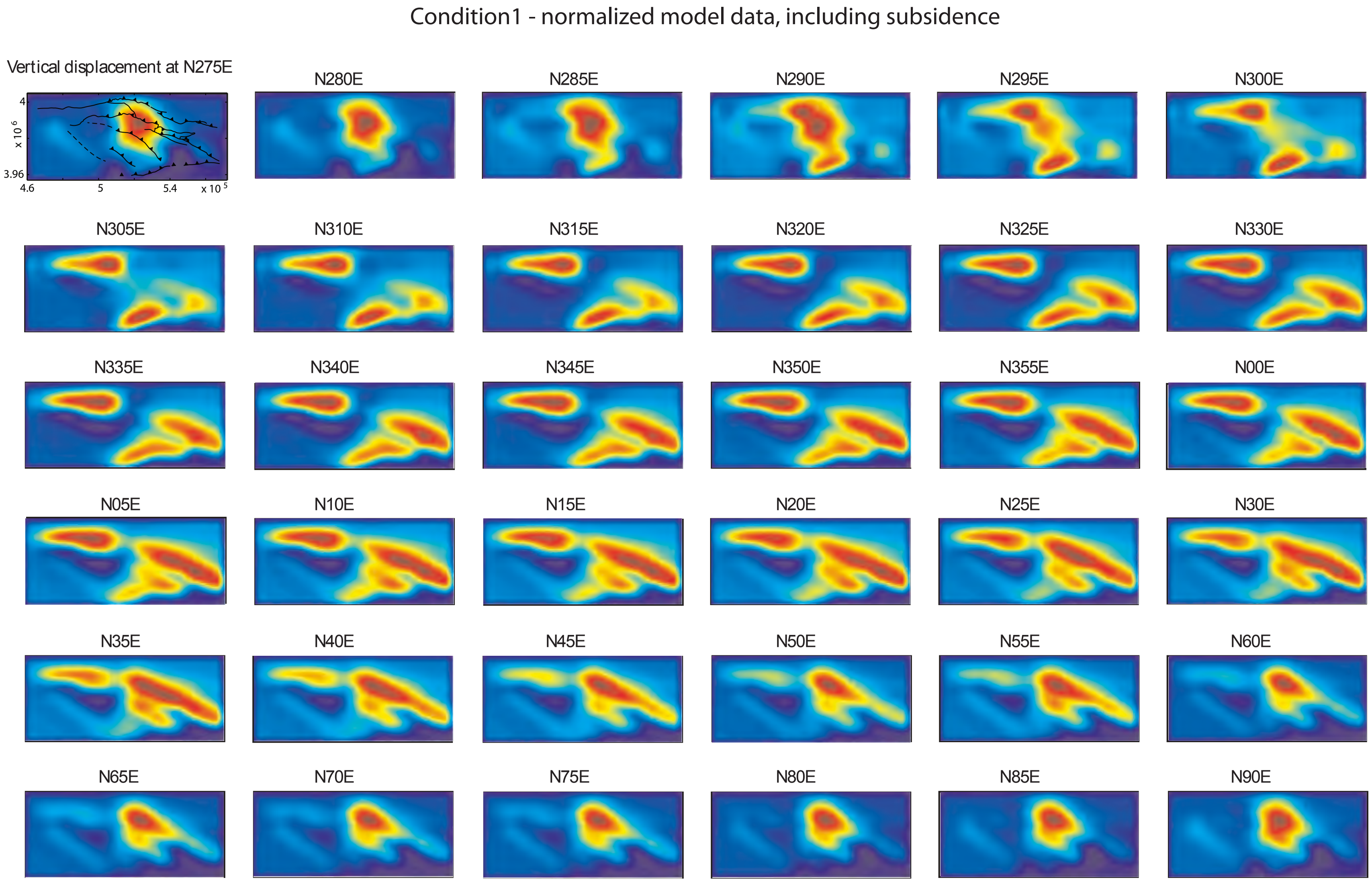

Figure B.5: Normalized vertical displacement fields of all interaction models, calculated at 5° increment changes in compression direction. Here, normalization was calculated using condition1, which includes subsidence (cf. Methods section). The fault array causes interaction between the segments which at different compression directions cause different areas in the array to uplift or subside, respectively.

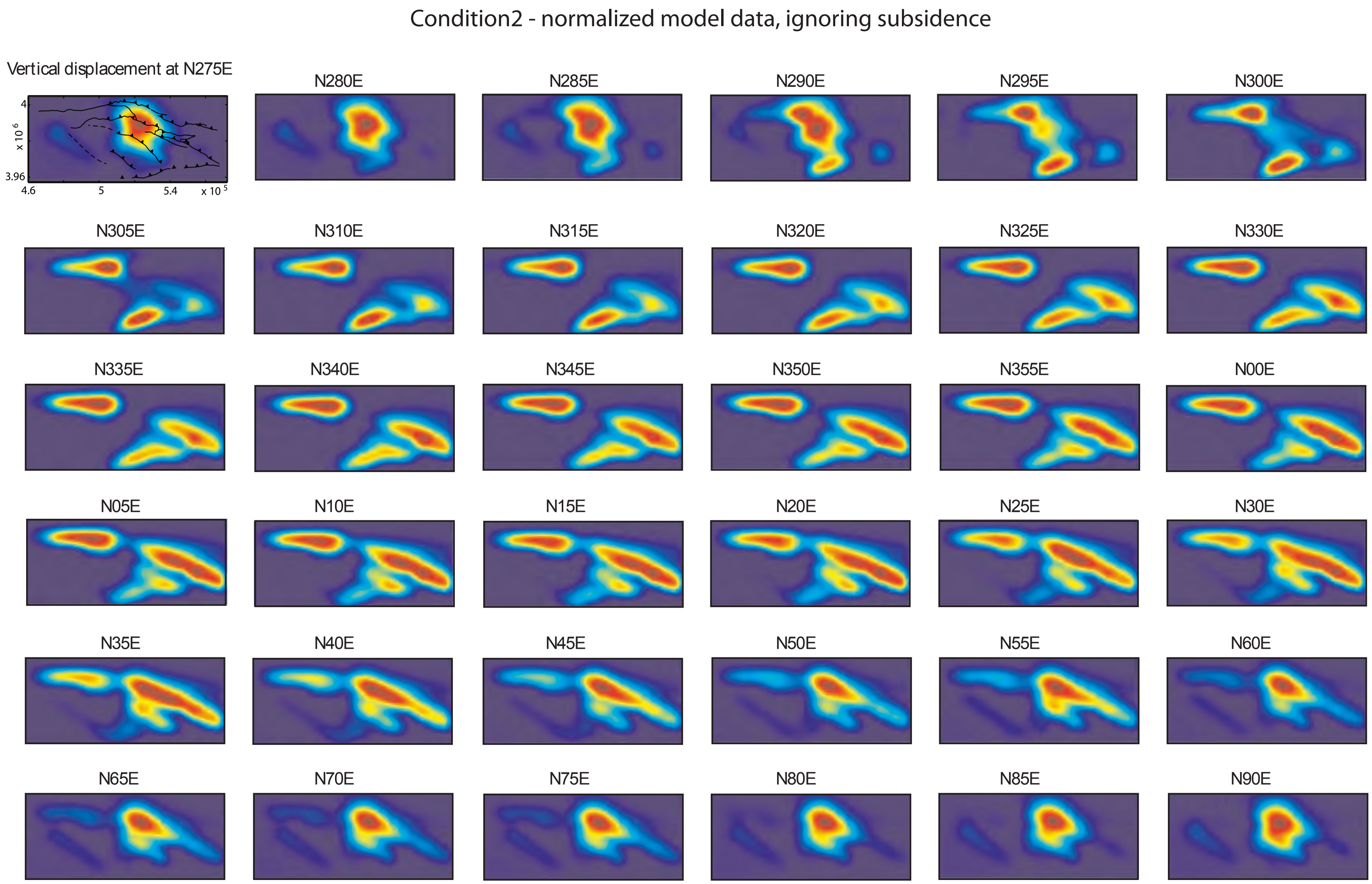

Figure B.6: Normalized vertical displacement fields of all interaction models, calculated at 5° increment changes in compression direction. Here, normalization was calculated using condition2, which ignores subsidence (cf. Methods section), i.e., areas, which do not undergo uplift are set at zero. The fault array causes interaction between the segments which at different compression directions cause different areas in the array to uplift or subside, respectively. However, the correlation coefficient between model and topographic metrics is generally higher in Condition2 models, i.e., subsidence cannot be handled or compared, probably, because such basins get refilled soon and thus lose their signature in the topographic metrics.

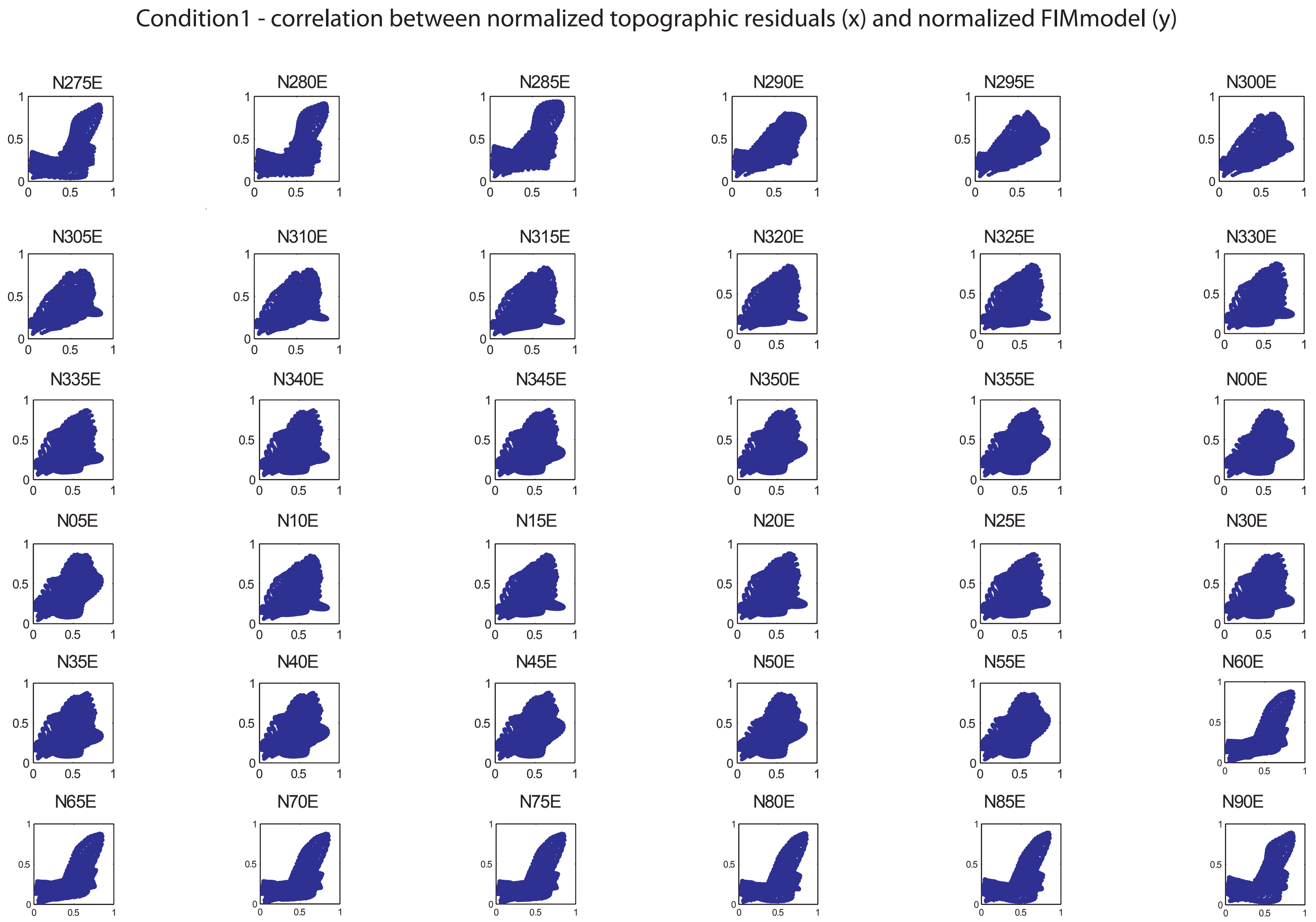

Figure B.7: Correlation plots, showing pixel-wise comparison between normalized topographic residuals (on x-axis) and normalized models (on y-axis), i.e., the vertical displacement, respectively. Here, normalization was calculated using condition1, which includes subsidence (cf. Methods section). Generally, a linear trend with some scatter seems to exist, suggesting that parts of the model results and topographic metrics correlate. However, in some models (N275E to N290E and N60E to N90E) a kink in the data cluster suggests that especially the small displacement values ($< 0.4$) do not correlate. Considering the normalization, this means that basically subsidence does not correlate with low topographic residuals or that areas, which undergo subsidence can correspond to small to moderate topographic residuals. However, also areas of only small uplift do not correlate well, as visible in Figure DR6, where subsidence is ignored, but the same kink in the data cluster is only suppressed to lower values.

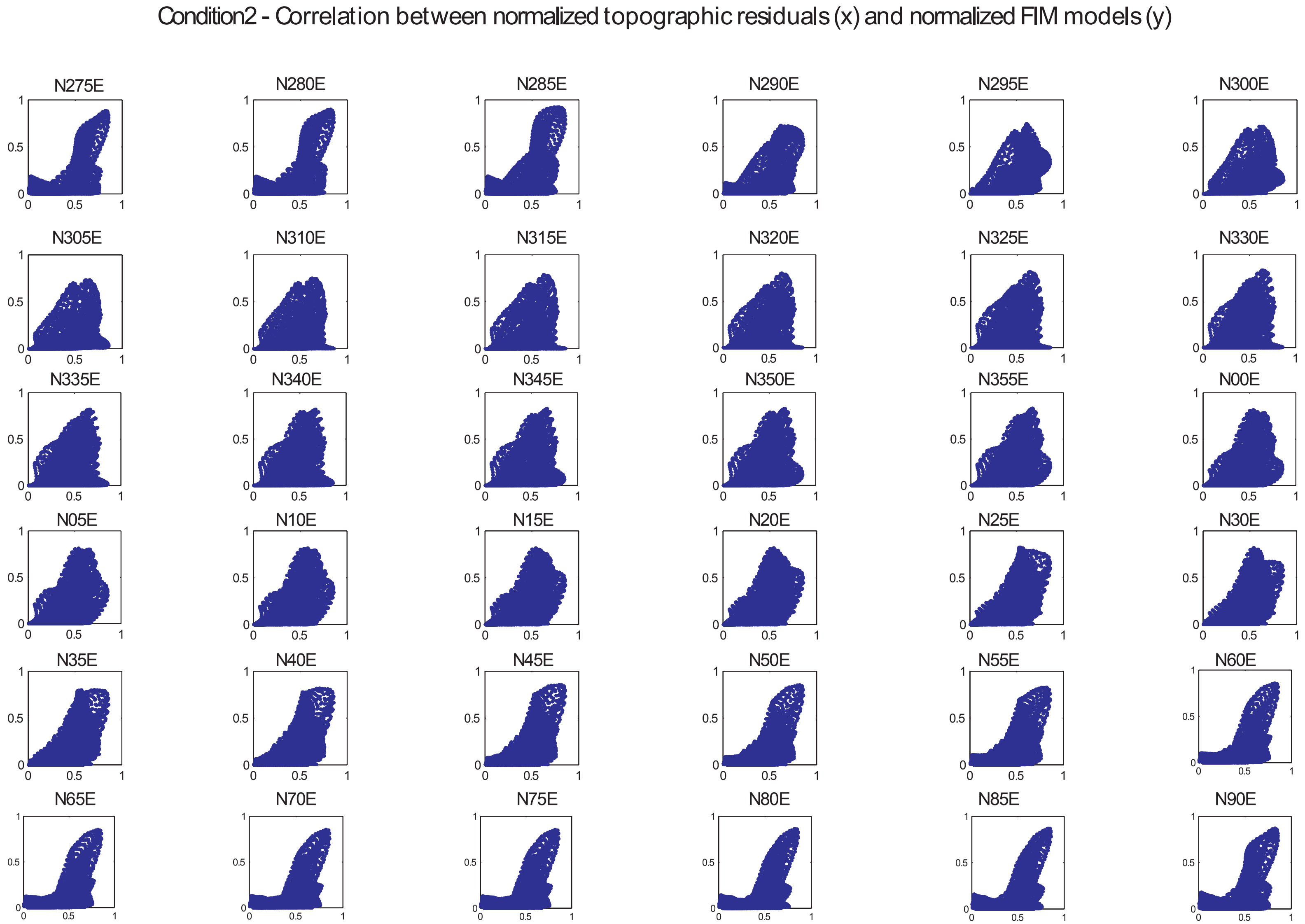

Figure B.8: Correlation plots, showing pixel-wise comparison between normalized topographic residuals (on x-axis) and normalized models (on y-axis), i.e., the vertical displacement, respectively. Here, normalization was calculated using condition2, which ignores subsidence (cf. Methods section), i.e., areas, which do not undergo uplift, get the zero value. The in Figure DR5 described kink is suppressed to lower values and the uplift is generally more stretched due to the normalization, which results in better general correlation.

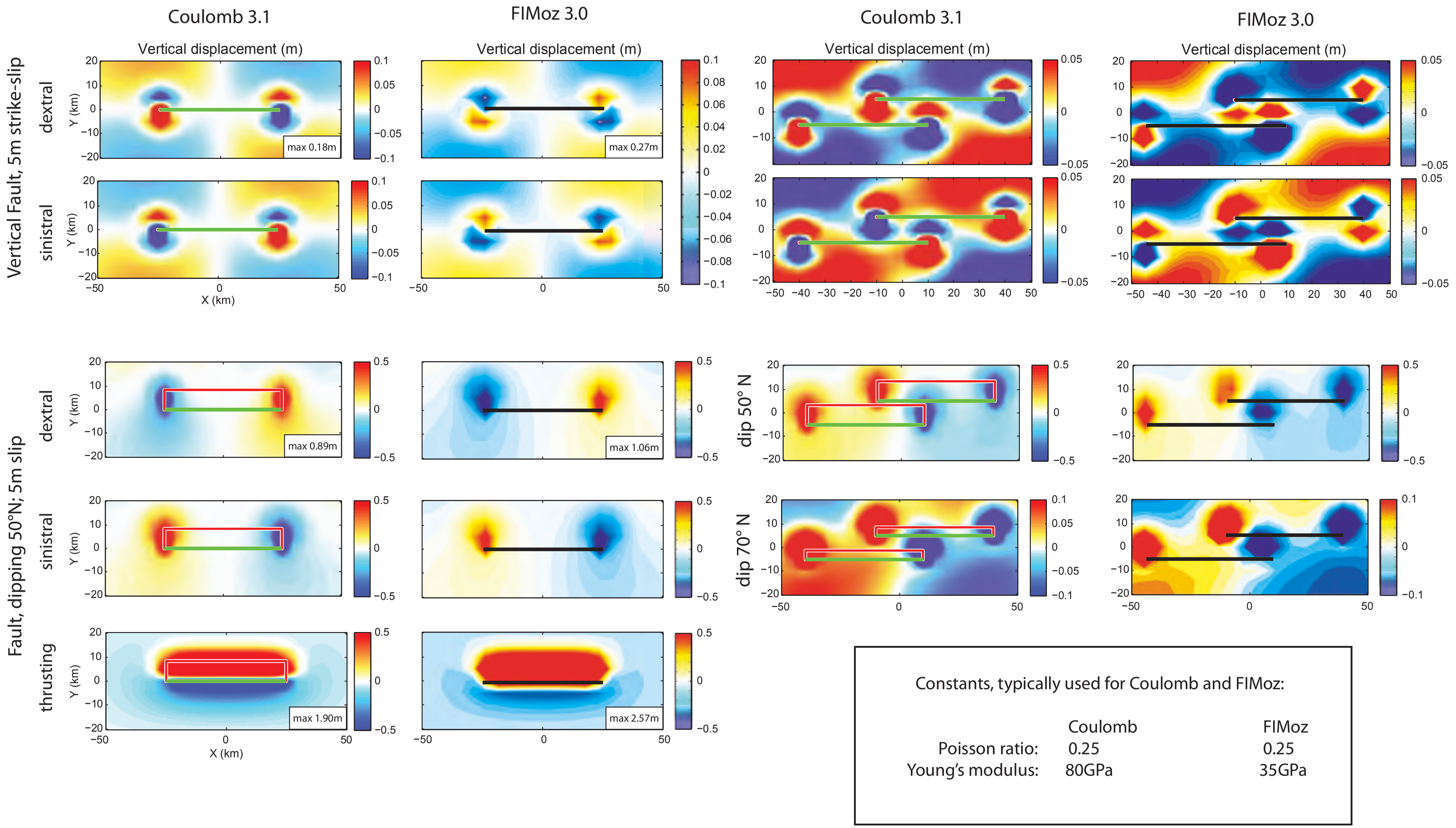

Constants, typically used for Coulomb and FIMoz:

| | Coulomb | FIMoz |
|---|---|---|
| Poisson ratio: | 0.25 | 0.25 |
| Young's modulus: | 80GPa | 35GPa |

Figure B.9: Comparison of results of some simple scenarios, calculated with Coulomb3.0 and FIMoz, respectively. To build confidence into the FIMoz program, we have cross checked results with another, well -known deformation and stress-change software (Coulomb 3.0) after Lin & Stein (2004) and Toda et al. (2005). However, applications of both programs differ in that Coulomb is not using regional stress for pre-defined receiver faults, but only for optimally oriented faults. We therefore have calculated and compared slip conditions for different scenarios of the same geometry, respectively. Besides small differences in the color scheme (different stretching; Coulomb is using interpolation, FIMoz filled contours), the basic geometry of uplift and subsidence agree.

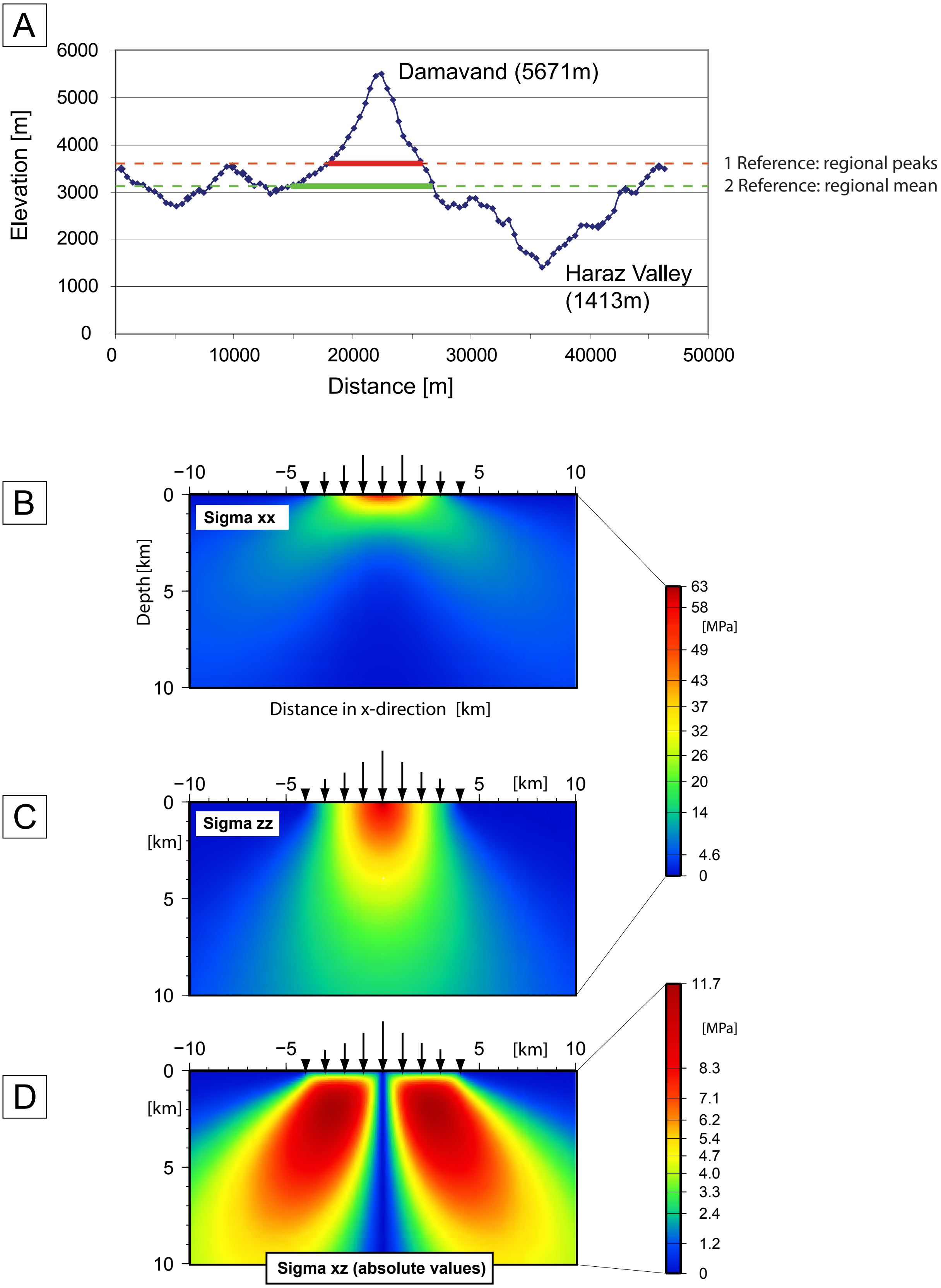
A
Elevation [m]
6000
5000
4000
3000
2000
1000
0
Damavand (5671m)
Haraz Valley
(1413m)
1 Reference: regional peaks
2 Reference: regional mean
0
10000
20000
30000
40000
50000
Distance [m]
B
Sigma xx
Depth [km]
Distance in x-direction [km]
−10
−5
5
10
0
5
10
63
58
[MPa]
49
43
37
32
26
20
14
4.6
0
C
Sigma zz
[km]
D
Sigma xz (absolute values)
11.7
[MPa]
8.3
7.1
6.2
5.4
4.7
4.0
3.3
2.4
1.2
0

Figure B.10: Calculation of stress distribution caused by topographic load of the Damavand volcano. Figure A shows the topographic E-W profile across the volcano, based on SRTM-DEM. Thus, the volcano has a height of about 2100 m above regional peaks, or of about 2600 m above the regional mean elevation, corresponding to an additional topographic load of 51.5 MPa, or 63 MPa at the reference base, respectively. Density is assumed to be 2500 kg/m$^3$. Using the formulas of Dahm (2000) and the regional mean elevation as reference, we have calculated the depth distribution of stress caused by the topographic load. While the horizontal stress diminishes fast after only 2-3 km (Fig. B), about 1/3 of the vertical stress (about 20 MPa) is still available in 10 km depth (approx. locking depth of the underlying fault), which is about a magnitude less than the assumed prevalent lithostatic stress of about 250 MPa at this depth (Fig. C). However, the additional amount of shear stress that is caused by the volcano has the maximum (about 12 MPa) in about 2 km depth (Fig. D). In 10 km depth are still about 5 MPa additional shear stress available.

# Appendix C

# (to Chapter 5)

to: **Quaternary deformation in the Tehran plain deduced from $^{10}Be$ and $^{36}Cl$ depth profiles of alluvial geomorphic surfaces (Chapter 5)**

# Abstract and Acknowledgements

**Abstract** Ongoing deformation in the south-central Alborz foreland results in oblique motion along the main structures in the Tehran plain, with fault-propagation folding along major faults, limited strike-slip motion and en-echelon arrays of second-order upper plate thrusts. While the Tehran Plain records Quaternary deformation, the majority of faulting took place in the early stages of Quaternary and before. The present analysis clearly shows that the two oldest recognized phases of alluviation, subsequent erosion, and faulting, which affect units A and B, occurred prior to the late Pleistocene. The rate of erosion is generally higher than expected, bringing Be-concentrations into saturation already between 200 and 300 ka. The oldest dated surface age is the Saboo erosional surface of 195 ka. Abandoned terrace ages that probably correspond to incision, subsequently to deposition of unit C, have late Pleistocene ages along the Kan River in the west and the Jajrud River in the east. This allows to infer a "background" incision rate and to relate increased pulses of Holocene incision to repeated earthquake ruptures.

**Acknowledgements** This work was funded by the German Research Council (DFG project STR 373/19 – 1 and funds from the DFG Leibniz Award to M. Strecker). We want to thank M.B. Bateman from the Sheffield Centre for International Drylands Research (SCIDR) luminescence laboratory for providing the optically stimulated luminescence (OSL) data. We greatly appreciate logistical help from the Tehran Building and Housing Research Center. In particular, we would like to thank A.H. Heidarinejad, T. Parhizkar, and A.H. Mirzaei for their encouragement. We wish to thank B. Fabian for her help with the illustrations and M. Wieprich, D. Pilz, and S. Andrae for help with sample preparation. C. Fischer is thanked for preparing the diorite thin section and C. Günter for XRD and microprobe analysis. We thank A. Musiol and K. Pou for ICP measurements. Our interpretations have benefited from discussions with G. Zeilinger, F. Kober, J.-F. Ritz, and J.R. Arrowsmith.

| **Sample name** | Latitude [dd] | Longitude [dd] | Elevation [m] | Elv/Pressure [mbar] | Thickness [cm] | Density [g/cm$^3$] | Shielding [] | Depth* [g/cm$^2$] | $^{10}Be$ [at/g] | $\pm^{10}Be$ [at/g] | $^{36}Cl$ [at/g] | $\pm^{36}Cl$ [at/g] | $^{26}Al$ [at/g] | $\pm^{26}Al$ [at/g] |
|---|---|---|---|---|---|---|---|---|---|---|---|---|---|---|
| **Upper Jajrud** | | | | | | | | | | | | | | |
| **13-1-1** | 35.757000 | 51.6927200 | 1570 | 839 | 10 | 1.75 | 0.998 | 105 | 384,391 | 23,125.75 | 1,470,980 | 26,344 | NaN | NaN |
| **13-1-3** | 35.757000 | 51.6927200 | 1570 | 839 | 10 | 1.75 | 0.998 | 192.5 | 134,746 | 6,458.96 | 978,310 | 17,781 | NaN | NaN |
| **13-1-4aA** | 35.757000 | 51.6927200 | 1570 | 839 | 6 | 2.2 | 0.998 | 281.6 | 196,181 | 5,669.35 | 1,109,503 | 20,429 | NaN | NaN |
| **13-1-4aB** | 35.757000 | 51.6927200 | 1570 | 839 | 6 | 2.2 | 0.998 | 282.6 | NaN | NaN | 1,050,260 | 33,054 | NaN | NaN |
| **13-1-4** | 35.757000 | 51.6927200 | 1570 | 839 | 10 | 1.75 | 0.998 | 262.5 | 102,116 | 5,855.49 | 651,362 | 11,785 | NaN | NaN |
| **13-1-5** | 35.757000 | 51.6927200 | 1570 | 839 | 10 | 1.75 | 0.998 | 332.5 | 121,766 | 5,131.74 | 665,345 | 11,764 | NaN | NaN |
| **15-1-1** | 35.757000 | 51.6927200 | 1570 | 839 | 10 | 1.75 | 0.998 | 420 | 45,194 | 3,307.79 | 595,637 | 11,700 | NaN | NaN |
| **Lower Jajrud** | | | | | | | | | | | | | | |
| **13-2-1** | 35.756972 | 51.6944000 | 1545 | 841 | 10 | 1.75 | 0.995 | 8.75 | 701,221 | 21,839.15 | 2,075,770 | 34,807 | NaN | NaN |
| **13-2-2** | 35.756972 | 51.6944000 | 1545 | 841 | 10 | 1.75 | 0.995 | 92.75 | 520,423 | 14,701.44 | 2,255,450 | 91,304 | NaN | NaN |
| **13-2-3** | 35.756972 | 51.6944000 | 1545 | 841 | 10 | 1.75 | 0.995 | 113.75 | 392,493 | 18,105.85 | 2,095,278 | 58,226 | NaN | NaN |
| **Saboo** | | | | | | | | | | | | | | |
| **23-1-0A** | 35.821167 | 51.6827222 | 1852 | 810 | 2 | 2.8 | 0.999 | 2.797 | 1,111,905 | 51,565 | 2,926,165 | 39,438 | NaN | NaN |
| **23-1-2a** | 35.821167 | 51.6827222 | 1852 | 810 | 10 | 1.75 | 0.999 | 113.750 | 1,979,585 | 213,550 | 2,457,067 | 29,475 | NaN | NaN |
| **23-1-3a** | 35.821167 | 51.6827222 | 1852 | 810 | 10 | 1.75 | 0.999 | 162.750 | 1,688,244 | 125,592 | 2,161,450 | 40,199 | NaN | NaN |
| **23-1-6a** | 35.821167 | 51.6827222 | 1852 | 810 | 10 | 1.75 | 0.999 | 323.750 | 493,425 | 136,860 | 1,047,035 | 19,418 | NaN | NaN |
| **23-1-8a** | 35.821167 | 51.6827222 | 1852 | 810 | 10 | 1.75 | 0.999 | 428.75 | NaN | NaN | 807,301 | 16,900 | NaN | NaN |
| **23-1-10a** | 35.821167 | 51.6827222 | 1852 | 810 | 10 | 1.75 | 0.999 | 533.750 | 266193 | 37283 | 647665 | 12354 | NaN | NaN |
| **23-1-1b** | 35.821167 | 51.6827222 | 1852 | 810 | 5 | 2 | 0.999 | 141.000 | 1,223,216 | 39,373 | 2,791,150 | 96,625 | NaN | NaN |
| **23-1-3b** | 35.821167 | 51.6827222 | 1852 | 810 | 20 | 2 | 0.999 | 280.000 | 428,676 | 44,712 | NaN | NaN | NaN | NaN |
| **23-1-4bA** | 35.821167 | 51.6827222 | 1852 | 810 | 10 | 1.96 | 0.999 | 440.325 | 231,068 | 9,869 | 1,068,999 | 25,589 | NaN | NaN |
| **23-1-4bB** | 35.821167 | 51.6827222 | 1852 | 810 | 10 | 1.96 | 0.999 | 440.325 | NaN | NaN | 1,044,366 | 20,127 | NaN | NaN |
| **23-1-5b** | 35.821167 | 51.6827222 | 1852 | 810 | 25 | 2.58 | 0.999 | 650.440 | 123,761 | 43,758 | NaN | NaN | NaN | NaN |
| **23-1-0B1** | 35.821167 | 51.6827222 | 1852 | 810 | 1 | 1.77 | 0.999 | 0.89 | 1,048,470 | 31,977 | 3,201,330 | 78,211 | NaN | NaN |
| **23-1-0B2** | 35.821167 | 51.6827222 | 1852 | 810 | 1 | 1.77 | 0.999 | 0.89 | NaN | NaN | 3,334,132 | 49,672 | NaN | NaN |
| **23-1-4c** | 35.821167 | 51.6827222 | 1852 | 810 | 13 | 2.86 | 0.999 | 190.390 | 1,530,800 | 44,058 | NaN | NaN | NaN | NaN |
| **23-1-5c** | 35.821167 | 51.6827222 | 1852 | 810 | 10 | 2.38 | 0.999 | 297.375 | 616,114 | 42,357 | NaN | NaN | NaN | NaN |
| **23-1-1c** | 35.821167 | 51.6827222 | 1852 | 810 | 20 | 2.53 | 0.999 | 430.100 | 166,713 | 15,554 | NaN | NaN | NaN | NaN |

Table C.1: Scaling parameters

Sample codes and background information used for site-specific scaling (Part 1). Depth* corresponds to density and thickness corrected depth, shielding factor corresponds to topographic shielding only.

| **Sample name** | Latitude [dd] | Longitude [dd] | Elevation [m] | Elv/Pressure [mbar] | Thickness [cm] | Density [g/cm$^3$] | Shielding [] | Depth* [g/cm$^2$] | $^{10}Be$ [at/g] | $\pm^{10}Be$ [at/g] | $^{36}Cl$ [at/g] | $\pm^{36}Cl$ [at/g] | $^{26}Al$ [at/g] | $\pm^{26}Al$ [at/g] |
|---|---|---|---|---|---|---|---|---|---|---|---|---|---|---|
| **Kan** | | | | | | | | | | | | | | |
| **K10-14** | 35.746444 | 51.2676666 | 1326 | 864 | 1 | 2.5 | 0.995 | 10.000 | 91,363 | 13,190 | NaN | NaN | NaN | NaN |
| **101006-15** | 35.743111 | 51.2695555 | 1345 | 862 | 2 | 2.5 | 0.999 | 10.000 | 360,527 | 34,084 | NaN | NaN | NaN | NaN |
| **22-1** | 35.743111 | 51.2695555 | 1345 | 862 | 10 | 2.5 | 0.999 | 10.000 | 274,652 | 20,779 | NaN | NaN | NaN | NaN |
| **22-4** | 35.743111 | 51.2695555 | 1345 | 862 | 10 | 2.5 | 0.999 | 230.000 | 495,228 | 25,584 | NaN | NaN | NaN | NaN |
| **22-6** | 35.743111 | 51.2695555 | 1345 | 862 | 10 | 2.5 | 0.999 | 360.000 | 263,086 | 20,076 | NaN | NaN | NaN | NaN |
| **22-7** | 35.743111 | 51.2695555 | 1345 | 862 | 10 | 2.5 | 0.999 | 410.000 | 177,975 | 23,789 | NaN | NaN | NaN | NaN |
| **RahadAbad** | | | | | | | | | | | | | | |
| **29-1-1** | 35.892111 | 51.6274722 | 2406 | 756 | 4 | 2.2 | 0.994 | 5.200 | NaN | NaN | NaN | NaN | NaN | NaN |
| **29-1-2** | 35.892111 | 51.6274722 | 2406 | 756 | 1.5 | 2.2 | 0.994 | 1.950 | 399253 | 12238 | NaN | NaN | 2,112,767 | 61,346 |
| **29-1-3** | 35.892111 | 51.6274722 | 2406 | 756 | 4 | 2.2 | 0.994 | 5.200 | 686,605 | 17,472 | NaN | NaN | 4,303,525 | 116,156 |
| **29-1-4** | 35.892111 | 51.6274722 | 2406 | 756 | 4 | 2.2 | 0.994 | 5.200 | 341,648 | 8,727 | NaN | NaN | 2,112,763 | 61,143 |
| **16-6** | 35.881750 | 51.6245278 | 2275 | 768 | 6 | 2.2 | 0.994 | 7.800 | 1,408,053 | 34,724 | NaN | NaN | 8,326,369 | 229,466 |
| **National Library** | | | | | | | | | | | | | | |
| **29-2-2** | 35.751111 | 51.4359444 | 1435 | 852 | 10 | 2.5 | 0.9996 | 74.9 | 398,566 | 18,367 | NaN | NaN | NaN | NaN |
| **29-2-4** | 35.751111 | 51.4359444 | 1435 | 852 | 10 | 2.5 | 0.9996 | 203.3 | 197,571 | 17,682 | NaN | NaN | NaN | NaN |
| **29-2-5** | 35.751111 | 51.4359444 | 1435 | 852 | 10 | 2.5 | 0.9996 | 267.5 | 135,592 | 36,241 | NaN | NaN | NaN | NaN |
| **29-2-6** | 35.751111 | 51.4359444 | 1435 | 852 | 10 | 2.5 | 0.9996 | 331.7 | 220,512 | 37,823 | NaN | NaN | NaN | NaN |
| **29-2-8** | 35.751111 | 51.4359444 | 1435 | 852 | 10 | 2.5 | 0.9996 | 460.1 | 185,970 | 32,880 | NaN | NaN | NaN | NaN |
| **29-2-9** | 35.751111 | 51.4359444 | 1435 | 852 | 10 | 2.5 | 0.9996 | 513.6 | 182,572 | 25,084 | NaN | NaN | NaN | NaN |
| **29-2-10** | 35.751111 | 51.4359444 | 1435 | 852 | 10 | 2.5 | 0.9996 | 588.5 | 105,409 | 9,588 | NaN | NaN | NaN | NaN |
| **Afjeh** | | | | | | | | | | | | | | |
| **30-1** | 35.833916 | 51.664750 | 1787 | 817 | 5 | 2.9 | 0.94 | 7.25 | NaN | NaN | 56,404 | 2,564 | NaN | NaN |
| **30-2** | 35.833916 | 51.664750 | 1784 | 817 | 5 | 2.9 | 0.77 | 7.25 | NaN | NaN | 28,631 | 1,821 | NaN | NaN |

Table C.2: Scaling parameters, continued

Sample codes and background information used for site-specific scaling (Part 2). Depth* corresponds to density and thickness corrected depth, shielding factor corresponds to topographic shielding only.

| **Sample name** | | **Exposure age (apparent) [yrs] Chlorine** | **Uncertainty [yrs]** Leached | **Exposure age (apparent) [yrs] Chlorine** | **Uncertainty [yrs]** Bulk | **Deviation** [%] | **Exposure age (apparent) [yrs] Beryllium** | **Uncertainty [yrs]** |
|---|---|---|---|---|---|---|---|---|
| **Upper Jajrud** | | | | | | | | |
| **13-1-1** | | 34334 | 2789 | 36458 | 2946 | 6.00 | 50833 | 3058 |
| **13-1-3** | | 43080 | 3566 | 38989 | 3284 | 9.97 | 29913 | 1434 |
| **13-1-4aA** | | 88760 | 8292 | 93508 | 8910 | 5.21 | 72957 | 2108 |
| **13-1-4aB** | | 83932 | 8171 | 93508 | 8910 | 10.79 | 72957 | 2108 |
| **13-1-4** | | 55048 | 5000 | 59777 | 5604 | 8.24 | 34147 | 1958 |
| **13-1-5** | | 70888 | 6844 | 76455 | 7659 | 7.56 | 60894 | 2566 |
| **15-1-1** | | 66073 | 6473 | 73375 | 7484 | 10.47 | 35914 | 2629 |
| **Lower Jajrud** | | | | | | | | |
| **13-2-1** | | 67590 | 5630 | NaN | NaN | NaN | 55680 | 1734 |
| **13-2-2** | | 100171 | 9757 | NaN | NaN | NaN | 69126 | 1953 |
| **13-2-3** | | 111423 | 10197 | NaN | NaN | NaN | 59024 | 2723 |
| **Saboo** | | | | | | | | |
| **23-1-0A** | | **62204** | **5976** | NaN | NaN | NaN | **67114** | **3112** |
| **23-1-2a** | | 75506 | 7161 | NaN | NaN | NaN | 248232 | 26778 |
| **23-1-3a** | | 92185 | 9123 | NaN | NaN | NaN | 287035 | 21353 |
| **23-1-6a** | | NaN | NaN | NaN | NaN | NaN | 203310 | 56392 |
| **23-1-8a** | | 120998 | 16945 | NaN | NaN | NaN | NaN | NaN |
| **23-1-10a** | | 140974 | 25084 | NaN | NaN | NaN | 313040 | 43845 |
| **23-1-1b** | | 125564 | 13257 | NaN | NaN | NaN | 176876 | 5693 |
| **23-1-3b** | | NaN | NaN | NaN | NaN | NaN | 137577 | 14350 |
| **23-1-4bA** | | 223350 | 36818 | NaN | NaN | NaN | 170817 | 7296 |
| **23-1-4bB** | | 215251 | 34800 | NaN | NaN | NaN | 170817 | 7296 |
| **23-1-5b** | | NaN | NaN | NaN | NaN | NaN | 231147 | 81726 |
| **23-1-0B1** | | **99701** | **9982** | NaN | NaN | NaN | **63052** | **1923** |
| **23-1-0B2** | | **95508** | **9558** | NaN | NaN | NaN | **63052** | **1923** |
| **23-1-4c** | | NaN | NaN | NaN | NaN | NaN | 306368 | 8818 |
| **23-1-5c** | | NaN | NaN | NaN | NaN | NaN | 224865 | 15459 |
| **23-1-1c** | | NaN | NaN | NaN | NaN | NaN | 115982 | 10821 |
| **Afjeh** | | | | | | | | |
| **30-1** | | 3290 | 408 | NaN | NaN | NaN | NaN | NaN |
| **30-2** | | 1591 | 223 | NaN | NaN | NaN | NaN | NaN |

Table C.3: Zero Erosion Ages

| | | Exposure age (apparent) [yrs] Aluminium | Uncertainty [yrs] | Exposure age (apparent) [yrs] Beryllium | Uncertainty [yrs] |
|---|---|---|---|---|---|
| **Kan** | | | | | |
| **K10-14** | | NaN | NaN | 8307 | 1199 |
| **101006-15** | | **NaN** | **NaN** | **31080** | **2938** |
| **22-1** | | **NaN** | **NaN** | **25078** | **1897** |
| **22-4** | | NaN | NaN | 175536 | 9068 |
| **22-6** | | NaN | NaN | 194739 | 14861 |
| **22-7** | | NaN | NaN | 170611 | 22805 |
| **RahadAbad** | | | | | |
| **29-1-1** | | NaN | NaN | NaN | NaN |
| **29-1-2** | | **23260** | **675** | **29754** | **912** |
| **29-1-3** | | **29108** | **786** | **28338** | **721** |
| **29-1-4** | | **14188** | **411** | **14051** | **359** |
| **16-6** | | **57076** | **1573** | **63890** | **1576** |
| **National Library** | | | | | |
| **29-2-2** | | NaN | NaN | 50886 | 2345 |
| **29-2-4** | | NaN | NaN | 54394 | 4868 |
| **29-2-5** | | NaN | NaN | 54169 | 14478 |
| **29-2-6** | | NaN | NaN | 128734 | 22081 |
| **29-2-8** | | NaN | NaN | 217128 | 38389 |
| **29-2-9** | | NaN | NaN | 278666 | 38287 |
| **29-2-10** | | NaN | NaN | 218414 | 19867 |

Table C.4: Zero Erosion Ages, continued

Table showing nuclide concentrations and corresponding (apparent) zero erosion ages. For the Saboo site, complete chemistry was analyzed from a leached sample (diamagnetic Calcite/Quartz/Feldspar mixture, after 10% acid leaching) and via X-Ray fluorescence before leaching, but after mineral separation. For the Jajrud site, leached sample was analyzed and bulk sample, before mineral separation. Here, with the exception of sample 13-1-3, all bulk samples reveal older ages. Compare Fig. 5.20H for comparison of the zero erosion ages. Note that deviation in ages derived using bulk and leached chemistry can be as high as 11%.

| **Sample** | **Spallation fast neutrons** [at/g/yr] | **Capture epith. neutrons** [at/g/yr] | **Capture th. neutrons** [at/g/yr] | **Capture slow muons** [at/g/yr] | **Epith. diffusion length** [g/cm$^2$] | **Th. diffusion length** [g/cm$^2$] |
|---|---|---|---|---|---|---|
| **Saboo** | | | | | | |
| 0A | 13.62 | 0.18 | -1.27 | 1.07 | 17.460 | 31.276 |
| 0B1 | 10.17 | 0.36 | -1.71 | 0.77 | 18.783 | 29.845 |
| 0B2 | 10.97 | 0.37 | -1.80 | 0.83 | 18.690 | 29.774 |
| 2a | 16.73 | 0.08 | -0.66 | 1.34 | 15.934 | 30.920 |
| 3a | 15.97 | 0.10 | -0.73 | 1.29 | 16.498 | 30.540 |
| 8a | 16.01 | 0.26 | -1.86 | 1.24 | 16.998 | 30.672 |
| 10a | 15.84 | 0.25 | -1.73 | 1.23 | 16.983 | 30.507 |
| 1b | 14.02 | 0.24 | -1.19 | 1.12 | 18.070 | 29.133 |
| 4bA | 13.30 | 0.32 | -1.54 | 1.04 | 18.214 | 29.016 |
| **Upper Jajrud bulk** | | | | | | |
| 13-1-1 | 22.89 | 1.09 | -9.09 | 1.55 | 16.127 | 30.731 |
| 13-1-3 | 20.07 | 1.86 | -10.45 | 1.30 | 17.709 | 29.650 |
| 13-1-4aA | 21.45 | 1.16 | -7.60 | 1.55 | 17.773 | 31.284 |
| 13-1-4 | 19.19 | 1.33 | -6.53 | 1.43 | 17.756 | 28.441 |
| 13-1-5 | 18.36 | 1.18 | -6.27 | 1.36 | 17.704 | 29.076 |
| 15-1-1 | 21.30 | 1.66 | -9.26 | 1.46 | 17.333 | 28.923 |
| **Upper Jajrud leached** | | | | | | |
| 13-1-1 | 24.69 | 0.98 | -10.63 | 1.59 | 15.732 | 32.860 |
| 13-1-3 | 22.20 | 1.62 | -12.13 | 1.36 | 17.425 | 32.087 |
| 13-1-4aA | 22.85 | 1.06 | -8.77 | 1.58 | 17.611 | 33.585 |
| 13-1-4 | 21.22 | 1.06 | -8.08 | 1.47 | 17.145 | 31.773 |
| 13-1-5 | 20.16 | 0.99 | -7.69 | 1.40 | 17.275 | 32.245 |
| 15-1-1 | 24.62 | 1.27 | -11.88 | 1.54 | 16.405 | 32.558 |
| **Lower Jajrud** | | | | | | |
| 13-2-1 | 16.98 | 1.20 | -7.44 | 1.16 | 17.384 | 30.055 |
| 13-2-2 | 19.68 | 0.70 | -5.87 | 1.45 | 16.822 | 32.211 |
| 13-2-3 | 18.70 | 0.65 | -5.45 | 1.31 | 16.534 | 31.510 |
| **Ajeh (PLG)** | | | | | | |
| 30-1 | 9.18 | 2.93 | -6.17 | 0.64 | 19.847 | 24.561 |
| 30-2 | 8.13 | 2.09 | -4.42 | 0.57 | 19.849 | 24.586 |

Table C.5: Table showing composition dependent production rate coefficients and diffusion length for $^{36}$Cl at surface. Attenuation length of neutrons is assumed to be 160 g/cm$^2$, of slow muons 1510 g/cm$^2$, data calculated using the tables from Schimmelpfennig et al. (2009)

| **Sample name** | **Target CaO** [wt-%] | **Cl** [ppm] | **36Cl Exp. Age [yrs]** | **36Cl Exp. Age [yrs]** | **Deviation [%]** | **36Cl Exp. Age [yrs]** | **Deviation [%]** | **36Cl Exp. Age [yrs]** | **Deviation [%]** |
|---|---|---|---|---|---|---|---|---|---|
| **Upper Jajrud leached** | | | | | | | | | |
| 13-1-1 | 35.94 | 85 | **34334** | 34575 | 0.70 | 34658 | 0.94 | 35471 | 3.31 |
| 13-1-1Bulk | 35.94 | 85 | **36458** | 36664 | 0.57 | 36736 | 0.76 | 37438 | 2.69 |
| 13-1-3 | 24.76 | 109 | **38989** | 39450 | 1.18 | 39374 | 0.99 | 40619 | 4.18 |
| 13-1-3Bulk | 24.76 | 109 | **43080** | 43481 | 0.93 | 43415 | 0.78 | 44496 | 3.29 |
| 13-1-4aA | 37.41 | 72 | **88760** | 89269 | 0.57 | 89658 | 1.01 | 91662 | 3.27 |
| 13-1-4aAbulk | 37.41 | 72 | **93508** | 93931 | 0.45 | 94254 | 0.8 | 95928 | 2.59 |
| 13-1-4aAxray | 37.41 | 72 | **87722** | 88269 | 0.62 | 88687 | 1.1 | 90838 | 3.55 |
| 13-1-4aB | 37.27 | 71 | **83932** | 84400 | 0.56 | 84779 | 1.01 | 86666 | 3.26 |
| 13-1-4aBxray | 37.27 | 71 | **80954** | 81492 | 0.66 | 81927 | 1.2 | 84086 | 3.87 |
| 13-1-4 | 34.84 | 73 | **55048** | 55340 | 0.53 | 55553 | 0.92 | 56699 | 3.00 |
| 13-1-4bulk | 34.84 | 73 | **59777** | 59988 | 0.35 | 60144 | 0.61 | 60983 | 2.02 |
| 13-1-5 | 33.07 | 68 | **70888** | 71243 | 0.50 | 71570 | 0.96 | 73046 | 3.04 |
| 13-1-5bulk | 33.07 | 68 | **76455** | 76720 | 0.35 | 76964 | 0.67 | 78074 | 2.12 |
| 15-1-1 | 31.9 | 100 | **66073** | 66730 | 0.99 | 66730 | 0.99 | 68636 | 3.88 |
| 15-1-1bulk | 31.9 | 100 | **73375** | 73863 | 0.67 | 73863 | 0.67 | 75286 | 2.6 |
| **Lower Jajrud** | | | | | | | | | |
| 13-2-1 | 25.06 | 75 | **67590** | 67910 | 0.47 | 68123 | 0.79 | 69367 | 2.63 |
| 13-2-2 | 37.45 | 51 | **100171** | 100478 | 0.31 | 101063 | 0.89 | 102778 | 2.6 |
| 13-2-3 | 33.17 | 49 | **111423** | 111750 | 0.29 | 112417 | 0.89 | 114296 | 2.58 |
| **Ajeh (PLG)** | | | | | | | | | |
| 30-1 | 11.96 | 74 | **3290** | 3294 | 0.12 | 3297 | 0.21 | 3315 | 0.76 |
| 30-2 | 11.96 | 53 | **1591** | 1593 | 0.13 | 1595 | 0.25 | 1601 | 0.63 |
| **Saboo** | | | | | | | | | |
| 23-1-0A | 34.97 | 12 | **62204** | 62206 | 0 | 62240 | 0.06 | 62294 | 0.14 |
| 23-1-2a | 45.78 | 6 | **75506** | 75509 | 0 | 75606 | 0.13 | 75750 | 0.32 |
| 23-1-3a | 43.41 | 7 | **92185** | 92190 | 0.01 | 92329 | 0.16 | 92538 | 0.38 |
| 23-1-8a | 39.88 | 18 | **120998** | 121039 | 0.03 | 121403 | 0.33 | 122027 | 0.85 |
| 23-1-10a | 39.79 | 17 | **140974** | 141012 | 0.03 | 141381 | 0.29 | 142006 | 0.73 |
| 23-1-1b | 36.48 | 13 | **125564** | 125585 | 0.02 | 125861 | 0.24 | 126313 | 0.6 |
| 23-1-4bA | 33.38 | 17 | **223350** | 223415 | 0.03 | 224040 | 0.31 | 225111 | 0.79 |
| 23-1-4bB | 33.47 | 17 | **215251** | 215315 | 0.03 | 215926 | 0.31 | 216973 | 0.8 |
| 23-1-0B1 | 23.93 | 18 | **99701** | 99710 | 0.01 | 99789 | 0.09 | 99928 | 0.23 |
| 23-1-0B2 | 25.94 | 19 | **95508** | 95515 | 0.01 | 95589 | 0.08 | 95718 | 0.22 |

Table C.6: Table showing deviation in zero erosion ages for different bulk-Chlorine estimates. 36Cl-zero erosion ages were calculated using the same Chlorine concentration for target and bulk. However, Chlorine in the surrounding might have an additional effect on the production. Here, we investigate the percentage of age deviation for three different (bulk) Chlorine estimates, which are the double of the target-Cl, 200, and 500ppm, respectively. Even with high Cl- content, the changes in age will be less than 5%.

| **Sample** | **Depth** [cm] | **P(spallation)** [at/g/yr] | **P(epithermal)** [at/g/yr] | **P(thermal)** [at/g/yr] | **P(muon)** [at/g/yr] | **P(radiogenic)** [at/g/yr] | **P(sum)** [at/g/yr] | **Spallation** [%] |
|---|---|---|---|---|---|---|---|---|
| **Saboo** | | | | | | | | |
| 0A | 0 | 45.75 | 0.35 | 1.12E+000 | 3.8 | 0.01 | 51.03 | 89.65 |
| 0B1 | 0 | 31.3 | 0.55 | 1.52E+000 | 2.6 | 0.01 | 35.98 | 86.99 |
| 0B2 | 0 | 33.94 | 0.58 | 1.60E+000 | 2.81 | 0.01 | 38.94 | 87.15 |
| 2a | 0 | 59.89 | 0.16 | 5.84E-001 | 4.93 | 0 | 65.58 | 91.34 |
| 3a | 0 | 56.78 | 0.2 | 6.56E-001 | 4.72 | 0 | 62.36 | 91.06 |
| 8a | 0 | 52.18 | 0.51 | 1.66E+000 | 4.32 | 0.01 | 58.69 | 88.91 |
| 10a | 0 | 52.06 | 0.49 | 1.56E+000 | 4.32 | 0.01 | 58.43 | 89.1 |
| 1b | 0 | 47.73 | 0.39 | 1.09E+000 | 3.98 | 0.01 | 53.19 | 89.74 |
| 4bA | 0 | 43.67 | 0.51 | 1.40E+000 | 3.63 | 0.01 | 49.22 | 88.72 |
| 4bB | 0 | 43.79 | 0.51 | 1.42E+000 | 3.65 | 0.01 | 49.38 | 88.68 |
| 2a | 60 | 31.07 | 0.17 | 1.32E+000 | 4.6 | 0 | 37.16 | 83.61 |
| 3a | 88 | 21.69 | 0.16 | 1.12E+000 | 4.26 | 0 | 27.23 | 79.64 |
| 8a | 240 | 3.78 | 0.11 | 6.96E-001 | 3.27 | 0.01 | 7.87 | 48.04 |
| 10a | 300 | 1.96 | 0.07 | 4.13E-001 | 3.05 | 0.01 | 5.5 | 35.59 |
| 1b | 68 | 20.4 | 0.35 | 1.86E+000 | 3.63 | 0.01 | 26.26 | 77.68 |
| 4bA | 220 | 2.95 | 0.11 | 5.15E-001 | 2.73 | 0.01 | 6.32 | 46.69 |
| 4bB | 220 | 2.96 | 0.11 | 5.24E-001 | 2.74 | 0.01 | 6.35 | 46.58 |
| **Lower Jajrud** | | | | | | | | |
| 13-2-1 | 0 | 26.18 | 1.75 | 5.32E+000 | 2.36 | 0.06 | 35.66 | 73.42 |
| 13-2-2 | 0 | 39.12 | 1.17 | 4.00E+000 | 3.49 | 0.02 | 47.8 | 81.84 |
| 13-2-3 | 0 | 37.52 | 1.1 | 3.78E+000 | 3.15 | 0.03 | 45.58 | 82.31 |
| 13-2-1 | 40 | 16.9 | 2.27 | 1.26E+001 | 2.25 | 0.06 | 34.08 | 49.6 |
| 13-2-2 | 88 | 14.94 | 0.94 | 7.24E+000 | 3.15 | 0.02 | 26.3 | 56.81 |
| 13-2-3 | 100 | 12.57 | 0.79 | 6.03E+000 | 2.81 | 0.03 | 22.22 | 56.55 |
| **Afjeh (PLG)** | | | | | | | | |
| 30-1 | 0 | 11.05 | 1.54 | 3.05E+000 | 0.94 | 0 | 16.58 | 66.63 |
| 30-2 | 0 | 13.04 | 1.22 | 2.42E+000 | 1.04 | 0 | 17.71 | 73.6 |

Table C.7: Table showing composition dependent production pathways for $^{36}$Cl at surface and at real depth (Part 1). Surface production shows the differences in composition only, while the real depth production accounts for the combined effects of depth and composition. Last column shows the percentage of spallation on production rate.

| **Sample** | **Depth** [cm] | **P(spallation)** [at/g/yr] | **P(epithermal)** [at/g/yr] | **P(thermal)** [at/g/yr] | **P(muon)** [at/g/yr] | **P(radiogenic)** [at/g/yr] | **P(sum)** [at/g/yr] | **Spallation** [%] |
|---|---|---|---|---|---|---|---|---|
| **Upper Jajrud bulk** | | | | | | | | |
| 13-1-1 | 0 | 38.34 | 1.91 | 6.57E+000 | 3.44 | 0.04 | 50.29 | 76.23 |
| 13-1-3 | 0 | 26.42 | 2.62 | 7.66E+000 | 2.38 | 0.09 | 39.16 | 67.46 |
| 13-1-4aA | 0 | 39.91 | 1.74 | 5.40E+000 | 3.58 | 0.03 | 50.66 | 78.78 |
| 13-1-4 | 0 | 37.17 | 1.75 | 4.86E+000 | 3.36 | 0.05 | 47.19 | 78.76 |
| 13-1-5 | 0 | 35.28 | 1.63 | 4.65E+000 | 3.19 | 0.04 | 44.79 | 78.76 |
| 15-1-1 | 0 | 34.03 | 2.36 | 6.90E+000 | 3.07 | 0.07 | 46.43 | 73.28 |
| 13-1-1 | 50 | 22.19 | 2.2 | 1.57E+001 | 3.25 | 0.04 | 43.42 | 51.1 |
| 13-1-3 | 100 | 8.85 | 1.93 | 1.11E+001 | 2.12 | 0.09 | 24.09 | 36.73 |
| 13-1-4aA | 140 | 5.82 | 0.65 | 4.03E+000 | 2.92 | 0.03 | 13.45 | 43.27 |
| 13-1-4 | 180 | 5.19 | 0.63 | 3.19E+000 | 2.73 | 0.05 | 11.78 | 44.04 |
| 13-1-5 | 200 | 3.96 | 0.5 | 2.61E+000 | 2.53 | 0.04 | 9.63 | 41.08 |
| 15-1-1 | 230 | 2.75 | 0.57 | 3.02E+000 | 2.35 | 0.07 | 8.76 | 31.4 |
| **Upper Jajrud leached** | | | | | | | | |
| 13-1-1 | 0 | 38.34 | 1.88 | 7.19E+000 | 3.39 | 0.03 | 50.84 | 75.41 |
| 13-1-3 | 0 | 26.42 | 2.6 | 8.49E+000 | 2.35 | 0.1 | 39.96 | 66.11 |
| 13-1-4aA | 0 | 39.91 | 1.74 | 5.90E+000 | 3.53 | 0.02 | 51.1 | 78.09 |
| 13-1-4aB | 0 | 39.76 | 1.72 | 5.84E+000 | 3.53 | 0.03 | 50.87 | 78.16 |
| 13-1-4 | 0 | 37.17 | 1.72 | 5.69E+000 | 3.29 | 0.05 | 47.91 | 77.57 |
| 13-1-5 | 0 | 35.28 | 1.61 | 5.36E+000 | 3.14 | 0.04 | 45.43 | 77.66 |
| 15-1-1 | 0 | 34.03 | 2.28 | 8.18E+000 | 3.02 | 0.05 | 47.57 | 71.54 |
| 13-1-1 | 50 | 22.19 | 2.15 | 1.85E+001 | 3.2 | 0.03 | 46.03 | 48.2 |
| 13-1-3 | 100 | 8.85 | 1.9 | 1.34E+001 | 2.1 | 0.1 | 26.36 | 33.57 |
| 13-1-4aA | 140 | 5.82 | 0.64 | 4.77E+000 | 2.88 | 0.02 | 14.14 | 41.18 |
| 13-1-4aB | 140 | 5.8 | 0.63 | 4.72E+000 | 2.88 | 0.03 | 14.06 | 41.24 |
| 13-1-4 | 180 | 5.19 | 0.61 | 4.23E+000 | 2.67 | 0.05 | 12.74 | 40.74 |
| 13-1-5 | 200 | 3.96 | 0.48 | 3.37E+000 | 2.49 | 0.04 | 10.34 | 38.28 |
| 15-1-1 | 230 | 2.75 | 0.53 | 4.09E+000 | 2.31 | 0.05 | 9.74 | 28.24 |

Table C.8: Table showing production pathways for $^{36}$Cl at surface and at real depth (Part 2). Surface production shows the differences in composition only, while the real depth production accounts for the combined effects of depth and composition. For the Upper Jajrud site, differences in production using bulk and leached chemistry are additionally listed. Note that while target spallation is the main contribution to the nuclide production, production at depth by thermal and epithermal neutrons, as well as muons changes significantly. Even with the relatively low Chlorine content, deviation in ages can be as high as 11% (Table C.3). Using bulk chemistry for the production calculation will thus reveal older ages. Last column shows the percentage of spallation on production rate.

| Sample name | Cl-leached [m/Ma] | Cl-bulk [m/Ma] | Beryllium [m/Ma] | effective age Cl [yrs] | effective age Be [yrs] |
|---|---|---|---|---|---|
| **Upper Jajrud** | | | | | |
| **13-1-1** | 42.9 | 40.46 | 25.2506 | | |
| **13-1-3** | 43.27 | 39.4 | 54.7086 | | |
| **13-1-4aA** | 19.43 | 18.59 | 20.7939 | | |
| **13-1-4** | 46.6 | 43.97 | 58.1758 | | |
| **13-1-5** | 38.25 | 36.1 | 38.8052 | | |
| **15-1-1** | 46.68 | 43.23 | 97.2266 | | |
| **Lower Jajrud** | | | | | |
| **13-2-1** | 18.62 | | 20.0898 | | |
| **13-2-2** | 13.58 | | 17.8849 | | |
| **13-2-3** | 12.1 | | 22.1341 | | |
| **Saboo** | | | | | |
| **23-1-0A** | 12.42 | | 10.2117 | **155,976** | **204,312** |
| **23-1-2a** | 18.1 | | 4.2470 | | |
| **23-1-3a** | 15.78 | | 3.8142 | | |
| **23-1-6a** | NaN | | 8.4590 | | |
| **23-1-8a** | 25.33 | | NaN | | |
| **23-1-10a** | 28.26 | | 10.6755 | | |
| **23-1-1b** | 8.55 | | 5.7347 | | |
| **23-1-3b** | NaN | | 10.7724 | | |
| **23-1-4bA** | 9.29 | | 14.7692 | | |
| **23-1-4bB** | NaN | | NaN | | |
| **23-1-5b** | NaN | | 18.4097 | | |
| **23-1-0B1** | 11.7 | | 17.1846 | **245,444** | **191,751** |
| **23-1-4c** | NaN | | 2.2287 | | |
| **23-1-5c** | NaN | | 5.1373 | | |
| **23-1-1c** | NaN | | 19.0914 | | |
| | | | **Beryllium [m/Ma]** | **effective age Be [yrs]** | |
| **Rahad Abad** | | | | | |
| **29-1-2** | | | 26.0118 | **116,438** | |
| **29-1-3** | | | 27.3765 | **110,699** | |
| **29-1-4** | | | 56.6781 | **53,778** | |
| **16-6** | | | 11.5486 | **258,480** | |

Table C.9: Maximum denudation of single nuclides and resulting effective ages after Lal (1991). For Chlorine, denudation has been calculated for leached and bulk chemistry, effective ages are bulk chemistry for Upper Jajrud and leached for Lower Jajrud and Saboo.

| Sample name | Exposure age [yrs] | Denudation [m/Ma] | Inheritance [at/g] | Chi$^2$ | Nuclide | Notes | |
|---|---|---|---|---|---|---|---|
| **Upper Jajrud** | steady state | **19.7** | no | 863.85 | 36Cl* | | |
| **(bulk)** | **135,000** | **22.86** | no | 353.15 | 10Be* | | |
| | 40160 | 0 | 15319 | 354.59 | 10Be | | |
| | 134137 | 22.86** | no** | 447.31 | 10Be | **fixed values | |
| **Lower Jajrud** | **60,361** | **0** | **6890** | 25.25 | 10Be | | |
| | **70,001** | 0 | 2533 | 9.43 | 36Cl | | |
| **Saboo** | 200000 | 0.29 | no | 258.63 | 10Be* | | |
| | **195,064** | **0** | no | 257.04 | 10Be | | |
| | steady state | **9.14** | no | 1217 | 36Cl* | | |
| **Kan** | 275000 | 3 | no | 1.03 | 10Be* | depth | |
| | **266,065** | **2.81** | no | 1.03 | 10Be | depth | |
| **Nat. Library** | steady state | 20.3 | no | 20.25 | 10Be* | one deposit | |
| | **96,418** | **21.21** | | | 10Be | Effective age / max. denudation | |

Table C.10: Results of Chi$^2$-inversion (*) and minimizing for both nuclides.

| | RFA | HNO3-Test | % deviation |
|---|---|---|---|
| 23-1-0a | 33.75 | 35.49 | 5.16 |
| 23-1-0b | 11.2 | 11.76 | 5.04 |
| 23-1-1b | 27.07 | 27.17 | 0.37 |

Table C.11: Deviation between RFA and HNO3 test.

| **Sample** | **Depth** | **Conc-meas** | **Uncertainty** | **Conc-theo** | **Conc-theo** | **Conc-theo** | **Conc-theo** | **Conc-theo** | **Conc-theo** |
|---|---|---|---|---|---|---|---|---|---|
| **Upper Jajrud (bulk)** | [cm] | [at/g] | [at/g] | 13-1-1 | 13-1-3 | 13-1-4a | 13-1-4 | 13-1-5 | 15-1-1 |
| 13-1-1 | 50 | **1471000** | 26300 | **1531325** | 1393146 | 1240946 | 1356388 | 1305767 | 1462663 |
| 13-1-3 | 120 | **978310** | 17800 | 962809 | **896513** | 753214 | 874861 | 845648 | 931825 |
| 13-1-4aA | 140 | **1109500** | 20400 | 862407 | 808620 | **678104** | 790298 | 764760 | 838290 |
| 13-1-4aB | 140 | **1050300** | 33100 | 862407 | 808620 | 678104 | 790298 | 764760 | 838290 |
| 13-1-4 | 180 | **651360** | 11800 | 714876 | 679537 | 575027 | **665960** | 645821 | 700865 |
| 13-1-5 | 200 | **665340** | 11800 | 661105 | 632527 | 539895 | 620578 | **602412** | 650771 |
| 15-1-1 | 230 | **595640** | 11700 | 598452 | 577794 | 500778 | 567614 | 551756 | **592391** |

Table C.12: Theoretical concentrations, considering the respective sample chemistry for one fixed exposure scenario (46 ka exposure, 285,000 at/g inheritance, and 23 m/Ma erosion).

# Bibliography

Abbassi, M.R. & Farbod, Y., 2009. Faulting and folding in quaternary deposits of Tehrans piedmont (Iran), *Journal of Asian Earth Sciences* **34(4)**, 522-531.

Alavi, M., 1991. Sedimentary and structural characteristics of the Paleo-Tethys remnants in northeastern Iran, *Bulletin Geol. Soc. America* **103**, 983-992.

Alavi, M., 1996. Sedimentary and structural characteristics of the Paleo-Tethys remnants in northeastern Iran, *Bulletin Geol. Soc. America* **103**, 983-992.

Alijani, B. & Harman, J.R., 1985. Synoptic Climatology of Precipitation in Iran, *Annals of the Association of American Geographers*, **75(3)**, 404-416.

Alijani, B., 2002. Variations of 500hPa flow patterns over Iran and surrounding areas and their relationship with the climate of Iran, *Theor. Appl. Climatol.*, **72**, 41-54.

Alijani, B., O'Brien, J. & Yarnal, B., 2007. Spatial analysis of precipitation intensity and concentration in Iran, *Theor. Appl. Climatol.*, DOI 10.1007/s00704-007-0344-y.

Allen, M.B., Ghassemi, M.R., Shahrabi, M. & Qorashi, M., 2003. Accommodation of late Cenozoic oblique shortening in the Alborz range, northern Iran, *J. Struct. Geology* **25**, 659-672.

Allenbach, P., 1966. Geologie and Petrographie des Demavand und seiner Umgebung (Zentral-Elburz, Iran), *Mitteilungen aus dem Geologischen Institut der Eidgenössischen Technischen Hochschule und der Universität Zürich* , 1-144.

Allmendinger, R.W., 1998. Inverse and forward numerical modeling of trishear faultpropagation folds, *Tectonics*, **17(4)**, 640-656.

Ambraseys, N.N., 1974. Historical seismicity of north-central Iran, *Material for the Study of Seismotectonics of Iran: North-central Iran*, Geological Survey of Iran, Report **29**, 47-96.

Ambraseys, N.N. & Melville, C.P., 1982. *A history of Persian Earthquakes*, Cambridge University Press, London, 219pp.

Amini, B. & Emami, M.H., 1993. Geological Map of Iran, 100000 Series, Sheet Tehran, *GSI*

Anderson, E.M., 1905. The dynamics of faulting, *Trans. edinburgh Geol. Soc.*, **8**, 387-402.

Anderson, E.M., 1951. *The dynamics of faulting and dyke formation with applications to Britain*, 2nd edn, Oliver and Boyd, Edinburgh.

Anderson, R.S., Repka, J.L. & Dick, G.S., 1996. Explicit treatment of inheritance in dating depositional surfaces using in situ $^{10}Be$ and $^{26}Al$, *Geology* **24(1)**, 47-51.

Anderson, G. & Ji, C., 2003a. Static stress transfer during the 2002 Nenana Mountain-Denali Fault, Alaska, earthquake sequence, *Geophys. Res. Letters* **30**, 1310-1315.

Anderson, G., Aagaard, B. & Hudnut, K., 2003. Fault interactions and large complex earthquakes in the Los Angeles area, *Science* **302**, 1946-1949.

Armijo, R., Meyer, B., King, G.C.P., Rigo, A. & Papanastassiou, D., 1996. Quaternary evolution of the Corinth Rift and its implication for the late Cenozoic evolution of the Aegean, *Geophys. J. Int.* **126(1)**, 11-53.

Armijo, R., Flerit, F. , King,G. C. P. & B. Meyer, 2003. Linear elastic fracture mechanics explains the past and present evolution of the Aegean, *Earth Planet. Science Letters* **217**, 85-95.

Arnold, M., Merchel, S., Bourlès, D.L., Braucher, R., Benedetti, L., Finkel, R.C., Aumaître, G., Gottdang, A. & Klein, M. 2010. The French accelerator mass spectrometry facility ASTER: Improved performance and developments, *Nucl. Instr. and Meth. in Phys. Res. B*, , in press.

Arrowsmith, R. & Strecker, M., 1999. Seismotectonic range front segmentation and mountain belt growth along the northern Pamir Mountains, Kyrgyzstan (India-Eurasia collision zone), *Bulletin Geol. Soc. America* **111**, 1665-1683.

Assereto, R., 1966. Explanatory notes on the geological map of Upper Djadjerud and Lar Valleys (Central Elburz, Iran), scale 1:50.000. University of Milan (Italy) Institute of Geology , 86pp.

Ashtari, M., Hatzfeld D. & Kamalian N., 2005. Microseismicity in the region of Tehran, *Tectonophysics* **395**, 193-208.

Avouac, J.-P. & Peltzer, G., 1993. Active Tectonics in Southern Xinjiang, China: Analysis of Terrace Riser and Normal Fault Scarp Degradation Along the Hotan-Qira Fault System, *J. Geophys. Res.*, **98(B12)**, 21773-21807.

Avouac, J.-P., Tapponier, P., Bai, M., You, H. & Wang, G., 1993. Active Thrusting and Folding Along the Northern Tien Shan and Late Cenozoic Rotation of the Tarim Relative to Dzungaria and Kazakhstan, *J. Geophys. Res.*,**98(B4)**, 6755-6804.

Axen, G.J., Lam, P.S., Grove, M. & Stockli, D.F., 2001. Exhumation of the west-central Alborz mountains, Iran, Caspian subsidence, and collision-related tectonics, *Geology* **29(6)**, 559-562.

Aydin, A. & Schultz, R.A., 1990. Effect of mechanical interaction on the development of strike-slip faults with echelon patterns, *J. Struct. Geology* **12(1)**, 123-129.

Bassir, M., 1971. Ingenieurgeologische Baugrunduntersuchungen in der Region Groß-Tehran/Iran. *Rheinisch-Westfälische Technische Hochschule, Dissertation*, 190pp.

Bachmanov, D.M., Trifonov, V.G., Hessami, Kh.T., Kozhurin, A.I., Ivanove, T.P., Rogothin, E.A., Hademi, M.C. & Jamali, F.H., 2004. Active faults in the Zagros and central Iran, *Tectonophysics* **380**, 221-241.

Balco, G., Stone, J., Lifton, N. & Dunai, T. , 2008. A complete and easily accessible means of calculating surface exposure ages or erosion rates from 10Be and 26Al measurements, *Quaternary Geochronology*, 3, 174-195.

Ballato, P., Nowaczyk, N., Landgraf, A., Strecker, M.R., Friedrich, A. & Tabatabaei, S.H., 2008: Tectonic control on sedimentary facies pattern and sediment accumulation rates in the Miocene foreland basin of the southern Alborz mountains, northern Iran, *Tectonics* **27**, TC6001.

Ballato, P., Uba, C.E., Landgraf, A., Strecker, M.R., Stockli, D.F., Friedrich, A. & Tabatabaei, S.H., 2009. Arabia-Eurasia continental collision and upper-plate deformation: insights from foreland-basin evolution in the Alborz mountains, N Iran., *Bulletin Geol. Soc. America*, accepted for publication.

Ballato, P., 2009. Tectonic and climatic forcing in orogenic processes: the foreland basin point of view, Alborz mountains, N Iran, (PhD-thesis), Potsdam, University of Potsdam, 158p.

Barka, A., Akyuz, H. S., Sunal, G., Cakir, Z., Dikbas, A., Yerli, B., Altunel, E., Armijo, R., Meyer, B., de Chabalier, J.B., Rockwell, T., Dolan, J.R., Hartleb, R., Dawson, T., Christofferson, S., Tucker, A., Fumal, T., Langridge, R., Stenner, H., Lettis, W., Bachhuber, J. & Page, W., 2002. The Surface Rupture and Slip Distribution of the 17 August 1999 Izmit Earthquake (M 7.4), North Anatolian Fault, *Bulletin Seism. Soc. America* **92(1)**, 43-60.

Bayasgalan, A., Jackson, J., Ritz, J.-F. & Carretier, S., 1999. 'Forebergs', flower structures, and the development of large intracontinental strike-slip faults: the Gurvan Bogd fault system in Mongolia, *J. Struct Geology*, **21**, 1285-1302.

Bennett, R, Furlong, K. & Friedrich, A., 2004. Codependent histories of the San Andreas and San Jacinto fault zones from inversion of fault displacement rate, *Geology* **32(11)**, 961-964.

Ben-Zion, Y., 2008. Collective behavior of earthquakes and faults: Continuum-discrete transitions, progressive evolutionary changes, and different dynamic regimes, *Rev. Geophys.* **46**, doi:10.1029/2008RG000260.

Berberian, M., 1979. Earthquake faulting and bedding thrust associated with the Tabas-e-Golshan (Iran) earthquake September 16, 1978, *Bulletin Geol. Soc. America*, **69(6)**, 1861-1887.

Berberian, M., 1983. Continental deformation in the Iranian Plateau, *Contribution of Seismotectonics of Iran*, Geological Survey of Iran, Report **52**, 625pp.

Berberian, M., Qorashi, M., Jackson, J. A., Priestley, K. & Wallace, T., 1992. The Rudbar-Tarom earthquake of 20 June 1990 in NW Persia: Preliminary field and seismological observations, and its tectonic significance, *Bulletin Geol. Soc. America*, **82(4)**,1726-1755.

Berberian, M. & Yeats, R.S., 1999. Patterns of historical earthquake rupture in the Iranian Plateau, *Bulletin Seism. Soc. America* **89**, 120-139.

Berberian, M. & Yeats, R.S., 2001. Contribution of archeaological data to studies of earthquake history in the Iranian Plateau, *J. Struct. Geology* **23**, 563-584.

Biermann, P.R., Gillespie, A.R., Ca!ee, M.W., 1995. Cosmogenic ages for earthquake recurrence intervals and debris flow fan deposition, Owens Valley, California, *Science*, **270**, 447-450.

Biermann, P.R., Marsella, K.A., Patterson, C., Davis, P.T. & Caffee, M., 1999. Mid-Pleistocene cosmogenic minimum-age limits for pre-Wisconsinan glacial surfaces in southwestern Minnesota and southern Baffin Island: a multiple nuclide approach, *Geomorphology* **27**, 25-39.

Bilham, R. and King, G., 1989. The morphology of strike-slip faults: examples from the San Andreas Fault, California, *J. Geophys. Research* **94(B8)**, 10204-10216.

Bloom, A. L., Broecker, W. S., Chappel, J. M. A., Matthews, R. K. & Mesolella, K. J., 1974. Quaternary sea level fluctuations on a tectonic coast: new 23Th/234U dates from the Huon Peninsula, New Guinea, *Quat. Res.*, **4**, 185-205.

Bookhagen, B., Thiede, R.C. & Strecker, M.R., 2005. Late Quaternary intensified monsoon phases control landscape evolution in the northwest Himalaya, *Geology*, **33**, 149-152.

Bookhagen, B. & Strecker, M.R., 2008. Orographic barriers, high-resolution TRMM rainfall, and relief variations along the eastern Andes, *Geophys. Res. Lett.*, **35**, doi:10.1029/2007GL032011.

Bookhagen, B. & Burbank, D. W., 2006. Topography, relief, and TRMM-derived rainfall variations along the Himalaya, *Geophys. Res. Lett.*, **33**, doi:10.1029/2006GL026037.

Bosworth, W. & Strecker, M.R., 1997. Stress field changes in the Afro-Arabian rift system during the Miocene to Recent period, *Tectonophysics* **278**, 47-62.

Brankman, C.M. & Aydin, A., 2004. Uplift and contractional deformation along a segmented strike-slip fault system: the Gragano Promontory, southern Italy, *J. Struct. Geology* **26**, 807-824.

Braucher, R., Brown, E.T., Bourlès, D. & Colin, F., 2003. In situ produced 10Be measurements at great depths: implications for production rates by fast muons, *Earth and Planetary Science Letters*, **211**, 251-258.

Braucher, R., Del Castillo, P., Siame, L., Hidy, A.J. & Bourlès, D., 2009. Determination of both exposure time and denudation rate from an in situ-produced 10Be depth profile: A mathematical proof of uniqueness. Model sensitivity and applications to natural cases, *Quaternary Geochronology* **4**, 56-67.

Brown, E.T., Edmond, J.M., Raisbeck, G.M., Yiou, F., Kurz, M.D. & Brook, E.J., 1991. Examination of surface exposure ages of Antarctic moraines using in situ produced 10Be and 26Al, *Geochim. Cosmochim. Acta*, **55**, 2269-2283.

Brown, E.T., & Bourlès,D.L., 2002. Use of a new 10Be and 26Al inventory method to date marine terraces, Santa Cruz, California, USA: Comment and Reply, *Geology*, **30(12)**, 1147-1148.

Brown, E.T., Bendick, R., Bourlès,D.L., Gaur,V., Molnar, P., Raisbeck, G.M. & Yiou,F., 2002. Slip rates of the Karakorum fault, Ladakh, India, determined using cosmic ray exposure dating of debris flows and moraines, *J. Geophys. Res.* **107 (B9)**, doi:10.1029/2000JB000100.

Brown, E.T., Molnar, P. & Bourlès,D.L., 2005. Comment on "Slip-Rate Measurements on the Karakorum Fault May Imply Secular Variations in Fault Motion", *Science* **309**, 1326b.

Bürgmann, R., Arrowsmith, R. & Dumitru, T., 1994. Rise and fall of the southern Santa Cruz Mountains, California, from fission tracks, geomorphology, and geodesy, *J. Geophys. Research* **99(B10)**, 20181-20202.

Bull, W., 2007. *Tectonic Geomorphology of Mountains. A New Approach to Paleoseismology*, Blackwell Publishing, Oxford.

Bullard, T.F. & Lettis, W.R., 1993. Quaternary fold deformation associated with blind thrust faulting, Los Angeles Basin, California, *J. Geophys. Research* **98**, 1303-1317.

Burbank, D.W., Meigs, A. & Brozovic, N., 1996. Interactions of growing folds and coeval depositional systems, *Basin Research*, **8**, 199-223.

Burbank, D.W., McLean, J.K., Bullen, M., Abdrakhmatov, K.Y. & Miller, M.M., 1999. Partitioning of intermontane basins by thrust-related folding, Tien Shan, Kyrgystan, *Basin Research*, **11**, 75-92.

Burbank, D.W. & Anderson, R.S., 2001. *Tectonic Geomorphology*, Blackwell Science, Oxford.

Camelbeeck T. & Meghraoui M., 1998. Geological and geophysical evidence for large palaeo-earthquakes with surface faulting in the Roer Graben (northwest Europe), *Geophys. J. Int.*, **132**, 347-362.

Camelbeeck, T., Alexandre, P., Vanneste, K. & Meghraoui, M., 2000. Long-term seismicity in regions of present day low seismic activity: the example of western Europe, *Soil Dynamics and Earthquake Engineering*, **20**, 405-414, DOI: 10.1016/S0267-7261(00)00080-4.

Célétier, B., 1995. Tectonic regime and slip orientation of reactivated faults, *Geophys. J. Int.* **121**, 143-161.

Chevalier, M.-L., Ryerson, F.J., Tapponnier, P., Finkel, R.C. Van der Woerd, J., Li, H. & Liu, Q., 2005. Slip-rate measurements on the Karakorum fault may imply secular variations in fault motion, *Science* **307**, 411-414.

Chevalier, M.-L., Ryerson, F.J., Tapponnier, P., Finkel, R.C. Van der Woerd, J., Li, H. & Liu, Q., 2005. Response to Comment on “Slip-Rate Measurements on the Karakorum Fault May Imply Secular Variations in Fault Motion”, *Science* **309**, 1326c.

Chmeleff, J., von Blanckenburg, F., Kossert, K. & Jakob, D., 2010. Determination of the 10Be half-life by multicollector ICP-MS and liquid scintillation counting, *Nucl. Instr. and Meth. in Phys. Res. B*, **268(2)**, 192-199.

Clark, M.K., Maheo, G., Saleeby, J. & Farley, K.A., 2005. The non-equilibrium landscape of the southern Sierra Nevada, California, *GSA Today*, **15(9)**, doi: 10:1130/1052-5173(2005)015<4:TNELOT>2.0.CO;2.

Clark, M.K., Royden, L.H., Whipple, K.X., Burchfield, B.C., Zhang, X. & Tang, W., 2006. Use of regional, relict landscape to measure vertical deformation of the eastern Tibetan Plateau, *J. Geophys. Research* **111** doi: 10.1029/2005JF000294

Cockburn, H.A.P. & Summerfield, M.A., 2004. Geomorphological applications of cosmogenic isotope analysis, *Progress in Physical Geography*, **28(1)**, DOI: 10.1191/0309133304pp395oa.

Cooke, M.L. & Marshall, S.T., 2006. Fault slip rates from three-dimensional models of the Los Angeles metroploitan area, California, *Geophys. Res. Letters* **33**, doi:10.1029/2006GL027850.

Cooke, M. L. & Kameda, A., 2002. Mechanical fault interaction within the Los Angeles Basin: A two-dimensional anlysis using mechanical efficiency, *J. Geophys. Research* **107(B7)**, doi:10.1029/2001JB000542.

Cortés, M., Angelier, J. & Colletta, B., 2005. Paleostress evolution of the northern Andes (Eastern Cordillera of Colombia): Implications on plate kinematics of the South Caribbean region, *Tectonics*, **24**, doi:10.1029/2003TC001551.

Cowgill, E., Yin, A., Arrowsmith, J.R., Whang, X.F., & Zhang, S., 2004. The Akato Tagh bend along the Altyn Tagh fault, northwest Tibet 1: Smoothing by vertical axis rotation and the effect of topographic stresses on bend-flanking faults, *Bulletin Geol. Soc. America* **116(11/12)**, 1423-1442, doi:10.1130/B25359.1.

Cowgill, E., 2007. Impact of riser reconstructions on estimation of secular variation in rates of strike-slip faulting: Revisiting the Cherchen River site along the Altyn Tagh Fault, NW China, *Earth and Planetary Science Letters* **254**, 239-255.

Cowie, P.A., Vanneste, C. & Srnette, D., 1993. Statistical physical model for the spatio-temporal evolution of faults, *J. Geophys. Research* **98**, 21809-21821.

Cowie, P.A., Gupta, S. & Dawers, N.H., 2000. Implications of fault array evolution for syn-rift depocentre development: insights from a numerical fault growth model, *Basin Research*, **12**, 241-261.

Crone A., Machette M. & Bowman J., 1997. The episodic nature of earthquake activity in stable continental regions revealed by paleoseismicity studies of Australian and North American Quaternary faults, *Australian Journal of Earth Sciences*, **44**, 203-214.

Crone, A.J., DeMartini, P.M., Machette, M.N., Okumura, K. & Prescott, J.R., 2003. Paleoseismicity of Two Historically Quiescent Faults in Australia: Implications for Fault Behavior in Stable Continental Regions, *Bulletin Seism. Society America*, **93(5)**, 1913-1934.

Crosby, B. T., Whipple, K. X., Gasparini, N. M. & Wobus,C. W., 2007. Formation of fluvial hanging valleys: Theory and simulation, *J. Geophys. Res.* **112**, doi:10.1029/2006JF000566.

Dahm, T., 2000. Numerical simulations of the propagation path and the arrest of fluid-filled fractures in the Earth, *Geophys. Journ. Int.* **141**, 623-638.

Davidson, J., Hassanzadeh, J., Stockli, D.F., Bashukooh, B., Turrin, B. & Pandamouz, A., 2004. The geology of Damavand volcano, Alborz Mountains, northern Iran, *Bulletin Geol. Soc. America* **116(1/2)**, 16-29, doi:10.1130/B25344.1.

Davoudzadeh, M. & Schmidt, K., 1984. A review of the Mesozoic paleogeography and paleotectonic evolution of Iran, *Neues Jahrbuch für Geologie und Paläontologie, Abhandlungen* **168(2/3)**, 182-207.

Dawers, N.H., Anders, M. & Scholz, Ch.H., 1993. Growth of normal faults: displacement-length scaling, *Geology* **21**, 1107-1110.

Dawers, N.H. & Anders, M.H., 1995. Displacement-length scaling and fault linkage *Journal of Struct. Geology* **17(5)**, 607-614.

Dellenbach, J., 1964. Contribution a I etude geologique de region situess a l est de Tehran (Iran), *Fac. Sci., Univ. Strasbourg (France), PhD dissertation* , 117p.

De Martini, P.M., Hessami, K., Pantosi, D., Addezio, G.D., Alinaghi, H. & Ghafory-Ashtiani, M., 1998. A geologic contribution to the evaluation of the seismic potential of the Kahrizak fault (Tehran, Iran), *Tectonophysics* **287**, 187-199.

Deng, Q., Zhang, P. & Chen, S.,1986. Structure and deformation character of strike-slip fault zones, *Pure and Applied Geophysics* **124**, 203-223.

Densmore, A. L., Ellis, M. A., & Anderson, R. S., 1998. Landsliding and the evolution of normal-fault-bounded mountains, *J. Geophys. Res.*, **103(B7)**, 15203-15219.

Densmore, A.L., Dawers, N.H., Gupta, S., Allen, P.A. & Gilpin, R, 2003. Fault growth and landscape evolution at extensional relay zones. *J. Geophys. Research* **108(B5)**, 2273.

Densmore, A. L., Dawers, N. H., Gupta, S.& Guidon, R., 2005. What sets topographic relief in extensional footwalls?, *Geology* **33(6)**, 453-456.

Densmore, A.L., Gupta, S., Allen, P.A. & Dawers, N.H., 2007. Transient landscapes at fault tips *J. Geophys. Research* **112**, F03S08.

Di Bucci, D., Massa, B. & Zupetta, A., 2006. Relay ramps in active normal fault zones: A clue to the identification of seismogenic sources (1688 Sannio earthquake, Italy), *GSA Bulletin***118(3/4**, 430-448.

Dolan, J.F., Bowman, D.D., and Sammis, C.G., 2007. Long-range and long-term fault interactions in Southern California, *Geology* **35(9)**, 855-858.

Dühnforth, M., Densmore, A.L., Ivy-Ochs, S., Allen, P.A. & Kubik, P.W., 2007. Timing and patterns of debris flow deposition on Shepherd and Symmes creek fans, Owens Valley, California, deduced from cosmogenic 10Be, *J. Geophys. Res.* **112**, doi:10.1029/2006JF000562.

Eberhart-Phillips, D., Haeussler, P.J., Freymueller, J.T., Frankel, A.D., Rubin, C.M., Craw, P., Ratchkovski, N.A., Anderson, G., Carver, G.A., Crone, J.A., Dawson, T.E., Fletcher, H., Hansen, R., Harp, E.L., Harris, R.A., Hill, D.P., Hreinsdóttir, S., Jibson, R.W., Jones, L.M., Kayen, R., Keefer, D.K., Larsen, C.F., Moran, S.C., Personius, S.F., Plafker, G., Sherrod, B., Sieh, K., Sitar, N. & Wallace, W.K., 2003. The 2002 Denali Fault Earthquake, Alaska: A large magnitude, slip-partitioned event, *Science* **300**, 1113-1118.

Ellis, M.A. & Dunlap, W.J., 1988. Displacement variation along thrust faults: implications for the development of large faults, *J. Struct. Geology* **10(2)**, 183-192.

Ellis, M.A., Densmore, A.L. & Anderson, R.S., 1999. Development of mountainous topography in the Basin Ranges, USA, *Basin Research*, **11**, 21-41.

Engalenc, M., 1968. Contribution a la Geologie, Geomorphologie, Hydrogeologie de la region de Tehran (Iran), *C.E.R.H., Montpellier, France* , 365p.

Engdahl, E.R., Jackson, J.A., Myers, S.C., Bergman, E.A. & Priestley, K., 2006. Relocation and assessment of seismicity in the Iran region *Geophys. J. Int.* **167(2)**, 761-778, doi:10.1111/j.1365-246X.2006.03127.x.

Enz, R., Zimmerli, P. & Schwarz, S., 2009. Natural catastrophes and man-made disasters in 2008: North America and Asia suffer heavy losses *sigma (Swiss Reinsurance* **2/2009**.

Fäh, D., Gisler, M., Jaggi,B., Kästli, Ph., Lutz, Th., Masciadri, V., Matt, Ch., Mayer-Rosa, D., Rippmann, D., Schwarz-Zanetti, G., Tauber, J. & Wenk, TH., 2009. The 1356 Basel earthquake: an interdisciplinary revision, *Geophys. Journ. Int.* **178(1)**, 351-374, doi: 10.1111/j.1365-246X.2009.04130.x.

Fakhari, M. D., Axen, G. J., Horton, B. K., Hassanzadeh, J. & Amini, A., 2008. Revised age of proximal deposits in the Zagros foreland basin and implications for Cenozoic evolution of the High Zagros, *Tectonophysics* **451**, 170-185.

Fazeli, H., Coningham, R.A.E. & Batt, C.M., 2004. Cheshmeh Ali revisited: Towards an absolute dating of the Late Neolithic and Chalcolithic of Iran's Tehran Plain, *Iran*, **42**, 25-45.

Friedrich, A.M., Wernicke, B., Niemi, N.A., Bennett, R.A. & Davis, J.L.,2003. Comparison of geodetic and geologic data from the Wasatch region, Utah, and implications for the spectral character of Earth deformation at periods of 10 to 10 million years *Journal of Geophysical Research* **108(B4)**, doi:10.1029/2001JB000682.

Gao, L. & Wallace, T. C., 1995. The 1990 Rudbar-Tarom Iranian earthquake sequence: Evidence for slip partitioning, *J. Geophys. Research*, **100(8)**, 15317-15332.

Gillmore, G.K., Coningham, R.A.E., Young, R., Fazeli, H., Rushworth, G., Donahue, R. & Batt, C.M., 2007. Holocene alluvial sediments of the Tehran Plain: sedimentation and archaeological site visibility, *in: Reconstructing Human-Landscape Interactions*, Cambridge Scholars, Newcastle, 37-67.

Golombek, M.P., McGill, G.E. & Brown, L., 1983. Tectonic and geologic evolution of the Espanola Basin, Rio Grande Rift: Structure, rate of extension, and relation to the state of stress in the western United States, *Tectonophysics* **94**, 483-507.

Gosse, J.C. & Phillips, F.M., 2001. Terrestrial in situ cosmogenic nuclides: theory and application, *Quaternary Science Reviews*, **20**, 1475-1560.

Graf, T., Kohl, C.P., Marti, K. & Nishiizumi, K., 1991. Cosmic ray produced neon in Antarctic rocks. *Geophys. Res. Lett.*, **18**, 203-206.

Granger, D. & Muzikar, P.F., 2001. Dating sediment burial with in situ-produced cosmogenic nuclides: theory, techniques, and limitations, *Earth and Planetary Science Letters* **188**, 269-281.

Griffith, W.A. and Cooke, M.L., 2005. How sensitive are fault-slip rates in the Los Angeles basin to tectonic boundary conditions?, *Bulletin Seism. Soc. America* **94(4)**, 1263-1275.

Guest, B., Axen, G.J., Lam, P.S. & Hassanzadeh, J., 2006a. Late Cenozoic shortening in the west-central Alborz Mountains, northern Iran, by combined conjugate strike-slip and thin-skinned deformation, *Geosphere* **2**, 35-52.

Guest, B., Stockli, D.F., Grove, M., Axen, G.J., Lam, P.S. & Hassanzadeh, J., 2006b. Thermal histories from the central Alborz Mountains, northern Iran: Implications for the spatial and temporal distribution of deformation in northern Iran, *Bulletin Seism. Soc. America* **118(11/12)**, 1507-1521.

Guest, B., Guest, A. & Axen, G., 2007. Late tertiary tectonic evolution of northern Iran: A case for simple crustal folding, *Global and Planetary Change*(58), 435-453.

Gupta, S., Cowie, P.A., Dawers, N.H. & Underhill, J.R., 1998. A mechanism to explain rift-basin subsidence and stratigraphic patterns through fault-array evolution, *Geology* **26(7)**, 595-598.

Gupta, S. & Scholz, C.H., 2000. A model of normal fault interaction based on observations and theory, *J. Struct. Geology* **22**, 865-879.

Hampel, A., Hetzel, R., Maniatis, G. & Karow, T., 2009. Three-dimensional numerica modeling of slip rate variations on normal and thrust fault arrays during ice cap growth and melting, *J. Geophys. Research*, **114**, doi: 10.1029/2008JB006113.

Hancock, P.L. & Skinner, B.J., 2000. *O*xford companion to the earth, Oxford University Press, 1174 p.

Hardebeck, J.L., Nazareth, J.J., and Hauksson, E., 1998. The static stress change triggering model: constraints from two southern California aftershock sequences, *J. Geophys. Research* **103(B10)**, 24427-24437.

Hartleb, R.D., Dolan, J.F., Akyüz, H.S., Dawson, T.E., Tucker, A.Z., Yerli, B., Rockwell, T.K., Toraman, E., Çakir, Z., Dikbaş, A. & Altunel, E., 2002. Surface Rupture and Slip Distribution along the Karadere Segment of the 17 August 1999 Izmit and the Western Section of the 12 November 1999 Düzce, Turkey, Earthquakes, *Bulletin Seism. Soc. America* **92(1)**, 67-78.

Hessami, K. & Jamali, F.,2006. Explanatory Notes to the Map of Major Active Faults of Iran, *JSEE* **8(1)**.

Hetzel, R., Tao, M., Niedermann, S., Strecker, M. R., Ivy-Ochs, S., Kubik, P. W. & Gao, B. (2004), Implications of the fault scaling law for the growth of topography: mountain ranges in the broken foreland of north-east Tibet, *Terra Nova* **16**, 157-162.

Heidbach, O., Tingay, M., Barth, A., Reinecker, J., Kurfeß, D. & Müller, B. (eds.),2008. The World Stress Map - Release 2008, *Commission for the Geological Map of the World, Paris, 1:46M.*

Hilley, G.E., Arrowsmith, J.R. & Bürgmann, R., 1997. Investigation of Active Deformation Using a Landscape Development Model and Field Examination of Landforms and Geology along the Northeastern Margin of the Southern Santa Cruz Mountains, Geological Society of America Abstracts with Programs, 1997 Annual Meeting.

Hilley, G.E. & Arrowsmith, J.R., 2000. Thrust fault slip rates deduced from coupled geomorphic and tectonic models of active faults and folds in the San Francisco Bay Area: Collaborative Research with Arizona State University, and University of California, Davis, *USGS Final Technical Report* **1434-H-97-GR-03113**, 82p.

Hilley, G.E., Strecker, M.R. & Ramos, V.A., 2004. Growth and erosion of fold-and-thrust belts with an application to the Aconcagua fold-and-thrust belt, Argentina, *J. Geophys. Research* **109**, doi:10.1029/2002JB002282.

Hilley, G.E., Blisniuk, P.M. & Strecker, M.R., 2005. Mechanics and erosion of basement-cored uplift provinces, *J. Geophys. Research* **110**, doi:10.1029/2005JB003704.

Hollingsworth, J., Jackson, J., Walker, R. & Nazari, H., 2008. Extrusion tectonics and subduction in the eastern South Caspian region since 10 Ma, *Geology* **36(10)**, 763-766, doi: 10.1130/G25008A.1.

Hollingsworth, J., Jackson, J., Walker, R. & Nazari, H., 2009. Extrusion tectonics and subduction in the eastern South Caspian region since 10 Ma: Reply *Geology* **37**, e199-e200, doi: 10.1130/G30529Y.1

Horton, B.K., Hassanzadeh, J., Stockli, D.F., Axen, G.J., Gillis, R.J., Guest, B., Amini, A., Fakhari, M.D., Zamanzadeh, S.M. & Grove, M., 2008. Detrital zircon provenance of Neoproterozoic to Cenozoic deposits in Iran: Implications for chronostratigraphy and collisional tectonics, *Tectonophysics*, **451**, 97-122.

Hubert-Ferrari, A., Barka, A., Jaques, E., Nalbant, S., Meyer, B., Armijo, R., Tapponier, P. & King, G.C.P., 2000. Seismic hazard in the Marmara Sea region following the 17 August 1999 Izmit earthquake, *Nature* **404**, 269-273.

Jackson, J. & McKenzie, D., 1984. Active tectonics of the Alpine-Himalayan Belt between western Turkey and Pakistan, *Geophys. J. R. astr. Soc.*, **77**, 185-264.

Jackson, J., 1992. Partitioning of Strike-Slip and Convergent Motion Between Eurasia and Arabia in eastern Turkey and the Caucasus, *J. Geophys. Research* **97**, 12471-12479.

Jackson, J., Haines, J. & Holt, W., 1995. The accommodation of Arabia-Eurasia plate convergence in Iran, *J. Geophys. Research* **100**, 15205-15219.

Jackson, J., Norris, R. & Youngson, J., 1996. The structural evolution of fault and fold systems in central Otago, New Zealand: Evidence revealed by drainage patterns, *J. Struct. Geology* **18**, 217-234.

Jackson, J., Ritz, J.F., Siame, L., Raisbeck, G., Yiou, F., Norris, R., Youngson, J. & Bennett, E., 2002. Fault growth and landscape development rates in Otago, New Zealand, using in situ cosmogenic 10Be *Earth Planet. Science Letters* **195**, 185-193.

Jackson, J., Priestley, K., Allen, M. & Berberian, M., 2002. Active Tectonics of the South Caspian Basin, *Geophys. J. Int.* **148**, 214-245.

Jackson, M.P.A., Cornelius, R.R., Craig, C.H., Gansser, A., Stocklin, J. & Talbot, C.J., 1990. Salt diapirs of the Great Kavir, central Iran, *Geological Society of America, Boulder, Colo.*, 139 p.

Johnston, A. C., 1996. Seismic moment assessment of earthquakes in stable continental regions - I Instrumental seismicity, *Geophys. J. Int.*, **124**, 381-414.

Johnston, A.C., 1996. Seismic moment assessment of earthquakes in stable continental regions- III. New Madrid 1811-1812, Charleston 1886 and Lisbon 1755, *Geophys. J. Int.*, **126**, 314-344.

Johnston, A.C. & Schweig, E.S., 1996. The enigma of the New Madrid earthquakes of 1811-1812, *Annu. Rev. Earth Planet. Sci*, **24**, 339-384.

Keller, E.A., Zepeda, R.L., Rockwell, T.K., Ku, T.L. & Dinklage, W.S., 1998. Active tectonics at Wheeler Ridge, southern San Joaquin Valley, California *Bulletin Geol. Soc. America* **110**, 298-310.

Keller, E.A., Gurrola, L. &Tierney, T.E., 1999. Geomorphic criteria to determine direction of lateral propagation of reverse faulting and folding, *Geology* **27**, 515-518.

King, G. C. P., Stein, R. & Rundle, J. B., 1988. The growth of geological structures by repeated earthquakes 1: Conceptual framework, *J. Geophys. Research* **93(11)**, 13307-13318.

King, G., Klinger, Y., Bowman, D. & Tapponnier, P., 2005. Slip-Partitioned Surface Breaks for the Mw 7.8 2001 Kokoxili Earthquake, China, *Bulletin Seism. Soc. America* **95(2)**, 731-738.

Kirby, E. & Whipple, K.X., 2001. Quantifiying differential rock-uplift rates via stream profile analysis, *Geology* **29(5)**, 415-418.

Kirby, E., Whipple, K.X., Tang, W. & Chen, Z., 2003. Distribution of active rock uplift along the eastern margin of the Tibetan plateau: Inferences from bedrock channel longitudinal profiles, *J. Geophys. Research*, **108(4)**, DOI: 10.1029/2001JB000861.

Kirby, E., Johnson, C.,Furlong, K. & Heimsath, A., 2007. Transient channel incision along Bolinas Ridge, California: Evidence for differential rock uplift adjacent to the San Andreas fault, *J. Geophys. Res.* **112**, doi:10.1029/2006JF000559.

Klein, J., Giegengack, R., Middleton, R., Sharma, P., Underwood, J. & Weeks, R.A., 1986. Revealing histories of exposure using in situ produced 26Al and 10Be in Libyan desert glass. *Radiocarbon*, **28**, 547-555.

Kober, F., Ivy-Ochs, S., Schlunegger, F., Baur, H., Kubik, P.W. & Wieler, R., 2007. Denudation rates and a topography-driven precipitation threshold in northern Chile: multiple cosmogenic nuclide data and sediment yield budgets, *Geomorphology*, **83**, 97-120.

Koons, P.O., 1994. Three-dimensional critical wedges: Tectonics and topography in oblique collisional orogens, *J. Geophys. Res.*, **99(B6)**, 12301-12315.

Koons, P.O., 1995. Modelling the topographic evolution of collisional mountain belts, *Annual Reviews of Earth and Planetary Sciences*, **23**, 375-408.

Korschinek, G., Bergmaier, A., Faestermann, T., Gerstmann, U.C., Knie, K., Rugel, G., Wallner, A., Dillmann, I., Dollinger, G., Lierse von Gostomski, Ch., Kossert, K., Maiti, M., Poutivtsev, M. & Remmert, A., 2009. A new value for the half-life of 10Be by Heavy-Ion Elastic Recoil Detection and liquid scintillation counting, *Nucl. Instr. and Meth. in Phys. Res. B*, **268(2)**, 187-191.

Kürsten, M., 1980. Zur geodynamischen Entwicklung des Iran, ein Beispiel intrakratonischer struktureller Vorgänge, *International Journal of Earth Sciences*, **69(1)**, 22-40.

Lal, D., 1991. Cosmic ray labeling of erosion surfaces: in situ nuclide production rates and erosion models, *Earth and Planetary Science Letters* **104**, 424-439.

Lal, D., & Chen, J., 2005. Cosmic ray labeling of erosion surfaces II: Special cases of exposure histories of boulders, soils and beach terraces, *Earth and Planetary Science Letters*, **236**, 797-813, doi:10.1016/j.epsl.2005.05.025.

Lal, D., & Chen, J., 2006. Erratum to "Cosmic ray labeling of erosion surfaces II: Special cases of exposure histories of boulders, soils and beach terraces", *Earth and Planetary Science Letters*, **241**, 360, doi:10.1016/j.epsl.2005.11.002.

Landgraf, A., Ballato, P., Strecker, M.R., Friedrich, A., Tabatabaei, S.H. & Shahpasandzadeh, M., 2009. Fault-kinematic and geomorphic observations along the North Tehran Thrust and Mosha Fasham Fault, Alborz mountains Iran: implications for fault-system evolution and interaction in a changing tectonic regime, *Geophys. J. Int.* **177(2)**, 676-690, DOI: 10.1111/j.1365-246X.2009.04089.x.

Lin, J. & Stein, R., 2004. Stress triggering in thrust and subduction earthquakes and stress interaction between the southern San Andreas and nearby thrust and strike-slip faults, *J. Geophys. Research* **109**, 975-978.

Liu, B., Phillips, F.M., Fabryka-Martin, J.T., Fowler, M.M. & Stone, W.D., 1994. Cosmogenic $^{36}Cl$ accumulation in unstable landforms 1. Effects of the thermal neutron distribution, *Water Resources Research* **30(11)**, 3115-3125.

Manighetti, I., Zigone, D., Campillo, M. & Cotton, F., 2009. Self-similarity of the largest-scale segmentation of the faults: Implications for earthquake behavior, *Earth and Planetary Science Letters* **288**, 370-381.

Marrett, R. A., Allmendinger, R.W., Alonso, R. N., & Drake, R. E., 1994. Late Cenozoic tectonic evolution of the Puna Plateau and adjacent foreland, northwestern Argentine Andes, *J. South Amer. Earth Sciences* **7**, 179-207.

Marshall, J.S. & Anderson, R.S., 1995. Quaternary uplift and seismic cycle deformation, Península de Nicoya, Costa Rica, *GSA Bulletin*, **107(4)**, 463-473.

Masson, F., Anvari, M., Djamour, Y., Walpersdorf, A., Tavakoli, F., Daignieres, M., Nankali, H., and Van Gorp, S., 2007. Large-scale velocity field and strain tensor in Iran inferred from GPS measurements: new insight for the present-day deformation, *Geophys. J. Int.* **170**,436-440.

McKenzie, D.P. & Morgan, W.J., 1969. Evolution of Triple Junctions, *Nature* **224**, 125-133.

Meigs, A. J., Cooke, M. L. & Marshall, S. T., 2008. Using vertical rock-uplift patterns to constrain the three-dimensional fault configuration in the Los Angeles Basin, *Bulletin Seism. Soc. America* **98(2)**, 106-123.

Melnick, D., Bookhagen, B., Echtler, H., & Strecker, M., 2006, Coastal deformation and great subduction earthquakes, Isla Santa María, Chile (37°S), *GSA Bulletin*, **118**, 1463-1480.

Melnick, D., Bookhagen, B., Strecker, M., & Echtler, H., 2009. Segmentation of megathrust rupture zones from forearc deformation patterns over hundreds to millions of years, Arauco Peninsula, Chile, *J. Geophys. Res.*, **114**, B01407.

Merchel, S., Arnold, M., Aumaître, G., Benedetti, L., Bourlès, D.L., Braucher, R., Alfimov, V., Freeman, S.P.H.T., Steier, P. & Wallner, A., 2008. Towards more precise $^{10}Be$ and $^{36}Cl$ data from measurements on the $10^{-14}$ level: Influence of sample preparation, *Nucl. Instr. and Meth. in Phys. Res. B*, **266(22)**, 4921-4926.

Merchel, S., Benedetti, L., Bourlès, D.L., Braucher, R., Dewald, A., Faestermann, T., Finkel, R.C., Korschinek, G., Masarik, J., Poutivtsev, M., Rochette, P., Rugel, G. & Zell, K.-O., 2010. A multi-radionuclide approach for in-situ produced terrestrial cosmogenic nuclides: $^{10}Be$, $^{27}Al$, $^{36}Cl$, and $^{40}Ca$ from carbonate rocks, *Nucl. Instr. and Meth. in Phys. Res. B*, in press.

Mériaux, A.-S., Ryerson, F.J., Tapponnier, P., Van derWoerd, J., Finkel, R.C., Xu, X., Xu, Z. & Caffee, M.W., 2004. Rapid slip along the central Altyn Tagh Fault: morphochronologic evidence from Cherchen He and Sulamu Tagh, *J. Geophys. Res.* **109 (B06401)**, doi:10.1029/2003jb002558.

Mériaux, A.-S., Tapponnier, P., Ryerson, F.J., Xu, X., King, G., Van der Woerd, J., Finkel, R.C., Li, H., Caffee, M.W., Xu, Z. & Chen, W., 2005. The Aksay segment of the northern Altyn Tagh fault: tectonic geomorphology, landscape evolution, and Holocene slip rate, *J. Geophys. Res.* **110** ,doi:10.1029/2004JB003210.

Merrits, D. & Vincent, K.R., 1989. Geomorphic response of coastal streams to low, intermediate, and high rates of uplift, Mendocino triple junction region, Northern California, *Bulletin Geol. Soc. America* **101**, 1373-1388.

Meyer, B.,Tapponnier, P.,Bourjot, L.,Metivier, F.,Gaudemer, Y., Peltzer, G.,Shunmin, G., & Zhitai, C., 1998. Crustal thickening in Gansu-Qinghai, lithospheric mantle subduction, and oblique, strike-slip controlled growth of the Tibet plateau, *Geophys. J. Int.* **135**, 1-47.

Mohajer-Ashjai, A. & Nowroozi, A. A., 1979. The Tabas earthquake of September 16, 1978 In East-Central Iran: A preliminary field report, *Geophys. Res. Letters*,**6(9)**, 689-692.

Moix, P., Beccaletto, L., Kozur, H.W., Hochard, C., Rosselet, F. & Stampfli, G.M., 2007. A new classification of the Turkish terranes and sutures and its implication for the paleotectonic history of the region, *Tectonophysics*, **451**, 7-39

Moinabadi, M.E. & Yassaghi, A., 2007. Geometry and kinematics of the Mosha Fault, south central Alborz Range, Iran: An example of basement involved thrusting, *J. Asian Earth Sciences* **29(5-6)**, 928-938.

Molnar, P. & Tapponnier, P., 1975. Cenozoic Tectonics of Asia: Effects of a Continental Collision, *Science*, **189**, 419-426.

Mora, A., Parra, M., Strecker, M.R., Kammer,A., Dimaté, C. & Rodríguez, F., 2006. Cenozoic contractional reactivation of Mesozoic extensional structures in the Eastern Cordillera of Colombia, *Tectonics*,**25**, doi:10.1029/2005TC001854.

Morley, C.K., Kongwung, B., Julapour, A.A., Abdolghafourian, M., Hajian, M., Waples, D., Warren, J., Otterdoom, H., Srisuriyon, K. & Kazemi, H., 2009. Structural development of a major late Cenozoic basin and transpressional belt in central Iran: The Central Basin in the Qom-Saveh area, *Geosphere*, **5**, 325-362, doi: 10.1130/GES00223.1.

Nazari, H., Ritz, J.-F., Salamati, R., Shafai, A., Ghassemi, A., Michelot, J.-L., Massault, M. & Ghorashi, M., 2009. Morphological and palaeoseismological analysis along the Taleghan fault (Central Alborz, Iran), *Geophys. J. Int.*, **178(2)**, 1028-1041, doi: 10.1111/j.1365-246X.2009.04173.x.

Nazari, H., Ritz, J.-F., Salamati, R., Shahidi, A., Habibi, H., Ghorashi, M. & Bavandpur, A.K., 2010. Distinguishing between fault scarps and shorelines: the question of the nature of the Kahrizak, North Rey and South Rey features in the Tehran plain (Iran), *Terra Nova*, **22**, 227-237.

Niemi, N.A., Wernicke, B.P., Friedrich, A.M., Simons, M. Bennet, R.A. & Davis, J.L., 2004. BARGEN continuous GPS data across the eastern Basin and Range province, and implications for fault system dynamics, *Geophys. J. Int.* **159**, 842-862.

Nowroozi, A.A.,1976. Seismotectonic provinces of Iran, *Bulletin Seism. Soc. America* **66(4)**, 1249-1276.

Nowroozi, A.A.,1979. Reply to M. Berberian Comparison between instrumental and macroseismic epicenter, *Bulletin Seism. Soc. America* **69(2)**, 641-649.

Okada, Y., 1992. Internal deformation due to shear and tensile faults in a half-space *Bulletin Seism. Soc. America* **82**, 1018-1040.

Parsons, T., 2002. Nearly frictionless faulting by unclamping in long-term interaction models *Geology* **30(12)**, 1063-1066.

Peacock, D.C.P. & Sanderson, D.J., 1991. Displacements, segment linkage and relay ramps in normal fault zones, *J. Struct. Geology*, **13(6)**, 721-733.

Peacock, D.C.P. & Sanderson, D.J., 1995. Strike-slip relay ramps, *J. Struct. Geology*, **17(10)**, 1351-1360.

Peltzer, G. & Tapponnier, P., 1988. Formation and evolution of strike-slip faults, rifts, and basins during the India-Asia collision: an experimental approach, *J. Geophys. Research* **93(12)**, 15085-15117.

Peltzer, G., Crampé, F., Hensley, S. & Rosen, P., 2001. Transient strain accumulation and fault interaction in the Eastern California shear zone, *Geology* **29(11)**, 975-978.

Perg, L.A., Anderson, R.S. and Finkel, R.C., 2001. Use of a new 10Be and 26Al inventory method to date marine terraces, Santa Cruz, California, USA, *Geology*, **29(10)**, 879-882.

Perg, L.A., Anderson, R.S. and Finkel, R.C., 2002. Use of a new 10Be and 26Al inventory method to date marine terraces, Santa Cruz, California, USA: Comment and Reply *Geology*, **30(12)**, 1148. 879-882.

Philip, H. & Meghraoui, M., 1983. Structural analysis and interpretation of the surface deformations of the El Asnam earthquake of October 10, 1980,*Tectonics* **2**, 17-49.

Phillips, F.M., Zreda, M.G., Gosse, J.C., Klein, J., Evenson, E.B., Hall, R.D., Chadwick, O.A. & Sharma, P., 1997. Cosmogenic $^{36}Cl$ and $^{10}Be$ ages of Quaternary glacial and fluvial deposits of the Wind River Range, Wyoming, *GSA Bulletin* **109(11)**, 1453-1463.

Phillips, F.M., Stone, W.D. & Fabryka-Martin, J.T., (2001). An improved approach to calculating low-energy cosmic-ray neutron fluxes near the land/atmosphere interface, *Chemical Geology*, **175**, 689-701.

Phillips, F.M., Zreda, M.G., Plummer, M.A., Elmore, D. & Clark, D.H., 2009. Glacial geology and chronology of Bishop Creek and vicinity, eastern Sierra Nevada, California, *GSA Bulletin* **121(7/8)**, 1013-1033, doi:10.1130/B26271.1.

Pollard, D.D. & Aydin, A., 1988. Progress in understanding jointing over the past century, *Bulletin Geol. Soc. America* **100**, 1181-1204.

Pollard, D.D. & Fletcher, R.C., 2005. *Fundamentals of Structural Geology*, Cambridge University Press, Cambridge.

Pollastro, R. M., Persits, F. M. & Steinshouer, D. W., 2000. Map showing geology, oil and gas fields, and geologic provinces of Iran, *U.S. Geological Survey Open File Report* **97-470G**, 1 CD.

Pollitz, F.F. & Sacks, S.I., 2002. Stress triggering of the 1999 Hector Mine eartquakes by transient deformation following the 1992 Landers earthquakes, *Bulletin Seism. Soc. America* **92(4)**, 1487-1496.

Power, W.L. & Tullis, T.E., 1991. Euclidean and Fractal Models for the Description of Rock Surface Roughnes, *J. Geophys. Research* **96(B1)**, 415-424.

Priestley, K., Baker, C. & Jackson, J., 1994. Implications of earthquake focal meccanism data for the active tectonics of the south Caspian Basin and surrounding regions, *Geophys. J. Int.* **118**, 111-141.

Radjaee, A., Rham, D., Mokhtari, M., Tatar, M., Priestley, K. & Hatzfeld, D., 2010. Variation of Moho depth in the central part of the Alborz Mountains, northern Iran, *Geophys. J. Int.*, **181**, 173-184.

Rastogi, B.K., Gupta, H.K., Prantik Mandal, Satyanarayana, H.V.S., Kousalya, M., Raghavan, R., Richa Jain, Sarma, A.N.S., Kumar, N. & Satyamurty, C., 2001. The deadliest stable continental region earthquake occurred near Bhuj on 26 January 2001, *J. of Seismology*, **5**, 609-615.

Raterman, N. S., Cowgill, E. & Lin, D., 2007. Variable structural style along the Karakoram fault explained using triple-junction analysis of intersecting faults, *Geosphere* **3(2)**, 71-85.

Reasenberg, P.A., & Simpson, R.W., 1992. Response of regional seismicity to the static stress change produced by the Loma Prieta earthquake, *Science* **255**, 1687-1690.

Renard, F., Voisin, C., Marsan, D. & Schmittbuhl, J., 2006. High resolution 3D laser scanner measurements of a strike-slip fault quantify its morphological anisotropy at all scales, *Geophys. Res. Lett.* **33**, doi:10.1029/2005GL025038.

Repka, J.L., Anderson, R.S. & Finkel, R.C., 1997. Cosmogenic dating of fluvial terraces, Fremont River, Utah, *Earth and Planetary Science Letters* **152**, 59-73.

Rezaeian, M., 2008. Coupled tectonics, erosion and climate in the Alborz mountains (PhD. thesis), Cambridge, University of Cambridge, 237p.

Rieben, H., 1955. The geology of the Teheran Plain, *American Journal of Science* **253**, 617-639.

Rieben, H., 1966. Geological observations on alluvial deposits in northern Iran, *Geological Survey of Iran*, **9**, 39p.

Ritz, J.F., Balescu, S., Sleymani, S., Abbassi, M., Nazari, H., Feghhi, K., Shabanian, E., Tabassi, H., Farbod, Y., Lamothe, M., Michelot, J.L., Massault, M., Chery, J. & Vernant, P., 2003. Geometry, kinematics and slip rate along the Mosha active fault, central Alborz: Nice, France, EGU-AGU-EUG Joint Assembly, Abstract EAE03-A-06057.

Ritz, J.-F., Nazari, H., Ghassemi, A., Salamati, R., Shafei, A., Solaymani, S. & Vernant, P., 2006a. Active transtension inside Central Alborz: A new insight into the northern Iran-southern Caspian geodynamics, *Geology* **34(6)**, 477-480.

Ritz, J.-F., Vassallo, R., Braucher, R., Brown, E.T., Carretier, S. & Bourlès, D., 2006b. Using in situ-produced $^{10}Be$ to quantify active tectonics in the Gurvan Bogd mountain range (Gobi-Altay, Mongolia), *GSA Special Paper* **415**, 87-110.

Ritz, J.-F., 2009. Extrusion tectonics and subduction in the eastern South Caspian region since 10 Ma: Comment *Geology* **37**, e191, doi: 10.1130/G25627C.1

Rockwell, T.K., Lindvall, S., Herzberg, D., Murbach, D., Dawson, T. & G. Berger, 2000. Paleoseismology of the Johnson Valley, Kickapoo, and Homestead Valley faults: clustering of earthquakes in the eastern California shear zone, *Bulletin Seism. Soc. America* **90**, 1200-1236.

Roe, G. H., Montgomery, D. R. & Hallet, B., 2003. Orographic precipitation and the relief of mountain ranges, *J. Geophys. Res.*, **108(B6)**, 2315, doi:10.1029/2001JB001521.

Roe, G. H., Stolar, D. B. & Willett, S. D., 2006. Response of a steadystate critical wedge orogen to changes in climate and tectonic forcing, in Tectonics, Climate, and Landscape Evolution, edited by S. D. Willett et al., Penrose Conf. Ser., *Spec. Pap. Geol. Soc. Am.*, **398**, 227-239.

Sagy, A., Brodsky, E.E. & Axen, G.J., 2007. Evolution of fault-surface roughness with slip *Geology* **35(3)**, 283-286.

Sanderson, D.J. & Marchini, W.R.D., 1984. Transpression, *J. Struct. Geology* **6(5)**, 449-458.

Schaller, M., von Blanckenburg, F., Hovius, N., Veldkamp, A., van den Berg, M. W., & Kubik, P. W., (2004). Paleoerosion rates from cosmogenic 10Be in a 1.3Ma terrace sequence: response of the River Meuse to changes in climate and rock uplift, *Journal of Geology* **112**, 127-144.

Schaller, M., Ehlers, T.A., Bluhm, J.D. & Kallenberg, M.A., 2009. Quantifying glacial moraine age, denudation, and soil mixing with cosmogenic nuclide depth profiles, *J. geophys. Res.*, **114**, doi:10.1029/2007JF0000921.

Schimmelpfennig, I., Benedetti, L., Finkel, R., Pik, R., Blard, P.H., Bourl'es, D., Burnard, P. & Williams, A., 2009. Sources of in-situ 36Cl in basaltic rocks. Implications for calibration of production rates, *Quarter. Geochronol.*, submitted.

Schmedes, J., Hainzl, S., Reamer, S. K., Scherbaum, F. & Hinzen, K. G. (2004). Moment release in the lower Rhine Embayment, Germany: Seismological Perspective of the deformation process, *Geophysical Journal International*, **160(3)**, 901-909.

Scholz, C.H., 1982. Scaling laws for large earthquakes: consequences for physical models, *Bulletin Seism. Soc. America* **72(1)**, 1-14.

Schumacher, M. E., 2002. Upper Rhine Graben: Role of preexisting structures during rift evolution, *Tectonics*, **21(1)**, doi:10.1029/2001TC900022.

Shabanian, E., Bellier, O., Abbassi, M.R., Siame, L.L. & Farbod, Y., 2009. Plio-Quaternary stress states in NE Iran: Kopeh Dagh and Allah Dagh-Binalud mountain ranges, *Tectonophysics*, **480**, 280-304.

Siame, L., Bellier, O., Braucher, R., Sébrier, M., Cushing, M., Bourlès, D., Hamelin, B., Baroux, E., de Voogd, B., Raisbeck, G. & Yiou, F., 2004. Local erosion rates versus active tectonics: cosmic ray exposure modelling in Provence (south-east France), *Earth and Planetary Science Letters* **220**, 345-364 .

Siame, L.L., Shabanian, E. & Bellier, O., 2009. Extrusion tectonics and subduction in the eastern South Caspian region since 10 Ma: Comment *Geology* **37**, e197-e198, doi: 10.1130/G25701C.1

Singh, S. K., Pacheco, J. F., Bansal, B. K., Perez-Campos, X., Dattatrayam, R. S. & Suresh, G., 2004. A source study of the Bhuj, India, earthquake of 26 January 2001 (M w 7.60), *Bulletin Geol. Soc. America*, **94(4)**, 1195-1206.

Southon, J.R. Vogel, J.S., Trumbore, S.E., Davis, J.C., Roberts, M.L., Caffee, M.W., Finkel, R.C., Proctor, I.D., Heikkinen, D.W., Berno, A.J. & Hornady, R.S., 1992. Progress in AMS measurements at the LLNL Spectrometer, *Radiocarbon*, **34**, 473.

Spotila, J. A. & Anderson, K. B., 2004. Fault interaction at the junction of the Transverse Ranges and Eastern California shear zone: a case study of intersecting faults, *Tectonophysics* **379**, 43-60.

Stampfli, G.M. & Borel, G.D., 2002. A plate tectonic model for the Paleozoic and Mesozoic constrained by dynamic plate boundaries and restored synthetic oceanic isochrons, *Earth Planet. Science Letters* **196**, 17-33.

Stearns, R.G., 1967. Warping on the Western Highland Rim Peneplain in Tennessee by groundwater sapping, *Bulletin Seism. Soc. America* **78**, 1111-1124.

Steiger, R., 1966. Die Geologie der west-Firuzkuh-Area (Zentralelburz, Iran).*Mitteilungen aus dem geologischen Institut der Eidgenössischen Technischen Hochschule und der Universität Zürich, Neue Serie* , 1-145.

Stein, R., King, G.C.P. & Rundle, J. B., 1988. The growth of geological structures by repeated earthquakes 2: Field examples of continental dip-slip faults, *J. Geophys. Research* **93(11)**, 13319-13331.

Stein, R.S., Barka, A.A., and Dieterich, J.H., 1997. Progressive failure on the North Anatolian fault since 1939 by earthquake stress triggering, *Geophys. J. Int.* **128**, 594-604.

Stein, S., 1992. Seismic gaps and grizzly bears, *NATURE*, **356**, 387-388.

Stein, S., Friedrich, A. & Newman, A., 2005. Dependence of possible characteristic earthquakes on spatial sampling: illustration for the Wasatch Seismic Zone, Utah, *Seism. Res. Letters*, **76(4)**, 432-436.

Stein, S. & Liu, M., 2009. Long aftershock sequences within continents and implications for earthquake hazard assessment, *NATURE*, **462**, 87-89.

Stein, S., Liu, M., Calais, E. & Li, Q., 2009. Mid-continent earthquakes as a complex system, *Seism. Res. Letters*, **80(4)**, 551-553.

Stirling, MW, Wesnousky, SG & Shimazaki, K.,1996. Fault trace complexity, cumulative slip, and the shape of the magnitude-frequency distribution *Geophys. J. Int.* **124**, 833-868.

Stolar, D. B., Willett, S. D. & Roe, G. H., 2006. Climatic and tectonic forcing of a critical orogen, in Tectonics, Climate, and Landscape Evolution, edited by S. D. Willett et al., Penrose Conf. Ser., *Spec. Pap. Geol. Soc. Am.*, **398**, 241-250.

Stolar, D., Roe, G. & Willett, S., 2007. Controls on the patterns of topography and erosion rate in a critical orogen, *J. Geophys. Res.*, **112**, F04002, doi:10.1029/2006JF000713

Stone, J.O.H., Allan, G.L., Fifield, L.K. & Cresswell, R.G., 1996. Cosmogenic chlorine-36 from calcium spallation, *Geochim. Cosmochim. Acta*, **60(4)**, 679-692.

Stone, J.O.H., Evans, J.M., Fifield, L.K., Allan, G.L. & Cresswell, R.G., 1998. Cosmogenic chlorine-36 production in calcite by muons, *Geochim. Cosmochim. Acta*, **62(3)**, 433-454.

Stone, J.O.H., 2000. Air pressure and cosmogenic isotope production, *J. geophys. Res.*, **105(B10)**, 23753-23759.

Strecker, M.R., Cerveny, P., Bloom, A.L., & Malizia, D., 1989. Late Cenozoic tectonism and landscape development in the foreland of the Andes: Northern Sierras Pampeanas (268-288S), Argentina, *Tectonics*, **8**, 517-534.

Strecker, M.R., Blisniuk, P. & Eisbacher, G.H., 1990. Rotation of extension direction in the central Kenya Rift, *Geology* **18**, 299-302.

Strecker, M.R. & Marrett, R., 1999. Kinematic evolution of fault ramps and its role in development of landslides and lakes in th enorthwestern Argentine Andes, *Geology* **27(4)**, 307-310.

Strecker, M.R., Hilley, G., Arrowsmith, J R. & Coutand, I., 2003. Differential structural and geomorphic mountain-front evolution in an active continental collision zone: the NW Pamir, southern Kyrgyzstan, *Bulletin Geol. Soc. America* **115**, 166-181.

Sodoudi, F., Yuan, X., Kind, R., Heit, B. & Sadidkhouy, A., 2009. Evidence for a missing crustal root and a thin lithosphere beneath the Central Alborz by receiver function studies, *Geophys. J. Internat.*, **177(2)**, 733-742, doi: 10.1111/j.1365-246X.2009.04115.x.

Taboada, A., Bousquet, J. C. & Philip, H., 1993. Coseismic elastic models of folds above blind thrusts in the Betic Cordilleras (Spain) and evaluation of seismic hazard, *Tectonophysics* **220**, 223-241.

Tatar, M., Jackson, J., Hatzfeld, D. & Bergman, E., 2007. The 2004 May 28 Baladeh earthquake (Mw6.2) in the Alborz, Iran: overthrusting the South Caspian Basin margin, partitioning of oblique convergence and the seismic hazard of Tehran, *Geophys. J. Int.*,**170**, 249-261.

Tchalenko, J.S., 1974. Tectonic framework of the Tehran region, *in: Material for the Study of Seismotectonics of Iran: North-central Iran, Geological Survey of Iran, Report* **29**, 7-46.

Tchalenko, J.S., 1975. Seismotectonic framework of the North Tehran Fault, *Tectonophysics* **29**, 411-420.

Teyssier, C., Tikoff, B. & Markley, M., 1995. Oblique plate motion and continental tectonics, *Geology* **23(5)**, 447-450.

Teyssier, C. & Tikoff, B., 1998. Strike-slip partitioned transpression of the San Andreas fault system: a lithospheric-scale approach, in *Continental Transpressional and Transtensional Tectonics*, eds. Holdsworth, R.E., Strachan, R.A. & Dewey, J.F., Geological Society, London, Special Publications **135**, 143-158.

Thatcher, W. (1990), Present-day crustal movements and the mechanics of cyclic deformation, *USGS Professional Paper* **1515**, 188-205.

Thiede, R.C., Bookhagen, B., Arrowsmith, J.R., Sobel, E.R. & Strecker, M.R., 2004. Climatic control on rapid exhumation along the Southern Himalayan front, *Earth Planet. Sci. Lett.*, **222**, 791-806.

Thorson, R.M., 1989. Glacio-isostatic response of the Puget Sound area, Washington, *GSA Bulletin*, **101**, 1163-1174.

Trauth, M. (2007), *MATLAB - Recipes for Earth Sciences*, 2nd edition, Springer Verlag, Berlin, Heidelberg, 288pp.

Tucker, G.E. & Slingerland, R., 1996. Predicting sediment flux from fold and thrust belts, *Basin Research* **8**, 329-349.

Tuttle, M.P. & Schweig, E.S., 1995. Archeological and pedological evidence for large prehistoric earthquakes in the New Madrid seismic zone, central United States, *Geology*, **23**, 253-256.

Vernant, P., Nilforoushan, F., Hatzfeld, D., Abassi, M.R., Vigny, C., Masson, F., Nankali, H., Martinod, J., Ashtiani, A., Bayer, R., Tavakoli, F. & Chery, J., 2004a. Present-day crustal deformation and plate kinematics in the Middle East constrained by GPS measurements in Iran and northern Oman, *Geophys. J. Int.* **157**, 381-398.

Vernant, P., Nilforoushan, F., Chery, J., Bayer, R., Djamour, Y., Masson, F., Nankali, H., Ritz, J. F., Sedighi, M. & Tavakoli F., 2004b. Deciphering oblique shortening of central Alborz in Iran using geodetic data, *Earth Planet. Science Letters* **223**, 177-185.

Vita-Finzi, C., 1969. Late quaternary alluvial chronology of Iran. *Geologische Rundschau*, **58**, 951-973.

Walsh, J.J., Nicol, A. & Childs, C., 2002. An alternative model for the growth of faults, *J. Struct. Geology* **24**, 1669-1675.

Wells, D.L. & Coppersmith, K.J., 1994. New Empirical Relationships among Magnitude, Rupture Length, Rupture Width, Rupture Area, and Surface Displacement, *Bulletin Seism. Society of America*, **84(4)**, 974-1002.

Wesnousky, S.G., 1988. Seismological and structural evolution of strike-slip faults, *Nature* **335**, 340-343, doi:10.1038/335340a0.

Wesnousky, S.G., 2006. Predicting the endpoints of earthquake ruptures, *Nature* **444**, 358-360.

Whipple, K.X., Kirby, E. & Brocklehorst, S.H., 1999. Geomorphic limits to climate-induced increases in topographic relief, *Nature* **401**, 39-43.

Whipple, K.X. & Tucker, G.E., 1999. Dynamics of the stream-power river incision model: Implications for heigth limits of mountain ranges, landscape response timescales, and research needed, *J. Geophys. Research* **104(B8)**, 17661-17674.

Whipple, K.X., Hancock, G.S. & Anderson, R.S., 2000. River incision into bedrock: Mechanics and relative efficacy of plucking, abrasion, and cavitation, *Bulletin Seism. Soc. America* **112(3)**, 490-503.

Whipple, K.X. & Meade, B.J., 2006. Orogen response to changes in climatic and tectonic forcing, *Earth Planet. Science Letters* **243**, 218-228.

Wobus, C., Hodges, K.V. & Whipple, K.X., 2003. Has focused denudation sustained active thrusting at the Himalayan topographic front?, *Geology*, **31**, 861-864, doi: 10.1130/G19730.1.

Wobus, C., Whipple, K.X., Kirby, E., Snyder, N., Johnson, J., Spyropolou, K., Crosby, B. & Sheehan, D., 2006. Tectonics from topography: Procedures, promise, and pitfalls, in Tectonics, Climate, and Landscape Evolution, edited by S. D. Willett et al., Penrose Conf. Ser., *Spec. Pap. Geol. Soc. Am.*, **398**, 56-75.

Wolkowinsky, A.J. & Granger, D.E., 2004.Early Pleistocene incision of the San Juan River, Utah, dated with 26Al and 10Be, *Geology*, **32(9)**, 749-752.

Yassaghi, A. & Madanipour, S., 2008. Influence of a transverse basement fault on along-strike variations in the geometry of an inverted normal fault: Case study of the Mosha Fault, Central Alborz Range, Iran, *J. Struct. Geology* **30(12)**, 1507-1519.

Zanchi, A., Berra, F., Mattei, M., Ghassemi, M.R. & Sabouri, J., 2006. Inversion tectonics in central Alborz, Iran, *J. Struct. Geology* **28(11)**, 2023-2037.

Zielke, O., & Arrowsmith, R.-J., 2006. Numerical Simulation of Fault Interaction in a Trans-Tensional Setting, the La Paz Los Cabos Region, Baja California, Mexico., Eos Trans. AGU, 87(52), Fall Meet. Suppl., Abstract T41D-1613.

Zielke, O., & Arrowsmith, R.-J., 2007. Empirical Relationships Among Magnitude and Surface Rupture Characteristics of Strike-Slip Faults: Effect of Fault (System) Geometry and Observation Location, Dervided From Numerical Modeling, Eos Trans. AGU, 88(52), Fall Meet. Suppl., Abstract T33C-1488.

Zoback, M.D., Zoback, M.L., Mount, V.S., Suppe, J., Eaton, J.P., Healy, J.H., Oppenheimer, D., Reasenberg, P., Jones, L., Raleigh, C.B., Wong, I.G., Scotti, O. & Wentworth, C..

1987. New evidence on the State of Stress of the San Andreas Fault System, *Science* **238**, 1105-1111.

Zreda, M.G., Phillips, F.M. & Elmore, D., 1994. Cosmogenic $^{36}Cl$ accumulation in unstable landforms 2. Simulations and measurements on eroding moraines, *Water Resources Research* **30(11)**, 3127-3136.